Electrochemical Detection of MicroRNA

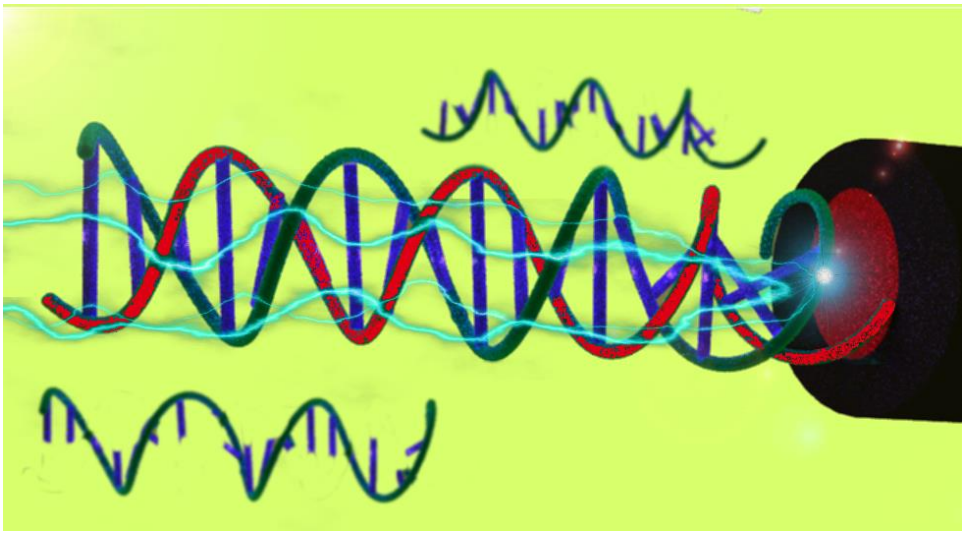

Daniel Aaron Smith

Cardiff University

School of Chemistry

A thesis submitted for the degree of Doctorate of Philosophy

September 2017

CARDIFF UNIVERSITY

PRIFYSGOL CAERDYDD

GWENT GROUP
ADVANCED MATERIAL SYSTEMS

Part of:-
SunChemical®
a member of the DIC group
Color & Comfort

BBSRC
bioscience for the future

Declaration

This work has not been submitted in substance for any other degree or award at this or any other university or place of learning, nor is being submitted concurrently in candidature for any degree or other award.

NAME: DANIEL SMITH

SIGNED:

DATE:

STATEMENT 1

This thesis is being submitted in partial fulfilment of the requirements for the degree of PhD.

NAME: DANIEL SMITH

SIGNED:

DATE:

STATEMENT 2

This thesis is the result of my own independent work/investigation, except where otherwise stated. Other sources are acknowledged by explicit references. The views expressed are my own.

NAME: DANIEL SMITH

SIGNED:

DATE:

STATEMENT 3

I hereby give consent for my thesis, if accepted to be available for photocopying and for inter-library loan, and for the title and summary to be made available to outside organisations.

NAME: DANIEL SMITH

SIGNED:

DATE:

For those who reach their ceiling and choose to break through it, because the only limit to your creativity is your tenacity, resolve and a touch of inspiration

"We keep moving forward, opening new doors, and doing new things, because we're curious and curiosity keeps leading us down new paths."

-Walt Disney

"I have great faith in fools; self-confidence my friends call it."

-Edgar Allen Poe

Acknowledgements

Oh what a long, stressful and yet incredible journey this has been. There have been lots of ups and just as many downs but now that the end is in sight it is necessary to thank the people that have joined me on this epic adventure, of which there are far too many to name individually.

First and foremost I would like to thank my supervisors, Dr. James Redman and Dr. Timothy Bowen for their incredible patience and guidance throughout this project, always being there to help steer my research back on course when the data wasn't working as hoped or when the stress was becoming too much. I would also like to thank the team at Gwent Electronic Materials, Dr. Robin Pittson, Phil Nicholas, Brian Harrop and Rebekah Stibbs for welcoming me during my placement and for helping me to learn new electrode printing skills. A special mention to Matteo Lo Cicero for helping to collect the AFM images in the final chapters.

I would also like to thank the WKRU and the Nephrology institute for welcoming me to the team from day 1 and helping me develop my biological skills. Special thanks to Professor Donald Fraser for helping with the purchase of the multiplexer and potentiostat used in the latter chapters of this thesis, Dr. Lucy Newbury for teaching me in the ways of RT-qPCR and for our long talks in the molecular biology lab on life, the universe, and everything in between while performing said PCRs, and Dr. Adam Midgley for helpful suggestions, both for my academic life, personal life and my future career, as well as the many drinks (liquid courage) he has generously given over the last couple of years.

I would like to thank my family, particularly my Mum for helping me both emotionally and financially to make it this far, without her support and frequent bouts of reverse psychology, ("just go back to Tesco® if it's too hard" comes to mind) I would probably have thrown it in long ago. Throughout all of my life you have been a solid pillar of support and the work on and production of this thesis is no exception, I only hope that I can continue to grow and make something of myself in a way that complements all the hard work you have put in raising me and guiding me through life.

Finally thanks to my friends, who include in addition to those mentioned previously: Sophie Wheeler and Sarah Morris, with whom I have spent many evenings dancing, watching

musicals and movies, having long chats ironing out the stresses of life and of course finally braving the sea; our future trip to Disney (hopefully being the first of a tradition of big excursions) celebrating all of our achievements and also cementing our connection for life. The strong bond and close friendship between us, formed during this PhD, being one which I have no doubt will last a lifetime.

Jordanna Dally who despite our occasional fall outs and arguments (fairly standard among close friends I like to think), still manages to brighten up my bad days and find a way to make me happy again, be it with a joke, sarcastic innuendo, an attempt at a Star Wars quote (you still don't get to use them until you have seen all the movies), and often by just being in the room. The genuine feelings of closeness and affection I've felt since meeting you, having grown exponentially with every experience or event we've shared, ensuring that our friendship will stand the test of time.

Finally Adam Birch and Glyn Morris for always being there to lend an ear when I was struggling and boosting my spirits when I thought I had hit the lowest point. Adam, being my oldest and closest friend, always made himself available to talk to me when I was low, despite moving to Florida and starting the next big step in his own life, he was there when I needed him, either by phone, messages or by playing some online video games, boosting my spirits all the way through from undergrad and throughout the PhD; and Glyn, for always being available for a beer, a chat or some fun and games at the points when everything was getting on top of me. It is no over exaggeration to say that without you I would not have made it to this point, the experiences I have shared with you have genuinely greatly impacted the person I am today, and really, who would have thought I would wind up doing tough mudder and the Cardiff half marathon… twice!?

My utmost gratitude and love to you all.

Publications

Electrochemical detection of urinary microRNAs via sulfonamide-bound antisense hybridisation, Sensors and Actuators B:- Chemical, volume 253, pages 335-341, accepted 10th June 2017.

Presentations

Annual Cardiff Institute of Tissue Engineering and Repair (CITER) meeting, 17th and 18th September 2014, Stradey Park Hotel, Llanelli. POSTER PRESENTED

*AWARDED HIGHLY COMMENDED CERTIFICATE.

Cardiff Bio-Organic conference, Cardiff University, School of Chemistry, 16th January 2015. TALK GIVEN

*AWARDED JOINT SECOND PLACE

14th Cardiff Chemistry Conference, Cardiff University, School of Chemistry, 11th and 12th May 2015. POSTER PRESENTED

RSC Bio-organic Group Postgraduate Symposium, School of Chemistry, University of Bristol, 19th May 2015. POSTER PRESENTED

Advances in Regenerative Medicine: the road to translation, 3rd South West Regional Regenerative Medicine Meeting, Cadbury House, Congresbury, 22nd and 23rd September 2015. POSTER PRESENTED

*AWARDED HIGHLY COMMENDED CERTIFICATE

Wales Kidney Research Unit (WKRU) annual meeting, Science Hub, Cardiff Bay, 4th December 2015. POSTER PRESENTED

*AWARDED 1ST PLACE

1st GW4 Biosensor Workshop, East Building, University of Bath, 24th March 2016. TALK GIVEN

15th Cardiff Chemistry Conference, Cardiff University, School of Chemistry, 9th and 10th May 2016. TALK GIVEN.

Southwest RNA club meeting, Dorothy Hodgkin building, University of Bristol, 26th May 2016. TALK GIVEN.

Wales Kidney Research Unit (WKRU) second annual meeting, Postgraduate Centre Morriston Hospital, Swansea, 2nd December 2016. POSTER PRESENTED

*AWARDED 1ST PLACE

Speaking of Science conference, Haydn Ellis building, Cardiff University, 4th May 2017. TALK GIVEN.

CITER Annual Scientific Meeting, Cardiff University Postgraduate Teaching Centre, Cardiff Business School, Cardiff University, 18th-19th September 2017. TALK GIVEN.

Organised events and awards

Chair of postgraduate representatives (PGR) for Chemistry years 2014-2016.

Co-chair of CITERSoc years 2014-2015, organiser of annual CITERSoc conference entitled "Science of Survival: Averting global threats to life on Earth", Dec 15th 2015.

"Pint of Science." Organiser in 'Atoms to Galaxies' team for annual Pint of Science festival, first to be held in Wales.

"I'm a scientist get me out of here." Voted best scientist in Protactinium zone, 23rd June 2017.

*Awarded £500 for science communication based event.

Abbreviations

3’-UTR	3’-Untranslated Region
AFM	Atomic Force Microscopy
A,G,T,C,U	DNA/RNA bases Adenine, Guanine, Thymine, Cytosine, Uracil respectively
AGO2	Argonaute 2 protein
AKI	Acute Kidney Injury
ANSA	4-amino-3-hydroxy-1-napthalenesulfonic acid
ANSAm-DNA	4-amino-3-hydroxy-1-napthalenesulfonyl amide with DNA
ANSAm-DNA/miRNA	4-amino-3-hydroxy-1-napthalenesulfonyl amide with DNA and RNA hybrid
ANSCl	4-amino-3-hydroxy-1-napthalenesulfonyl chloride
ATP	Adenosine Triphosphate
ATR – FTIR	Attenuated Total Reflectance - Fourier Transformed Infra-Red
bFGF	Basic Fibroblast Growth Factor
BSA	Bovine Serum Albumin
CV	Cyclic Voltammetry
DGCR8	Di George syndrome Syndrome Critical Region 8
DN	Diabetic (kidney) Nephropathy
DNA	Deoxyribonucleic Acid
DPV	Differential Pulse Voltammetry
Ds	Double strand
DSN	Duplex Specific Nuclease
EIS	Electrochemical Impedance Spectroscopy
Fmoc	Fluorenylmethyloxycarbonyl

FTC	Follicular Thyroid Carcinoma
GCE	Glassy Carbon Electrode
GEM	Gwent Electronic Materials
hsa-(miR-xxx)	*Homo sapiens* i.e. human, (miR species-xxx)
ITO	Indium Tin Oxide
LA-ICPMS	Laser Ablation - Inductively Coupled Plasma Mass Spectrometry
LNA	Locked Nucleic Acid(s)
MiR	Specific Micro RNA species
MiRNA	Micro RNA
mRNA	Messenger RNA
NHE	Normal Hydrogen Electrode
NHS	National Health Service
Nt	Nucleotide(s)
PBS	Phosphate Buffer Solution
PCTFE	Polychlorotrifluoroethylene
PNA	Peptide Nucleic Acid(s)
Pri-miRNA	Primary Micro RNA
PTC	Papillary Thyroid Carcinoma
RCA	Rolling Circle Amplification
RISC	RNA- induced Induced Silencing Complex
RNA	Ribonucleic Acid
RRT	Renal Replacement Therapy
RT-qPCR	Reverse Transcriptase Transcription – Quantitative Polymerase Chain Reaction
SPPS	Solid Phase Peptide Synthesis
TGFBR2	Transforming Growth Factor β Receptor II
TM-AFM	Tapping Mode - Atomic Force Microscopy
TMD	A buffer of Tris. HCl and $MgCl_2$

VEGF	Vascular Endothelial Growth Factor

Abstract

Members of the recently discovered family of short non-coding RNAs, termed microRNAs (miRNAs), regulate the expression of most genes encoded by the human genome by repressing translation of messenger RNAs to proteins. MiRNAs are stably expressed throughout the body and can be detected robustly and reproducibly by RT-qPCR in body fluids such as blood and urine. Alterations in circulating miRNA profiles have been associated with cancers of the brain, breast and liver, and miRNAs hold great promise as biomarkers of numerous other diseases. However, current methods for miRNA biomarker detection rely on laborious, expensive and expert techniques, and involve invasive biopsy acquisition. The research contained within this thesis focusses on the development of a non-invasive, inexpensive and rapid electrochemical analytical test to quantify miRNA in human urine samples.

Therefore we describe how glassy carbon and disposable screen printed carbon electrodes (SPCEs), were modified through electropolymerisation of a naphthalene sulfonic acid derivative. DNA complementary to a target miRNA was attached and the sensor analysed via electrochemical methods using a ferri/ferrocyanide electrolyte. After hybridising with a miRNA target, this analysis was repeated and compared to the original DNA-only analysis to give a corresponding change. This was performed using buffered solutions and shown to be sensitive to 20 fM and selective against sequences with a single mismatch; urine analysis was also performed. The method was then adapted for use with screen printed electrodes, using a new chlorination solvent system, to a lowest detected concentration of 10 fM. The ink materials used for the production of the SPCEs were optimised and a new design developed to allow for multiple analyses on one sensor. A small number of diabetic kidney nephropathy (DKN) patient and healthy control urine samples were then analysed for biomarkers we have recently identified, comparing their relative expression levels.

Table of Contents

Declaration i
Acknowledgements iv
Publications vi
Presentations vi
Organised events and awards viii
Abbreviations ix
Abstract xii
Table of Contents xiii
Chapter 1: Introduction 2
1.1: MicroRNAs 2
1.1.1: MicroRNA History 2
1.1.2 MicroRNA Biogenesis. 3
1.1.3 Biological role of miRNA 4
1.1.4 MiRNAs as biomarkers. 6
1.1.5 MiRNAs in Kidney disease and Nephropathy 9
1.2: Current microRNA detection methods. 12
1.2.1: Base pairing theory, hybridisation and antisense probes. 12
1.2.2: Peptide Nucleic acid 15
1.2.3: Reverse transcription-quantitative polymerase chain reaction (RT-qPCR) 21
1.2.4: Fluorescence and chemiluminescence 23
1.2.5: Northern blotting 29
1.2.6: Electrochemical based techniques 32
1.3: Electrochemistry fundamentals 32
1.3.1: Redox chemistry and general electrochemical set-up 32
1.3.2: Cyclic voltammetry (CV) 35
1.3.3: Chronocoulometry / amperometric analysis 38
1.3.4: Electrochemical impedance spectroscopy (EIS) 43
1.4: Surface chemistry analysis techniques 49
1.4.1: Attenuated total reflectance - Fourier transform infra-red spectroscopy (ATR-FTIR) 49
1.4.2: Atomic force microscopy (AFM) 51
1.4.3: Laser ablation - inductively coupled plasma mass spectrometry (LA-ICPMS) 52
1.5: Research aims and impact 54
Chapter 2: Glassy Carbon Electrode Results 57
2.1: Glassy carbon and other electrode materials 57

2.2: Modification procedure 59
2.3 Sensitivity and Selectivity Results 66
2.4 Synthetic urine experiments 75
2.5 Urine analysis 78
2.6 Summary of the results obtained. 89
Chapter 3: Screen printed electrode prototypes. 92
3.1: Introduction to screen printed electrodes 92
3.2: Initial prototyping of the electrodes. 94
3.3: Using SPCEs with an increased working area diameter. 106
3.4: Surface imaging and analysis techniques. 109
3.5: Chapter conclusions. 125
Chapter 4: Multi-electrode array prototyping 128
4.1: Introduction to screen printing methodology 128
4.2: Aims for the design of the multi-electrode array and remaining prototyping. 130
4.3: Testing the carbon ink materials. 131
4.4: Optimising the silver/silver chloride and dielectric inks. 134
4.5: New design for multiple miRNA detection. 139
4.6: Optimising the deposition procedure 141
4.7: Optimising the chlorination procedure 144
4.8: First sensitivity tests 145
4.9: Comparison between healthy control urine and patient samples 150
4.10: AFM imaging of new carbon ink 152
4.11: Conclusion 159
Chapter 5: Epilogue 163
5.1: Appraisal and discussion 163
5.2: Future work 165
Chapter 6: Materials and methods 170
6.1 Experimental procedures used throughout Chapter 2. 171
6.1.1 Glassy carbon electrode polishing procedure. 171
6.1.2 Electrode modification procedure 172
6.1.3 Hybridisation timescale optimisation 173
6.1.4 Sensitivity determination 173
6.1.5 Selectivity determination 173
6.1.6 Synthetic urine analyses 174
6.1.7 Urine analysis 174
6.1.8 RT-qPCR based calibration 176

6.1.9 RT-qPCR urine analysis 176
6.1.10 PNA based negative control 177
6.1.11 PNA based positive control 177
6.1.12 RNase controls 178
6.1.13 Shelf life of the sensor 178
6.1.14 Biosensor regeneration procedure 178
6.2 Experimental procedures of Chapter 3 179
6.2.1 Initial testing of the full modification procedure 179
6.2.2 Solvent compatibility testing 179
6.2.3 IR analysis 180
6.2.4 Modification procedure using hexane solvent 180
6.2.5 Final modification procedure using hexane and applied nail hardening resin 181
6.2.6 Sensitivity determination of screen printed electrodes 181
6.2.7 AFM based surface imaging 181
6.3 Experimental procedures of Chapter 4 182
6.3.1 Testing the carbon ink 182
6.3.2 Testing the silver/silver chloride ink 182
6.3.3 Testing the dielectric inks. 183
6.3.4 Optimising the deposition of sulfonic acid 183
6.3.5 Optimising the chlorination 184
6.3.6 miR-21 sensitivity testing 184
6.3.7 Optimised modification procedure for urine analysis 185
6.3.8 AFM imaging of new inks 186
References 187
Appendix 1: Chapter 2 additional data. 197
Appendix 2: Chapter 3 additional data. 209
Appendix 3: Chapter 4 additional data 215
Appendix 4: Sensors and Actuators B: Chemical publication. 218

Chapter 1: Introduction and Literature Review

Chapter 1: Introduction

1.1: MicroRNAs

1.1.1: MicroRNA History

MicroRNAs are a class of small (19-23 nt), single stranded and non-coding RNA molecules that were first discovered by Lee *et al.*[1] in the *Caenorhabditis elegans* species of roundworm. This group first isolated the microRNA species Lin-4 and found it to have antisense complementarity to the messenger RNA (mRNA) Lin-14, which encodes the embryonic protein of the same name. The binding of several Lin-4 miRNAs to the 3' untranslated region (UTR) of Lin-14 results in a downregulation of the downstream Lin-14 protein, which in turn changes the developmental timing of the roundworm larvae.[1,2] Despite this, when first isolated it was assumed that, due to their size and relative instability, they were most likely specific only to the simpler roundworm organisms. However when the developmental timing miRNA species, let-7, was found to be conserved across various other species, interest into their biological importance exploded.[3,4] This particular family of miRNA is also believed to be the first human microRNA discovered, and is now known to play a key role in the development of certain cancers.[5,6]

Since then the number of publications on miRNAs and their biological significance has grown exponentially, with many new miRNA species being discovered each year. In fact, at the time of writing there are currently 28645 entries in the miRNA database (miRbase) with over 2000 of these being human, targeting more than 30% of the human genome.[7–9] Owing to their small size, miRNAs are able to hybridise with target mRNAs with perfect or minor imperfect complementarity, also their relatively short sequences compared to these mRNAs results in any one microRNA sequence being found either in a close or perfect match in a number of mRNA families. The high potential for a particular miRNA sequence to occur multiple times throughout mRNA species often result in one miRNA having multiple mRNA targets, also meaning that each miRNA species can have a variety of downstream phenotypic effects on the gene expression and protein production.[7] Although in healthy biological processes there will be a driving bias towards the biogenesis of sequences required to maintain phenotypic status quo.

1.1.2 MicroRNA Biogenesis.

MiRNAs are biosynthesised according to sequence information given in the miRNA gene via a multiple step biogenesis pathway. Initially they are transcribed according to the sequence of their antisense DNA, found in the miRNA gene, by the enzyme RNA polymerase II.[10] This produces the hairpin structured primary miRNA termed "pri-miRNA" which is approximately 1000-3000 nucleotides (nt) in length. This pri-miRNA is then converted into smaller stem loop strands of approximately 70-100 nt length using the Drosha RNase III enzyme and the complex subunit Di George syndrome critical region gene 8 (DGCR8), a double stranded RNA-binding protein also known as Pasha in *Drosophila melanogaster* and *Caenorhabtis elegans*.[7,11–13] This newly formed pre-miRNA (precursor miRNA) is transported out of the nucleus, to the cytoplasm of the cell, via the karyopherin (transport protein) Exportin-5.[11,14] Once inside the cytoplasm the pre-miRNA undergoes further cleavage and processing via dicer proteins, RNase III enzymes and an RNA binding protein to form a double-stranded (ds) miRNA duplex miRNA:miRNA*. This duplex contains two single stranded (ss) miRNA molecules, the guide strand miRNA and the passenger strand miRNA*.[11] Finally this duplex is denatured to reveal the guide strand, which is incorporated into an RNA-induced silencing complex (RISC), while the passenger strand is often degraded and the nucleotides recycled.

The RISC complex is then able to bind, perfectly or imperfectly, to the 3'-untranslated region (3'-UTR) of its target mRNA, which in turn results in downstream regulation of gene expression through mRNA degradation or by inhibiting the translation of said mRNA. This final complexation mechanism is what gives miRNA their profound effect on protein and gene regulation.[1,7,11,12,14,15] Figure 1.1 shows a general summarised overview of this biogenesis pathway as adapted from reference 10.

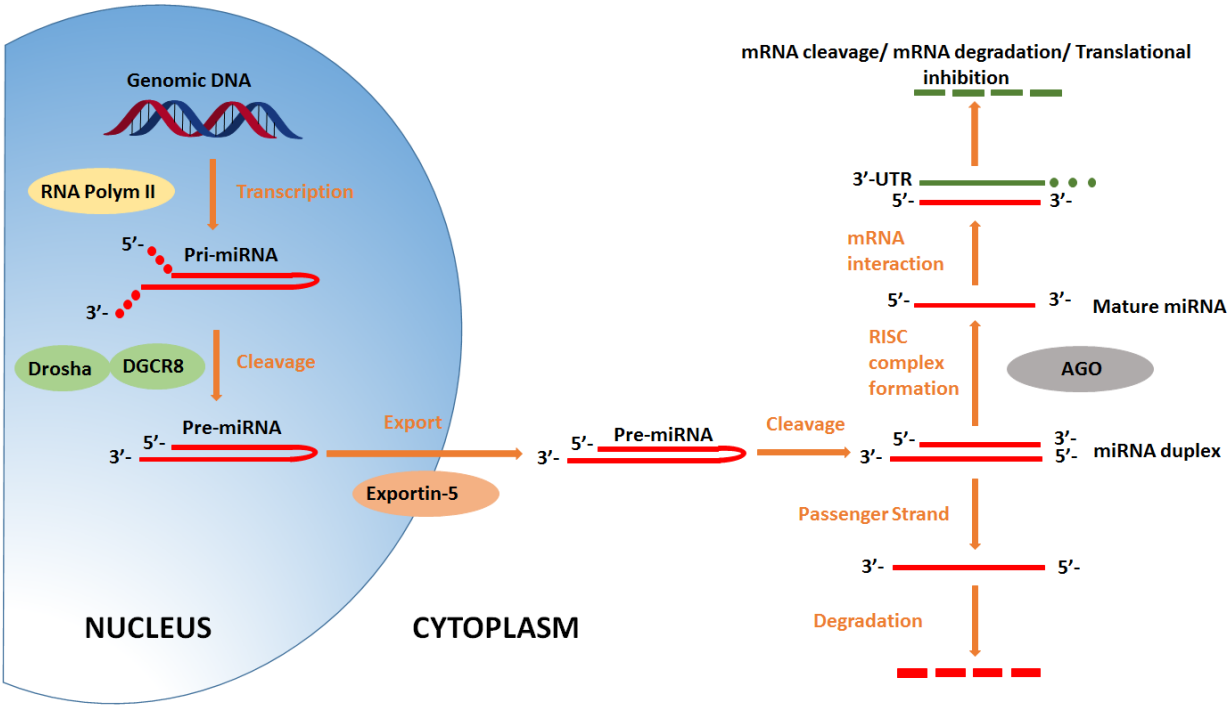

Figure 1.1 A summarised overview of miRNA biogenesis.

1.1.3 Biological role of miRNA

As mentioned, miRNAs have a detrimental effect on mRNA translation and act, therefore, as post-transcriptional regulators of gene expression. Upon incorporation into the RISC complex, including argonaute (AGO2) protein a Mg^{2+} dependant endonuclease,[11,16,17] the miRNA sequence behaves as an antisense sequence in order to bind to the 3'-UTR of its mRNA target. This it does either perfectly, allowing the endonuclease and AGO2 proteins to cleave the mRNA, or imperfectly leading to inhibition of translation and/or further degradation of the mRNA strand.[18]

Controlling the expression of genes is essential for a number of cellular processes, not just the larval developmental timing mentioned earlier. MiRNAs have also been found to be important in cell proliferation and death, apoptosis, cell differentiation and even fat metabolism.[19–22] Combined studies have also suggested that they are important in removing persistent mRNA that have fulfilled their purpose in the cell but whose continued presence could be potentially harmful. MiRNA induced degradation removes such strands faster than their own intrinsic decay mechanisms, such as enzymatic hydrolysis and degradation by exoribonucleases e.g. Xrn1.[22–24]

The relatively short length of miRNAs, compared to mRNAs, results in a high potential for complementarity with a number of different mRNA species sequences, thus one species of microRNA could possibly have multiple mRNA targets. For example miR-21 targets over 30 gene targets for apoptosis alone, including B-cell chronic lymphocytic leukaemia/lymphoma 2 (BCL2)[25] and transforming growth factor - beta receptor II (TGFBR2),[26] as well as having at least one target in each stage of the development of cancer cells as described by Hanahan *et al.*[27,28] and shown in Figure 1.2 adapted from reference 24. This miRNA species has been shown to be oncogenic by having an inhibitory effect on cellular apoptosis, and is therefore often highly abundant in cancerous cells.[29,30]

However another species, miR-16, which among many other things is also associated with various forms of cancer, actually displays tumour suppression activity.[31,32] It does this in a number of ways, primarily through targeting the genes responsible for vascular endothelial growth factor (VEGF) and basic fibroblast growth factor (bFGF) proteins and repressing their expression,[33,34] as a result, in multiplying cancerous cells, this miRNA species often displays a much lower expression. These two brief examples show that microRNA not only have multiple mRNA gene targets, but they can also have an inhibitory effect on a cells growth processes or an activation effect depending on its target.

Of course, it is important to note that miRNA also have the potential to block mRNA expression in other areas of physiology, including those that are common to all cells. Because of this it has been suggested that there are certain genes that have been pre-programmed to avoid miRNA regulation, termed “antitargets”, and have sequences that are under selective pressure to resist miRNA binding, often via shortened 3’UTR’s with fewer potential miRNA binding sites.[35,36] These mRNA can be found intact in cells where miRNAs are also expressed.[37] The target mRNA however tend to be localised to specific cells and used in developmental processes.

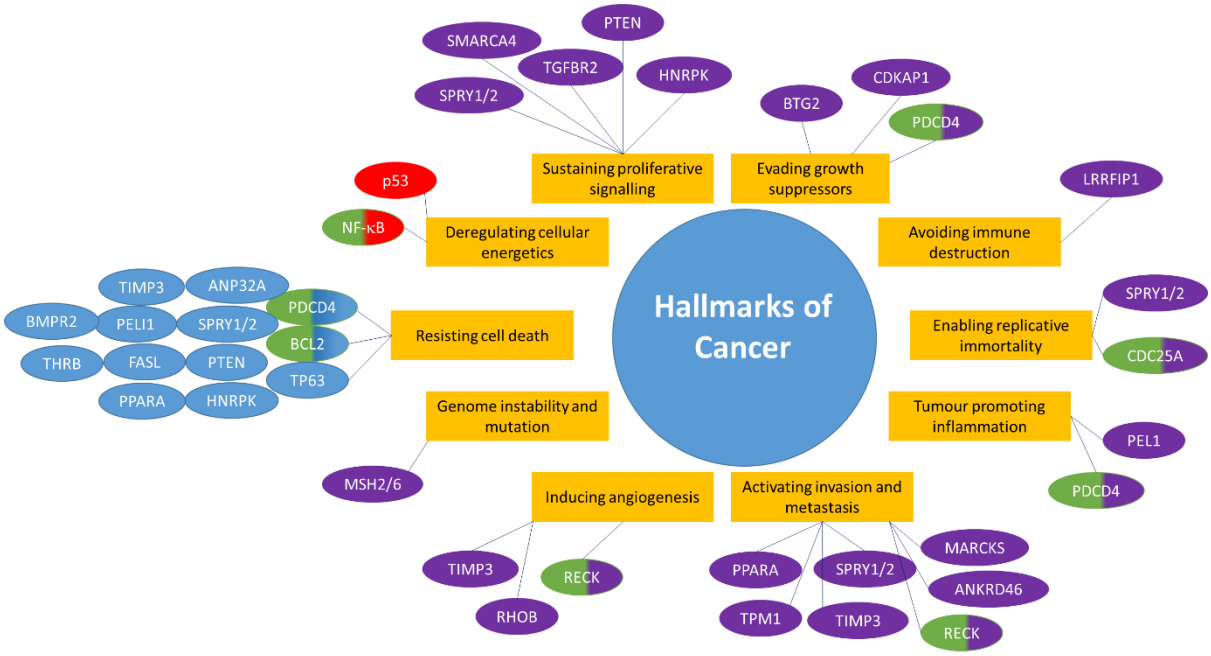

Figure 1.2 The gene targets for miR-21 that form the hallmarks of cancer. Those in blue are apoptosis specific, those in red are involved in glucose flux and oxidative phosphorylation. The green targets show those that are also targeted by miR-16 showing how multiple miRNAs can also target the same genes.[27,38–43]

1.1.4 MiRNAs as biomarkers.

As mentioned previously, the influx of research into the biological roles of miRNAs has shown that they have the potential to target many cellular processes. However as these processes are overstimulated or impeded in diseased states, as is the case in cancers,[44] trauma[45] and acute kidney injury (AKI),[46] interest grew into whether or not the microRNAs that target the genes involved in these processes would also change in expression. This would allow microRNA levels to be related back to a specific disease, and therefore give them significant biomarker potential.

In late 2002, Calin *et al.* were one of the first groups to formally identify microRNA expression as a biomarker for B cell chronic lymphocytic leukaemia (B-CLL).[47] They successfully managed to show that the genes for both miR-16 and miR-15 are located at chromosome 13q14, and that when this chromosomal region is deleted in B-CLL patients, the miRNAs expression is either down regulated or absent completely in at least 68% of cases. This finding confirmed the potential of miRNAs as biomarkers, and even more excitingly, as biomarkers for otherwise deadly diseases such as cancers. Since then, research into the field of miRNA discovery, as well as their use as therapeutics[48] and as biomarkers, has grown exponentially with new miRNAs and methods to quantify them being published every week.

MiRNA have been shown to be prevalent not only in cell lysates[49] and tissue samples[50], but also in blood[51], serum[52], faeces[53], saliva[54] and urine[11,55]. This last source is of particular interest, and as such forms the basis of the research in later chapters, due to its easy collection, relatively easy handling and high availability in clinical settings. Due to the presence of multiple RNase enzymes in biological extracts and excreta these miRNAs need to be protected to prevent their hydrolysis and allow them to be found in sufficient quantity for detection. Conveniently organisms actually supply this protection themselves, during natural cellular processes, in the form of AGO proteins and extracellular vesicles.[56]

By binding to an AGO protein the miRNAs are prevented from entering the active site of the RNase enzymes, therefore slowing their rate of degradation enough to allow them to be detected and analysed. In fact, Beltrami *et al.*[57] have shown that association with AGO proteins can stabilise the miRNAs in such a way that a miR-16 sample was still detectable in urine medium, at more than 50% of its starting expression, after being left at room temperature for 24 hours, compared to a miR-39 control which dropped to less than 10% expression after only 1 hour. This stabilisation was even effective enough to protect the miR-16 from complete degradation via additional RNase A treatment for 15 minutes whereas the miR-39 spike was completely hydrolysed in less than 1 minute. Once removed from these AGO proteins, however, the miRNAs once again become susceptible to rapid degradation by the RNase enzymes in the biological matrix. This effect was also shown in the work performed by Beltrami *et al.* through their use of proteinase K to degrade the associated proteins, resulting in a significant drop in relative expression after 30 minutes incubation, vs. a sample that remained untreated.

Although the miR-16 species investigated in the work performed by Beltrami is predominantly protein associated, some miRNA species are maintained within extra-cellular vesicles. These include miRNAs found in saliva and serum particularly, but also to a lesser extent in urine.[57,58] Being encased by vesicles also helps to protect the RNA from enzymatic degradation and, for the purposes of miRNA detection and analyses, the vesicles have to be broken apart to release the miRNA into bulk aqueous solution. This has been done in a number of ways but the most common of these are either with chemical lysing agents[57,59,60] or by mechanical breakdown using a sonicator.[60] These stabilisation effects are vital in allowing the endogenous

microRNAs, present in patient urine samples, to survive long enough to be effectively extracted, isolated and quantified for the purposes of biomarker analysis.

As eluded to earlier, the relative expression levels of microRNA have been shown to relate directly to a number of disease states. This, along with the fact that they are sufficiently protected from degradation in various biological fluids, makes them ideal for use in biomarker diagnostics. Throughout the work presented in later chapters there are two microRNA species of interest, miRNAs 21 and 16, whose expression levels have been associated with the onset of cardiac disease[61] and B-CLL[47] respectively as well as both being linked to various cancers.[32,62] However they have been chosen specifically due to our interest in urinary biomarkers for kidney diseases.

Work performed by Wang *et al.*[63] has shown that an increase in miR-21 expression is observed in urine of fibrotic kidney patients, and Mukhadi *et al.* report that miR-16 is down regulated in patients with acute kidney injury (AKI).[64] These observations are important, not only as useful biomarkers in nephrotic diseases, but also because it shows an important feature of microRNAs as biomarkers. This being that microRNA expression can be either up regulated or down regulated in disease states, therefore any change in relative expression should be explored as an important observation. It is important to note however that, owing to one microRNA being related to multiple diseases, the expression of multiple microRNA species should be investigated simultaneously in order to increase the reliability of any diagnosis made from their analysis.

Another important microRNA of note that is used in later chapters is *C. elegans* miR-39, this is used not only as a house-keeping miRNA in RT-qPCR but also as a control target sequence in electrochemical urine analyses. This target has no known human orthologue and can therefore be used to distinguish between a true miRNA analysis and any interference.

Seeing that the levels of microRNA are directly linked to a number of diseases throughout the body, it may also be possible to analyse other sequences, and assist with the diagnosis of patients with a variety of different illnesses through the analysis of these miRNAs' expression levels. For instance, miRNAs 21 and 16 have already been discussed as targets in kidney disease, heart disease, B-CLL and cancers;[32,62] however there are a vast number of other miRNA species which have a direct role in a number of ailments and may potentially be used

as an indicator for a wide array of disorders from the aforementioned cancers and auto immune diseases,[65] right through to genetic disorders,[66] malaria[67] and arthritis.[68] Figure 1.3 shows how miRNA expression can be linked to diseases throughout the body, giving a visual indication of how important a microRNA biosensor could be to the medical community.

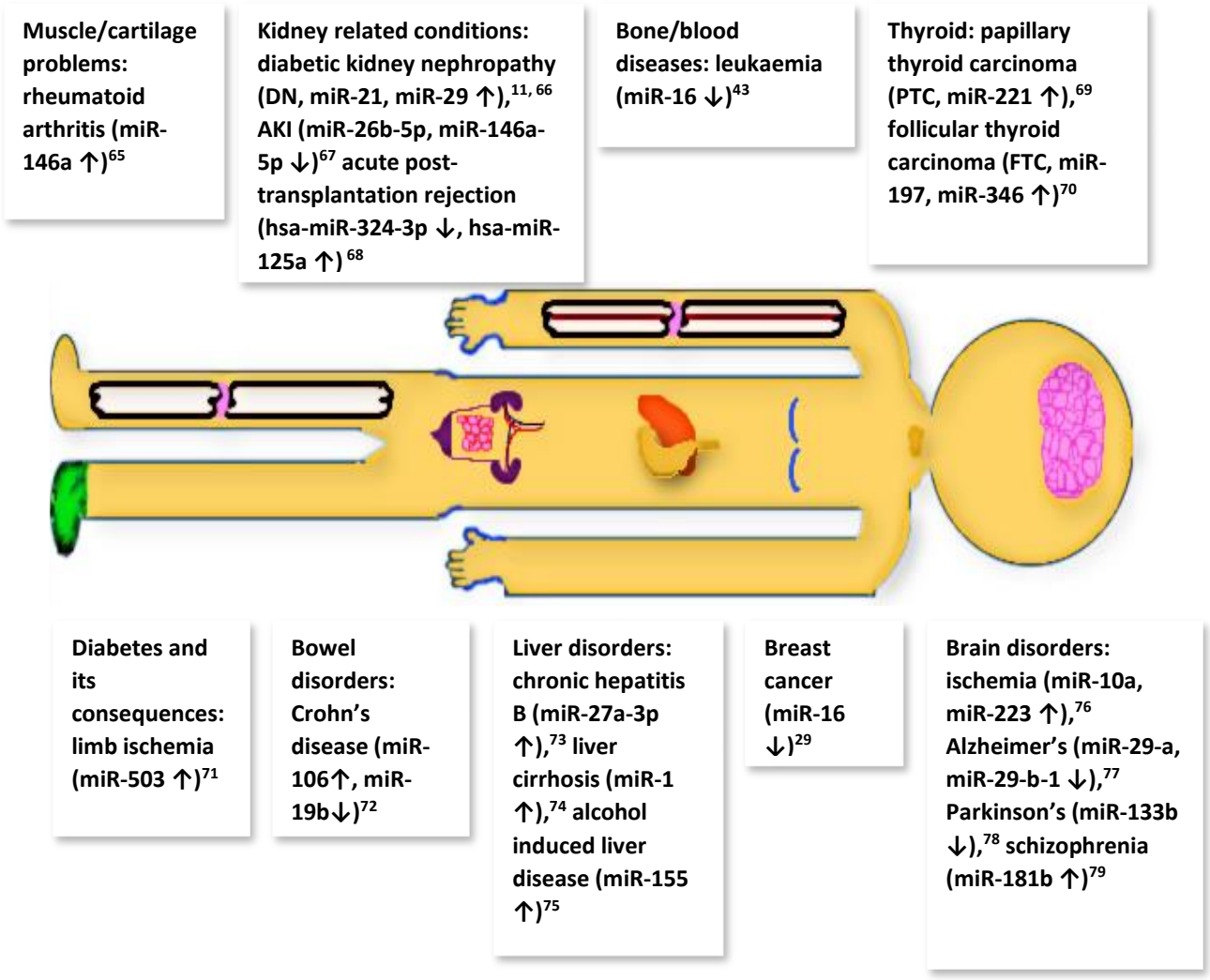

Figure 1.3 A pictorial representation of how microRNA expression may act as an important biomarker for diseases throughout the body. The corresponding dysregulation is indicated by the arrow, ↑ being an up-regulation and ↓ being a down regulation, the ability to detect these dysregulations would demonstrate the potential diagnostic application of a new quantification technique.[11,69–83]

1.1.5 MiRNAs in Kidney disease and Nephropathy

Of interest to the research performed in the Institute of Nephrology at Cardiff University is the role microRNAs play in kidney diseases, nephropathy and acute kidney injury. In particular a number of researchers are doing work dedicated to determining which microRNA species expression levels can be related to a particular disease state. With these results indicating the subsequent need for fast and accurate quantification of these miRNAs.

According to kidney research UK,[84] and reports and newsletters from the Renal Association UK renal registry, chronic kidney disease costs the national health service (NHS) around £1.45bn each year in England alone, and by the end of December 2012, ≈55,000 people were receiving renal replacement therapy (RRT). Of these 27,621 were given a kidney transplant, 22,331 were receiving haemodialysis at hospital, 3,792 were on peritoneal dialysis and 1,080 were on haemodialysis at home;[85] and the latest report shows that these numbers are rising rapidly.[86] Despite this, currently around 3,700 people die each year while on dialysis and 250 die waiting for a transplant.[84] It is also mentioned that the majority of renal failure incidents occur as a result of diabetes complications and with 3,590,501 people having been registered as diagnosed in the 2016 quality and outcomes framework. With the inclusion of undiagnosed cases, an approximate 4.5 million people are living with diabetes according to Diabetes UK,[87] setting the stage for kidney problems to become an even bigger strain on the NHS and its patients.

Having a way to quickly and painlessly predict the onset, or presence of, kidney disease or diabetes could therefore help to lower the number of new kidney patients requiring RRT, thus decreasing the financial impact on the NHS, but also giving potential sufferers an 'early warning' allowing them to receive the most appropriate treatment in a timely manner improving their prognosis and their quality of life.

To this end, research mentioned earlier, performed by members of the Cardiff Institute of Nephrology, has shown that the levels of microRNA in urine has the potential to predict chronic kidney disease (CKD) and injury,[55] and for those already on peritoneal dialysis (PD) their 'cloudy' PD fluid can also be analysed for the expression of a second miRNA species to gain information on the presence and/or extent of peritonitis.[88] It is also worth mentioning that in some cases the expression of select microRNA species analysed can be specific to a particular stage of a disease or a particular infectious bacteria,[89] giving specific details of, and not just being indicative of, the disease present. Thus if it were possible to quickly, cheaply and accurately analyse a patient's urine sample/PD fluid for microRNA quantification, a personalised care approach may become possible. An approach resulting not only in better prognoses for the patients, but also lowering the use of broad spectrum antibiotics (which is becoming a significant problem due to resistant bacteria e.g. MRSA),[90] and reducing the

number of kidney transplants or dialysis treatments required. All of this potentially saving the NHS money that may usually have been spent on more ineffective treatments.

As a result of these benefits the work performed throughout this project focussed on the development of a new method of microRNA detection and then applying it to the analysis of isolated solutions of synthetic miRNAs, before moving on to the analysis of clinical urine samples. Currently the extraction, isolation and quantitative analysis of microRNA involves the use of time consuming, laborious, expensive and often specialist techniques. In particular these include blotting techniques,[91] electrophoresis,[92] fluorescence tagging[93] and, the current 'gold-standard' technique for nucleic acid quantification, RT-qPCR.[57] Each of which will be described in detail, with some examples of research groups who implement them and how, in subsequent sections. However, these techniques all suffer from significant drawbacks, limiting their widespread application in medical devices and diagnostics.

First and foremost these techniques are expensive and most currently require some form of expertise, such as adequate knowledge of how to handle lysing agents, nucleotide primers and organic solvents for RNA extraction. A knowledge of the technique being necessary particularly for any times where the extraction does not occur as standard. Alternatively specialist equipment may also be required, such as PCR machines, automated thermocyclers and/or spectrophotometers. Also with the need for specialist equipment comes an increased time demand. An RT-qPCR with extraction for example can take 2-3 days, but also the need for a point of care diagnostician to send samples to a central laboratory, where the equipment is maintained, also results in a time expense. This obviously also increases the likelihood of contamination and/or handling errors, but also increases the time between assessment and diagnosis, possibly causing a disease to spread or become more severe. Finally, an often overlooked issue is that at present the majority of these analyses are performed with blood, serum or tissue samples, requiring uncomfortable or even painful invasive procedures and increasing the chance of secondary infection.

The research presented in this project therefore focuses on electrochemical analytical methods for the detection of microRNA from urine samples. Electrochemical methods, requiring relatively cheap equipment, being simple to perform (blood glucose sensors are already utilising a similar technique),[94] and giving results within seconds, are the obvious choice of analysis for adapting microRNA quantification techniques into point of care

diagnostics. Furthermore, the ability to use readily available urine as the analyte removes any need for invasive sample collection procedures, improving the assessment experience for both patients and diagnosticians. Any new diagnostic biosensor that can be developed based on these techniques, with an eye towards future commercialisation and practical application as a one-time use 'dip stick', will therefore not only be important for clinical nephropathy, but also in the wider medical community as well.

The majority of the sensor examples discussed later will describe themselves as biosensors, as is the case in our own research, however it should be noted that this may not be strictly the correct definition of the technology described. A biosensor would tend to indicate a probe that is able to be used and then regenerated completely over multiple cycles, however most of the examples described throughout are either single use after modification (as in Northern blotting and fluorescence based) or are moderately reproducible for 2 or 3 iterations. A better description of these technologies would be to call them dosimeters. These describe a single use test where once the result has been obtained the probe either needs to be fully recycled before it can be reused (recoverable dosimeter) or is disposed of completely. The disposable screen printed electrodes described in chapters 3 and 4 are examples of a dosimeter. Another common example are radiation dosimeters for determining radiation exposure levels in medical professionals.[95]

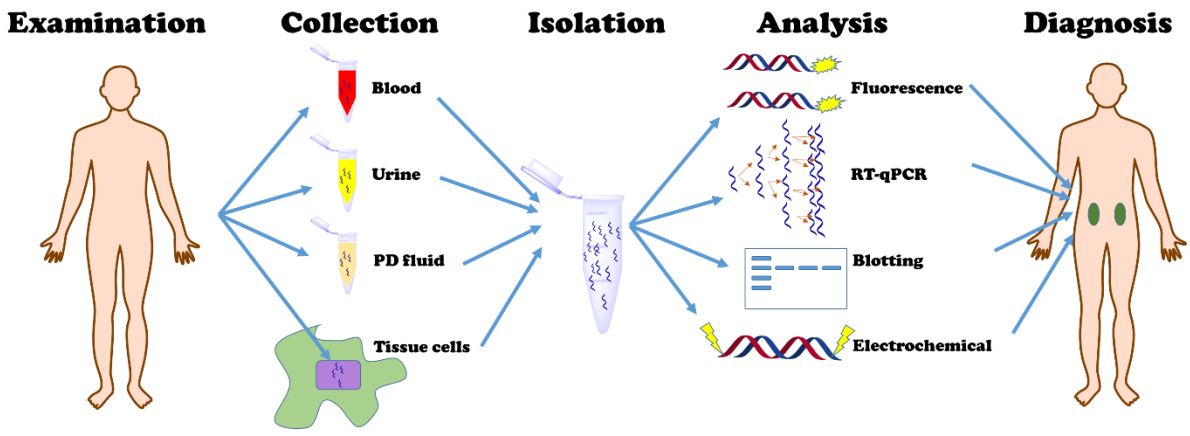

Scheme 1.1 A schematic of the process by which microRNA can be used as a diagnostic biomarker.

1.2: Current microRNA detection methods.

1.2.1: Base pairing theory, hybridisation and antisense probes.

There are a number of analytical techniques currently used in the analysis of microRNAs, each of which will be discussed briefly in the following section, however they are generally all based

around the same nucleotide pairing and antisense phenomenon. Therefore it is fitting to give a short overview into the structure of DNA and RNA nucleotides and importantly how they can come together to form duplexes and hybrids that are sequence specific, thus giving the analysis techniques their specificity.

DNA and RNA chains are made up of nucleotide monomers, which in turn contain a ribose (RNA) or a deoxyribose (DNA) sugar, a phosphate linker forming the backbone and a nitrogenous base. These bases are either purine in nature as is the case for adenine (A) and guanine (G), or pyrimidine based as with thymine (T :- DNA only), cytosine (C) and uracil (U :- RNA only).[96] It is then the order that these bases are found in the DNA or RNA strand that define its sequence and thus the organism's phenotypical properties, which are established downstream by the presence and regulation of both genes, and the proteins that are being coded for by the organisms messenger RNA (mRNA). The sequence of these proteins being, in turn, determined according to its cellular DNA.[96,97]

Of particular importance for the purposes of antisense based nucleotide detection, be it DNA, RNA or miRNA based, are the bonds that form between two corresponding nucleobases in a duplex. So called Watson-Crick base pairs, they are formed by hydrogen bonding between two nucleotides from opposing purine/pyrimidine families that share the same number of hydrogen bond donation/acceptor sites, i.e. between cytosine and guanine, and between Adenine and thymine/uracil.[96,98] These pairs, consisting of 3 hydrogen bonds for cytosine and guanine and 2 for adenine with thymine/uracil, allow a single strand of nucleotides to act in molecular recognition of its sequence complement, thus allowing for the specific detection of one sequence in a solution of many. The generalised structures of these bases and their Watson-Crick base pairings are shown in Figure 1.4.

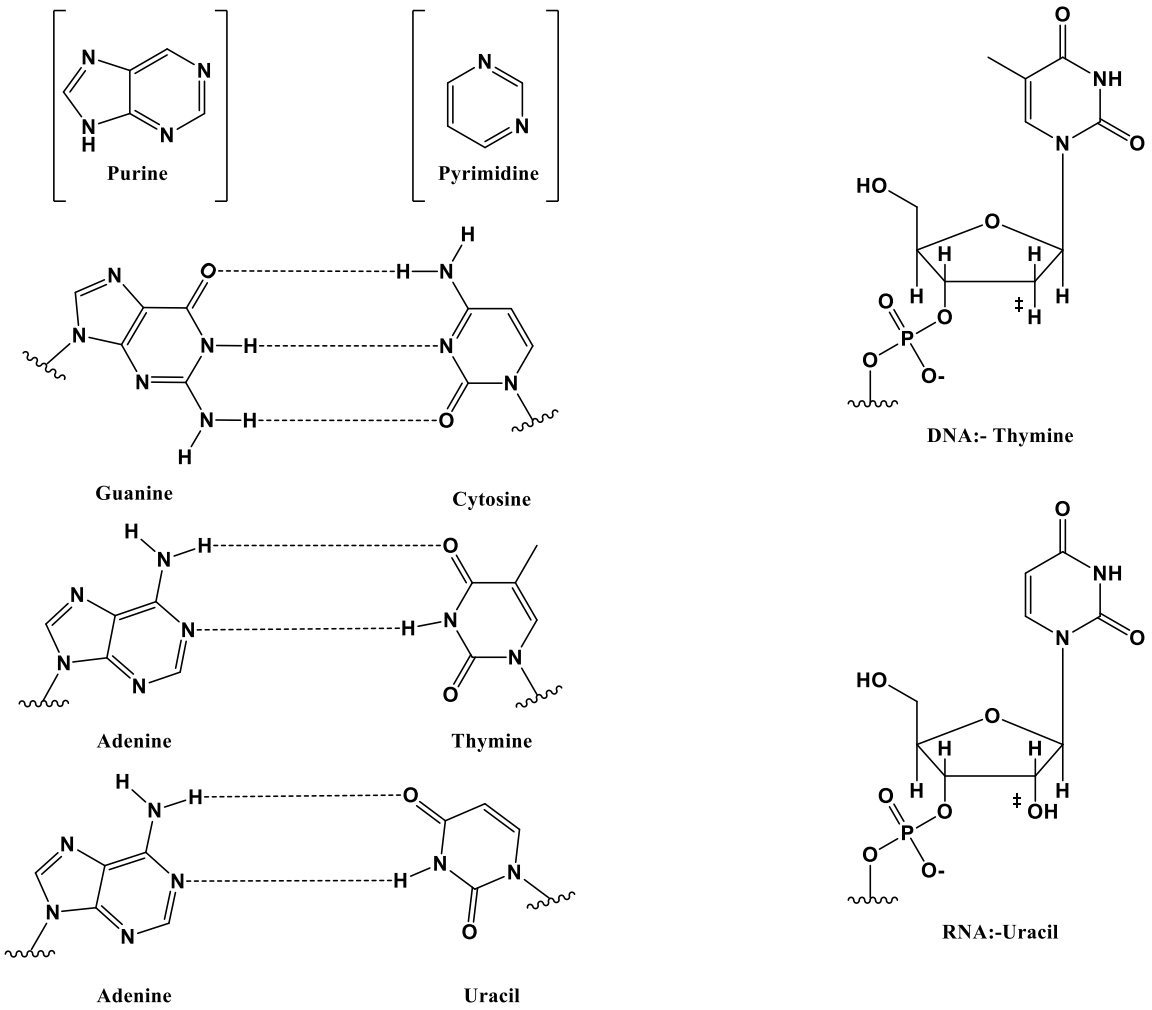

Figure 1.4 The different DNA and RNA bases shown with their Watson Crick base pairings and a generalised structure of both RNA and DNA. The difference in the ribose sugar for DNA and RNA is indicated with ‡ and the bases are placed according to their purine/pyrimidine family.

An important structural feature to note here is that RNA contains an extra OH group at the C2 position. This extra group has a structural effect of causing the ribose sugar to adopt the N-type confirmation (resulting in A type duplexes) which will be described further when discussing LNA analogues. However another important effect of this extra OH group is the resulting decreased stability of RNA towards hydrolysis, this extra OH group allows the base/enzyme catalysed attack of the neighbouring phospho-ester resulting in the cleavage of the ester bridge and separating the strand into two pieces.[99] This is the predominant reason for using DNA probe strands over RNA in many antisense based sensors and is also responsible for the rapid degradation of miRNA in particular, in the presence of RNases.

However, these are only the natural nucleotides, there have since been many synthetic analogues developed in order to increase the binding affinity towards a natural nucleotide

target sequence, resulting in greater sensitivities of the detection method and often enhancing the specificity. Before delving further into the specific techniques used for miRNA detection, using some examples of research groups that have used them and how, it is worthwhile to describe these unnatural analogues in order to further understand the theory behind them and why certain groups throughout the field implement them in their own biosensor technology.

1.2.2: Peptide Nucleic acid

The first of these unnatural analogues to be briefly discussed are peptide nucleic acids (PNAs), which contain the same nucleobases, however the sugar and phosphate backbone has been replaced by a series of amide linkages, making them similar in structure to a peptide, albeit with an ethyl spacer in the backbone between each base which would not be present in peptides. In PNA the nucleobase is bound to the amino moiety "*N*-terminus" via an amide linkage, generally with a bridging methylene (Figure 1.5).[100]

Since their initial invention, by Nielsen *et al*. in 1991,[101] the synthesis and resulting properties, particularly their binding affinities with naturally occurring DNA and RNA sequences, have been highly researched and modified. Generally these PNA molecules are synthesised using Fmoc based solid phase synthesis (SPPS),[102] however as the number of modifications that are possible with PNA have been researched some have been produced using DNA synthesisers which can fully automate the SPPS technique, while others have even been developed using solution based methods.[103,104] In most cases the most important features of PNAs are their resistance to enzymatic degradation due to the structure and shape not being recognised by an organism's hydrolytic enzymes such as nucleases and proteases,[105] and their increased binding affinity with DNA and RNA targets. The latter of which is predominantly due to its lack of charged phosphate groups in its backbone reducing the electrostatic repulsion that would normally be present in a DNA/DNA, RNA/RNA or DNA/RNA hybrid.[106] The extent to which this holds true is still being investigated, with recent research showing that negatively charged groups can be added to PNA without resulting in significant detrimental reductions in hybridisation efficiency.[107]

The enhanced physiological resistance and increased DNA/RNA hybridisation efficiency give PNAs great potential in antisense based nucleotide detection, and it is these property that most research groups are attempting to influence with the most recent structural

modifications. For example, Akisawa *et al.* have developed a PNA sequence containing a vinyl cross linking group on the purine bases, which they found further enhanced the binding affinity of the PNA towards thymine of DNA and uracil of RNA (Figure 1.5A). They further found that this property could inhibit the Drosher processing of pre-miRNA and thus regulate the production of miR-122, a microRNA determined to play a role in the life cycle of hepatitis C, thus showing the displaying the potential importance of microRNA targets, and of PNA antisense, in therapeutics.[108]

Alternatively the high affinity binding of PNA to DNA and RNA targets can also be used to investigate cellular processes by using synthetic PNA designed for hybridisation and RNA inhibition studies in place of the DNA/RNA alternatives. Ellipilli *et al*. have shown, in a couple of their own publications, that fluorination is possible at various different positions of the PNA to increase cellular uptake albeit with some hybrid destabilisation (Figure 1.5B).[104,109] Also Kiviniemi *et al*. have shown that when ^{19}F is used, once uptaken the investigation of PNA hybridisation with DNA/RNA targets through ^{19}F NMR techniques is possible as well as the standard fluorescence microscopy techniques.[110] With this in mind however, there have been cases where hybridisation efficiency is susceptible to great reductions upon modifications to some positions on the sequence, therefore careful design of the PNA is required.[111]

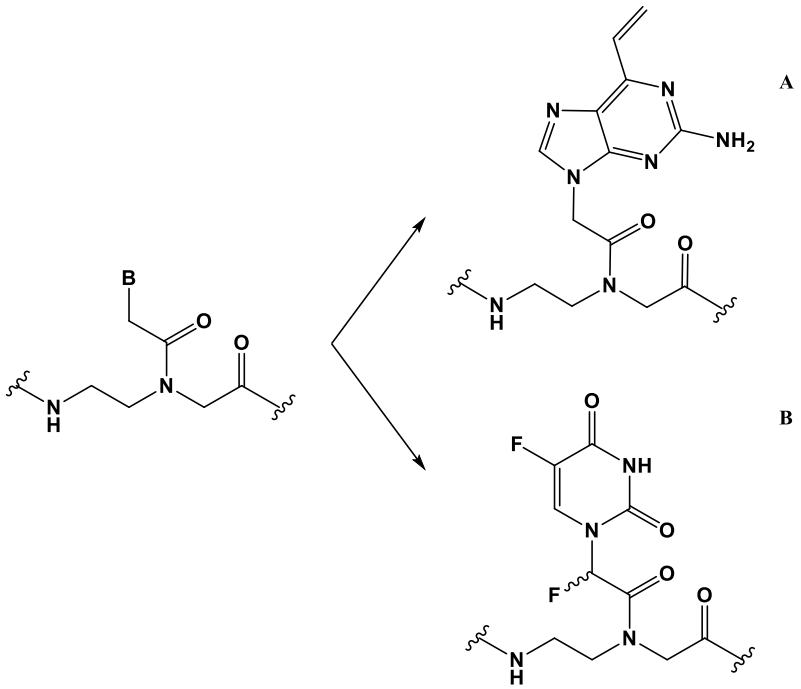

Figure 1.5 The general structure of a PNA monomer, where B indicates the nucleobase A, G, C, T or U. Along with some modified examples from Akisawai et al. (A) and Ellipilli *et al.* (B).[104,108]

It should be noted however that with certain PNA sequences, and also owing to the uncharged nature of the PNA backbone, solubility issues have been encountered. Therefore further PNA modifications may be required in order to increase their solubility in aqueous buffered media, for example the inclusion of positively charged lysine residues.[112]

1.2.3: Locked Nucleic acid analogues

Another interesting class of synthetic oligonucleotide analogues, also used by various research groups mentioned later for the sensitive and selective detection of DNA and RNA targets, are the so called locked nucleic acids (LNAs). Similar to PNA these nucleotides also have greater hybridisation efficiency to DNA and RNA targets than a naturally occurring nucleotide strand, unlike PNA however, they still retain a pentose sugar (albeit a modified form) and the phosphate of the natural oligomer and thus the increased affinity is not due to a lack of electrostatic repulsion. Instead the ribose sugar contains a bridging chain between the 2'C and the 4'C, the first of which, synthesised by Singh *et al.* in 1998,[113] and then shortly after by Koshkin *et al.*,[114] comprised of an oxymethylene link. These researchers were the first to develop a synthetic oligonucleotide of this type using thymine and guanine as the nucleobases, and found that the introduction of this bridge resulted in a conformational lock of each LNA monomer that favoured DNA and RNA binding; a phenomenon that was attributed to the LNA monomer introduction causing the growing oligonucleotide to adopt the RNA like N conformer (see Figure 1.6).[114] This conformational lock resulted in each case in either an equal or greater binding efficiency, measured by change in melting temperature, of the LNA/DNA or LNA/RNA target compared to the corresponding DNA based hybrids with a particular increase in affinity with RNA targets being reported with the addition of each LNA monomer. For DNA based antisense strands this locking of N conformation is not present, therefore the ribose sugar is free to switch between the N conformer (A type with a phospho-ester separation of distance of 5.9Å) and the S conformer (B type with a phosphor-ester separation of 7.0Å),[115] this gives the DNA sugar more flexibility which, upon hybridisation, results in a larger entropic penalty than for RNA hybrids.[116] This lowers the free energy of DNA/DNA hybridisation meaning that they become harder to form and are less stable than RNA/DNA, RNA/RNA and all LNA based hybrids where at least one strand is locked in the N conformation.[117]

Since this initial data showed the potential of LNA in antisense based biomarker detection and therapeutics, a great deal of further research into their biological behaviour and their synthetic scope for more active analogues has been performed by a number of groups. For example, Ørom *et al*. successfully showed that the use of LNA as an antisense strand was able to inhibit miRNA activity, thus allowing for the investigation of miRNA specific activity in a cell but also potentially in the therapeutic deactivation of said miRNAs.[118] Indeed Nedaeinia *et al*. have recently shown that the transfection of anti-miR-21 LNA into a colorectal cancer cell line LS147T, which displays increased expression levels of miR-21 in colorectal cancer patients, results in a decreased expression of miR-21 after 72 h exposure resulting in the cells growth being inhibited and the induction of apoptosis,[119] thus displaying the potential for LNAs in miRNA therapeutics.

However, LNAs can also be employed in the detection of oligonucleotides for the purposes of biomarker analysis. An example of this is implemented by Dean *et al.* where the 3D invasion of breast cancer cells is analysed through fluorescence microscopy techniques using a dsLNA sequence containing a fluorophore and quencher. In the dual stranded form, the fluorophore and quencher of the LNA are in close proximity and so no fluorescence occurs, however in the presence of the target mRNA the quencher is displaced and fluorescence is observed. This allowed the group to determine a relationship between the gene Notch-1 and the protein dll4, in particular they found that the presence of a Notch-1 ligand decreased the expression of dll4 mRNA and thus Notch-1 acts as a tumour suppressor, this was not able to be as confidently concluded via previous methods.[120] Other applications in electrochemical based biosensors will be discussed later.

Similar to PNA, many synthetic routes are available towards LNA and a wide range of synthetic analogues have been sought in order to improve the biophysical characteristics of the LNA, and to decrease the potential for hepatotoxicity (liver toxicity) which unmodified LNA displays.[121] Most groups target the nature of the oxymethylene bridge, either by adding a methyl group to increase the potency of the antisense properties while decreasing liver toxicity,[122] extending the bridge via an amino moiety to increase RNA and duplex DNA selectivity,[123] or, by substituting the oxygen based bridge for a nitrogen based bridge in order to allow side chains to be projected into the minor groove of duplexes.[124] Alternatively the bases themselves can be modified via the addition of triazole or alkynyl groups such as those

shown using the uracil base by Kumar *et al*. to increase the affinity towards DNA and RNA targets.[125] The general structure of LNA compared to DNA and RNA, along with some of the next generation LNAs described are given in Figure 1.6.

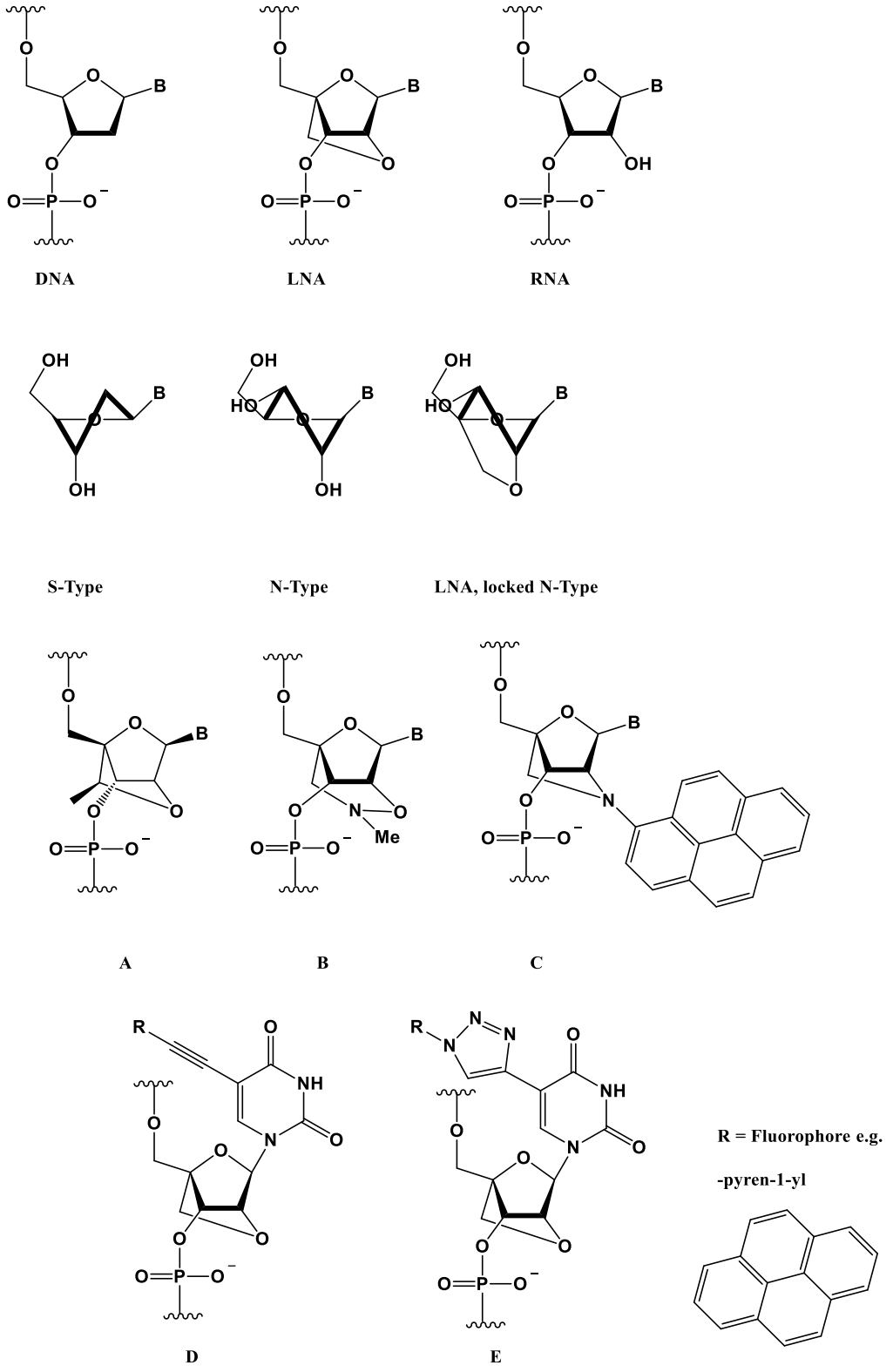

Figure 1.6 The general structure of LNA compared to DNA and RNA, including a depiction of the locked N-type conformation.[114] Also shown are some second generation LNAs by A) Seth et al. B) Abdur Rahman et al. C) Hrdlicka et al. D + E) Kumar et al.[122–125]

Both PNA and LNA hybrids with DNA and/or RNA are more susceptible to destabilisation due to mismatches, this in turn means that both PNA and LNA display greater specificity towards the target nucleotide sequence than a natural DNA or RNA oligomer, thus giving them great potential in aptamer based recognition and detection applications.[126] One final thing to note however, about both PNA and LNA, is that despite both systems possessing great resistance to proteases and nucleases and having increased hybridisation efficiencies both have potential downfalls in biosensor applications, in addition to those mentioned. For PNA the lack of phosphate backbone results in them being generally more hydrophobic and thus harder to dissolve in aqueous solvents, and more susceptible to non-specific hydrophobic adsorption.[127] Whereas for LNA the heightened binding efficiency does result in unwanted self-assembled structures such as hairpins and LNA/LNA duplexes, particularly in long sequences with multiple self-complementary sections, which in turn can be difficult to remove.[128] Thus careful consideration of these potential problems needs to be taken when deciding whether or not to apply them to the research of interest.

1.2.3: Reverse transcription-quantitative polymerase chain reaction (RT-qPCR)

Currently RT-qPCR is considered the 'gold standard' in detection and analysis of miRNA as well as being used for determining the expression of other longer RNA strands.[129,130] The inherent advantages of this method being that multiple samples can be analysed at one time, up to 384 samples in some cases, the ultra-sensitivity of the technique due to the amplification processes involved,[131] and the ability to use the amplified samples to perform sequencing.[132] As many investigations into miRNAs and their targets require the screening of hundreds if not thousands of different sequences it is clear why RT-qPCR provides a firm basis for expression level analysis and potential biomarker identification. Many research groups employ a variety of techniques based on the fundamental amplification processes involved in RT-qPCR in order to analyse known, and unknown miRNA sequences in a wide variety of different matrices. Some examples of these will be discussed in the following section along with a general overview of how RT-qPCR works.

RT-qPCR analysis of miRNA from biological matrices generally requires a 3 step process, extraction/isolation, transcription into c-DNA and then amplification of the DNA via PCR. The extraction procedure can be performed on a number of different matrices, from cell cultures and tissue extracts,[126,133] through to blood,[134] and even through to non-invasively collected

urine samples.[55,57] The isolation of miRNA from biological matrices is generally performed first using a commercial kit with a phenol/chloroform based extraction via a lysis reagent, i.e. guanadinium thiocyanate such as in Qiazol®,[57] or Trizol,[135] and a column based filtration via centrifugation. However, depending on the kit and the particular biological sample, a phenol/chloroform extraction is not always necessary.[134] This isolation procedure is required to remove any proteins, fats, and other non-nucleic acid macromolecules, while breaking down any extracellular vesicles and purifying the RNA from DNA (if a DNAse is used) and any potential RT-qPCR inhibitors. Once isolated, the miRNA samples are often stored at −80 °C to prevent degradation prior to any further analysis.

The miRNA once isolated can then be analysed by RT-qPCR. For the RT step the miRNA is mixed with a series of buffers containing: RNase inhibitors to prevent degradation of the sample, deoxynucleotide triphosphate monomers (dNTP) of each of the bases to build the complementary cDNA, reverse transcriptase enzyme to act as the polymerase for the growing cDNA, and a short primer specific to the sequence of interest to act as the starting point for cDNA growth and to increase the melting temperature of the cDNA.[136,137] This primer is often stem-looped as this has been found to increase the stability of the growing RNA/DNA heteroduplex (due to base pi stacking) and also enhances the efficiency of the efficiency of the RT process over a linear counterpart.[136] The reverse transcription process can then be completed manually, by annealing and heating to the reaction temperature for a set time period, followed by denaturation of the enzymes by heating to 80-90 °C and then cooling to 4 °C for short term storage. Alternatively the same procedure can be set into a pre-programmable thermocycler.

Finally the qPCR analysis is performed, generally using TaqMan™ analysis for miRNA derived expression or through SYBR green for less specific and lower quantitation of other gene expressions. During this step the miRNA (or other analyte) is mixed with the TaqMan™ universal master mix and a primer specific to the miRNA target, at which time the mixture undergoes a number of heating and cooling cycles causing the TaqMan probe to attach to the cDNA target along with the primer. As the nucleotides in the master mix begin to bind to the denatured cDNA, in order to replicate, the DNA polymerase will cause the annealed TaqMan probe to be cleaved from the cDNA causing a fluorescent dye to be separated from a quencher. Only annealed TaqMan probes are affected and the higher the concentration of

miRNA in the initial sample, the more cDNA will be produced at RT and analysed at PCR, and thus fewer cycles of this probe annealing and subsequent enzymatic cleavage will be required to generate a fluorescent signal. In short, a smaller number of cycles indicates a higher concentration of the target sequence. This process is shown diagrammatically in Scheme 1.2.

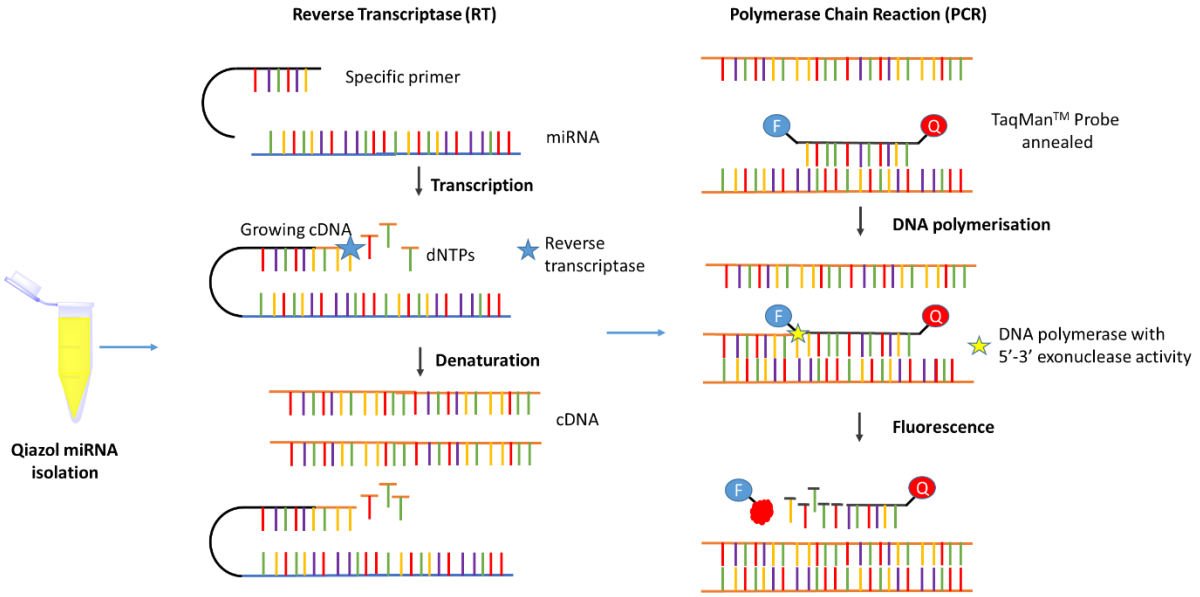

Scheme 1.2 A schematic to show the stages of TaqMan™ based RT-qPCR for miRNA from urine.

The benefit of using RT-qPCR for miRNA analysis is that, due to the amplification of the miRNA during the RT step, to form many more copies of cDNA, only a very small amount of target is required. In fact, when testing 1 and 2 step RT-qPCR techniques Tiechen Li found that 1 step RT-qPCR could detect samples as low as 1 pg/µL. This is particularly important as it allows the different biological matrices mentioned previously to be analysed with high reliability despite the very low miRNA concentration compared to total RNA content. It does however have drawbacks which limits its application in large scale diagnostic applications, the first of which being the timescale and costs related to running the analyses. The specialist chemical kits required to run an RT-qPCR experiment, along with the specialist laboratory based personnel and highly expensive qPCR analyser needed all result in potentially high costs per sample. Also the matrices used often require chemical extraction and filtration techniques which increases the likelihood of human error and potential imprecise absolute quantification data obtained.

1.2.4: Fluorescence and chemiluminescence

Another important method often employed for miRNA detection revolves around some form of luminescence, be this via fluorescence, a molecular dye that can naturally fluoresce after

absorption of light of a particular wavelength, or chemiluminescence, where a chemical reaction generates an emission of light. These techniques are often used for *in situ* analysis of miRNA expression in cellular *in vitro* studies and in some cases even *in vivo* studies are possible.[93,138] The advantage of an excitation induced light based detection method is that they generally require relatively cheap (compared to RT-qPCR) and simple to use equipment such as a fluorescence or UV-vis spectrometer, or in some cases only a microscope is required, and very little sample purification, if any, is required.[139] Also as mentioned previously *in situ* analysis can be performed on cell cultures and tissues, allowing for the direct imaging of the localisation of miRNA in a biological system, not only allowing the quantitative analysis of miRNA expression, but also helping towards the elucidation of where these miRNA are affecting biological or disease pathways.

The exact methodology utilised to obtain a luminescent signal varies widely between different research groups, with some using inorganic nanoparticles, some using organic dye tags and most recently molecular beacons. One such example of using an organic dye tag is that of the work performed by the Wang research group of Agilent Technologies.[140] In their research they use a T4 RNA ligase to attach a cytidine with attached cyanine dye to the 3' end of the total RNA population, with the exception of the hairpin pre-miRNA which were not labelled. Then in order to make their microarray specific only to the target miRNA they used complementarity based DNA micro-arrays with multiple sequence targets and introduced a hairpin loop in order to prevent the hybridisation of longer RNA strands. The fluorescence signal obtained was then proportional to the concentration of miRNA target with a sensitivity calculated to be below 0.2 aM. This work proved that fluorescence based labelling techniques can allow for detection of multiple RNAs in micro-array technology, with great sensitivity. Despite this, the researchers do report that they had some discrepancies in the hybridisation yields for certain sequences, namely miR-126, 384 and 296, which resulted in data outliers and were cases where the response did not show the strong signal vs. concentration correlation seen with their other miRNA targets. They also mention how the hybridisation efficiencies are on average only around 30% with higher efficiencies only being available at the expense of specificity. Also direct labelling of the total RNA beforehand is a specialist technique that will require a laboratory based technician and an extra analytical step to

ensure the dye tag has been sufficiently attached to the entire RNA population. This method is shown schematically in Figure 1.7.

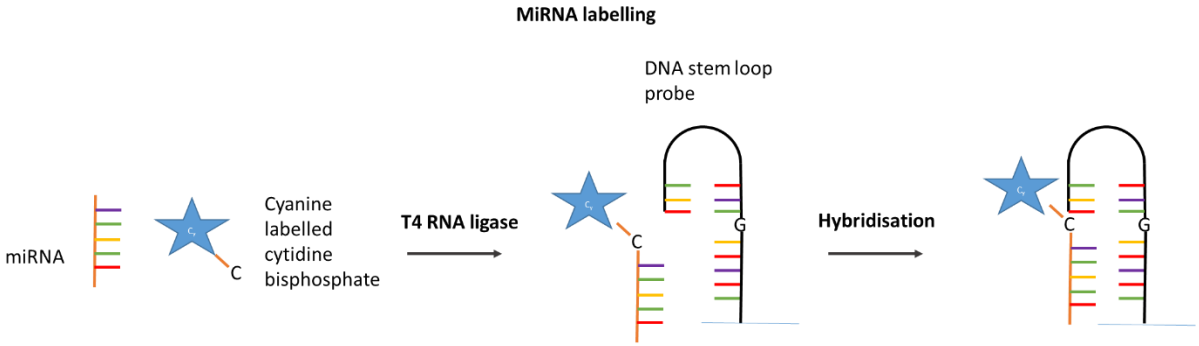

Figure 1.7 An example of the strategy employed in fluorescence based miRNA detection via miRNA labelling by the Wang group at Agilent.[140]

Neely *et al*. adopted a similar approach of using a label based fluorophore, however this group used labelled DNA and LNA chimeric probes to bind to the miRNA target.[141] The DNA probe and the LNA probe had different coloured fluorophores allowing them to use red and green laser technology to have double coincident events. Any unhybridised labelled probes were then reacted with a DNA probe containing a quencher to minimise false positives. This method did not require the miRNA to be labelled, but the use of currently expensive laser technology and the lowered limit of detection of 100 fM does limit its adaption into commercial use.

Alternatively the use of inorganic, metal based, nanoclusters as the source of excitation based fluorescence has recently gained in popularity. For example Wang *et al*. have designed a method that incorporates copper nanoclusters as the fluorophore, copper chosen in order to avoid the solubility issues of previously used silver nanoclusters.[142] Their approach uses a long template strand of DNA with an AXAXB repeat unit, where the A section is complementary to the microRNA, the X section is an endonuclease recognition site and the B section is a scaffold for the fluorescent copper nanoclusters. In their methodology the microRNA binds to the initial A section beginning the amplification cycle, at which point dNTPs are added with DNA polymerase to extend the chain after which the first section is nicked by the nuclease. After completion of the second dsDNA the final B section starts to be copied and the second dsDNA section is nicked. Finally when complete the B section copy strand acts as a reporter which binds to a complementary DNA strand and this duplex acts as the template for the fluorescent dsDNA-Cu nanocluster via reduction of the Cu^{2+} in the presence of ascorbic acid. Although

highly complex this method overcomes the expense and solubility issues of silver based nanoclusters, however the sensitivity is lacking at only 1 pM and the selectivity is only tested via mismatches between the miR-200 family, thus the long repeat units could result in undesired target hybridisation with 1 or 2 mismatches. Once again this methodology is shown schematically in Figure 1.8.

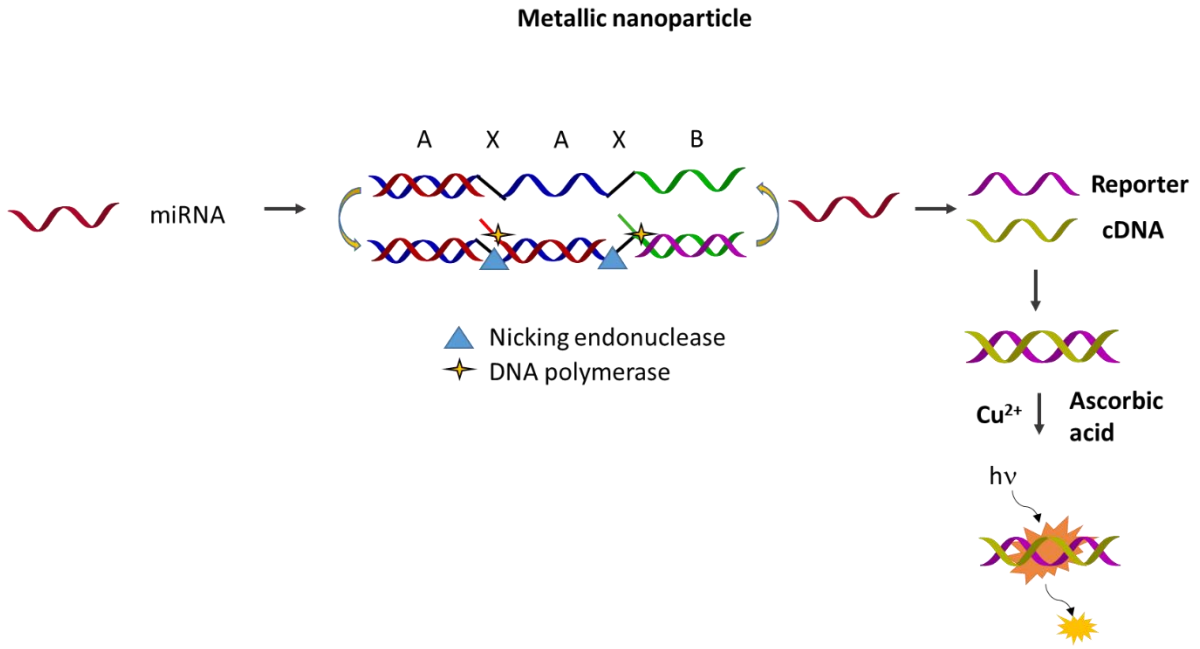

Figure 1.8 An example of the main strategies employed in fluorescence based miRNA detection via metallic nanoparticles by Wang et al.[142]

More recently Zhao *et al*. have used gold based quantum dot fluorescence for their microRNA sensing, both in vitro and in vivo.[143] Their method instead used fluorescent quantum dots (CdSe/ZnS), a combination of quantum dot labelled DNA and a partially complementary DNA hair-pin structure, which in turn become quenched when attached to a gold nanoparticle. These were then able to be inserted into cells both in vitro and in vivo whereupon the binding of the miRNA target disrupted the hair pin structure and regenerated the fluorescence. This particular technique is again interesting as it allows the visualisation of microRNA both quantitatively for the purposes of expression calculations, but also shows where the localisation of this microRNA occurs, which they used to indicate the presence of miR-21 in mouse tumours. The method is also shown to be specific down to 1 mismatch. However a mild lack of sensitivity towards miR targets dissolved in buffer, only being sensitive down to 1 pM, and the long incubation times of 4 hours for most experiments limits the application of their methodology at the point of care environment.

Finally the use of molecular beacons, that being a labelled oligonucleotide that forms a hair pin structure where the fluorescent label is quenched by either a quencher or a surface until the target sequence binds, is becoming more popular in the fluorescent detection of miRNAs. A good example of how this can be done in a relatively simple manner is given by Li *et al*. using a DNA hair pin with a section complementary to let-7a and a group of 5 bases at the 3' and 5' ends that were complementary to each other to form the hair pin stem (see Figure 1.9).[144]

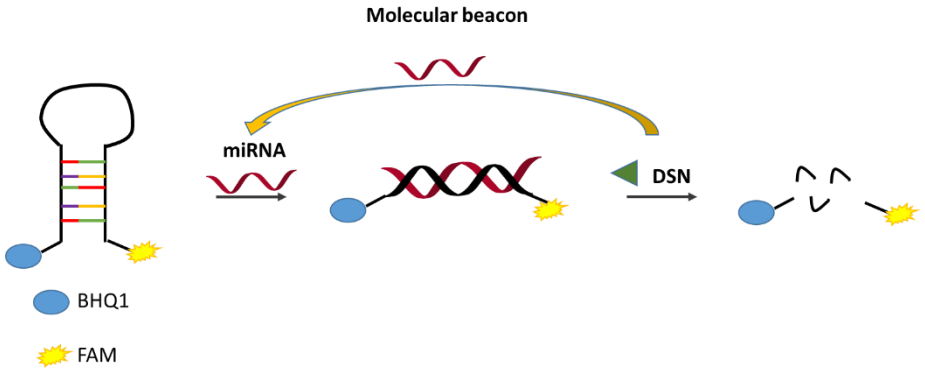

Figure 1.9 An example of the strategy employed in fluorescence based miRNA detection via a moleculars beacon by Li et al.[144]

To the 5' end they added a fluorescein and to the 3' end they added the quencher BHQ1 (Black Hole Quencher®), resulting in a hairpin sequence that gave no fluorescence. However when the target miRNA is added the stem-loop opens and the fluorescence signal is once again obtained. A duplex specific nuclease (DSN) selectively degrades the new DNA/RNA hybrid section, fully separating the fluorophore from the quencher and leaving the miRNA intact to bind to another hairpin. Thus resulting in rolling circle amplification (RCA), i.e. the produced miRNA can bind to the molecular beacon repeatedly resulting in increased response per miRNA strand, and an increased fluorescent signal, allowing for a limit of detection down to 3.8 pM and a selectivity down to 1 mismatch. Unfortunately however, many more researchers have achieved greater sensitivity as has been, [142,143] and will be, discussed in future sections. The timescale of the reaction, requiring 2 hours reaction time, also limits the commercialisation of this technique. However its simplicity does make it of interest.

Prior to this, Tu *et al*. had used a combination of this molecular beacon technology and gold nanoparticles for their method.[145] In their research they used a hairpin probe DNA strand labelled with fluorescein isothiocyanate via a thiourea linkage at its 5' terminus, which was attached to a gold nanoparticle via an Au-S bond through a thiol on the 3' terminus. Once

attached to the gold the proximity of the fluorophore to the gold surface results in its quenching, then, when the target microRNA binds, as with the previous example the stem loop opens and the fluorescence is once again observed. This led to a limit of detection, using the miRNA extracted from cell lysates, of 20 fM and 10 fM for synthetic miR-122, while also being selective to a 34% fluorescence loss with 1 mismatch. There are of course many more example methods of utilising fluorescence for the purposes of miRNA detection,[93,146] however for a brief overview only a few examples have been given.

Alternatively chemiluminescence, i.e. a chemical reaction that results in emission of light, could also be use in place of fluorescence. This often involves the reaction of luciferin to oxyluciferin using a luciferase enzyme and ATP (adenosine triphosphate), which generates a light response in a process also called bioluminescence. This luminescence can then be measured using a spectrophotometer at wavelengths from 230 to 280 nm.[147] An early example of this technique was employed by Ma *et al*. who attached an LNA probe sequence to a cover slip which can in turn hybridise with a target miRNA that is complementary, at which point UTP (uridine triphosphate monomer) and a polymerase add a poly U tail to the miRNA.[148] This in turn releases lots of inorganic phosphate (PPi) which can be converted into ATP with adenosine phosphosulfate (APS) and ATP sufurylase which act as the feedstock to convert luciferin into oxyluciferin via luciferase. The technique is shown schematically in Figure 1.10A. This gave a limit of detection of 50 fM which is greater than most of the fluorescence based methods mentioned previously. However this procedure does require a number of chemical steps prior to analysis, including several enzymatic processes which may become expensive and thus not be suitable at the point of care environment. Another potential issue of the research by Ma *et al*. is that only testing of a complete non-complementary strand of miRNA is reported, and thus the selectivity for only one or two mismatches may not be ideal.

One final example that also utilises bioluminescence was proposed by Xu *et al*. in 2017 and uses the miRNA target itself as the source of ATP for the luciferin to oxyluciferin reaction.[147] In general terms a 3'-phosphorothioate modified DNA probe is mixed with the miRNA target and an exonuclease III enzyme added to digest the RNA but not affecting the modified DNA strand. The resulting AMP (adenosine monophosphate) monomer is then enzymatically converted to ATP as the feedstock for the luciferin reaction, which results in the regeneration

of the AMP, setting up a cyclic reaction system. Interestingly this approach was specific even to 1 mismatch and had a calculated limit of detection of 7.6 fM. Finally, the technique was able to be applied to cancer cells and lung cancer tissue extracts by using DNA probes modified with a biotin label and attaching them to streptavidin labelled magnetic beads, the miRNA can then be pulled from the sample and removed from the interferent endogenous ATP, ADP and AMP in the samples before being treated with exonuclease III and analysed as in Figure 1.10B. This work is highly useful for commercialisation as it is highly sensitive and can be performed easily using premade buffers, however it remains to be seen how well this would perform when directly applied to biological matrices such as blood and urine, hence if extraction of miRNA is required then it may not be applicable for point of care analysis. These bioluminescent variants and the luciferin to oxyluciferin reaction are shown in Figure 1.10.

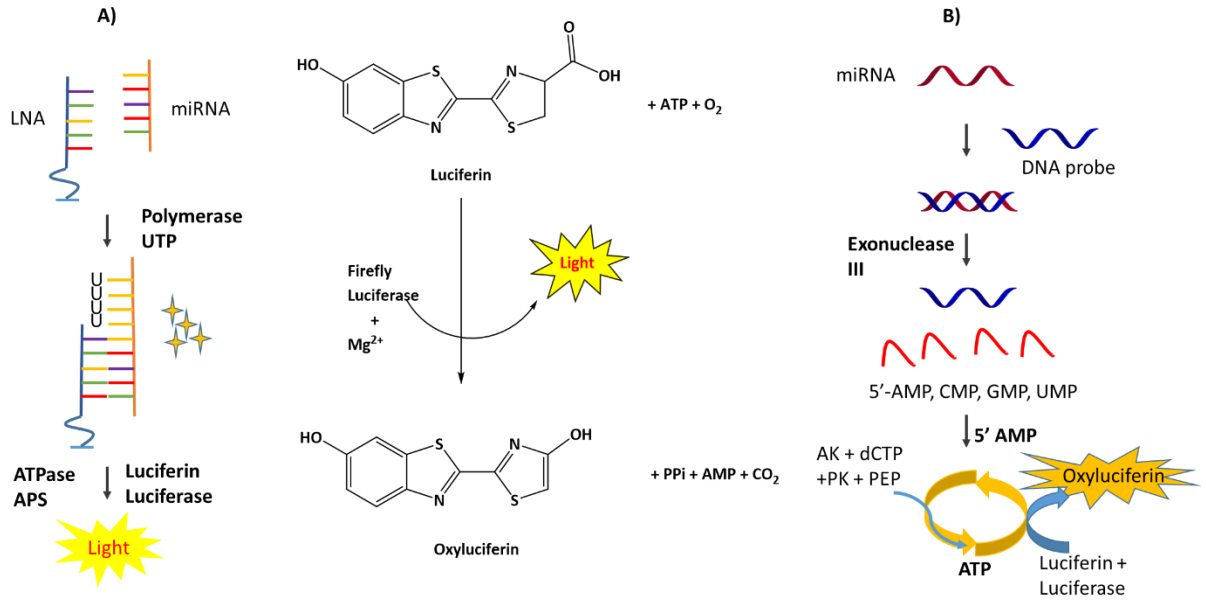

Figure 1.10 Examples of how luciferin bioluminescence can be used for miRNA detection. A) A route by Ma et al. (APS - adenosine phosphosulfate).[148] B) A route by Xu et al. (AK :- adenylate kinase, PK :- pyruvate kinase, PEP :- phospho(enol)pyruvic acid monosodium salt hydrate, dCTP :- deoxycytidine triphosphate).[147]

1.2.5: Northern blotting

Before the use of TaqMan™ based probes for miRNA detection northern blotting was considered the "gold standard" for miRNA quantification, and is still used for the detection of new and multiple species of miRNA where possible.[139] As such, a description of how northern blotting works and some examples of where the method has been applied in the literature is required before continuing. Due to their small size (19-23 nt) the general procedure for miRNA blotting analysis differs slightly from the norm.[149,150] In short, the miRNA is denatured,

generally using formamide, and separated using high percentage denaturing polyacrylamide gel, or urea-polyacrylamide gel, electrophoresis, however due to the use of this gel a transfer to positively charged nylon is required. Once transferred the target miRNA is hybridised with a ^{32}P-radiolabelled DNA or RNA probe and detected by autoradiography or phosphorimaging (see Scheme 1.3). The issue with this form of analysis being that it is relatively insensitive (1 nM),[148] requires large amounts of sample (2-10 µg),[151] requires careful handling of radiolabelled materials, some with a short shelf life (^{32}P has a ½ life of 2 weeks) and is time and labour intensive.[139,148,150–152]

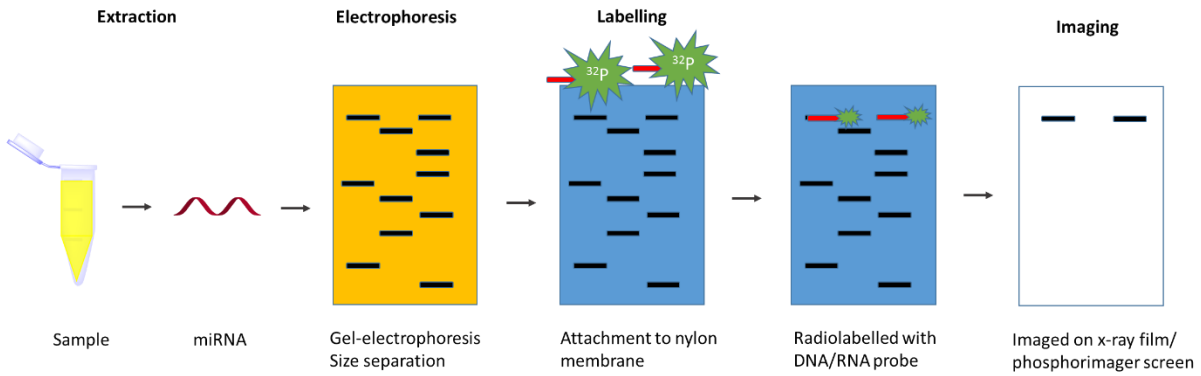

Scheme 1.3 The generalised steps for RNA based northern blotting.

Owing to the potential drawbacks, recent research into miRNA detection via blotting techniques has focussed on overcoming some of these disadvantages, particularly the lowered sensitivity compared to other methods. The first such example, employed by Válóczi *et al*.,[153] uses LNA based hybridisation probes in place of DNA in order to increase the efficiency of the hybridisation process thus resulting in greater sensitivity and selectivity. The researchers claim that the increase in sensitivity is approximately 10 fold and it can be seen from their data that, even at 2.5 µg quantities of total RNA sample, miRNAs 171 and 319 can be seen after 6 hours exposure. Várallyay *et al*. have since improved on this, again using LNA based probes, and have a complete hybridisation to detection time of 4 hours again,[91] however this timescale, and the relative difficulty in performing the specialist analysis still makes this technique unfeasible for point of care use.

Pall *et al*. instead chose to look at improving the binding of the DNA/RNA probe to nylon as a way of increasing sensitivity.[154] In their work they hypothesised that, as UV is used to attach the DNA/RNA probe to the nylon prior to hybridisation, and that as this attachment occurs through thymine/uracil bases, this is resulting in the loss or reduced availability of this base

for the hybridisation event, with small molecules such as miRNA this is having a more pronounced effect. Thus they suggested that using a 1-ethyl-3-(3-dimethylaminopropyl) carbodiimide cross linker to attach the RNA (used in their example) to the nylon prior to irradiation, through a 5' terminal phosphate, prevents this potential loss of hybridisation efficiency. This results in the RNA binding to the nylon at least as efficiently if not more so, leading to improved detection of miRNA over the standard irradiation procedure. Once again however, this procedure takes far too long (multiple hours) for its application in diagnostic points of care.

Taking these adaptations, and substituting the ^{32}P radiolabel for a digoxigenin label with chemiluminescent detection, Kim *et al*. were able to greatly improve the sensitivity of their northern blotting technique and also greatly shorten the exposure time required.[155] The use of this new label, and combined LNA and carbodiimide cross linker modifications, resulted in an improved sensitivity to 0.05 fmol and a 1400 fold shortening of the length of time the blot membrane is exposed to the phosphorimager screen (30 s vs. 12 hours). The use of digoxigenin is also much safer than the use of radiolabels.[156] However the technique is still rather laborious and requires 3 µg of total RNA to perform which is high compared to fluorescence and electrochemical based techniques.

Finally, and very recently, Choi *et al*. have discovered that there is a lot of bias involved with the detection of small and miRNAs by northern blotting techniques.[157] That is to say that standard miRNA northern blotting techniques have no difficulty detecting oligonucleotides around 24 nt long (e.g. miR-52) at 10 fmol quantities but are barely able to detect a truncated miR-52 sequence of 16 nt even at 50 fmol quantities. As some miRNA sequences can be as low as 15 nt, this bias needs to be removed. Hence they modified the method to use shorter (15 nt) probes and a lower hybridisation temperature in order to detect the shorter sequences as well as the longer ones. They found that even a 15 nt DNA oligonucleotide was able to detect complementary sequences in species containing 14 to 23 nt, thus showing that the smaller probes could be used for detection of species longer than itself.

Despite the sensitivity being greatly improved with new linking techniques, LNA based probes and the avoidance of potentially dangerous radiolabels being possible, northern blotting techniques still suffer from long preparation times and specialist labour being required thus limiting its use in the point of care environment.

1.2.6: Electrochemical based techniques

All of the previous techniques used for the detection and quantification of miRNA in biological matrices have suffered from some severe drawbacks that limit their application in the target point of care diagnostic environment. Be it a lack of sensitivity (northern blotting), a long timescale and large cost requirement (RT-qPCR) or a high level of technical knowledge and a laboratory based analytical requirement (fluorescence). Electrochemical based methods however have been developed that can achieve sensitivities towards nucleotide targets as low as attomolar (10^{-18} M) and have relatively short analysis timescales, from 30 – 90 minutes.[158] This, along with the ability of miRNA to be analysed in non-invasive urine samples,[55,57] makes electrochemical based detection a very attractive means of analysing miRNA expression for the purposes of future commercial application in point of care based diagnostics. The fundamentals of electrochemical analyses, including a brief description of each electrochemical measurement used throughout this project (CV, coulometry, EIS, DPV) will be described in the next section along with examples from the literature of research groups who have used this particular technique.

1.3: Electrochemistry fundamentals

1.3.1: Redox chemistry and general electrochemical set-up

Electrochemistry is an analytical technique that has bridged the gap between biology, chemistry and electronics since its accidental discovery by Galvani in 1791.[159,160]

In general, it uses an electrical potential input (voltage) that can be varied with time to induce a current that is detected. In general, in order for this to take place the analyte must allow for the movement of electrons from one element to another via a redox based coupling. This is not necessarily the case for electrochemical impedance spectroscopy (EIS) which can have a capacitive current.[161] In short, for certain redox active (often metal based) molecules when a voltage is applied in the positive/forward direction the molecule in solution will be oxidised, and when a voltage is applied in a negative direction the compound will be reduced. Both of these events generate a current, with the cathodic current resulting from the reduction of the analyte and an anodic current resulting from its oxidation.[162,163] This is depicted in Scheme 1.4.

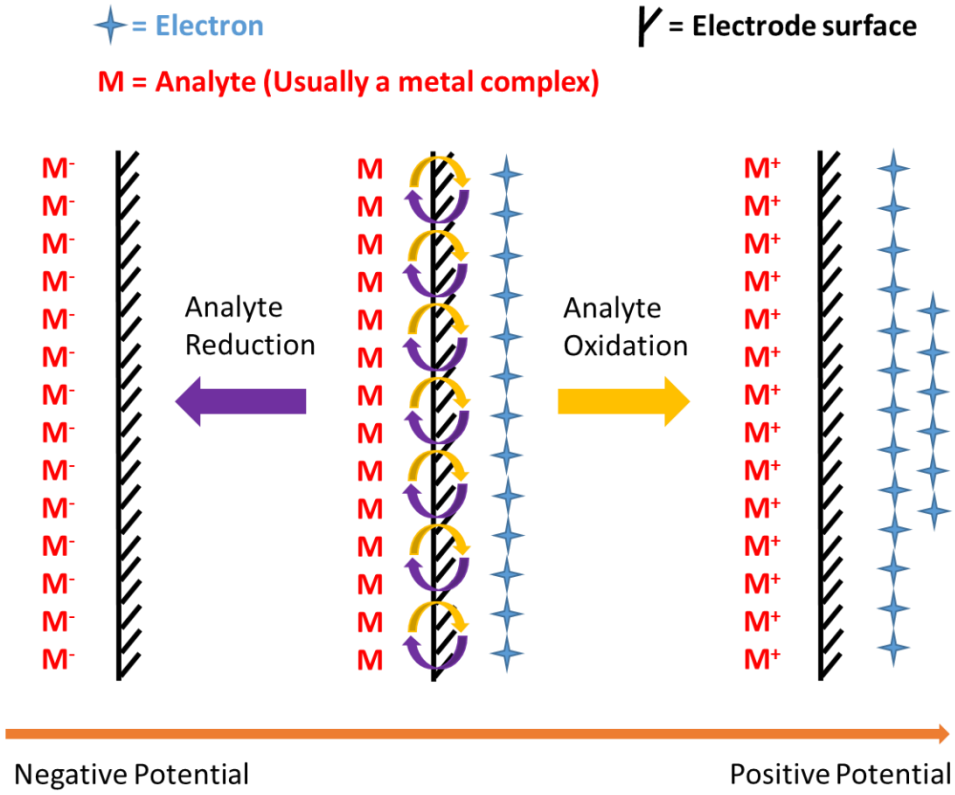

Scheme 1.4 A diagrammatic representation of how application of a potential at an electrode surface results in a redox reaction, the basis for electrochemistry.

The potential at which these events occur is known as the redox potential and varies with each compound and referenced generally to either a normal hydrogen electrode (NHE 0 V, by definition), a saturated calomel electrode (0.241 V vs. NHE) or a silver/silver chloride electrode (0.2224 V vs. NHE).[164] These reference electrodes are used in analytical electrochemistry to monitor and maintain a known and constant potential to the system so that the working electrode potential is at the correct voltage, however they themselves can vary slightly from the norm depending on temperature and filling solution. The half equations for these references are given below, along with an example of how the Nernst equation shows how they are concentration and temperature dependant (Equations 1-4).[164,165]

$$(1)\ E = E^{\circ} - \left(\frac{RT}{nF}\right)\ln Q$$

$$(2)\ Hg_2Cl_2 + 2e^- \leftrightarrow 2Hg + 2Cl^- \quad E^{\circ} = 0.241\ V$$

$$(3)\ AgCl + e^- \leftrightarrow Ag + Cl^- \quad E^{\circ} = 0.2224\ V$$

$$(4)\ 2H^+ + 2e^- \leftrightarrow H_2 \quad E^{\circ} = 0.00\ V$$

Equations 1-4. Nernst equation (1) and half equations for SCE (2), Silver/Silver chloride electrode (3) and NHE (4). E = potential, E° = standard potential, R = gas constant 8.314 $JK^{-1}mol^{-1}$, T = temperature (K), n = number of electrons, F = Faraday constant 96485 $Cmol^{-1}$, Q = reaction quotient / concentration dependence (a_{ox}/a_{red}).

These half equations describe the reactions at the reference electrode of a standard three electrode system, where the other two electrodes are a working electrode and an auxiliary/counter electrode. The reference electrodes supply a constant known potential as their internal redox chemistry occurs, thus giving the potentiostat a reference potential in order to generate its own applied potential.

The second electrode in the 3 electrode system (or can be combined with the reference in a 2 electrode system) is the auxiliary or counter electrode. This tends to be a coil, mesh or wire of an inert material such as gold, platinum or carbon, and is used to balance the redox reaction occurring at the working electrode. That is to say that it acts to close the circuit, when the working electrode is anodic, the counter electrode is cathodic allowing a current to flow between the two. The electrode does not take part in the electrochemical reaction being analysed, but will balance the potential applied to the working electrode and can, if a glass frit is used, prevent by-products from the cell (such as oxygen bubbles or salts), from interfering with the analytical measurements.[166] Also, by having a surface area larger than that of the working electrode it prevents the kinetics of the electron transfer at the counter electrode from being a rate limiting step, and thus affecting the analytics of the reaction at the working electrode. The larger counter electrode area thereby ensures that the currents and potentials that occur at the working electrode are not limited by the currents at the counter.[167]

Finally the third electrode is the working electrode, these can be made in different sizes from a range of reasonably chemically inert materials and can be either stationary (non-moving) or rotating disk. These materials are discussed in more detail in the next chapter. However, for the purposes of a three electrode cell the working electrode is where the electrochemical

reaction of interest takes place, it is the electrode where the current generated by the redox active analyte is measured. To be measurable the analyte also has to be redox active, and thus has its own set of half equations relating to the reaction taking place. For the research performed throughout this project the analyte in question is a mixture of ferri and ferrocyanide, $K_4[Fe(CN)_6]/K_3[Fe(CN)_6]$, in a solution of KCl as an electrically conductive electrolyte allowing the flow of electrons through the electrochemical circuit. The equation for this reaction is also given below (Equation 5).

$$(5)\ [Fe(CN)_6]^{3-} + e^- \rightarrow [Fe(CN)_6]^{4-}$$

The remaining sections will describe the various electrochemical techniques that can be employed in the quantification of nucleotide targets including miRNA, including how they are performed, the data that is generated and examples from recent literature of research groups that have employed them.

1.3.2: Cyclic voltammetry (CV)

The first of the electrochemical methods to be discussed is the voltammetric technique cyclic voltammetry. In this technique the potential is swept from a low voltage to a higher voltage, at which point the direction of sweep is reversed and the voltages are swept from the higher point to the origin. This is one cycle of the voltammogram and can be repeated for a number of cycles and at varying speeds (mV/s) depending on the measurement requirements. As the potential is swept in the positive direction, electrons are drawn from the analyte solution causing the oxidation of the analyte and thus increasing the concentration of the oxidised molecule at the surface in relation to the Nernst equation. This causes a change in the current, giving a peak maximum at the point where all of the analyte is oxidised around the surface of the electrode at the maximum rate of conversion, resulting in depletion of the reduced form of the analyte at the surface. Over time a bilayer is formed of the oxidised analyte at the electrode surface, and as the thickness of the bilayer increases the concentration gradient of this oxidised species decreases and thereby the rate of diffusion is slowed so that the current begins to fall. This lowering of current is due to the rate of analyte movement to the electrode surface being diffusion controlled, according to Fick's law, and thus becoming slower as the bilayer thickens. When the potential is reversed this reaction occurs in reverse, the bilayer becoming reduced and again results in another peak this time with a negative current. This is true for a one electron transfer system that is fully reversible.

Due to Fick's law affecting the rate of diffusion to the surface according to the formation of the analyte bilayer, the scan rate of the experiment will also affect the amplitude of the current. A faster scan rate will cause the current to be measured faster than the bilayer can build up, and thus the current peak will be of greater magnitude, a slower scan rate however, gives the bilayer a longer time to form before the peak current is measured and thus gives a lower peak amplitude.[163] Fick's second law for diffusion and the resulting Randles-Sevcik equation for how this relates to the maximum current at 25 °C is given below (equation 6 and 7) and example cyclic voltammograms for a 1 electron reversible system, a 2 electron system and a non-reversible system are given in Figure 1.11.[163,168]

$$(6)\ \frac{\partial c}{\partial t} = D\left(\frac{\partial^2 c}{\partial x^2}\right)$$

$$(7)\ i_{max} = 2.69 \times 10^5 \times n^{\frac{3}{2}} \times A \times D^{\frac{1}{2}} \times c_0 \times \nu^{\frac{1}{2}}$$

Fick's second law for diffusion (6) and the Randles-Sevcik equation (7). Where c_0 = concentration (M), t = time, A = electrode surface area (cm^2) D = diffusion coefficient (cm^2s^{-1}), x = distance from electrode(cm), j_{max} = max current (A), n = number of electrons and v = sweep rate (Vs^{-1})

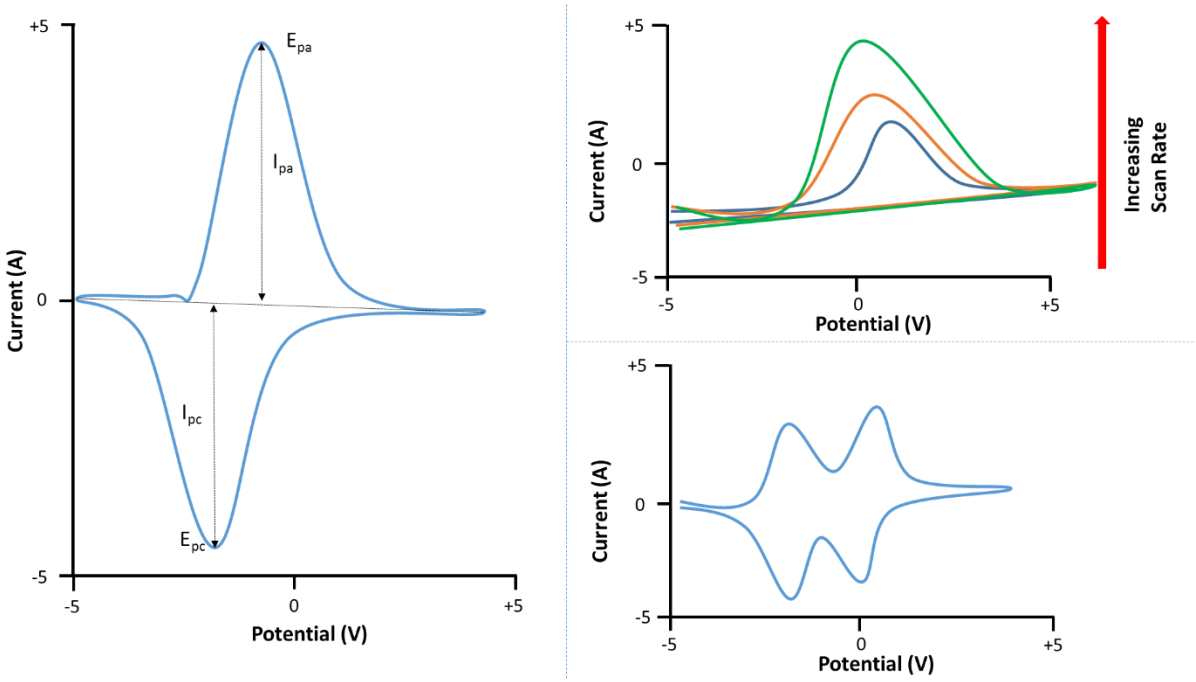

Figure 1.11 Left a diagrammatic example of a 1 electron reversible redox reaction including peak cathodic and anodic currents (I_{pc}/I_{pa}) and peak potentials (E_{pc}/E_{pa}). Top right, a one electron irreversible oxidation of analyte with the effect of increasing scan rate. Bottom right, 2 electron reversible redox reaction.

Due to its simplicity to perform and analyse, many research groups have employed CVs in assisting with the detection and quantification of miRNA, as such it has also been

implemented in different areas of our own research and why it is important to discuss some of the work performed by these research groups here. Often cyclic voltammetry is not used as a direct quantitative measurement, but is instead used to determine how well the electrode modification procedure is occurring and what potential to use for quantification using other voltammetric or amperometric techniques. One group that does however, at least for initial feasibility studies, is Gao and Yu.[169] In their research they labelled a Let-7b miRNA target with a ruthenium phenanthroline-dione complex ($Ru(PD)_2Cl_2$) which is redox active. They then modified an indium tin oxide (ITO) electrode with an alkoxysilane and then with a Let-7b complementary DNA capture probe. The hybridisation of this probe with the labelled miRNA target brought the redox active ruthenium complex into close proximity with the electrode surface and thus, when a voltage is applied, an electrochemical response was generated. The procedure is summarised diagrammatically in Figure 1.12.

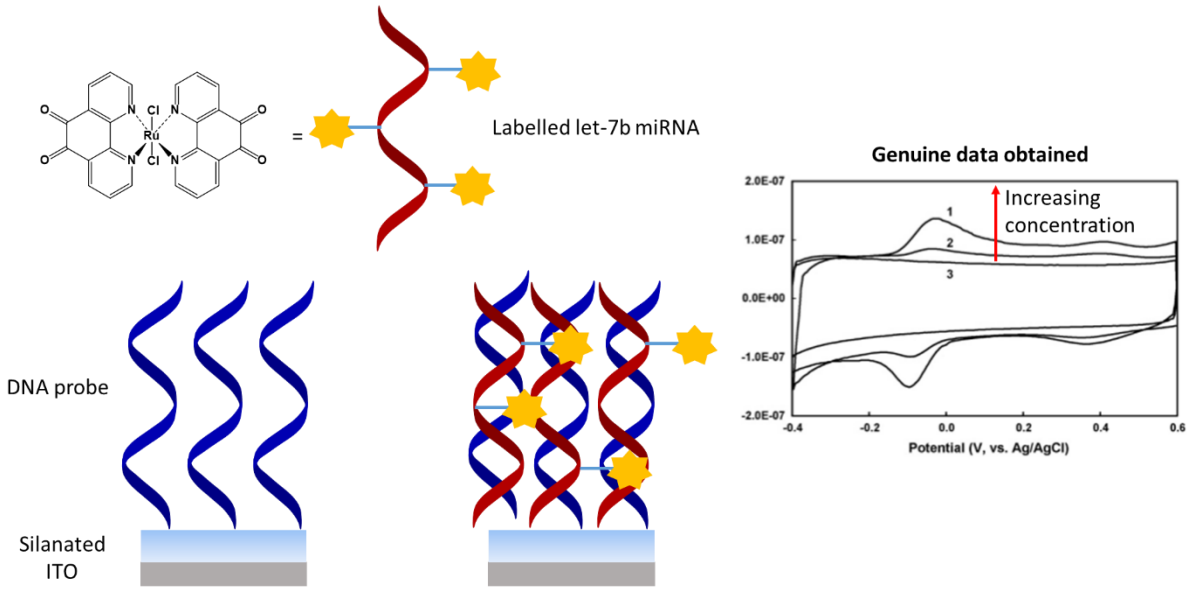

Figure 1.12 An example of how CV is used by Gao and Yu in the preparation of their biosensor. Peaks 1-3 have been labelled with 1 being 50 nM target, 2 being 10 nM target and 3 being 10 nM of non-complementary RNA. The CV peak current is proportional to target concentration.[169]

The researchers were therefore able to perform feasibility studies using CV and found that when hybridised with 10 nM and 50 nM of the target a set of oxidation and reduction peaks are obtained, the amplitude of which is directly proportional to the concentration of the target. They also performed the same procedure with a non-complementary miR-92 which resulted in no observable peaks. These findings demonstrated that the response being obtained was through target hybridisation and not through non-specific binding. Through this

they were able to use $Ru(PD)_2Cl^+$ as the redox indicator to give an initial limit of detection of 2 nM.

As mentioned before other groups have used CV based analysis more for feasibility studies, or for performing and characterising their electrode modifications. For example Wang *et al*. use CV to electrochemically deposit a substituted naphthalene sulfonic acid onto their electrode and then use a separate set of CVs to check each step in their modification,[170] a technique that has been adapted in later chapters of this thesis.

Alternatively Gao *et al*. have used CV measurements to optimise their choice of redox reporter, to give the highest signal to noise ratio and potentially a negligible R_{ct} value (a measure of impedance discussed later), using a variety of different redox active analytes to determine which is best to use in their future calibration impedance plots.[171] These reports show how CV can be employed universally throughout electrochemical analysis for a variety of purposes, and surprisingly, only infrequently in the direct determination of analyte concentrations themselves.

Cyclic voltammetry can, and has, also been used for a number of applications other than just nucleotide quantification. It has also been successfully applied to investigation of reaction kinetics,[172] food and drink analysis including the determination of polyphenols and sulfur dioxide in wine,[173] and determining the oxidation and reduction potentials of organic compounds for use in electrochemical synthetic methodologies.[174]

1.3.3: Chronocoulometry / amperometric analysis

Unlike CV, chronocoulometry and amperometric analyses are based around using a fixed potential and measuring the change in current or charge over time. In amperometric and coulometric based techniques a voltage where there is no electrolysis is initially applied, and then switched after a certain timepoint to a potential that results in a net oxidation or reduction, i.e. from a reduction potential to an oxidative one or vice versa, at which point a change in the current (and thus charge) occurs. This causes a build-up of the redox product (oxidised or reduced depending on potential used) over time, initially there is a redox spike which continues to generate this current/charge at a slower and slower rate until the potential is removed at the analysis completion time. The relationship between the analyte

concentration and the current or charge is given by the Cottrell equation (Equations 8 and 9), which also takes the diffusion rate (flux) into account over time.[163,166,175,176]

$$(8)\ \mathrm{i} = \frac{\mathrm{nFAc}\sqrt{\mathrm{D}}}{\sqrt{\pi\,\mathrm{t}}}$$

$$(9)\ \mathrm{Q} = \frac{2\mathrm{nFAc}\sqrt{\mathrm{Dt}}}{\sqrt{\pi}}$$

The Cottrell equation for current from analyte concentration (8) and the integrated form for charge dependence (9). Where n = number of electrons transferred, F = Faraday's constant (96485 $Cmol^{-1}$), A = surface area of electrode (cm^2), c = analyte concentration (M), D = diffusion coefficient (cm^2s^{-1}), t = time (s).

This shows that the concentration of the analyte at the electrode surface is therefore proportional to the charge/current generated, and thus a higher current indicates more of the electroactive species being able to reach the surface at the time of the potential being applied. For amperometric based analysis the current is measured and for coulometric analysis this current is integrated with respect to the analysis time to give the charge, in both cases time is the second variable. As with voltammetric analyses these techniques can have multiple switching steps, for example in chronocoulometry it is possible to switch from an oxidative potential to a reductive potential after set periods of time. This gives what is known as double step chronocoulometry. Double step chronocoulometry is used analytically as a method to give a defined charge peak for each analyte concentration over time, however it also is used for characterisation of the electrode charge during adsorption of species.[166] Figure 1.13 shows the example outputs for single and double step amperometry and equivalent chronocoulometry.

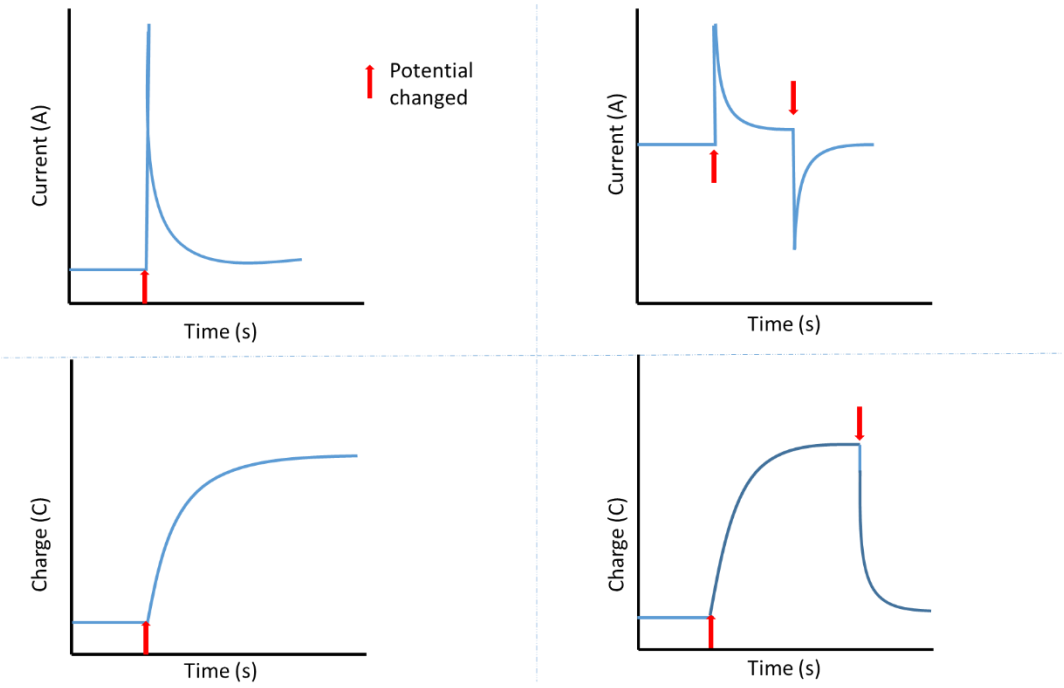

Figure 1.13 Example outputs from amperometric (top) and chronocoulometric (bottom) analyses, the left hand plots have an initial potential which is then switched to another in one step, the right hand is double step, starting at one potential, switching to a second for a time and then finally to a third (or back to the first). The time where the potential is changed is marked.

Many groups have used amperometric based analysis for the quantification of nucleotide targets including miRNA. Two researchers from one particular group, Zhou *et al*. have utilised this analytical technique in a number of their reports, one of which uses a gold electrode, modified with gold nanoparticles which increases the electron transfer ability (determined using electrochemical impedance spectroscopy, EIS, using a ferri/ferrocyanide redox couple), to attach a thiol tagged hairpin DNA sequence, containing a section complementary to miR-21, via a strong Au-S bond. Once this hairpin modified electrode had been prepared, they then set about producing a reporter cluster by attaching a series of DNA aptamer strands and a DNA capture strand to free gold nanoparticles. Hybridisation of the miR-21 target to the probe opens the hairpin structure of the electrode bound DNA, leaving a section complementary to the capture strand of the cluster, which also hybridises to the probe. Finally a hemin solution was added to the probe causing an electrochemically active hemin-G quadruplex complex to form between the folded DNA aptamer strands and the hemin, after which amperometric based analyses were performed.[177] This method gave a limit of detection of 3.96 pM, which was high compared to other miRNA detection methods mentioned previously and some of their own previous works. A diagram of the system adapted from the research is given in Figure 1.14.

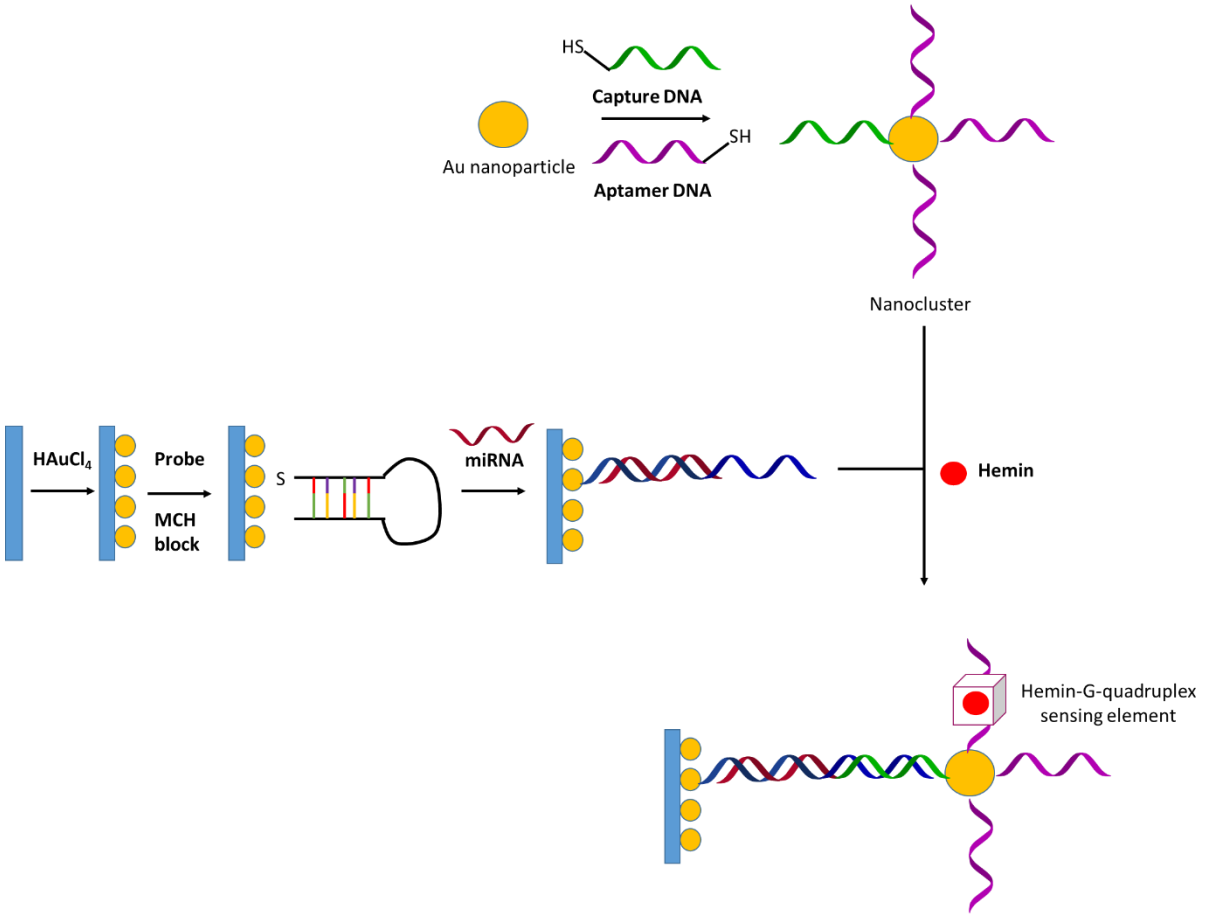

Figure 1.14 Gold nanocluster and hemin-G-quadruplex based miRNA biosensor development as described by Zhou et al.[177]

Before they published this work they had produced a system that uses the same gold nanoparticle/DNA cluster, this time however using a streptavidin and horse radish peroxidase (HRP) combination as a reporter, firstly with 3 reporters per miRNA target and then a simpler method for 1 reporter per target for limits of detection of 6 fM and 60 fM respectively.[178,179] As a final modification they attempted to maintain the sensitivity and specificity of their sensor by employing a hairpin DNA probe containing occasional bases produced using LNA, and a biotin label for attaching streptavidin-HRP complex directly, rather than as part of a cluster, thus simplifying the modification procedure. This option did achieve an increase in sensitivity over the hemin-G based method mentioned earlier, at a limit of detection of 400 fM, however it did not reach the same sensitivity as their earlier works. In each case however the sensitivity analysis was performed using amperometric techniques.[180]

As for coulometric analysis, Yao *et al*. have employed a RCA based technique for detection of microRNA using a gold electrode chip fabricated on a polystyrene substrate, having chosen chronocoulometry as their analytical technique due to its ability to allow for absolute

quantification of biomolecules at the electrode surface.[181] In their work, a thiolated DNA probe is attached to a gold electrode, after which the target miR-143 and a second DNA strand is added, the miRNA hybridising with sections of both and then a phi29 DNA polymerase joins the DNA strands together along with an additional added padlock probe. Over time (4 hours) this is repeated, generating a RCA cycle, during which a cationic ruthenium(III) hexamine complex is added which becomes electrostatically trapped to the negatively charged phosphate groups and acts as the redox reporter. The more DNA probes that have been added during the amplification cycle, the greater the coulometric response and the better sensitivity can be achieved.

Figure 1.15 shows their procedure diagrammatically. Using this method the group achieved a sensitivity down to 100 fM which is comparable to the works done by Yin and Zhou,[179,180] but also allowing them to determine the exact surface coverage of the DNA probes and the resulting percentage of probes hybridised, using the Cottrell equation mentioned earlier. These examples show how amperometry and coulometry can be readily used in the quantification of miRNA targets and are often employed to do so, they also help to show some of the advantages of coulometry and amperometry over other methods, such as allowing the simple absolute quantification and surface coverage of biomolecules at the electrode surface.

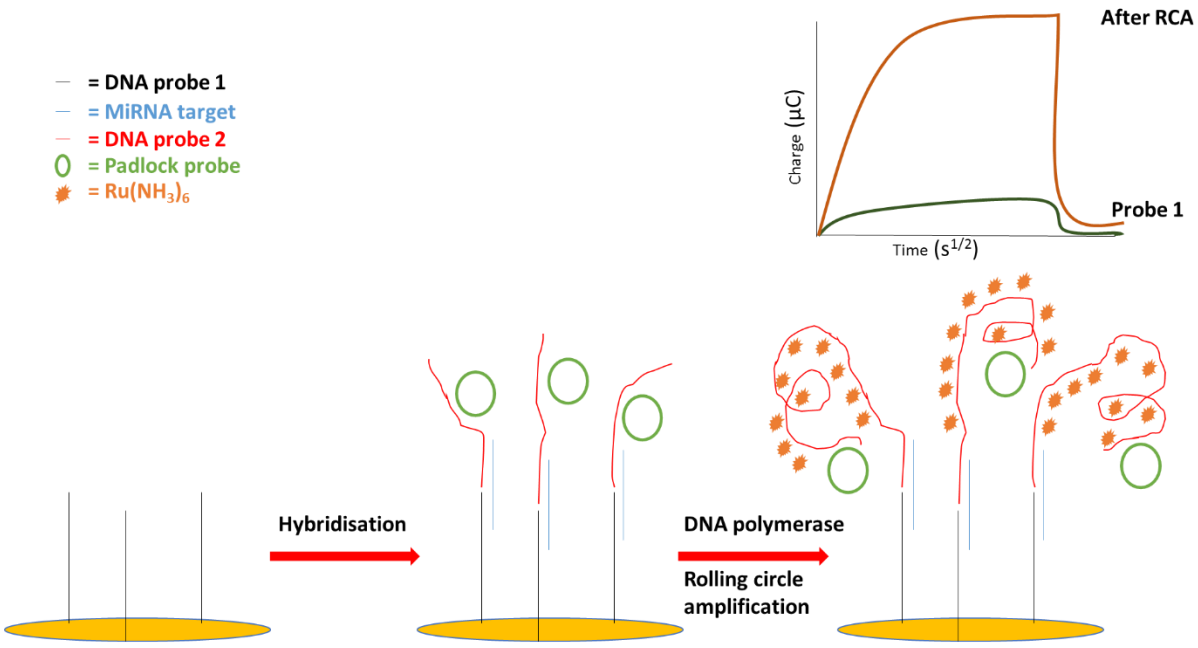

Figure 1.15 The procedure employed by Yao et al. for the detection of miRNA using chronocoulometric analysis.[181] The example graph is not to scale and is for illustration purposes only.

Along with miRNA detection, coulometry is also used in common electrochemistry for measurement of the electrode active surface area, diffusion coefficients and kinetics of electron transfer reactions.[175,176]

1.3.4: Electrochemical impedance spectroscopy (EIS)

The final electrochemical technique used throughout the remainder of this thesis, and thus discussed here, is electrochemical impedance spectroscopy (EIS). In the simplest terms EIS is an electrochemical technique that uses alternating current (AC). In EIS the applied potential is fluctuating which results in an alternating current possessing both a phase and an amplitude which are measured as the frequency of the potential is swept. Combining these elements results in a measure of the impedance of the cell, which is composed of contributions from the electrode, the electrode/solution interface, the analyte solution and diffusion of the bulk. Impedance can be thought of as a similar phenomenon to resistance, however it takes both resistance and capacitance into account and is dependent upon frequency. The potential applied is oscillating in a sinusoidal manner over time which generates a corresponding current that is also sinusoidal in nature (AC), however the voltage lags behind the current resulting in a phase shift (θ) of $\pi/2$ for capacitors. Taking both of these points into account and remembering that from Ohms law resistance (R) is equal to potential divided by current, it is possible to calculate impedance by substituting these frequency dependant terms for current and potential into the equation for Ohms law.[182] These are shown (Equations 10-12) along with the sinusoidal current and potential for a capacitor in Figure 1.16. It should be noted that there is no shift for a resistor and for an inductance the voltage is the leading waveform.

$$(10)\ E(t) = E_m \sin(2\pi ft)$$
$$(11)\ i(t) = i_m \sin(2\pi ft + \theta)$$
$$(12)\ Z(f) = \frac{E(t)}{i(t)}$$

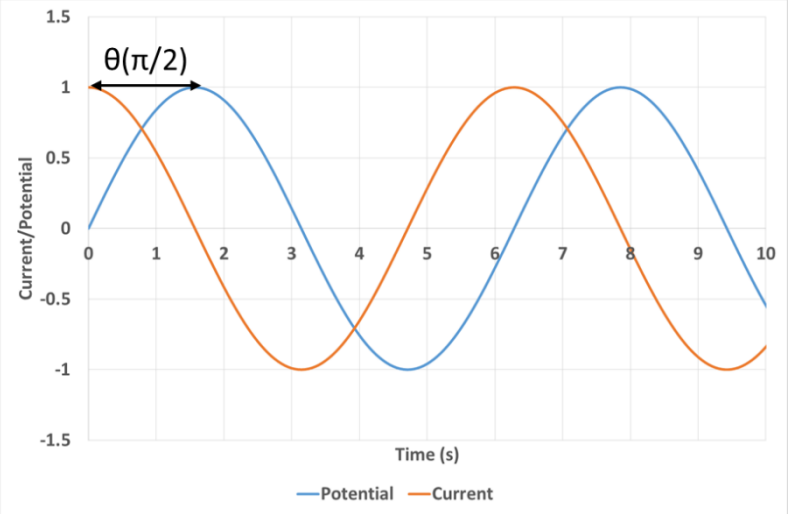

Figure 1.16 The sinusoidal waveforms of a.c potential showing the phase shift and the equations for frequency dependant potential (E) of a capacitor (10), current (i) (11) and impedance (Z) (12). E/i (t) is the potential/current at time t, E/i_m is the maximum potential/current amplitude and f is the frequency in hertz.

Taking the equations from Figure 1.16 and noting that, although for a capacitor alone the phase shift is π/2, for any real complex circuit it can adopt any value and this can depend on the frequency. Thus the true impedance value can be split into two further values, Z' which is also known as Z_{real} and Z'' which is $Z_{imaginary}$, the two values described mathematically by the following Equation 13:

$$(13)\ \mathrm{Z(f)} = \mathrm{Z'}\sin(2\pi\mathrm{ft}) - \mathrm{Z''}\cos(2\pi\mathrm{ft})$$

Z = total impedance (Ohms = Ω), Z' = impedance real (Ω), Z'' = impedance imaginary (Ω), t = time (s) and f = frequency (Hz).

Typically, during EIS experiments the impedance data is plotted in the form of a Nyquist plot, these are plots of Z' (Z_{real}) vs. –Z''($Z_{imaginary}$), and the resulting vector between the origin and the point in question represents the total impedance with the angle between the vector and the x axis being the phase angle. For single electrolytic capacitors, or for an electrical circuit with a capacitor and resistor in series (i.e. attached to each other directly) this is a linear plot with no change in Z'. However for an electrochemical circuit there is often an electrical bilayer that forms as the electrochemical reaction takes place, this in turn acts as a capacitor in parallel to the resistor. Thus at high frequencies the current is able to pass freely through the capacitor with ease, however at lower frequencies the current passes preferentially through the resistor. Owing to the relationship between Z' and resistance and –Z'' and capacitance this variation with frequencies results in a semi-circular Nyquist plot. These mathematical relationships are shown below in Equation 14:

$$(14)\ Z' = R\ \ - Z'' = \frac{1}{2\pi C_d}$$

Z' = impedance real (Ω), R = resistance (Ω), Z'' = impedance imaginary (Ω) and C_d = differential capacitance.

Finally, for a standard 3 electrode circuit undergoing an electrolytic reaction the impedance behaviour for the cell often follows behaviour similar to a Randles circuit. In this circuit there is a resistor in series with a capacitor (C_{dl}), which arises from the double layer at the interface, which is in turn in parallel with a second resistor (R_{ct}). This generates a semi-circular Nyquist plot at lower frequencies as mentioned previously, with the resistor in series shifting the x-axis by the value of its resistance. At higher frequencies the current can pass freely through the capacitor, however in this system there is a new Warburg constituent describing the frequency dependence of diffusion of the bulk analyte to the surface on the impedance. Therefore at high frequencies the resistance is low and the solution resistance is the only contribution, and the reaction can be thought of as non-electrolytic with the double layer providing the path of negligible resistance.

As the frequency decreases however this is no longer true and electrolysis starts to take place, therefore the current starts becoming impeded due to the charge transfer resistance (R_{ct}) and the double layer capacitance (C_{dl}) giving the characteristic semi-circle. Then at low frequencies the bilayer no longer has an effect on the resistance and there is a large rise in the impedance at the end of the semi-circle which is modelled by Warburg impedance. This final impedance increase is due to concentration changes as a result of the a.c. current which is diffusion determined and gets increasingly difficult to reverse as frequency is lowered due to the diffusion distance increasing at lower frequencies.[163,166,183] The different impedance plots mentioned above along with the equivalent circuits used to simulate and model the data for analysis are given in Figure 1.17

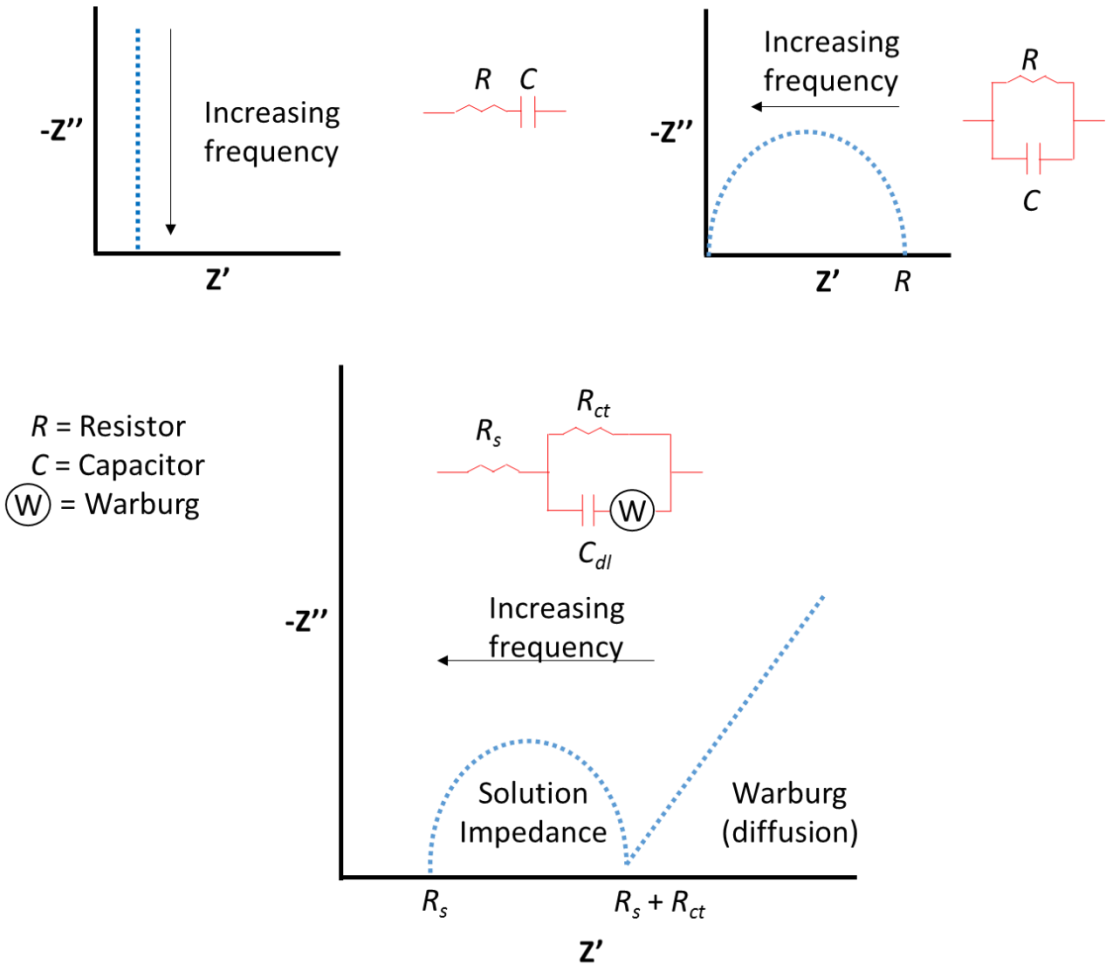

Figure 1.17 The various forms of Nyquist impedance diagrams that can arise depending on the properties of the electrochemical cell. The general diagram for an electrolytic reaction is given at the bottom showing how the impedances are dependent on the electrolyte solution and the diffusion to the bilayer surface. Also given are the model circuits used to fit the data.

Due to its high sensitivity and ability to show the exact nature of the impedance response, be it due to the electrode/solution interface or via the diffusion of the bulk analyte, electrical impedance spectroscopy is the analysis technique of choice for a great deal of published methodologies. One particular group that has used a combination of voltammetric techniques and electrical impedance to detect miRNA at ultra-low concentrations is that of Labib *et al*. In one example of their work they have managed to detect a miRNA target to concentrations as low as 5 aM.[184] For reference a diagrammatic summary is given in Figure 1.18.

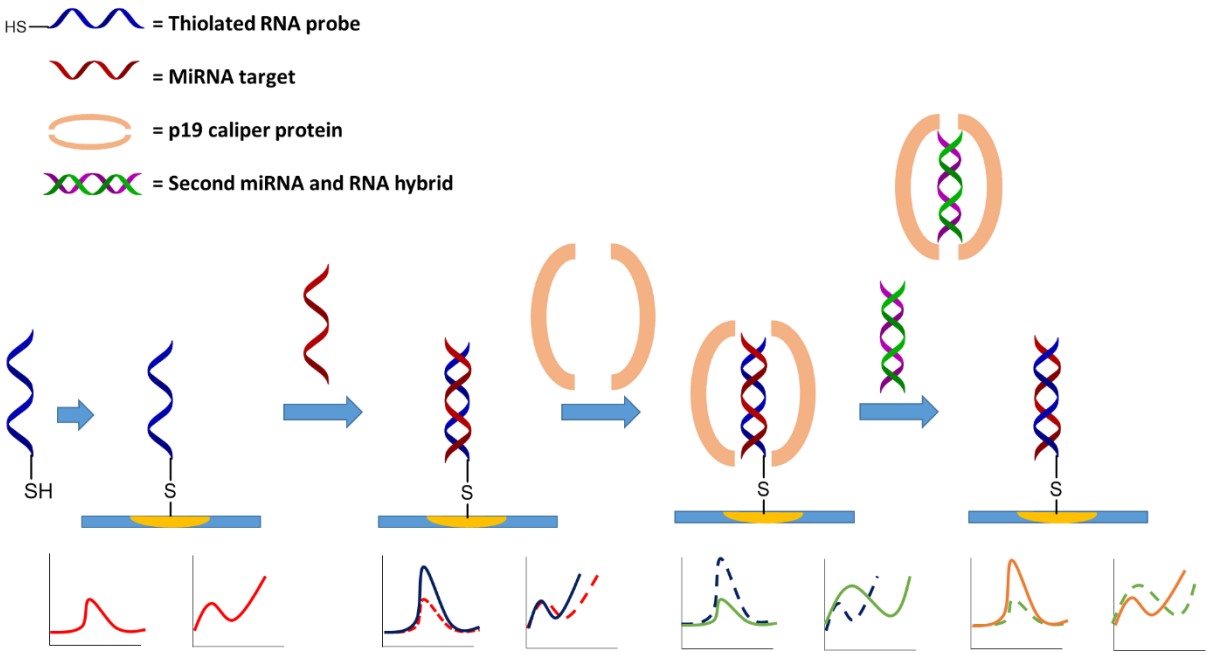

Figure 1.18 The electrode modification procedure for miRNA analysis by Labib et al. Also shown are the effect of each stage on the square wave voltammetric response (left) and impedance spectra (right).

This is a particularly interesting example, not only because it shows incredibly good sensitivity, but more importantly because it has the ability to switch miRNA targets once one has been analysed. Their initial stage is similar to many other examples, a 3'-thiolated RNA probe strand, this time with a second modification in the form of a 5'-phosphate, is attached to a gold nanoparticle modified screen printed carbon electrode. This is then used to hybridise with the target and square wave voltammetry and electrical impedance spectroscopy analyses used to determine the sensitivity at this stage which is given as 0.4 fM.

In the second mode of the three mode technique, a p19 caliper protein is used which causes a 'signal off' response in the voltammetry (and thus a larger impedance) at higher concentrations of target miRNA, so called as the voltammetric current response is lower (impedance response larger) than that obtained for the DNA modified electrode alone due to shielding from the protein. This 'signal off' response then allows for greater sensitivity than the hybridisation step alone, hence by using concentrations from 10 aM to 10 fM they determined a limit of detection of 5 aM, thus increasing the sensitivity over the first mode.

Finally, in the third mode, a pre-hybridised combination of a second miRNA target and its complementary RNA probe (this time not thiolated) is added which causes the p19 protein to be displaced leaving behind just the original miRNA target and its probe. This displacement is again concentration dependant which indicates the potential for detection of two different

miRNAs via a single sensor, however the authors mention that the surface cannot be fully regenerated in this way and thus the limit of detection is worse at this stage at 50 pM.

This work is particularly important for this third stage however, being particularly useful if it could be optimised to reduce the hybridisation times required (1 hour at every hybridisation stage) and increase the sensitivity at the second target stage. Unfortunately they also appear to only perform the impedance measurements once as they do not give any error bars for its data analysis.

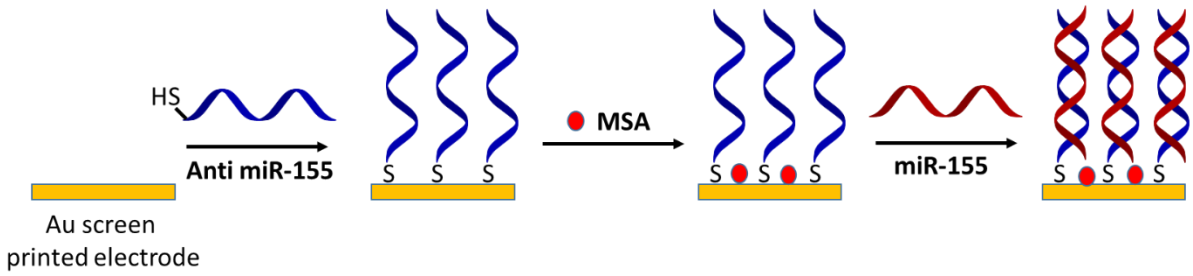

*Figure 1.*19 *The preparation of a gold screen printed electrode biosensor for miRNA detection described by Cardoso et al.*[185]

A second interesting example from Cardoso *et al*., summarised in Figure 1.19, should also be mentioned.[185] This research is an example of how simple electrochemical miRNA detection has the potential to be. In their example, a synthetic thiolated RNA probe is attached to a gold screen printed electrode via an Au-S bond, and any unreacted surface blocked through binding with mercaptosuccinic acid (MSA). This RNA modified sensor is then hybridised with varying concentrations of the miRNA target and a combination of voltammetry and EIS experiments are performed to determine the sensitivity. Which, despite the simplistic nature of the technique is quoted as being as low as 5.7 aM in real human serum samples (1 aM is potentially reachable in buffer), and subsequently also shows the ability to detect miR-155 in extracts from a breast cancer cell line. They also demonstrate some ability to regenerate the sensor surface, after the hybridisation measurement, by using heat treatment to denature the RNA duplex. The regenerated surface is then available for use in another hybridisation event and measurement.

Despite these promising results and the great sensitivity achieved, the simplicity of the technique may be its downfall, as there is nothing which allows it to be patent protected and thus is not ideal for commercialisation and use in point of care diagnostics. They also only show responses obtained from the sample analysis using their sensor corroborated by serial

dilution analysis, they do not compare their values to concentrations determined by PCR or for a healthy vs. diseased comparison. It does however pose an interesting starting point towards very simple electrochemical miRNA detection.

1.4: Surface chemistry analysis techniques

1.4.1: Attenuated total reflectance - Fourier transform infra-red spectroscopy (ATR-FTIR)

The first surface analysis technique to be discussed, and potentially most straight forward, is infra-red spectroscopy. Infra-red spectroscopy uses light in the infra-red region (generated a red hot filament) to cause the bonds in a molecule to vibrate, absorbing and releasing energy as they do so and thus allowing for the identification of that bond. For measurement of an infra-red spectrum by attenuated total reflectance (ATR), the sample, in this case an electrode surface, is loaded onto a crystal, usually of germanium, zinc selenide, silicon, KRS-5 (eutectic mix of thallium bromide and thallium iodide) or diamond.[186] After which an IR beam, which has been generated internally by a heat element, is collimated (each ray made parallel) passed through a beam splitter in the interferometer which passes half of the beam to and from a fixed mirror and the other half to a moving mirror, which changes the path length of the light compared to that of the fixed mirror. The beams are then recombined via the interferometer, with the difference in path lengths creating constructive and destructive interference i.e an interferogram. The combined beams are then and passed through the crystal holding the sample. Upon hitting the crystal the beam is reflected, creating an evanescent wave which extends into the sample causing vibrations within the sample as it is absorbed at specific wavelengths. The beam is passed to the detector which detects the intensity of the absorbed wavelengths, with the wavelengths absorbed showing no response in the interferogram. Finally this is analysed by the computer which performs a Fourier transform (FT) to convert the interferogram into an infrared spectrum of wavenumber (1/wavelength λ) vs. transmission of that light through the sample. This is shown in Scheme 1.5.[187]

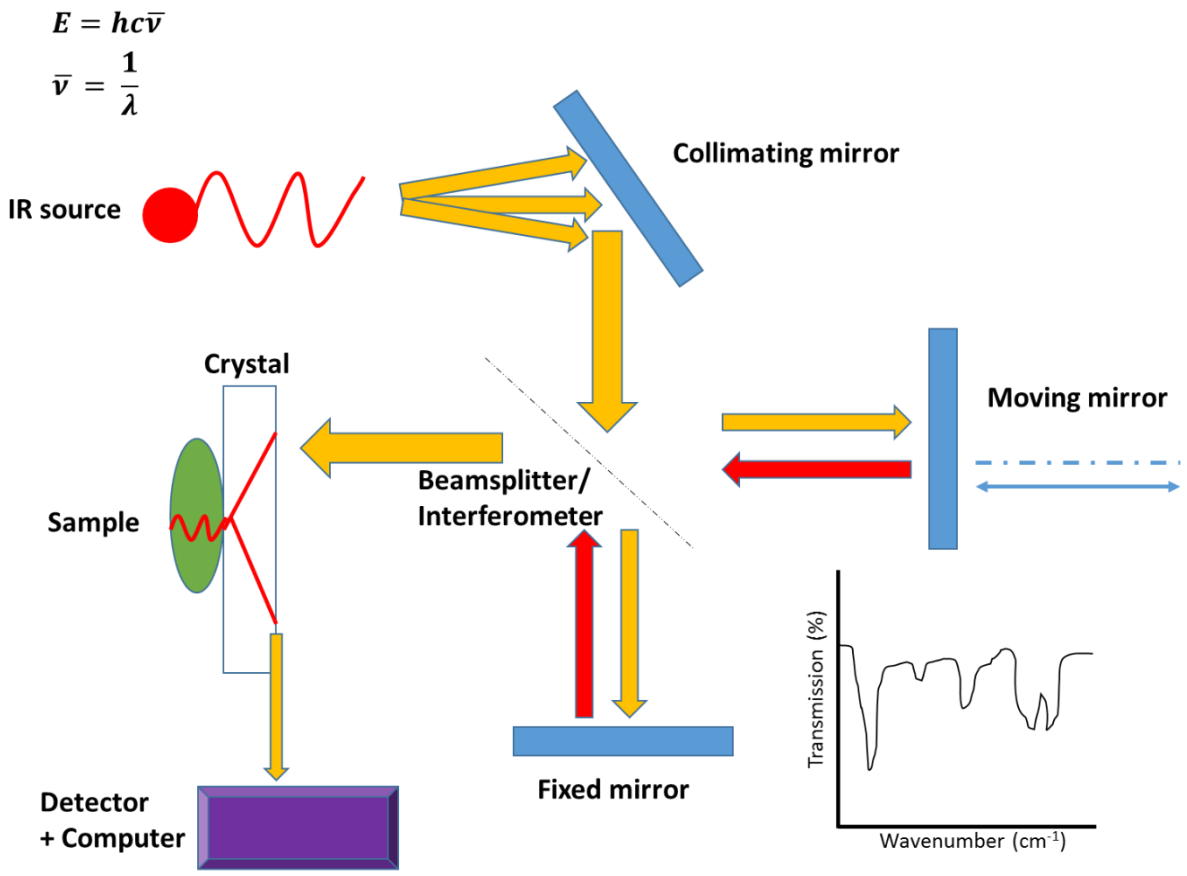

Scheme 1.5 A schematic of how ATR-FTIR takes place inside the spectrometer, including the relationship between energy and wavenumber (frequency) and a diagrammatic example of an IR spectrum. Adapted from reference 181.[187]

The wavelength (and thus wavenumber) of light that is absorbed by the sample depends on the functional groups present. Upon absorbing the infrared radiation, in the form of the evanescent wave, the functional groups on the molecule consisting of differently atoms of different mass will begin stretching and contracting (vibrations) and/or bending, often these atoms are visualised simply as balls on a spring, however this is not strictly true. The energy needed for this to occur depends on the mass of the atoms and the 'rigidity' of the bond as determined by the bond strength. Stronger bonds such as C=O carbonyls require higher wavenumbers (≈1700 cm^{-1}) than weaker bonds such as C-O single bonds (≈1100 cm^{-1}).[188] As long as this vibration also fulfils the selection rule of resulting in a change in dipole moment it will be excited by the IR photon, then as long as there is enough sample and the wavelength absorbed is within range it may be detected by an IR spectrometer.[189] Each functional group is found at a particular wavenumber of absorption and thus allows for the identification of functional groups present on the surface/sample. These relationships are shown below for diatomic molecules in the Hooke's law Equation (15) and the reduced mass Equation (16).[189]

$$(15)\ \overline{\nu} = \frac{1}{2\,\pi\,\mathrm{c}}\sqrt{\frac{\mathrm{k}}{\mu}}$$

$$(16)\ \mu = \frac{\mathrm{m}_1\mathrm{m}_2}{\mathrm{m}_1 + \mathrm{m}_2}$$

Top equation (15) is Hooke's law for a diatomic molecule, relating the frequency (wavenumber) of a vibration to the force constant and mass of atoms, with the reduced mass equation also shown in the bottom equation (16). $\overline{\nu}$ *= frequency (wavenumbers), c = speed of light (2.998 × 10^8 ms^{-1}), k = force constant (variable describing bond stiffness/strength), μ = reduced mass and m = atomic mass.*

1.4.2: Atomic force microscopy (AFM)

An imaging method often employed for the study of surfaces is atomic force microscopy (AFM).[190] AFM, uses direct physical contact with the atoms on the surface in order to determine its topography. A silicon based tip (usually Si, SiO_2 or Si_3N_4) attached to a micro cantilever that acts as a microscopic spring is able to oscillate if an alternating voltage is applied to a piezoelectric crystal, often in the cantilever holder and/or the sample holder. This is known as tapping mode AFM, alternatively the tip does not have to oscillate as is the case for contact mode AFM. In either mode the tip is then passed along the surface to come into contact with the atoms on the surface. Two imaging modes are then available, if contact mode is used, the tip is passed over the surface of the sample and a feedback loop is used to monitor the deflection of the cantilever, if this falls below or rises above a set value the sample is moved up or down respectively, by applying a different voltage to the piezoelectric crystal, to return to the set value, with the voltage applied being related back to the height of the surface.

However if tapping mode is used the AFM tip oscillates at a set amplitude and is intermittently brought in and out of contact with the surface, the whole time being monitored by a feedback loop, if the sample has a bump the tip has less room to oscillate and the amplitude decreases and vice versa for a depression in the surface, the feedback loop then changes the sample/tip separation distance to restore the amplitude to the set value. This movement is detected via a laser and a position based detector which generates a topographical map of the surface, sensitive up to a maximum depth of 10-20 μm and a maximum lateral resolution of 1 nm.[191] This is shown diagrammatically with an example from our work in Figure 1.20. [163,192]

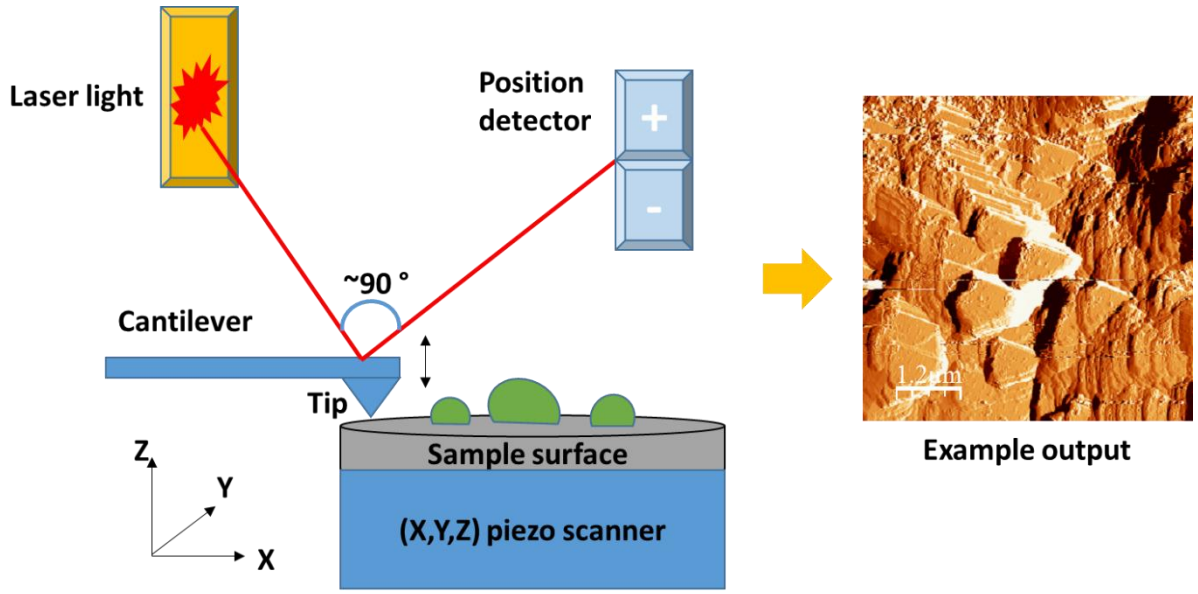

Figure 1.20 A diagram showing how the AFM technique works including sample output from our own research shown in Chapter 2.[192]

AFM also has other advantages in that it does not require vacuum unlike the similar technique scanning electron microscopy (SEM),[193] and can also be used where there is negligible change in topography, such as imaging the frictional properties of a material (sometimes known as lateral force microscopy LFM).[194] In this case the output from the position detector (a photodiode) is used to generate the height Z and the piezo scanner voltages supply the X and Y information. It can also be used for other purposes as well as it is possible to perform atomic manipulations on the surface using the tip, such as moving one atom from one location to another, bringing two atoms into close contact with each other for the purposes of catalysis, or for stimulation of individual cells.[195–197]

1.4.3: Laser ablation - inductively coupled plasma mass spectrometry (LA-ICPMS)

A final imaging technique employed in this research is laser ablation-inductively coupled plasma mass spectrometry, first invented in 1985.[198] As with the ATR-FTIR this technique is used to identify the chemical species present on the surface, rather than directly imaging the topography as in AFM. However unlike ATR-FTIR this technique is able to directly quantify the elemental composition of the surface, down to values as low as parts per trillion (ppt),[199] rather than identifying the functional groups present. Standard ICPMS techniques require a liquid sample or one that has been dissolved in a solvent, often requiring concentrated acids and microwave radiation, this poses problems when the sample is unstable or particularly insoluble.

This problem is overcome using LA-ICPMS however as a solid sample can be loaded directly into the instrument, at which point a UV laser is focussed onto the sample in raster (parallel scan) lines of 10-100 of µm width which results in aerosolisation of all constituents in the path of the laser. The aerosol is then passed through to the plasma torch of the ICPMS using a carrier gas of helium or argon, the sample is held at this torch for up to a millisecond at 6000 K where the aerosol constituents become vaporised, atomised and finally ionised. Finally the atomised sample is passed to the MS under ultra-high vacuum where ion optics separate the positively charged ions from the neutral and negatively charged ions, the positive ions are then passed through a quadrupole mass analyser which separates them according to *m*/*z* value. The detector then receives a signal for each ion passed to it, giving a quantitative output of ion current, in reference to a calibrated standard, and thus the amount of each element present in the original sample.[200,201] This process is summarised in Scheme 1.6.

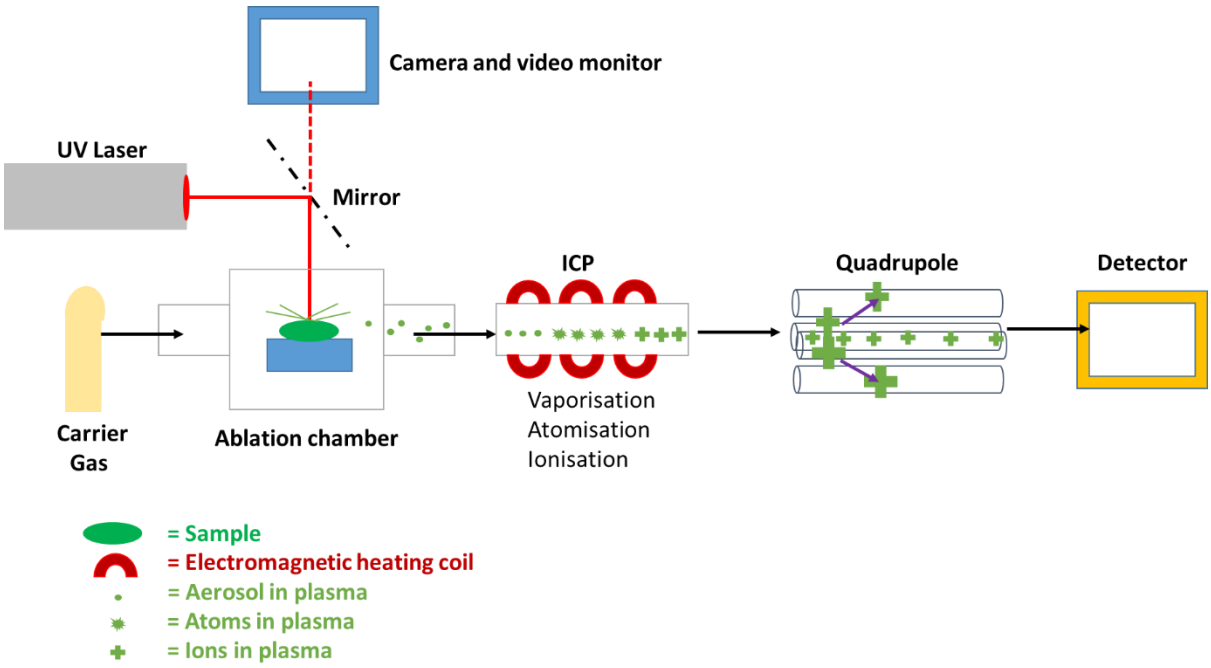

Scheme 1.6 A simplified schematic showing how laser ablation - inductively coupled plasmon mass spectrometry (LA-ICPMS) is performed.

The data obtained through LA-ICPMS can also be used to create visual maps indicating the localisation of the elements throughout the sample, and, with more specialist forms of mass spectrometer, the concentration of each element or isotope can also be used to determine the age of the sample. This gives it great use throughout other areas of science, particularly in biology and archaeology where tissues such as hair, leaves, teeth and even brain tissues

have been analysed,[202–205] allowing for monitoring of pharmaceuticals or biological processes; and in archaeology it is used to analyse historical items to determine their chemical composition to better understand our ancestors.[206,207]

1.5: Research aims and impact

At the start of this chapter the importance of different miRNA expression levels throughout medicine was discussed, particularly its direct correlation with diabetes disease and resulting kidney nephropathy. The prevalence of both diabetes and kidney disease throughout western populations was also discussed, with the inherent problems to the health services and the detrimental effect on the patient's lifestyle being described, thus emphasising the need for faster and less specialised miRNA detection for implementation in point of care diagnostics. Therefore it is the aim of the research described throughout the rest of this thesis to describe a method of modifying a set of carbon based electrodes for use in quantifying miRNA in a urine matrix. The direction of travel is towards a commercially available biosensor that can be used in the point of care environment by non-scientist end users for the diagnosis of the early stages of kidney disease, hopefully resulting in the patient being diagnosed before requiring dialysis or transplants.

We will start by modifying a commercially available and industry standard stationary glassy carbon electrode (GCE) chemically with a naphthalene sulfonic acid in order to generate a surface of sulfonic acid functionalities, before further modifying these to sulfonyl chlorides to allow the attachment of DNA probe strands. This will then allow us to electrochemically detect and quantify a miRNA with a sequence complementary to this DNA probe strand. Doing this with varying miRNA target concentration will allow for the determination of the sensitivity of the biosensor. This method was chosen to begin with as it requires only 3 steps to go from a clean carbon surface to a DNA based sensor, meaning that it should be relatively quick to produce the sensor each time it is required which is one of our target parameters. The relatively simple DNA/miRNA hybridation based procedure will also keep the analysis simple and requires very few additional chemicals which is also preferred if the technique is to be adapted for point of care use. Different miRNA sequences and sample matrices can then be used to determine the selectivity of the biosensor and its application in the detection of urinary miRNAs.

Should this prove successful then we will be looking to develop the methodology for adaptation onto disposable screen printed electrodes. Using disposable screen printed electrodes will allow us to produce multiple sensors at any one time and will move us closer to our overall aim of developing a commercially viable biosensor. Finally, we will be looking towards producing disposable electrodes of our own design for the detection of multiple miRNA species on one biosensor as this will be required for a diagnostic test. Should we will be looking to test our sensor on patient urine samples in order to determine whether or not a significant difference can be detected between a healthy individual and a patient with diabetic kidney nephropathy. By combining all of these objectives together we will be one step closer to the development of a biosensor that shows viability for use in a clinical point of care environment.

Thus the aims of the project were as follows:

1. Develop an electrode modification procedure that could be applied to an industry standard carbon electrode for detection of miRNAs in solution, and quantification by electrochemical analysis.
2. Develop the methodology described following aim 1 for implementation on a screen printed carbon electrode as a disposable biosensor.
3. Design a screen printed carbon electrode that could perform simultaneous repeated detection of a single miRNA target to obtain repeatable data on a single electrode. The potential for future adaptation towards multiple microRNA detection on one electrode was discussed.
4. Detect existing urinary miRNA biomarkers in healthy control and diabetic kidney nephropathy patients, showing the difference in expression levels and discriminating between them.

Chapter 2: Glassy Carbon Electrode Results

Chapter 2: Glassy Carbon Electrode Results

2.1: Glassy carbon and other electrode materials

The electrochemical data described in this chapter were generated using a modified commercially-available glassy carbon electrode (GCE). Commercially available multi-use electrodes, of which a GCE is an example, are manufactured in a variety of shapes, sizes and materials. The standard stationary electrodes made with a PCTFE tube of 7.5 cm length and 6 mm overall diameter, with an embedded 1.6-3 mm working area disk of an inert material such as gold, platinum, silver, nickel, pyrolytic carbon paste or glassy carbon, and in some cases palladium. Alternatively rotating disk electrodes, in which the electrode is mounted in an automated rotator prior to submersion in the analyte, are also available and are often used to determine redox reaction mechanisms.[208] A final class known as microelectrodes, in which a wire of inert gold, platinum or carbon fibre of ≈10 µm diameter, can also be produced to enable faster scan rates and lower capacitance.[209]

While each of these electrodes has its own specific use, the work described here focuses on the use of the standard tubular stationary electrode with a 3 mm glassy carbon surface. To develop electrochemical miRNA detection, glassy carbon was preferred to better gold or platinum alternatives on the basis of its lower price. Cost is an essential consideration for diagnostic testing, and work in later chapters describes the use of disposable screen-printed electrodes, also based on carbon materials, following the proof-of-principle glassy carbon electrode analysis described in this chapter.

The use of noble metal electrodes is common to a wide range of products used extensively in academic and industrial research laboratories. This popularity is due to their extreme chemical inertness, high anodic range and the ease by which they can be obtained in pure form from ore.[210] The use of gold electrodes in the study of biological molecules such as proteins and nucleic acids is particularly popular due to the simplicity of immobilising these types of molecules onto the electrode surface. Gold surfaces have a highly exploitable affinity to thiols and disulfides that allows them to bind to these groups via a strong Au-S link, either through the removal of the thiol hydrogen, or cleavage of the S-S bond in a disulphide. DNA sequences may readily be purchased with thiol modifications at their 3’ or 5’ ends, allowing very simple surface monolayer generation.[211,212] Gold is thus a good electrode material for

DNA based analysis, but is limited to anodic potentials as positive potentials have the potential to oxidise its surface, starting at 1.36 V.[213] It should be mentioned, however, that reductive potentials can also be problematic for thiol-bound gold surfaces, as reduction can cause the desorption of thiolates from the surface. These are able to be re-adsorbed through oxidative potentials, particularly where cyclic voltammetry is used, but the extent of re-adsorption depends heavily on the alkyl thiol used.[214] By contrast, platinum may be used in these ranges, and while the same bonding to thiols is not possible, it is still a highly modifiable material,[215,216] and shows stable electrochemical behaviour. However, the presence of any water or acid in the analyte can result in a reduction reaction and hydrogen evolution even at previously useable negative potentials.[217] Both of these materials are also expensive in comparison with carbon.

Consequently, carbon-based electrodes have also been developed, with three main types of glassy, pyrolytic and carbon paste. These are markedly cheaper per unit mass than either platinum and gold, and, owing to their inertness to both chemical attack and oxidation/reduction reactions, are useable across a much larger potential window (-0.8 V to 2.2 V compared to ≈-0.2 V to 1.8 V and -0.5 V to 1.9 V for platinum and gold respectively)[218] Also, due to the brittleness of carbon to mechanical strain, it is straightforward to polish and chemically clean the electrode before each new modification or experiment, leaving a fresh carbon surface for a good signal to noise ratio.

Glassy carbon is the most expensive of the above three types, but the surface chemistry of glassy carbon has been investigated extensively, and activation and modification of these electrodes is a highly researched area.[219] This type of carbon also has a high amount of surface order which allows for better electrochemical responses in comparison with carbon paste electrodes, while still retaining small defects as possible nucleation zones for an increased chemical modification potential than the highly orientated pyrolytic graphite.[220,221] Interestingly, the exact structure of glassy carbon remains a highly disputed topic. It has previously been assumed that the structure is similar to that of graphite,[222] or even a polymer of carbyne chains due to its electrochemical behaviour.[223] However this would not account for its extreme resistance to even strongly acidic solutions, thus recent work done by P. J. Harris suggests that it has a much more fullerene-like structure.[224]

The advantages mentioned above, the extreme inertness to chemical attack, high potential for modification, suitability with biological systems and relative cheapness compared to noble metal based electrodes suggest that glassy carbon is highly suitable for our investigation. Also, as mentioned previously, the aim of this project is to develop a biosensor that can be applied to a series of screen printed carbon electrodes for potential future commercial application. These electrodes are based more on a polymer based carbon ink, thus having a carbon electrode allows for better comparison between the disposable electrode and the research standard than the use of a noble metal based electrode. Nevertheless carbon paste, despite being closer in nature to the disposable electrodes than glassy carbon, is not ideally suited to proof-of-principle testing due to inherent surface malformations of the disordered electrode material. Therefore all of the results performed in this chapter were generated using the relatively high order, and well researched glassy carbon electrode material.

2.2: Modification procedure

In order to detect mature microRNAs (miRNAs) in solution, the GCE first needed to be modified to allow the addition of a DNA probe strand complementary to the target miRNA sequence, for Watson-Crick base pairing. Unlike gold surfaces, which are able to form strong sulfur-gold linkages to thiol groups on 3' or 5' modified DNA strands in order to immobilise them,[225,226] glassy carbon surfaces require functionalising before a probe oligonucleotide can be deposited. A number of ways have been reported for doing this.[170,227,228] Due to its simplicity, a similar version of the modification procedure described by Wang *et al.* was used for the production of our sensor. An overview of the procedure and the theory of how this effects the electrochemical response is described below.

Firstly, the surface of the electrode must be refreshed to ensure no crossover or contamination from previous experiments. To achieve this with a GCE, an alumina polish was used at consecutively smaller grades, the largest as an abrasive to remove any compounds attached at the surface, and the smaller to smooth the surface to an even 'mirror-like' finish. It is important that this is done evenly over the entire the surface, therefore a 'figure 8' motion was employed to ensure that the abrasion was reproducible after each experiment.[229] Finally, the polished electrode was sonicated in acetone, ethanol and deionised water to remove any residual alumina.

The cleanliness of the electrode was then tested by performing cyclic voltammetry measurements using a mixture of ferri and ferrocyanide in KCl. For a 'factory fresh' and machine cleaned electrode the peak separation should be close to 59 mV.[230] The polishing technique and an example of a clean voltammogram are shown in Figure 2.1, the best and most robust separation achieved was 101 mV, and this was carried forward. The absolute peak separation was likely also to be dependent on the precise surface of the glassy carbon, as well as the exact conditions of the cell e.g. concentration, supporting electrolyte, scan rate et cetera.[231]

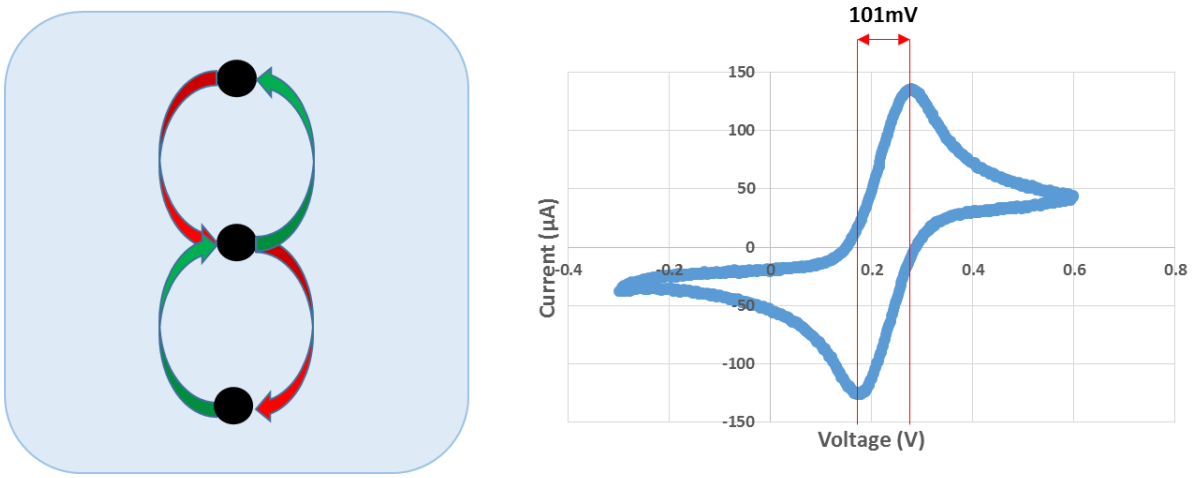

Figure 2.1 A diagram of the polishing technique and an example of a 'clean' cyclic voltammetry obtained. The black spots are points of possible slight pressure increase due to direction changes with the arrows indicating polish direction. CV performed using 5 mM $K_3[Fe(CN)_6]/K_4[Fe(CN)_6]$ in 0.1 M KCl electrolyte at room temperature.

The electrode preparation procedure was followed by electrode modification. Firstly, the GCE surface was modified by electrochemical deposition of the naphthalenesulfonic acid derivative *4*-amino-3-hydroxy-1-napthalenesulfonic acid (ANSA) via multiple cyclic voltammetry cycles. Despite an absence of detail from Wang *et al.* it is believed that under voltammetric deposition the ANSA amino group is oxidised, allowing it to bind to the carbon surface of the electrode, and that subsequent polymerisation results in the formation of an ANSA monolayer across the GE surface. An investigation into the compound's chemically induced oxidative polymerisation revealed a possible monomer bonding pathway, the details of which will be briefly described.

Doğan *et al.* have shown, through the use of the chemical oxidant NaOCl, that under oxidative stress the naphthalene aryl systems become joined through the amino functionality at position 4 and the naphthalene carbon 9, possibly through a radical pathway. This is made

possible due to the availability of the ring system to delocalise the unpaired electronic spin density.[232] It is believed that the same process is occurring on the glassy carbon surface at the oxidation potential during electrochemical deposition, with the polymer forming a covalent film along the surface. The proposed polymerisation pathway is shown schematically in Scheme 2.1, adapted from published data.[232]

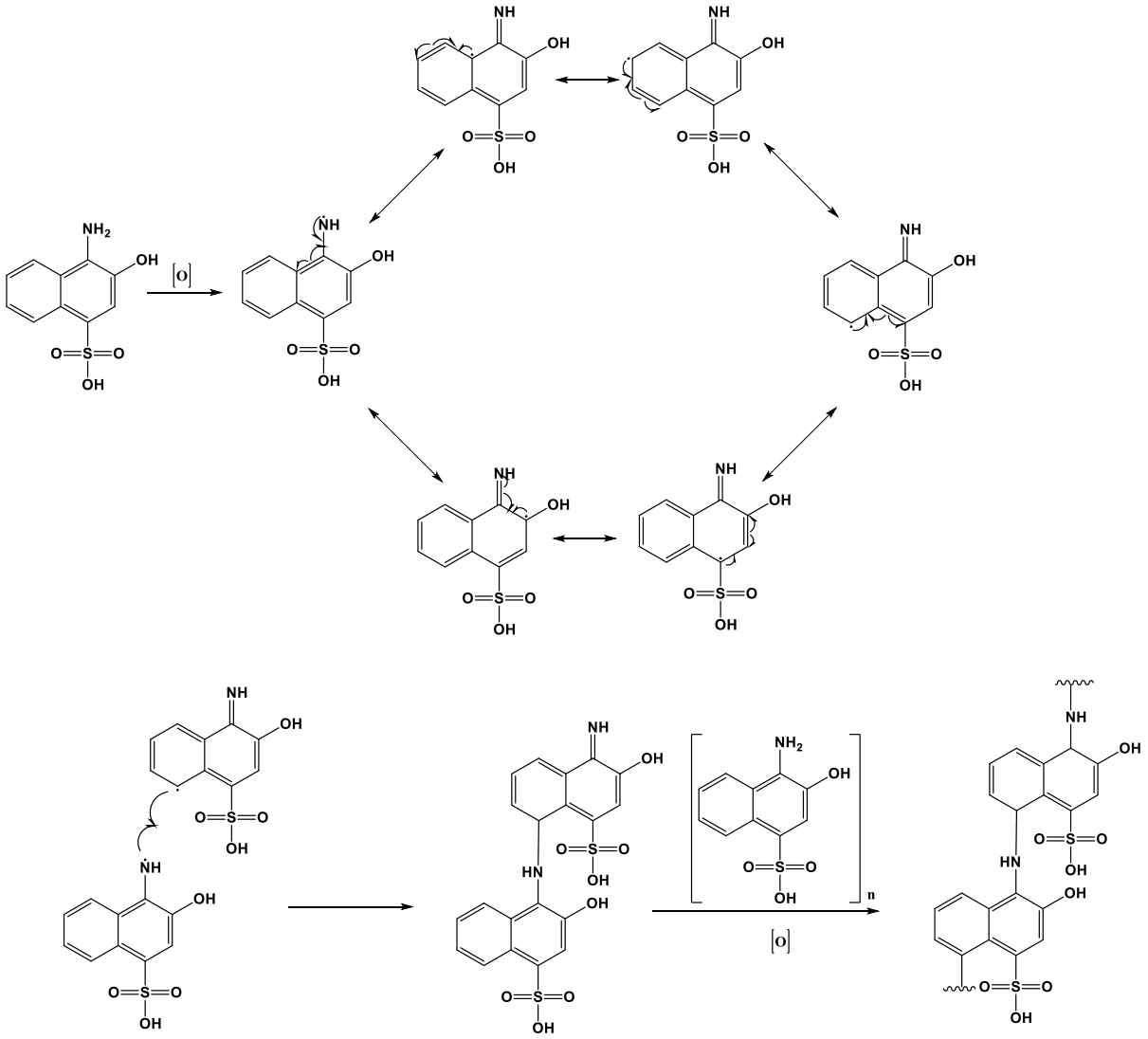

Scheme 2.1 A schematic showing a potential pathway of how 4-amino-3-hydroxy-1-naphthalenesulfonic acid (ANSA) is polymerised via oxidative stress and resonance of the unpaired spin through the aryl napthalene.[232]

The cyclic voltammogram obtained during the electrochemical deposition procedure was used as an indicator of sulfonic acid deposition (Figure 2.2). Over multiple cycles it was seen that the oxidation peak at ≈0.32 V became progressively less intense, and the other minor peaks flattened out. After 4-5 cycles the intense oxidation peak reached a steady state current response, and the remainder of the cycles were uniform in peak intensity, indicating that the

maximum surface coverage of ANSA had been obtained. A total of 8 cycles were therefore performed in order to ensure that the maximum coverage was obtained each time the electrode was modified, allowing for the greatest reproducibility between experiments. An example of the voltammogram obtained during the deposition, indicating the gradual decline in peak intensity, is shown in Figure 2.2. The deposition was visually apparent as the development of a red hue in the solution around the electrode surface during voltage application.

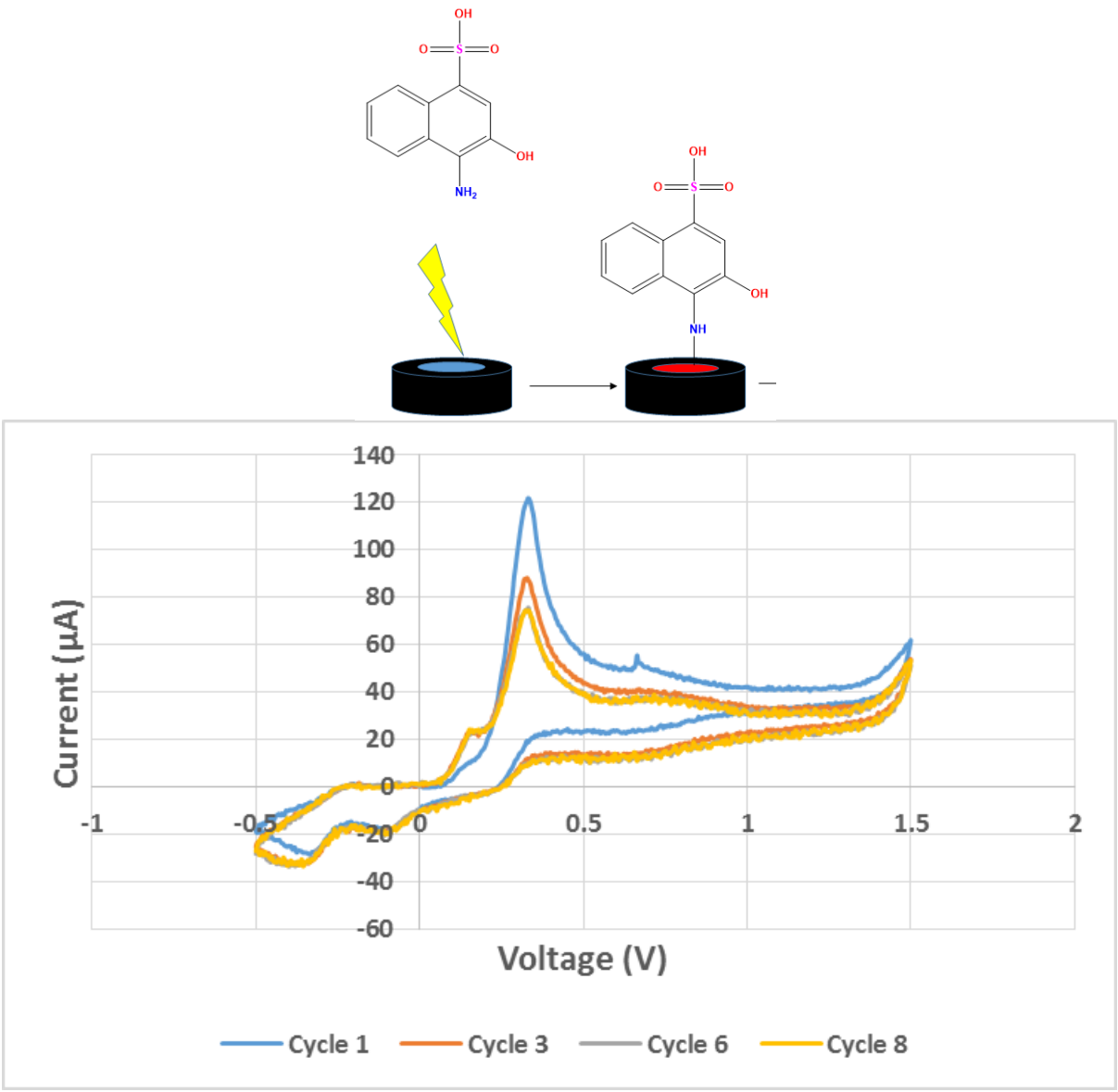

Figure 2.2 An example of the cyclic voltammograms obtained during deposition of ANSA onto the GCE. A clear lowering of peak intensity can be seen at the oxidation peak of 332mV over increasing cycles. Performed in 10 mM ANSA in 25 mM pH 7.0 PBS. The deposition is also shown schematically (top).

Following ANSA deposition, a cyclic voltammogram performed in ferricyanide solution showed that the surface was hindered from electron transfer due to the vastly decreased current response for oxidation and reduction. This was as predicted for a fully coated surface. Having confirmed that the deposition procedure was successful, the sulfonic acid functionality on the electrode was chemically modified to a sulfonyl chloride, to activate it towards nucleophilic attack from the amine tagged probe DNA sequence. The probe sequence could then be covalently linked to the ANSA surface for miRNA hybridisation. Therefore the electrode was then submerged in a solution of PCl_5 in acetone to substitute the hydroxyl of the sulfonic acid with a chloride, thereby generating the required sulfonyl chloride (see Scheme 2.2).

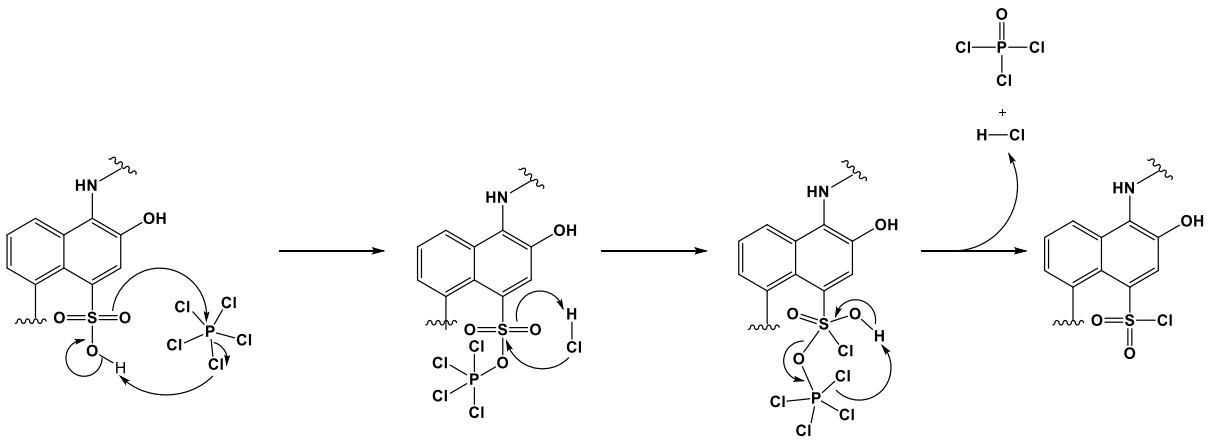

Scheme 2.2 A summarised mechanism for sulfonyl chloride formation from PCl_5 and ANSA, the true mechanism likely not being concerted. Adapted from the mechanism for acyl chloride formation.[233]

Again the electrode modification was tested to ensure successful adaptation of the sulfonic acid to the sulfonyl chloride by cyclic voltammetry in ferricyanide solution. These showed that the oxidation and reduction peaks increased in current response, most likely due to the reduced negative charge across the surface of the newly modified 4-amino-3-hydroxy-1-napthalenesulfonyl chloride (ANSCl). This charge reduction resulted from the absence of acidic hydroxyl groups to deprotonate in solution and form negatively charged sulfonate, which in turn would repel the ferricyanide electrochemical analyte from the surface.

With the surface chemistry of the electrode suitably modified, a C_6 amino tagged DNA probe complementary to the target miRNA sequence was covalently attached via sulfonamide bond

formation. Placement of a droplet of the amine tagged DNA, dissolved in aqueous buffer, on the ANSCl modified electrode led to reaction between the amine functionality and the sulfonyl chloride via a nucleophilic substitution, resulting in the formation of the 4-amino-3-hydroxy-1-napthalenesulfonyl amide-DNA probe (ANSAm-DNA) as shown in Scheme 2.3.

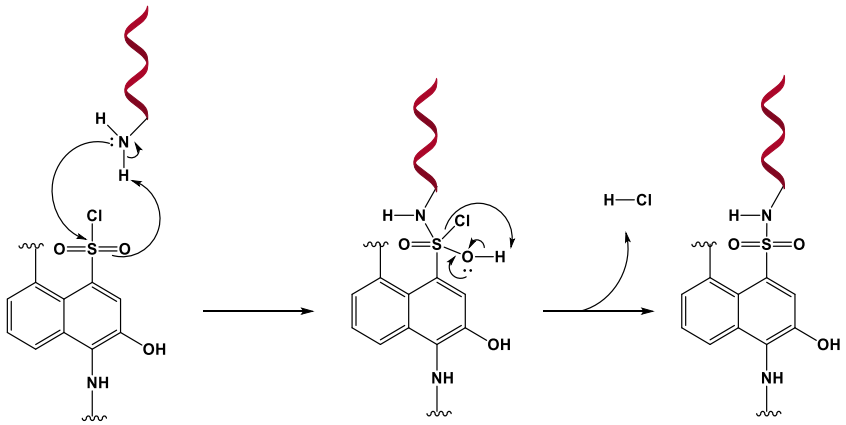

Scheme 2.3 Proposed summarised mechanism for the attachment of a C_6 amine tagged DNA sequence via sulfonamide coupling, again certain steps are likely not concerted. The DNA is shown pictorially by the red helix.

Once prepared, the electrochemical response of the ANSAm-DNA probe was analysed in ferricyanide solution. This showed that a modest decrease in current response compared to the ANSCl response, which was expected due to the increased negative charge of the DNA phosphate backbone and the size-related increase in surface coverage.

Finally, to ensure that the probe functioned as a detection tool for miRNA, the ANSAm-DNA probe was submersed in a solution of the target miRNA sequence in buffer and heated for 30 minutes to allow hybridisation between the DNA probe and the target miRNA. As predicted, and shown later with further data, this again resulted in decreased current response due to the further increased negative charge and surface coverage. This modification procedure is summarised diagrammatically in Figure 2.3. Examples of the changes in cyclic voltammetry and Nyquist impedance responses for each stage of the modification procedure are also shown.

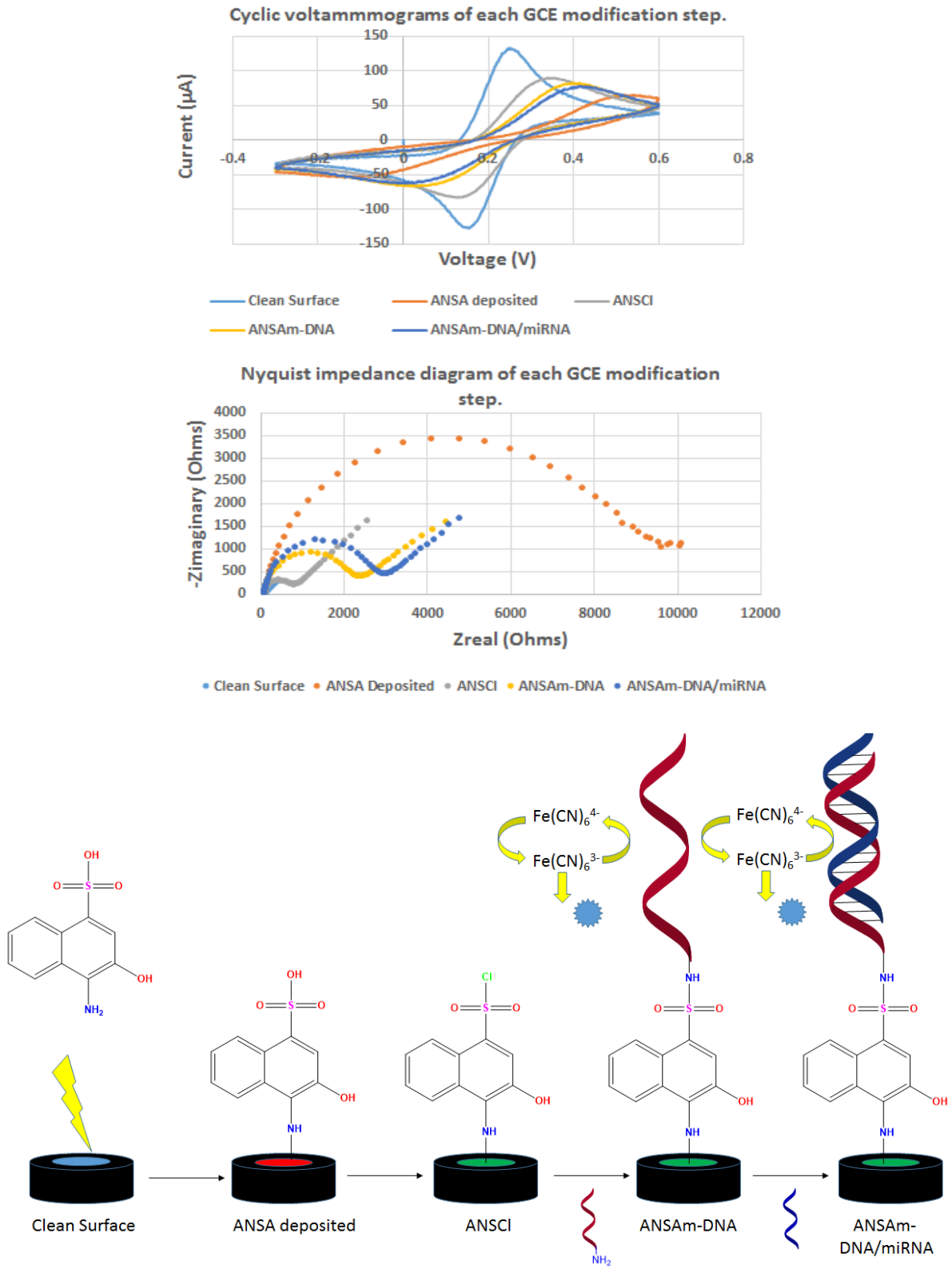

Figure 2.3 A summarised schematic of the procedure for modifying a glassy carbon electrode for miRNA detection, DNA is displayed red and the miRNA in blue. Also shown are example cyclic voltammograms and impedance data for each modification step, performed using 5 mM $K_3[Fe(CN)_6]/K_4[Fe(CN)_6]$ in 0.1 M KCl electrolyte at room temperature.

2.3 Sensitivity and Selectivity Results

The above data describe testing the GCE modification procedure and confirming that it resulted in a measurable change at each stage and displayed a difference before and after probe DNA:target microRNA hybridisation. Probe sensitivity was then analysed across a range of miRNA concentrations compared to a buffered "blank" sample.

DNA sequences complementary to mature miR-21 and miR-16 were selected for use as probes, since these miRNAs are highly abundant and widely expressed throughout human tissues. The sequences of the mature miRNA species and their DNA complements are given in Table 2.1.

Table 2.1 DNA and RNA sequences used for initial sensitivity testing, shown in 5'-3' orientation.

Species Name	**Species Sequence**
Anti-miR-21 (DNA)	5'NH_2-C_6-TCA ACA TCA GTC TGA TAA GCT A
miR-21 (RNA)	UAG CUU AUC AGA CUG AUG UUG A
Anti-miR-16 (DNA)	5'NH_2-C_6-CGC CAA TAT TTA CGT GCT GCT A
miR-16 (RNA)	UAG CAG CAC GUA AAU AUU GGC G

For sensitivity experiments, the probe was initially produced by modifying the electrode surface and applying the desired antisense strand, as described above, at which point an initial set of electrochemical measurements was performed for baseline comparison. The chronocoulometric and EIS responses provided the most defined and analysable data, and the most reproducible analytical data, and were therefore deemed to be the most informative electrochemical measurements. Cyclic voltammetry was also performed, however, as the data obtained from the voltammograms did not give a clear relationship with miRNA concentration, this chapter will focus on the coulometric and impedance responses for the production of sensitivity plots. It should also be noted that double step coulometry was

performed, as the change in voltage provided easily interpretable peak minima for direct and consistent comparison between each concentration analysed.

DNA bearing probes underwent chronocoulometry and EIS analysis to generate an initial origin DNA only response. After this, the probe was submerged in buffered miRNA solutions of varying concentrations to allow hybridisation of the attached DNA and the miRNA target. The resulting hybridised DNA/miRNA probe was then electrochemically analysed for a second time, and the response obtained at this point was compared with that of the origin response to give a change in either charge (ΔQ) or charge transfer resistance (Ohms = Ω, ΔR2) for coulometry and EIS respectively. Prior to obtaining the full data set for miR-21, the hybridisation event was performed using 10^{-10} M over defined periods (60, 40, 30 and 10 mins) to determine the optimum hybridisation time. These results are shown in Appendix 1 Figure A1.2 at the end of this thesis, 30 minutes hybridisation gave a response close to that after 60 minutes and so was selected for further experimental hybridisations. Once optimised the hybridisation after 30 minutes was repeated 3 times for each concentration, and the average change plotted against its corresponding concentration as a $\log_{10}$ scale. This resulted in a linear correlation with a regression coefficient of 0.98 for the coulometry data and 0.90

for the EIS data, as shown in Figures 2.4-2.5 and 2.6-2.7, respectively. The raw data is displayed in Appendix 1 Table A1.1 and A1.2 respectively.

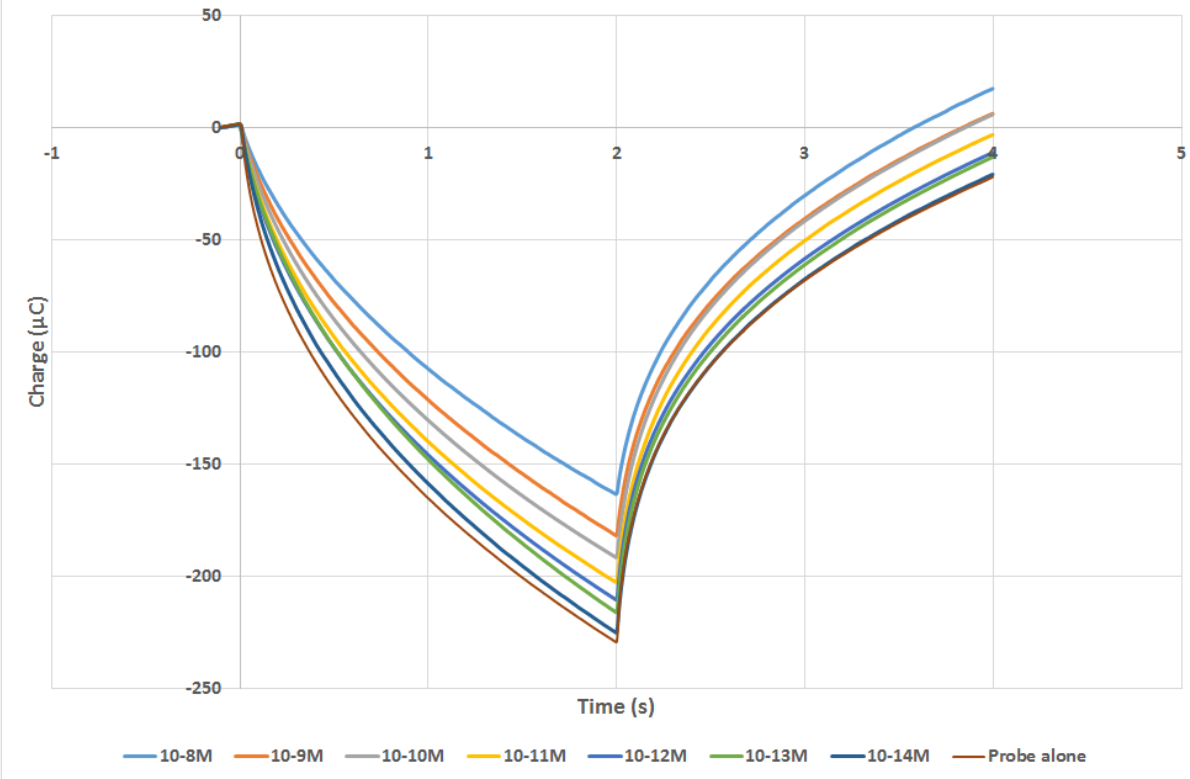

Figure 2.4 The chronocoulometric response obtained for different concentrations of miR-21. Performed using 5 mM $K_3[Fe(CN)_6]/K_4[Fe(CN)_6]$ in 0.1 M KCl electrolyte at room temperature.

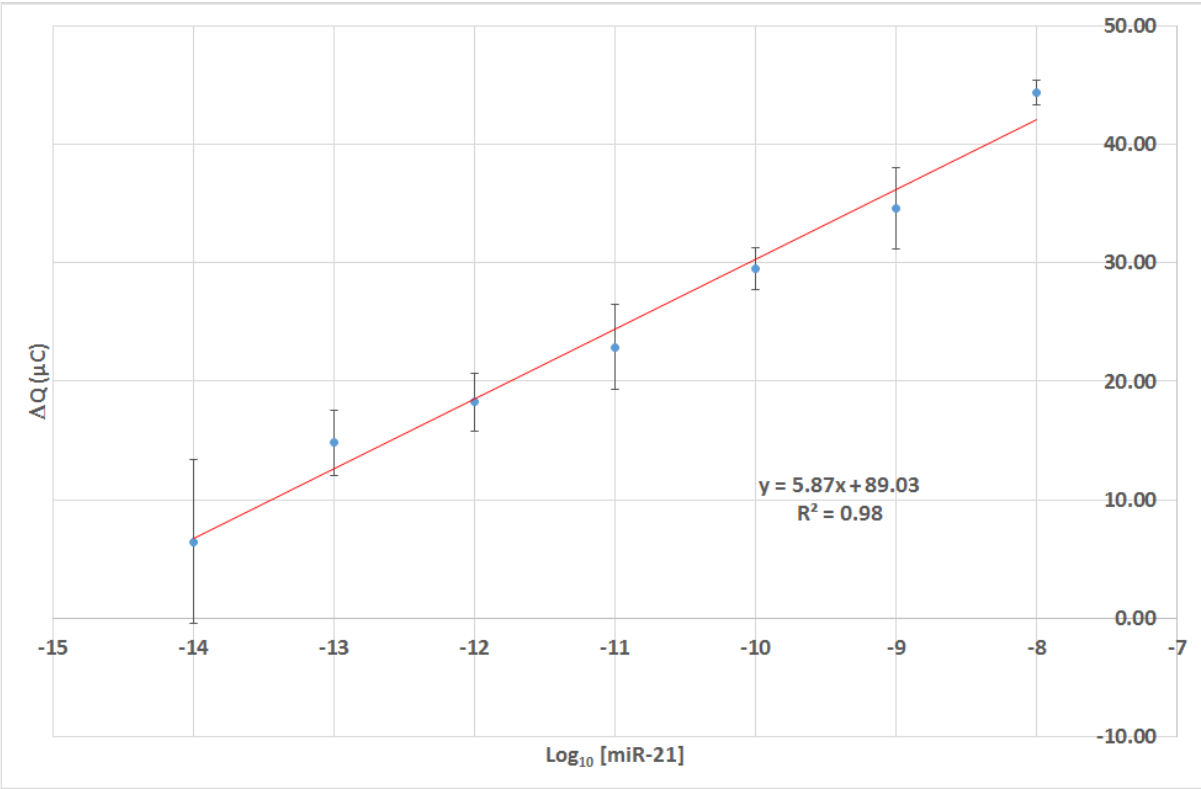

Figure 2.5. Change in coulometric response between the electrode modified with complementary DNA strand alone and following RNA incubation (ΔQ) with log_{10} [miR-21] (M), performed in triplicate. The calculated limit of detection is 2 × 10^{-14}M (20 fM) and the Pearson regression coefficient is 98%

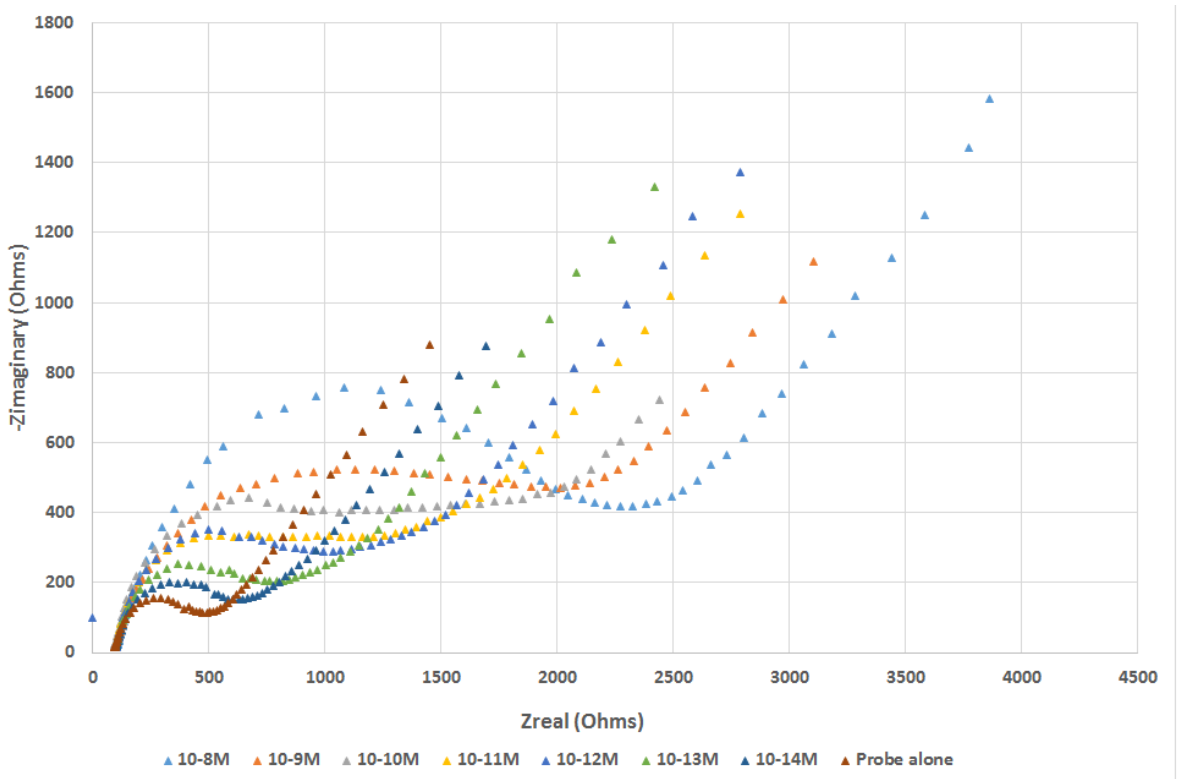

Figure 2.6 The impedance response obtained for varying concentrations of miR-21. Performed using 5 mM $K_3[Fe(CN)_6]/K_4[Fe(CN)_6]$ in 0.1 M KCl electrolyte at room temperature.

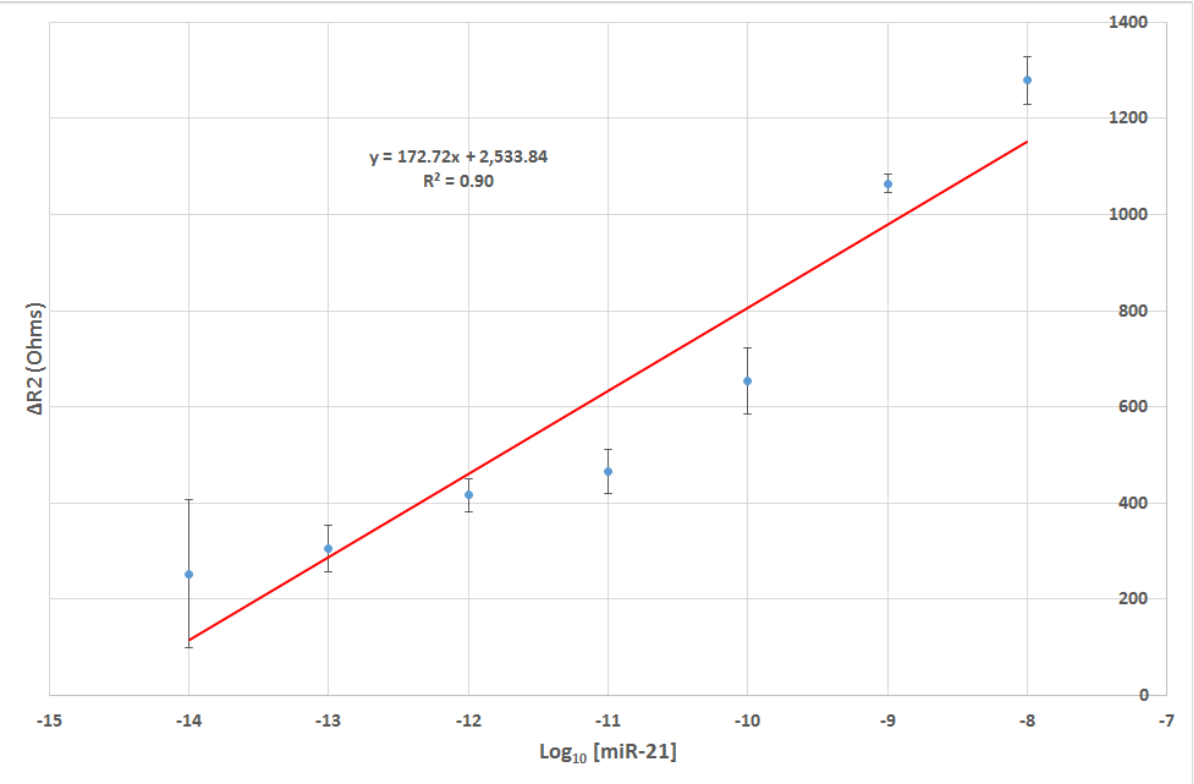

Figure 2.7 Change in charge transfer resistance (ΔR2) between the electrode modified with complementary DNA strand alone and following RNA incubation (ΔQ) with log_{10} [miR-21] (M), performed in triplicate. The Pearson regression coefficient is 90%. Fitted to the following equivalent circuit:

The above data were used to calculate an extrapolated hypothetical sensitivity of 0.68 fM for coulometry, and of 2.14 fM for impedance. Analysis of buffered solutions in the absence of miRNA provided a measure of experimental noise. This was calculated by performing the blank experiment in triplicate and then adding triple the standard deviation to the average response obtained. The resulting change in response from these blank solutions gave a simulated worst case scenario of noise response and gives a limit of detection of 20 fM, the calculation for this is described in Appendix 1 Table A1.3 at the end of the thesis.

The data collected for this sensitivity plot were obtained in triplicate by starting the electode preparation and modification procedures anew for each replicate, to measure the variability across the whole procedure, including the cleaning step. However, it was also possible to obtain replicates by using heat treatment to denature surface-bound DNA/miRNA hybrids,

regenerating the single DNA strands at the probe's surface and recapitulating the initial electrochemical response magnitude. By performing this heat treatment repeatedly it was determined that 2 surface replenishments, i.e. 3 data points, could be obtained accurately before the response dropped significantly. This is also shown in Appendix 1 Figure A1.1 at the end of this thesis.

The selectivity of the miR-21 probe characterised above was then investigated. Since mature miRNAs are typically 19-23 nucleotides in length, determination of probe selectivity between closely-related sequences is particularly important. This point is emphasised in miRNA families such as the let-7 miRNA family. Mature human let-7a and let-7b sequences differ by two nucleotides, with adenine residues at positions 17 and 19 of hsa-let-7a and corresponding guanines in hsa-let-7b; with hsa-let-7c differing only by the guanine residue at position 19.[234] Mindful of these potential sequence similarities, the following experiments were undertaken to investigate probe sensitivity.

To this end, a series of synthetic miRNA targets were designed with central and/or peripheral sequence mismatches. Mature miR-16 was included as an example of a highly expressed human miRNA with comparatively little sequence identity, with 8 of 22 matching nucleotides.

To maximise response from the mismatched sequences, the maximum concentration of 10 nM used previously in the sensitivity testing was used. The miRNA sequences used for selectivity testing are shown in Table 2.2 and the coulometric (ΔQ) and impedance charge transfer resistance (ΔR2) responses for each sequence are shown in Figure 2.8.

Table 2.2 Sequences of oligonucleotides used for selectivity testing of the miR-21 probe. Sequence mismatches are indicated in bold and underlined.

MiRNA description	Sequence
miR-21	UAG CUU AUC AGA CUG AUG UUG A
1 mismatch	UAG CUU AUC **G**GA CUG AUG UUG A
2 mismatches	UAG CUU AUC **G**GA CUG AUG UUG **C**
3 mismatches	**A**AG CUU AUC **G**GA CUG AUG UUG **C**
miR-16	UAG C**AG** **CA**C **GU**A **AAU** AU**U** **GGC** **G**

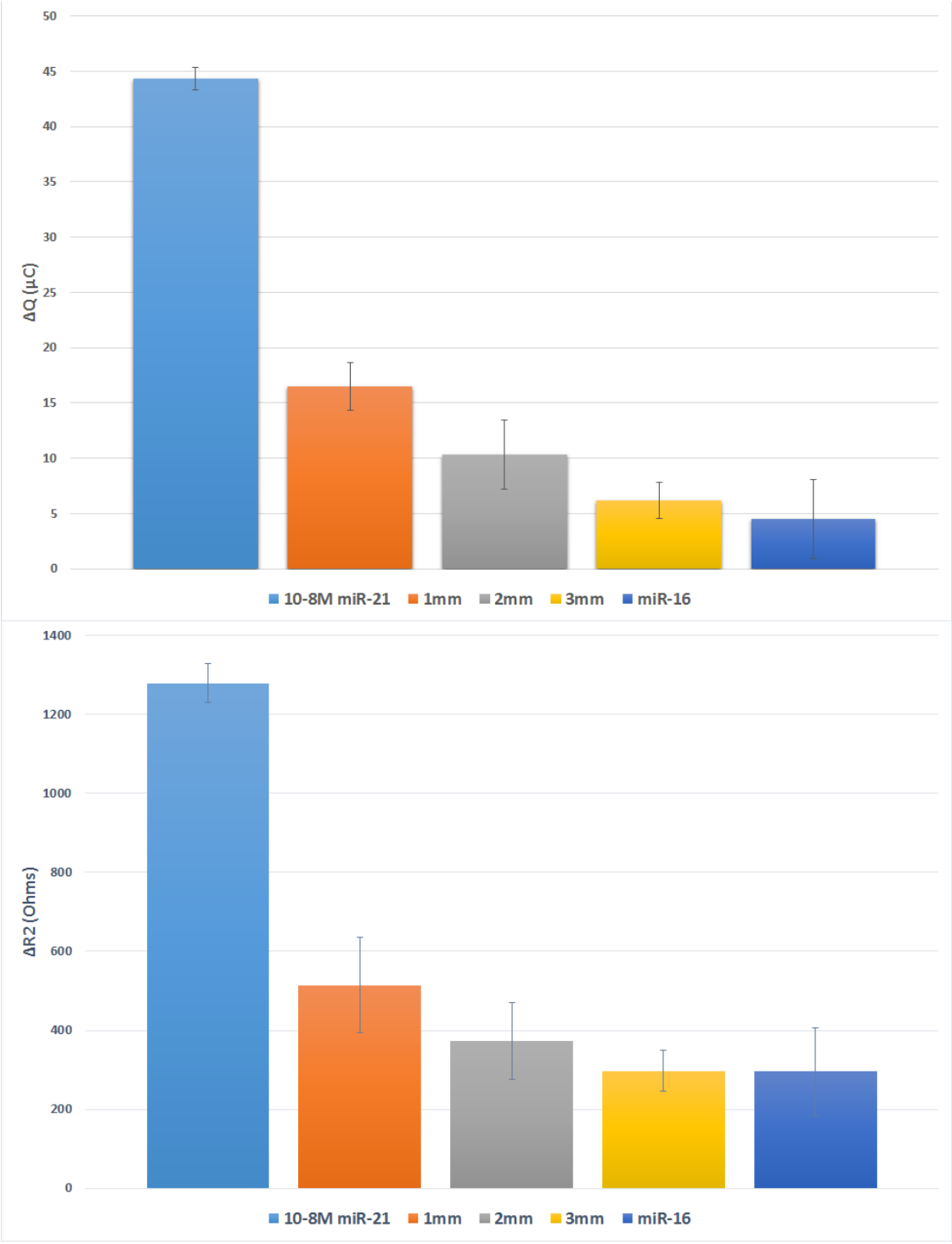

Figure 2.8 The response obtained for coulometry (top) and Nyquist impedance (bottom) experiments performed using 10^{-8} M solutions of mismatched (mm) miRNA targets. Experiments were performed in triplicate and are shown against the response obtained for 10^{-8} M miR-21 for comparison. Performed using 5 mM $K_3[Fe(CN)_6]/K_4[Fe(CN)_6]$ in 0.1 M KCl electrolyte at room temperature.

The data shown in the above figure (raw data and % signal drop is also given in Appendix 1 Table A1.4 and A1.5 respectively) demonstrates probe specificity, with significant differences between the miR-21 response and all other readouts. The smallest difference in

magnitude was observed with the single base mismatch sequence, which nevertheless resulted in a significant drop in response of almost 63% of the miR-21 signal, i.e. a response resembling detection of a concentration of between 10^{-12} and 10^{-13} M. The response then decreased with each increase in the number of mismatches. These data demonstrated probe selectivity, and further testing was then carried out as described below.

As each nucleotide has slightly different electronic effects and sizes, they may show different response curves when analysed with the ferricyanide analyte. This is potentially complicating and time consuming if the biosensor for each target miRNA sequence required a separate calibration plot and would make their implementation difficult. A universal calibration plot would not only alleviate this problem, but also act as further proof that the responses obtained for the miR-21 target resulted from probe:miRNA interactions, and were not artefactual. To ensure that the general relationship between concentration and electrochemical response was independent of the miRNA target sequence, sensitivity testing was repeated using anti-miR-16 as the probe strand and miR-16 as the target. The results of this overlaid with the original sensitivity plots for the miR-21 coulometric (ΔQ) and impedance charge transfer resistance (ΔR2) are displayed in Figure 2.9.

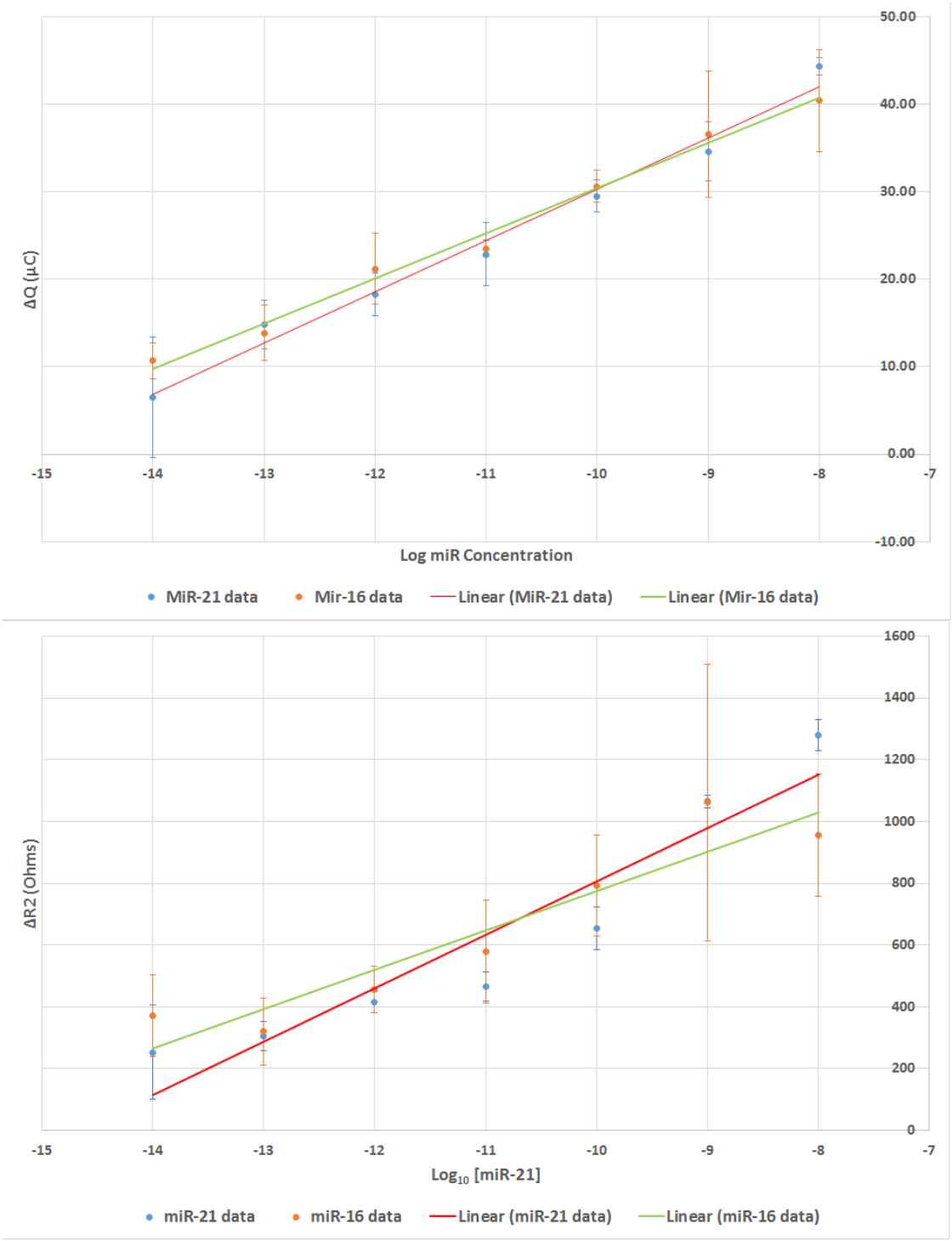

Figure 2.9 Sensitivity testing for target miR-16 using its complementary DNA strand as probe. MiR-16 data are shown in orange and the corresponding coulometry (top) and Nyquist impedance data (bottom) miR-21 data in blue. Performed in triplicate using 5 mM $K_3[Fe(CN)_6]/K_4[Fe(CN)_6]$ in 0.1 M KCl electrolyte at room temperature.

Figure 2.9 (raw data Appendix 1 Table A1.6 and 1.7) shows that, despite some variance at higher miRNA concentrations (e.g. 1 nM and 10 nM), the responses obtained for both miR-16 and miR-21 were comparable. With the exception of the 10^{-8} data, the coulometry points for both miR-16 fell within and miR-21 the error bars.

This indicates an overall concordance for the data for these two miRNA sequence with significantly different base compositions and suggests that this method is broadly applicable for miRNA detection.

2.4 Synthetic urine experiments

Before testing the probe for urinary miRNA detection, synthetic miRNA targets dissolved in a variety of urine-like matrices were tested. MiRNAs were dissolved in a solution containing urine's principal constituents: salt (NaCl), protein and urea. To a 0.1 nM miR-21 aqueous solution NaCl was added to a concentration of 3 mg/mL and 10 mg/mL to simulate the lower and upper salt concentrations limits possible in patient urine samples. The choice of salt, and later protein, concentrations were chosen according to a report published by NASA on the constituents of human urine.[235]

Once the miRNA had been dissolved in the buffer matrix, containing the desired concentration of salt, the probe was added and allowed to hybridise with the target miR-21 as normal. The coulometry (ΔQ) and impedance charge transfer resistance ($\Delta R2$) were then measured as before, comparing the response obtained from the probe alone to that after hybridisation with the target miRNA. This was repeated for both the 3 mg/mL and 10 mg/mL salt matrices containing the miRNA and the response plotted against that obtained from the synthetic miRNA in the buffer alone. The resulting comparative graphs are shown in Figure 2.10.

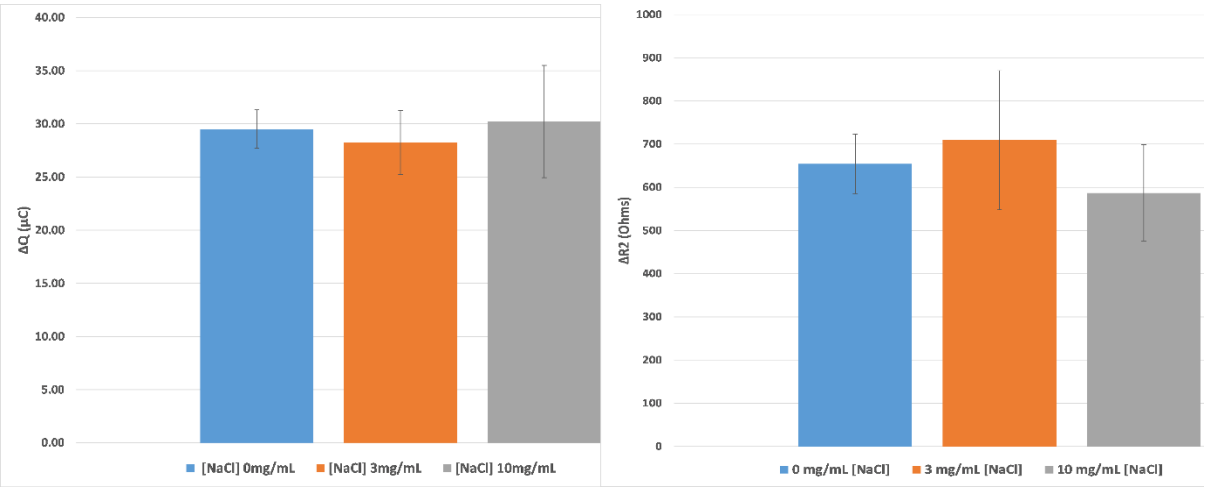

Figure 2.10 A comparative graph of coulometry (left), and charge transfer resistance (right), responses obtained for a solution 0.1 nM miR-21 in buffer and with different salt concentrations. Each experiment was performed in triplicate using 5 mM $K_3[Fe(CN)_6]/K_4[Fe(CN)_6]$ in 0.1 M KCl electrolyte at room temperature.

These comparative graphs show that neither high nor low salt concentrations significantly affected miRNA electrochemical responses. In both cases the standard deviations of the responses (shown by the error bars) were within that of the response obtained with buffer alone, suggesting that the salt content in a urine sample would not have a significant effect on miRNA quantification.

To test the effect of urea on miRNA electrochemical response, powdered urea was dissolved to a 9.3 g/L aqueous urea solution. This concentration was again chosen from the NASA report mentioned above. Target miR-21 was then diluted to a concentration of 10 pM in this urea solution and the resulting mixture was then used as the hybridisation solution. Coulometric responses using probe alone and miRNA were then compared (Figure 2.11).

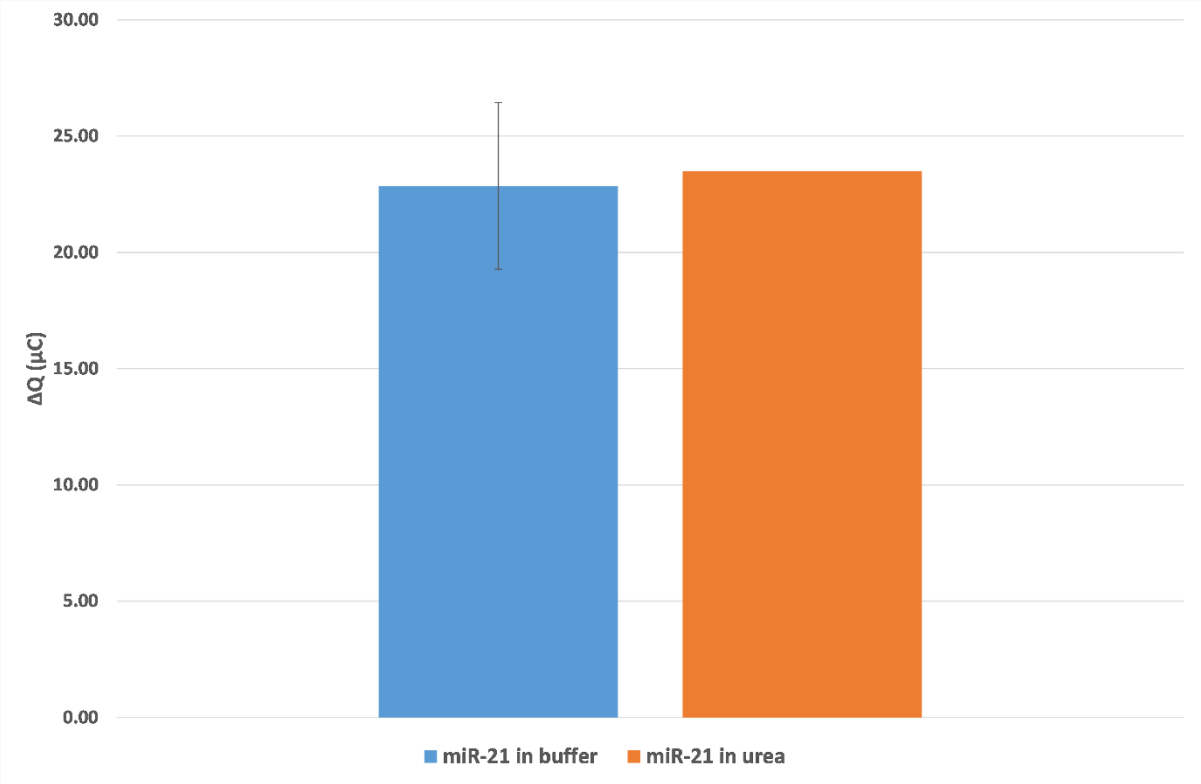

Figure 2.11 The coulometric response obtained following hybridisation with 10 pM miR-21dissolved in both buffer (performed in triplicate), and 9.3 g/L urea (performed once). Performed using 5 mM $K_3[Fe(CN)_6]/K_4[Fe(CN)_6]$ in 0.1 M KCl electrolyte at room temperature.

Although only performed once, these data show no significant effect on miR-21 coulometric response of 9.3 g/L urea (1 mL, 155 mM), suggesting urinary DNA/miRNA hybridisation is unlikely to be affected by urea.

The last urinary constituent tested was the readily available protein bovine serum albumin (BSA), which was used to mimic the effect of urinary proteins on probe responses. Urinary protein concentration is low in healthy individuals, but increases in kidney disease patients, where it can be monitored as albuminuria.[236,237]

Proteins are potentially problematic since attachment of these macromolecules to the electrode surface is likely to inhibit the electrochemical analyte from reaching the glassy carbon surface. This would result in an observed surface resistance that is much higher than the resistance caused by the DNA/miRNA hybrid, thereby falsely inflating the miRNA concentration.

To investigate the effect of urinary proteins on the electrochemical readout, 1 mg of BSA was added to a 1 mL solution of 0.1 nM miR-21 prior to probe hybridisation. The probe was analysed by EIS and the resulting Nyquist spectrum is shown in Figure 2.12.

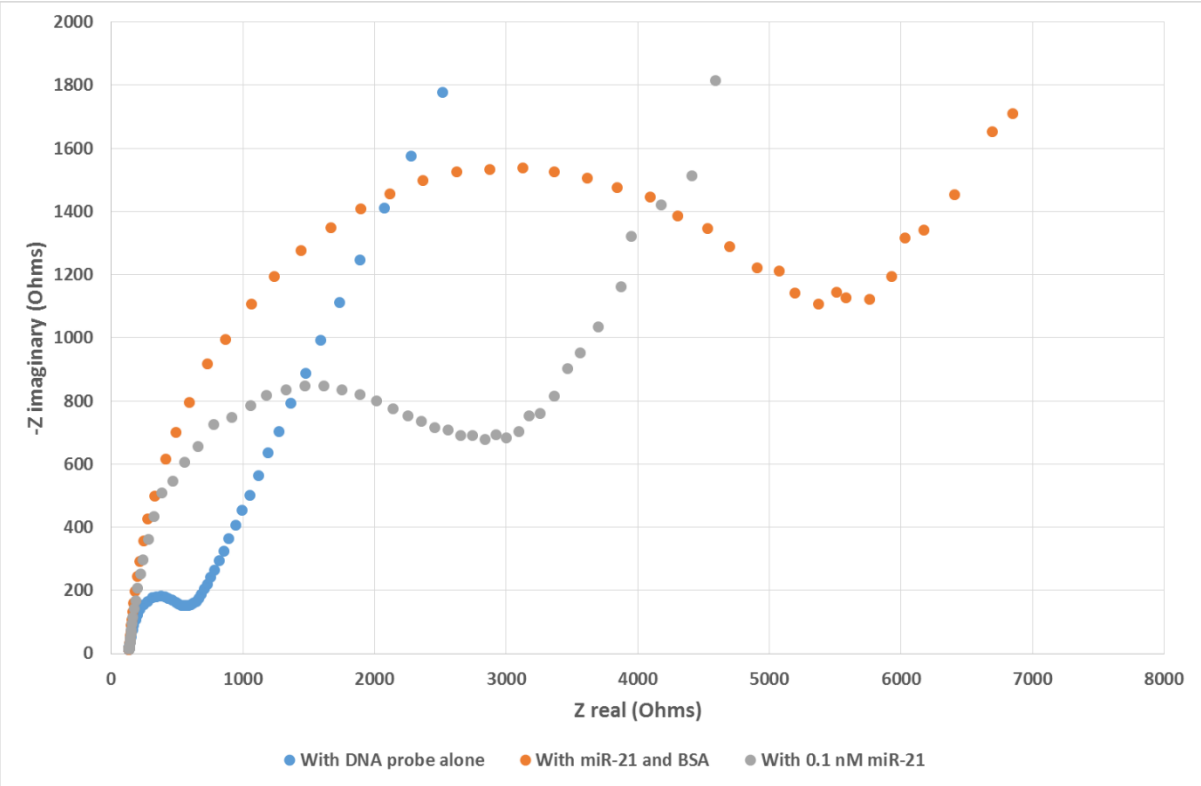

Figure 2.12 A Nyquist impedance plot showing increased resistance of a solution of 10^{-10} M miR-21 in the presence of 1 mg/mL BSA. Performed using 5 mM $K_3[Fe(CN)_6]/K_4[Fe(CN)_6]$ in 0.1 M KCl electrolyte at room temperature.

Figure 2.12 shows that when BSA was added to the miRNA solution, the resulting impedance was markedly higher than that observed for the same miRNA concentration in buffer. This suggested that the protein was covering the electrode surface, resulting in an apparent

concentration that was vastly different to the true miRNA concentration. In a urine sample from a kidney disease patient, the protein concentration is likely to be significantly higher than in a healthy individual. Therefore analysis of a patient urine samples would be potentially problematic.

In order to avoid this protein electrode "caking", the electrode was submerged in 1 mg/mL buffered proteinase K solution for a further 30 minutes. Proteinase K is a non-specific serine protease used widely for protein digestion in biological samples.[238] The resulting impedance response following proteinase K treatment is shown in Nyquist format in Figure 2.13.

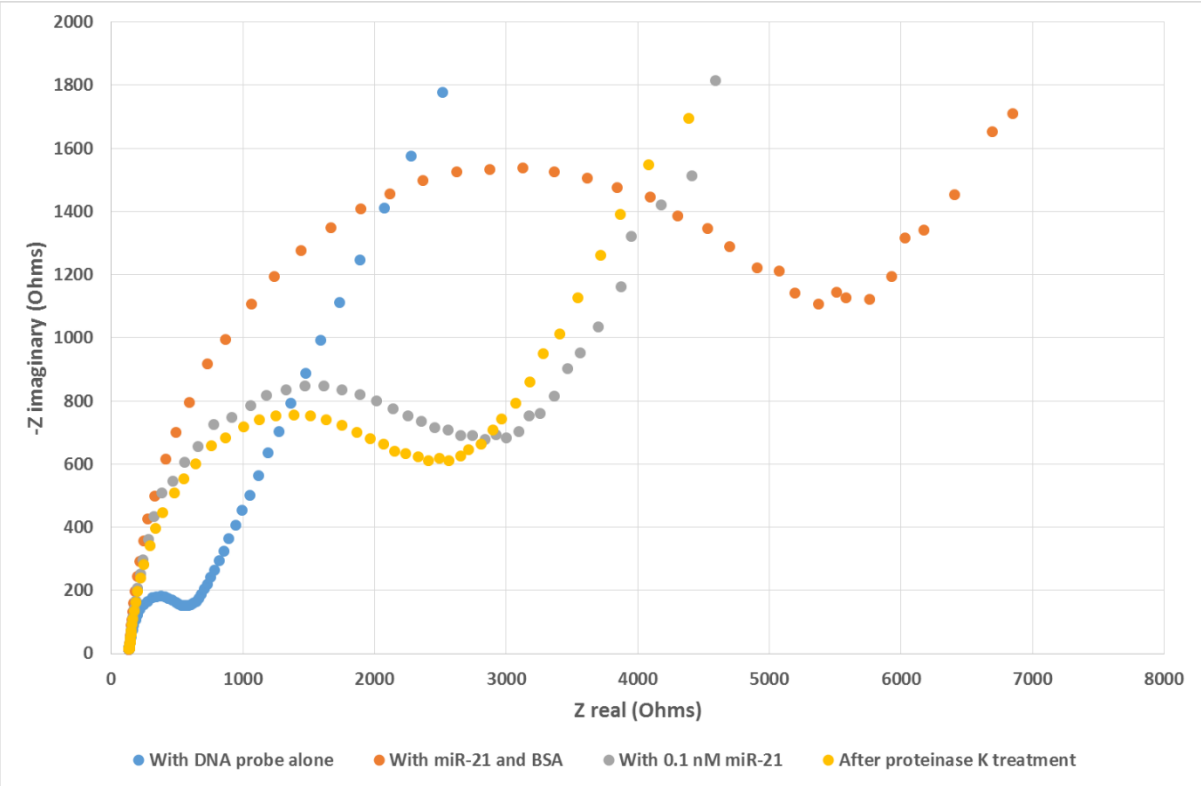

Figure 2.13 A Nyquist impedance plot showing the effect of probe incubation in proteinase K following BSA and 10^{-10}M miR-21 incubation. Performed using 5 mM $K_3[Fe(CN)_6]/K_4[Fe(CN)_6]$ in 0.1 M KCl electrolyte at room temperature.

The impedance plot data shown in Figure 2.13 show that proteinase K digestion resulted in a pronounced signal decrease to a level close to that obtained for miR-21 in buffer alone. This observation suggested that proteinase K could be used in analysis of human urine samples to prevent protein "caking" on the probe surface.

2.5 Urine analysis

Following the initial testing of synthetic urine matrices described above, analysis of urine samples was carried out. Ideally, urinary biosensor analysis should be quick, cheap and

straightforward at the point of care. To this end, it is important that the urine sample should require very little pre-treatment prior to analysis.

To test the biosensor, firstly urine was used completely untreated, submerging the anti-miR-21 DNA functionalised probe into a sample of urine for 30 minutes, with heating to promote hybridisation (Figure 2.14).

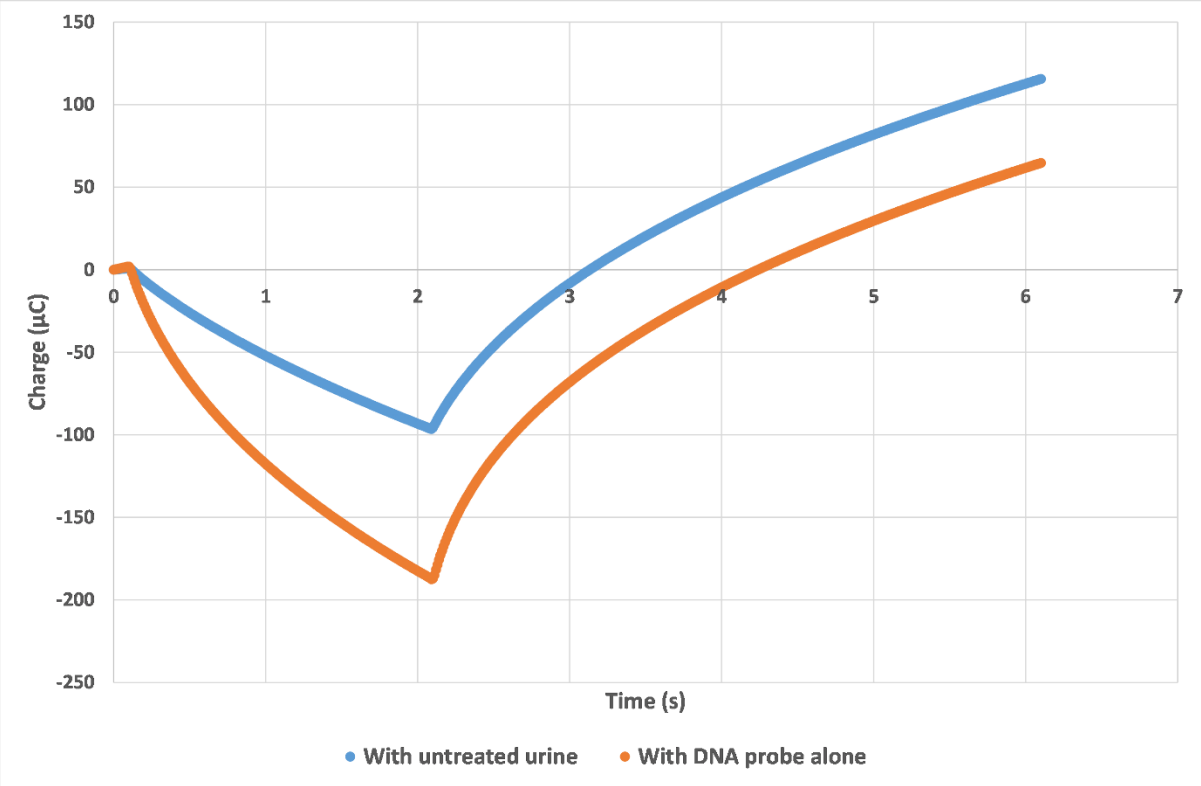

Figure 2.14 Coulometry plot showing the response with anti-miR-21 DNA probe alone and with the untreated urine sample. Performed using 5 mM $K_3[Fe(CN)_6]/K_4[Fe(CN)_6]$ in 0.1 M KCl electrolyte at room temperature.

As shown in Figure 2.14, the change in charge between the DNA probe alone and the untreated urine response was greater than the 10 nM highest concentration used in the original sensitivity testing. This would indicate a urinary miR-21 concentration of over 10 nM which was not anticipated, therefore it was hypothesised that this result was due to adsorption of protein to the probe surface. To prevent this, a brief initial proteinase K incubation was used, following which the digest was spin-filtered to remove any undigested proteins (including remaining proteinase) and lipids. This procedure is summarised in Figure 2.15 alongside an example of the data output with and without proteinase K digestion.

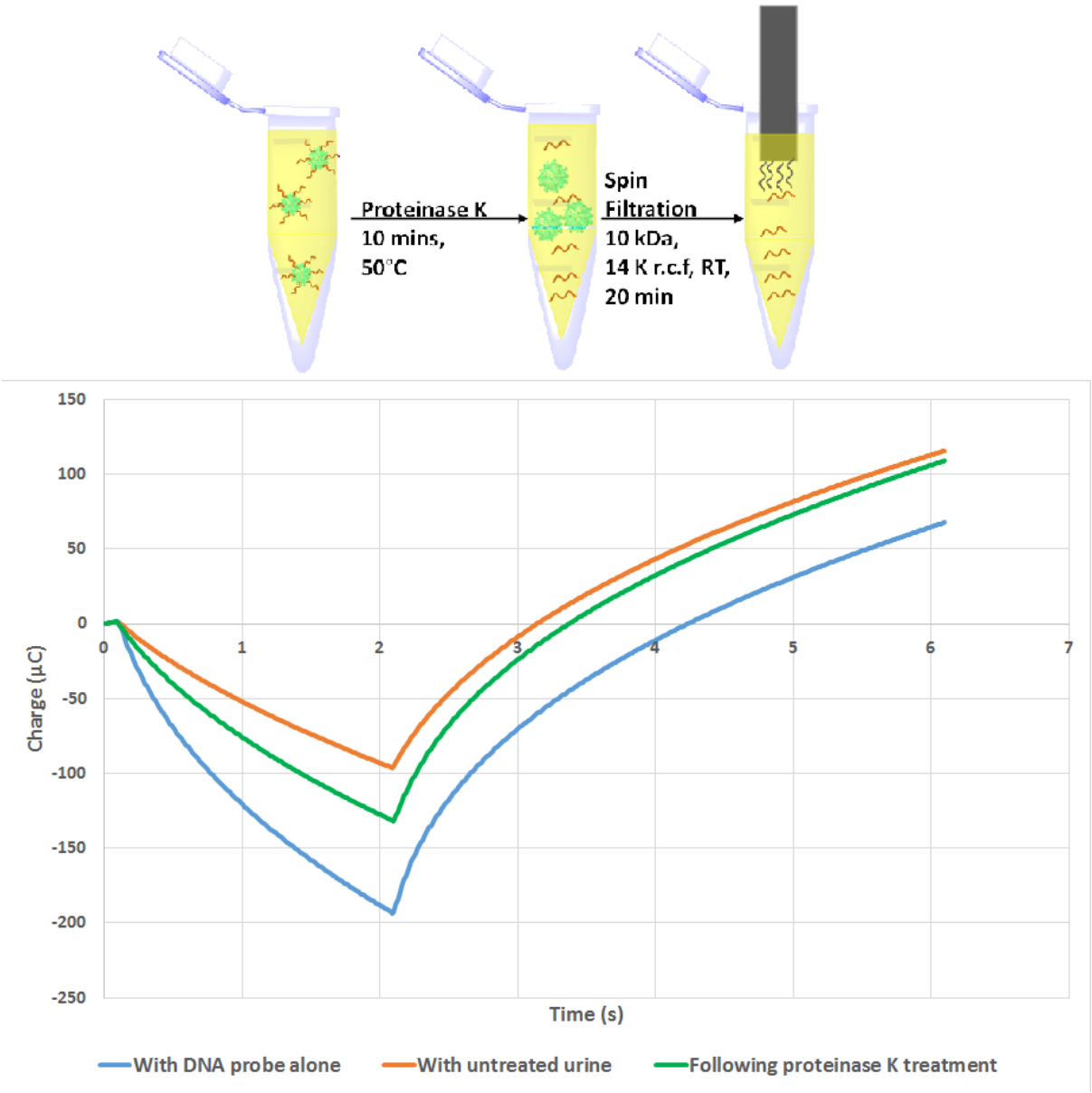

Figure 2.15 Urine pre-treatment procedure (top panel), and coulometry data showing how the use of proteinase K at 37 °C for 20 minutes affects the response following incubation in urine. Performed using 5 mM $K_3[Fe(CN)_6]/K_4[Fe(CN)_6]$ in 0.1 M KCl electrolyte at room temperature.

Figure 2.15 shows that the probe response obtained was greater than expected in untreated urine. However, following probe pre-treatment in proteinase K at 37 °C for 20 minutes, the resulting coulometric response was markedly increased. On the basis of the above data, future urine analyses used proteinase K treatment prior to probe/miRNA hybridisation.

Five urine samples from healthy control subjects were obtained from the Wales Kidney Research Tissue Bank for miRNA detection analysis. For electrochemical analysis, urine samples were incubated with 10 µL of 20 mg/mL proteinase K and then filtered through a spin filter prior to probe insertion and hybridisation. Analyses were performed three times for

each urine sample to ensure data reproducibility. The miR-21 concentration of each sample was then determined from the coulometry data, and was compared to the calibration curve (Figure 2.5). The urine analysis results are shown in Figure 2.16.

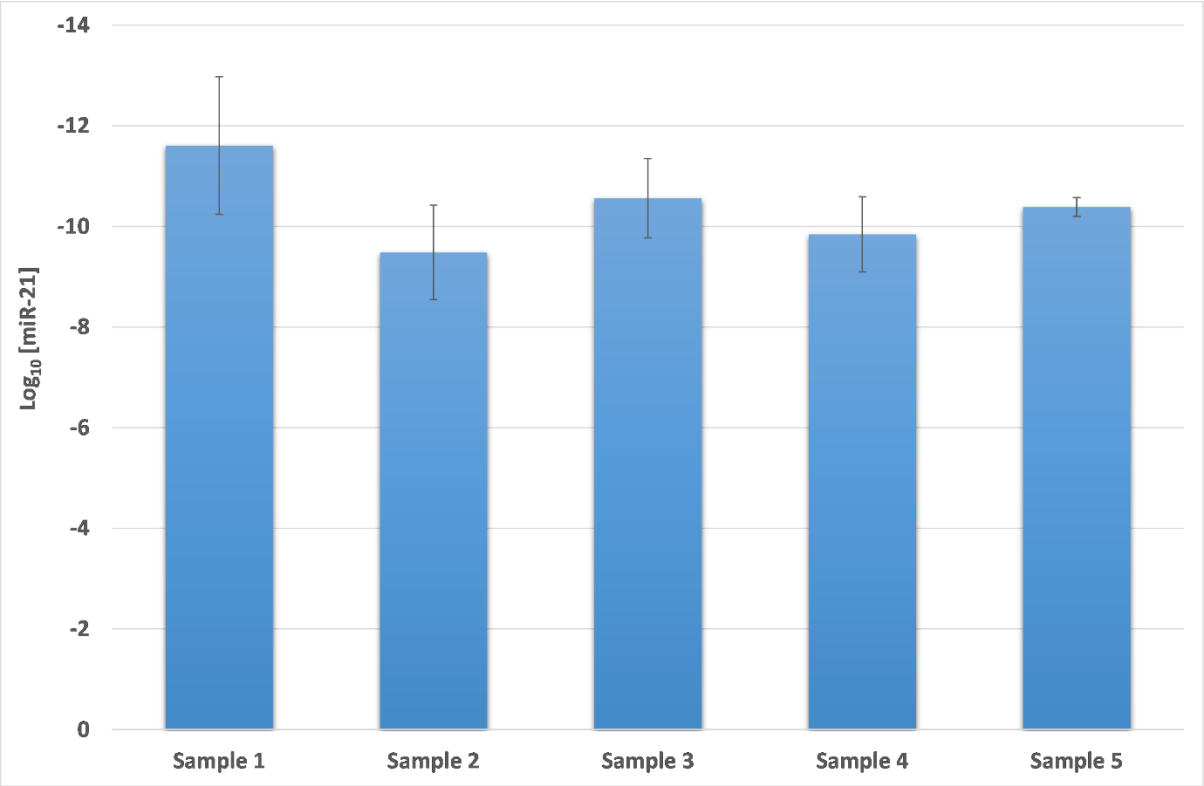

Figure 2.16 MiR-21 concentrations in 5 control subject urine samples calculated using coulometric analysis. As the concentration axis is negative, shorter bar means signify lower miR-21 concentrations. Performed in triplicate using 5 mM $K_3[Fe(CN)_6]/K_4[Fe(CN)_6]$ in 0.1 M KCl electrolyte at room temperature.

The data (Figure 2.16, raw data Appendix 1 Table A1.8) showed some variation between samples, with sample 1 having the lowest miR-21 concentration and sample 2 the greatest, and averaged around 10^{-10} M (0.1 nM). This variation was predicted on the basis of previous unpublished analyses by the host laboratory.

Quantification of miRNAs using reverse transcription – quantitative polymerase chain reaction (RT-qPCR) was carried out by calculating relative expression in comparison with *cel*-miR-39. Currently this represents the "gold-standard" for miRNA detection and analysis,[239] and so data obtained through this technique were therefore chosen as the best with which to compare our electrochemical data.

Firstly, a calibration curve was generated using a serial dilution series of synthetic miR-21 solutions as templates for RT-qPCR analysis, made up in biological grade water and therefore

not requiring an initial chemical extraction step. The resulting graph of threshold cycle (CT) versus concentration, from 10^{-8} M to 10^{-14} M miR-21, is shown below. The CT values in the linear region were then plotted against their respective initial miR-21 concentrations to generate a calibration curve.

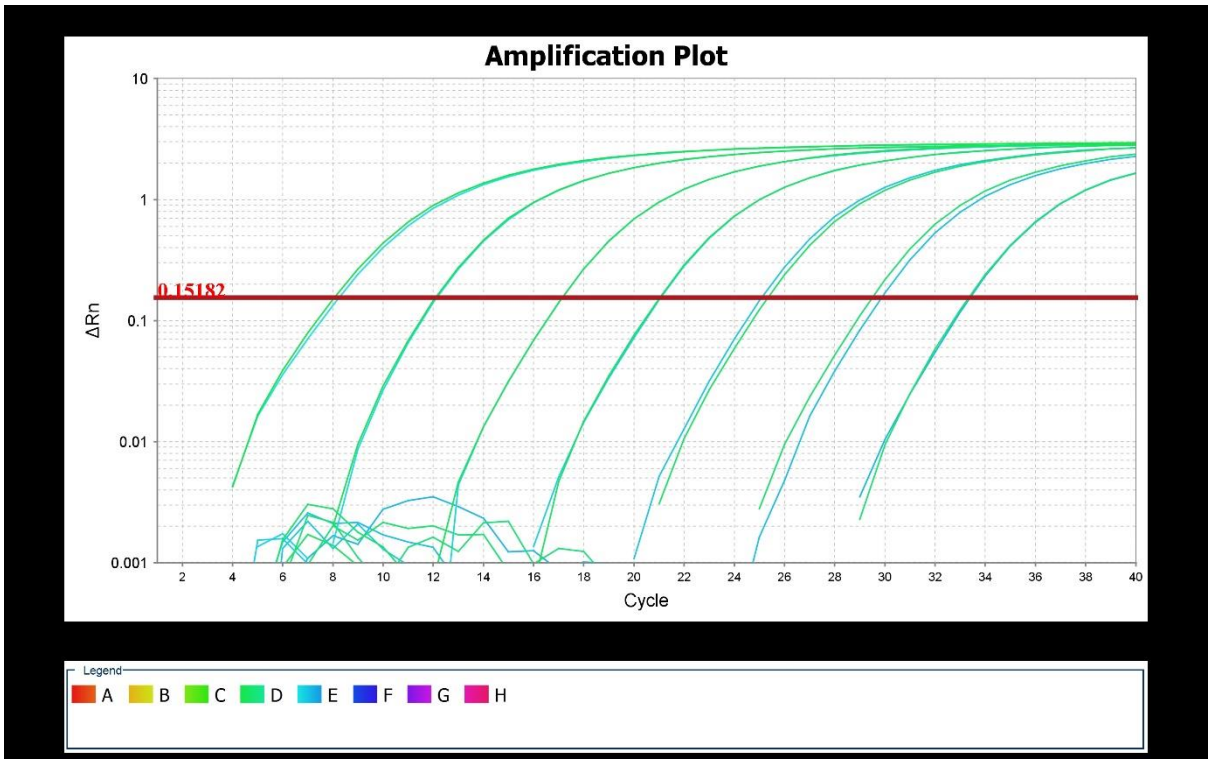

Figure 2. 17 The raw data amplification plot showing the number of cycles required for each buffered miR-21 concentration. Left to right 10^{-8}, 10^{-9}, 10^{-10}, 10^{-11}, 10^{-12}, 10^{-13}, 10^{-14} M.

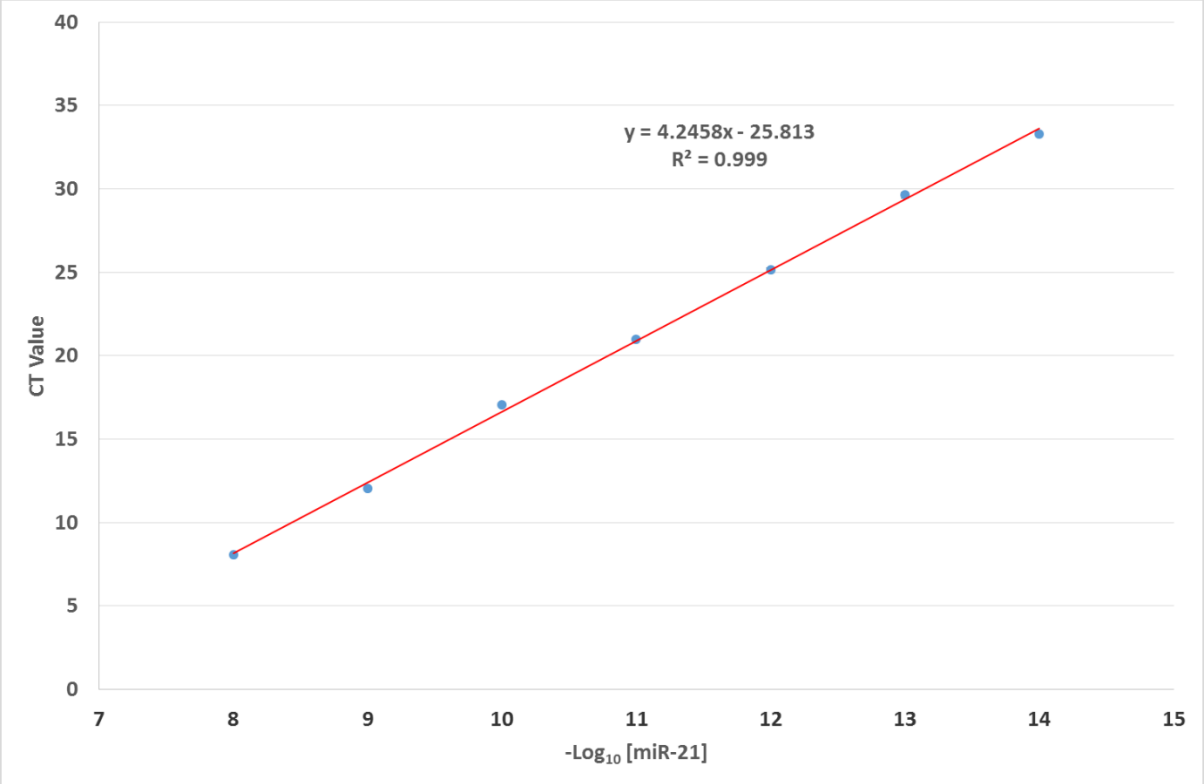

Figure 2.18 Calibration plot of CT versus miR-21 concentration (-log$_{10}$[miR-21]) obtained using the PCR amplification plot shown in Figure 2.17.

The calibration curve (Figure 2.18 raw data Appendix 1 Table A1.9) had a Pearson regression coefficient of 99.9%. This showed that the RT-qPCR amplification procedure was highly reproducible, reflecting a linear relationship between CT and concentration.

The calibration curve was then available to be used to convert CT values to miR-21 concentrations, and therefore a quantitative comparison between the electrochemical measurements and the PCR analysis would be obtainable, thus proving whether or not the probe was functioning correctly.

For urine sample analysis, miRNAs were extracted using the spin column-based miRNeasy kit from Qiagen. The resulting aqueous filtrate was used for subsequent RT and Taqman® qPCR analysis. The calibration plot equation was then used to convert the resulting CT values to concentrations, and then plotted graphically alongside the previously obtained electrochemical data for comparison, as shown in Figure 2.19.

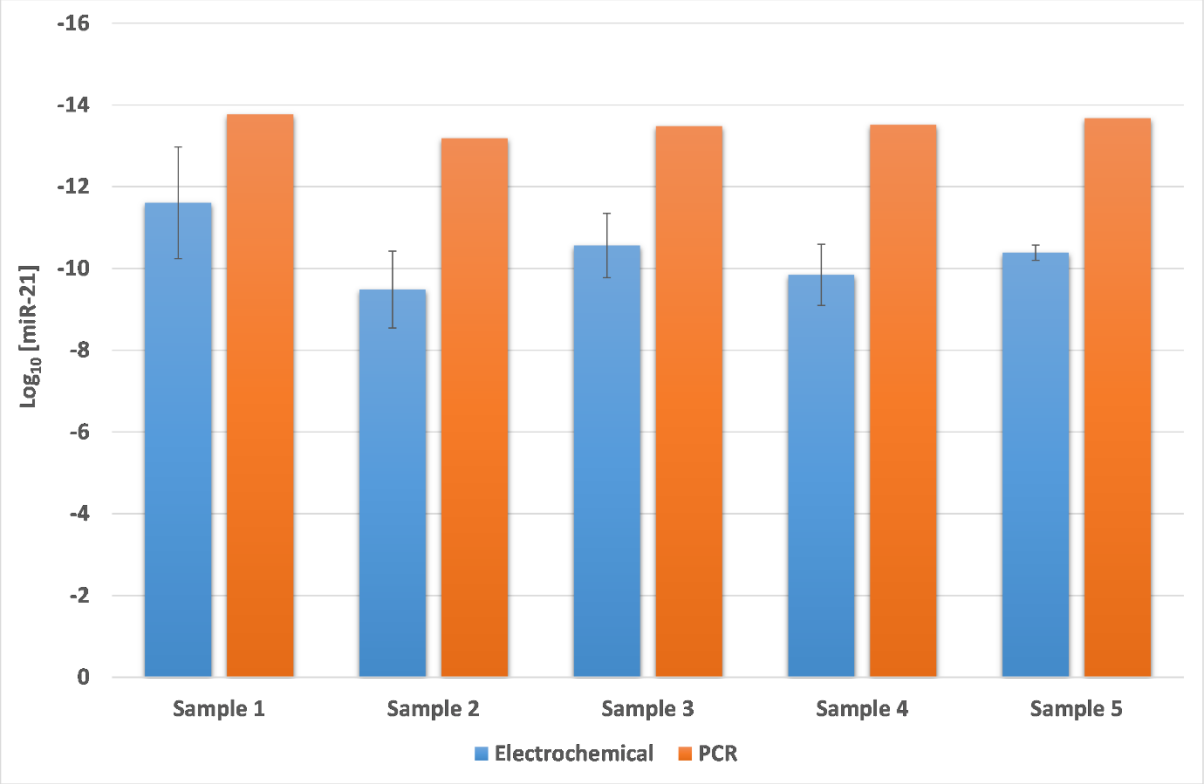

Figure 2.19 Comparison of miR-21 concentrations for 5 urine samples calculated via electrochemistry and RT-qPCR. Electrochemical measurements performed in triplicate using 5 mM $K_3[Fe(CN)_6]/K_4[Fe(CN)_6]$ in 0.1 M KCl electrolyte at room temperature.

Figure 2.19 (PCR raw data Appendix 1 Table A1.10) shows that the miR-21 concentration values obtained using electrochemical detection were consistently greater than the corresponding RT-qPCR data. Qualitatively however, sample 1 had the lowest miR-21 concentration and sample 2 the highest as was the case for the electrochemically measured concentrations.

To evaluate the validity of these concentration differences, a series of control experiments were performed. The first of these used a 1 nM PNA sequence complementary to miR-21 to hybridise to urinary miR-21 and thereby block any urinary miR-21 signal detected by the probe following proteinase K treatment. As described above, since PNA does not have a negatively charged sugar phosphate backbone that is electrostatically repulsive to other phosphate backbones, it has a greater RNA binding efficiency than DNA. Probe:PNA binding would therefore be favoured, preventing hybrid denaturation and subsequent miR-21 annealing to the DNA on the probe., decreasing the electrochemical response in comparison with PNA-free urine. Following data collection, exogenous synthetic miR-21 was added to a final concentration of 0.1 nM (Figure 2.20).

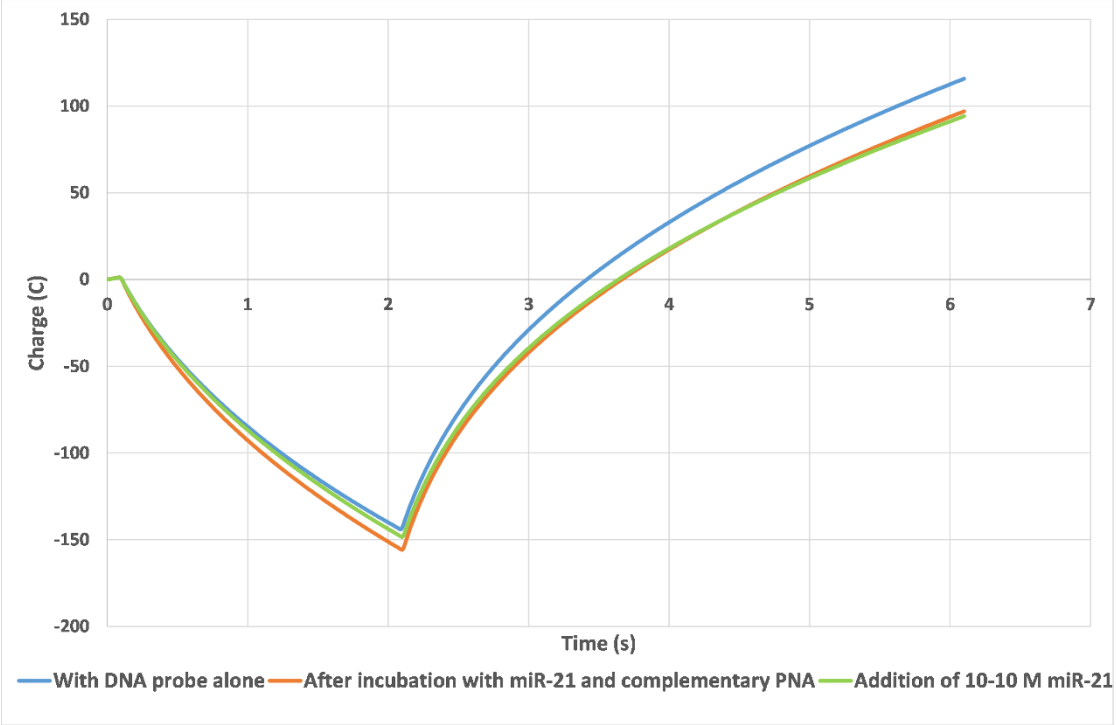

Figure 2.20 Coulometry analysis of urinary miR-21 detection using a complimentary miR-21 DNA probe in untreated urine, in urine containing 0.1 nM PNA complimentary to miR-21 PNA, and in PNA-treated urine following addition of 10^{-10} M synthetic miR-21. Performed using 5 mM $K_3[Fe(CN)_6]/K_4[Fe(CN)_6]$ in 0.1 M KCl electrolyte at room temperature.

As seen in Figure 2.20, the addition of PNA complementary to the target miR-21 produced a slight increase in the probe response. By contrast to the change observed in untreated urine, the magnitude was greatly reduced. This reduction was similar to that seen when the probe was suspended in a heated solution of water or buffer in the absence of miRNA. In the latter case, the slight drop in response intensity may have been the result of a marginal reduction in electrode surface electrochemical hindrance resulting from a small of number of the DNA strands of the probe being lost, possibly by very weak hydrolysis of the sulfonamide linkage, or small numbers of the DNA strands being hydrolysed.

These data suggest that the PNA:target miR-21 hybridisation occurred and thus the miR-21 was not detected in this experiment whereas it was in previous experiments. In the presence of 0.1 nM miR-21, a slight decrease in response was observed that was considerably reduced in comparison to untreated urine. This might indicate that some of the exogenous miR-21 bound to the PNA, but that a small quantity remained to interact with the probe. However, degradation by urinary RNases cannot be excluded.

A positive control was then carried out in which the urine sample and added PNA solution was prepared as before, but the sequence of the DNA probe strand was complementary to

miR-16. The proteinase K-treated urine sample was filtered, and spiked with miR-21 specific PNA, the miR-16 probe was incubated to induce hybridisation and the resulting coulometry response is shown in Figure 2.21.

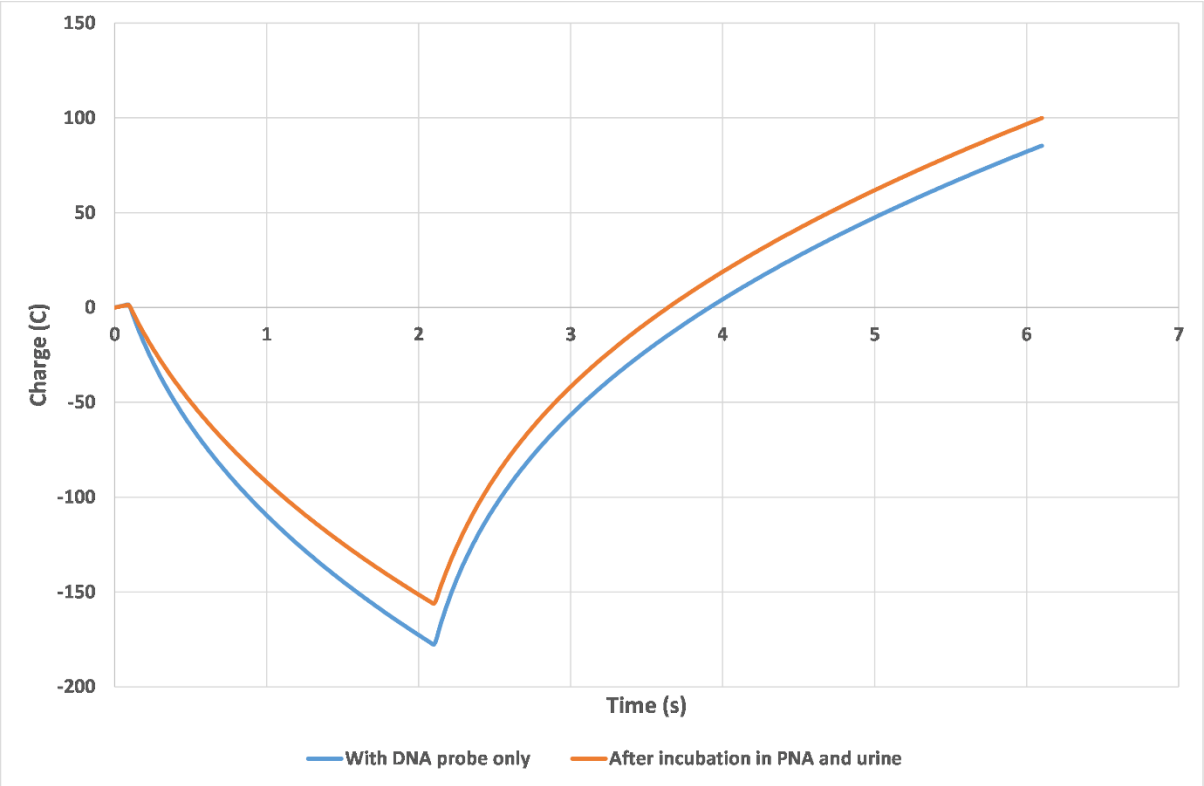

Figure 2.21 Coulometry analysis of urinary miR-16 detection using a complimentary miR-16 probe in urine in the presence and absence of 0.1 nM PNA. Performed using 5 mM $K_3[Fe(CN)_6]/K_4[Fe(CN)_6]$ in 0.1 M KCl electrolyte at room temperature.

Figure 2.21 shows that miR-16 detection was not affected by the presence of miR-21-specific PNA. These data suggest that the loss of response observed in Figure 2.20 was due to sequence-specifc PNA:miRNA hybridisation, and not a non-specific artefact. They also support the qualitative and quantitative miR-21 detection in Figures 2.16 and 2.19.

A further control experiment used RNA digestion enzyme RNase A to digest all urinary RNAs, following which samples were treated with proteinase K as above prior to coulometry analysis with a miR-16-specific probe. Subsequently, exogenous 10 pM miR-16 was added and the coulometry analysis was repeated, as shown in Figure 2.22.

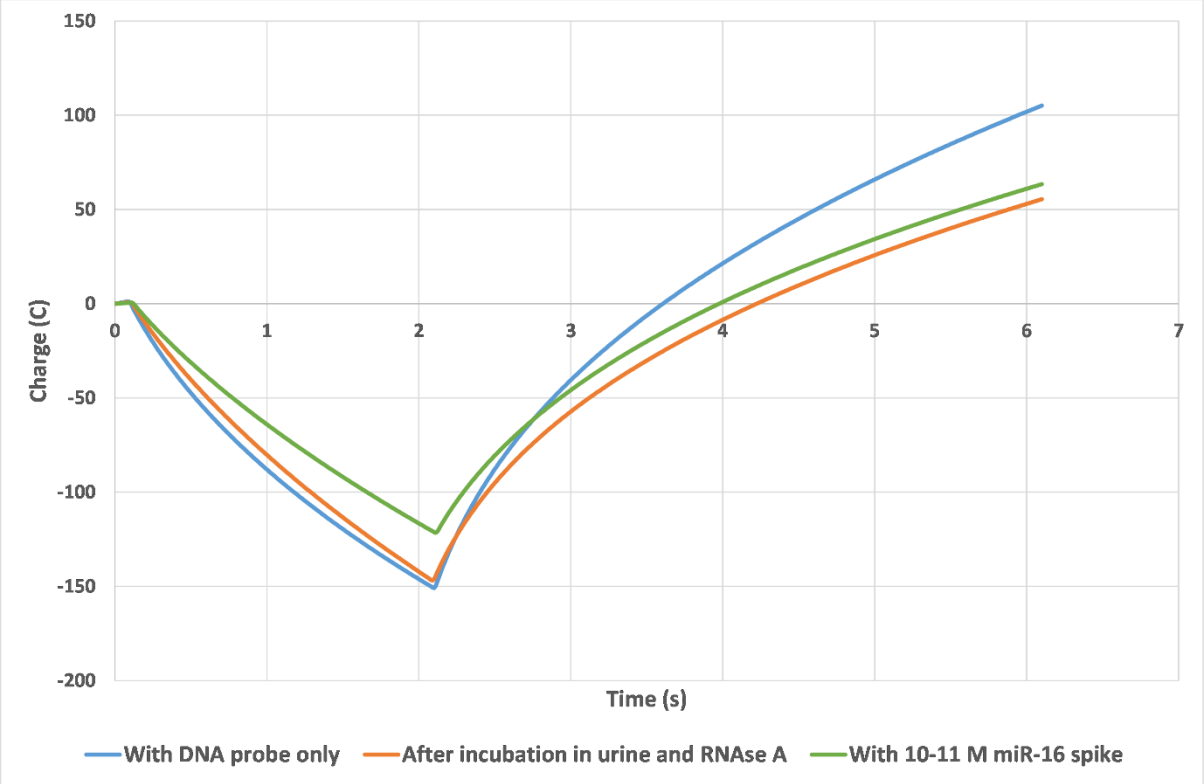

Figure 2.22 Coulometry analysis of urinary miR-16 detection using a complimentary miR-16 probe in RNase-treated urine, and in RNase-treated urine in the presence and absence of 10 pM PNA exogenous miR-16. Performed using 5 mM $K_3[Fe(CN)_6]/K_4[Fe(CN)_6]$ in 0.1 M KCl electrolyte at room temperature.

The data shown in Figure 2.22 again provided evidence of hybridisation between probe and urinary miRNA. These findings also suggest that the concentration differences observed in Figure 2.19 was not due to interferents or artefactual, and that electrochemical detection was more sensitive than RT-qPCR.

The practical protocols from which the conflicting data seen in Figure 2.19 were generated have a number of differences. One key difference is the RNA purification procedure required prior to RT-qPCR that is not needed for electrochemical detection. To assess miRNA losses occurring via the extraction procedure, 10 nM, 100 pM, 1 pM and 10 fM solutions of synthetic miR-21 were made up in buffer and extracted using the standard miRNeasy kit protocol. RT-qPCR was then used to detect miR-21 in these solutions before and after extraction. The calibration curve described above (Figure 2.18) was then used to determine miR-21 concentrations. A plot of miR-21 concentration obtained before and after extraction is shown in Figure 2.23.

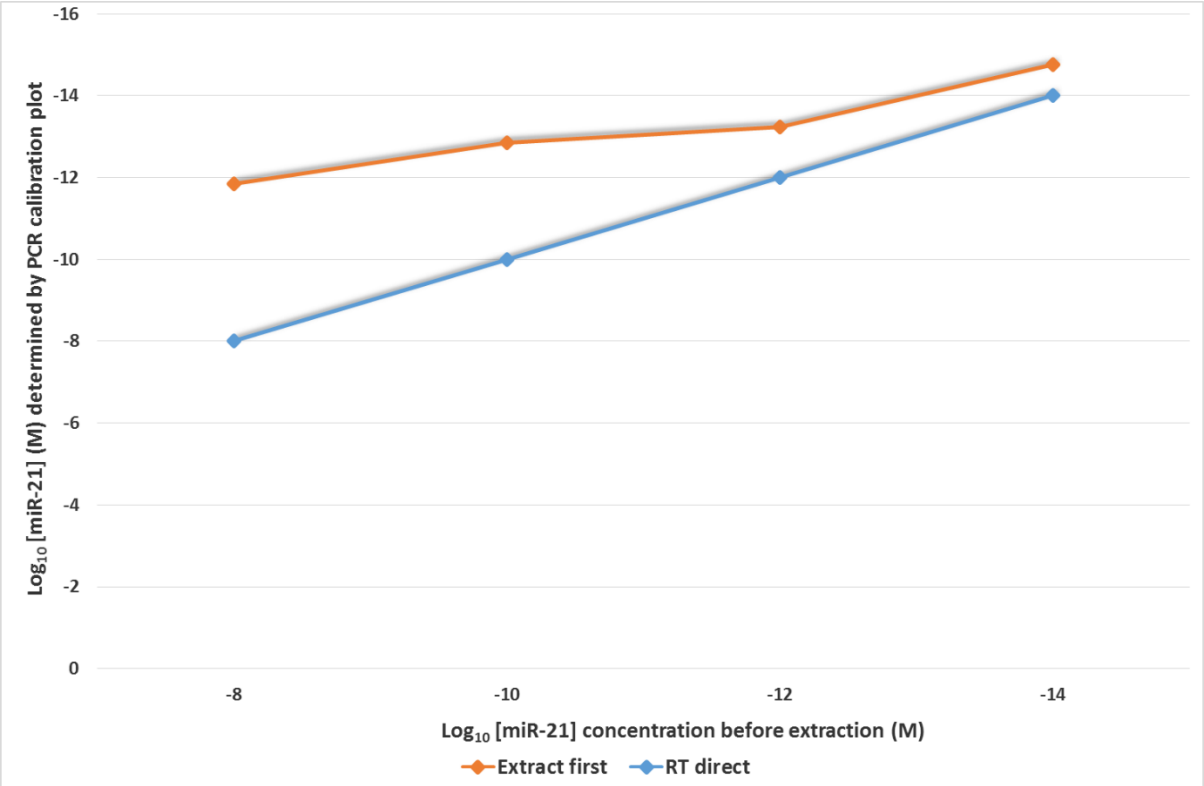

Figure 2.23 Comparison of miR-21 concentrations detected before (blue line) and after (orange line) miRNeasy kit extraction.

Figure 2.23 (raw data Appendix 1 Table A1.11) shows that for each concentration, a lower concentration was detected via RT-qPCR following extraction. For a 10 nM solution there was an approximate 7000 × reduction in concentration, and the quantitative differences detected decreased with reduction in miR-21 concentration. These data suggest that losses during extraction contributed to the differences in concentration detected using RT-qPCR compared to electrochemistry.

To assess the probe shelf life, artificial probe ageing was carried out by storing the probe for 24 hours at a range of different temperatures: 4 °C, 25 °C, 30 °C, 40 °C and 50 °C. The extra data generated are presented at the end of the thesis (Appendix 1 Figures A1.3 and A1.4 and Table A1.12).

These data are displayed graphically in the Arrhenius plot shown in Figure 2.24. Assuming first order kinetics, a theoretical storage times to 50% of the reference signal of 129.9 h (at 4 °C), 68.3 h (25 °C), 59.4 h (30 °C), 45.5 h (40 °C) and 35.4 h (50 °C) were calculated (Figure 2.24).

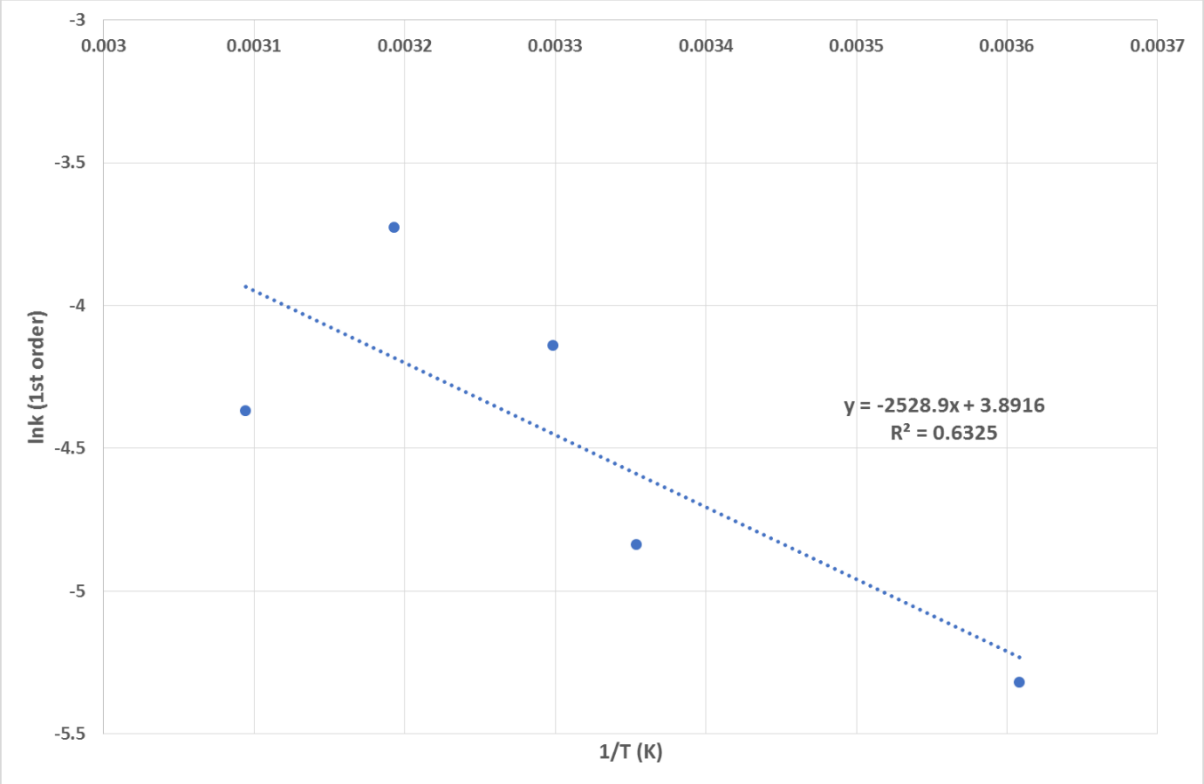

Figure 2.24 Arrhenius plot of ln k vs. 1/T (K) for a DNA modified electrode stored for 24 hours at 4 °C, 25 °C, 30 °C, 40 °C and 50 °C.

2.6 Summary of the results obtained.

In this chapter a glassy carbon electrode-based probe was used to detect miRNAs in a variety of solutions ranging from a buffered miR-21 to more complicated mixtures of enzyme-treated urine with spiked in miRNAs and PNAs.

The procedure used initially to modify the electrode ready for use as a probe was explained in detail effectively detected miR-21 by electrochemically. The modified electrode was then used to analyse buffered solutions of synthetic miR-21 over a range of concentrations from 10 nM to 10 fM, and was found to have a sensitivity limit of 20 fM. The probe successfully discriminated mismatched sequences from mature miR-21 and miR-16, and probe flexibility was demonstrated by preparation of a miR-16 probe. Later tests in synthetic urine matrix showed no effect by salt and urea, but albumin proteins in the form of BSA were detrimental to the probe response via a blocking effect at the probe surface.

The use of proteinase K was necessary to remove BSA protein and endogenous human proteins in urine samples. A number of urine samples were tested both electrochemically and using RT-qPCR, and showed a significant concentration difference between the two analytical

methods. Several control experiments were performed to show that the probe response resulted from miRNA:probe hybridisation. In addition, the extraction procedure used to prepare miRNA solutions for RT-qPCR analysis was shown to result in decreased detection of urinary miRNAs. Finally the storage lifetime of the probe to 50% of the reference result was determined at varying temperatures.

The work presented builds upon work performed by Wang *et al.* on the detection of DNA sequences to a sensitivity of 72 fM.[170] Our work was found to be only slightly more sensitive when applied to the detection of miR-21 giving a detection limit of 20 fM, however the significant advances are the application of our research to the detection of microRNA targets in real world urine samples and as well as indicating the specificity to 1, 2, 3 and full mismatches rather than the 3 and fully mismatched sequences explored by Wang.

The next chapters explore this adaptation of the GCE protocol for use with screen printed electrodes for the detection of human miRNA.

Chapter 3: Screen Printed Electrode Prototypes

Chapter 3: Screen printed electrode prototypes.

3.1: Introduction to screen printed electrodes

In the previous chapter a set of experiments were performed on a glassy carbon electrode, but, due to the need to constantly renew the electrode surface for each analysis, this is not suitable for high-throughput testing, nor for use at the point of care. Therefore it is the aim of this project to adapt the method for use in screen printed electrodes which can be produced and modified in bulk quantities and then disposed of after use. This is made possible through a collaboration with Gwent Electronic Materials® who have kindly supplied a selection of prototypes for testing and troubleshooting throughout the work presented herein.

Unlike the glassy carbon electrode used previously, screen printed carbon electrodes are made using a carbon 'ink', typically consisting of graphite or graphene particles that are suspended in a volatile solvent and a polymer binding resin for ultra-thin dispersion onto a chemically resistant substrate.[240–242] Although these are typical contents of the easily produced, easily modified and cheap screen printed electrodes of the type tested later, numerous other materials have also become popular in similar disposable electrodes. For example the advent of carbon nanotubes, within which reactive molecules may be embedded, has led to their use in screen printed electrodes manufacture.[242] Gold has also been used for nucleotide analysis due to its ability to easily bind to thiol functional groups which are a common tag for DNA and RNA sequences.[243]

The choice of ink materials is essentially limitless as the vast majority of inks, be they carbon, silver, platinum or any other base material, may be modified during formulation. For example nanoparticles of noble metals such as gold or platinum can be added to improve electrochemical outputs and for use as catalysts, but the costs associated with this make them unpopular.[244] Other, less expensive, chemical additives have also been added for certain applications. Mixing the base carbon ink with manganese dioxide has been used for ascorbic acid and nitrite detection,[245] bismuth oxide has been applied for lead and cadmium detection in water,[246] Prussian blue has been added for pesticide detection,[247] and even enzymes can be formulated into the ink for screen printable enzyme electrodes.[248]

The choice of electrode base material, i.e. the conductive element/mixture used as the electrically active surface, is not the only property that needs to be explored for a particular application. The substrate material, i.e. the material that the electrode is printed onto, also has to be chosen according to the desired application. In the past the substrate materials that could be used were simple plastic or polymer based materials such as PTFE, Valox (polybutylene terephthalate), poly vinyl chloride (PVC) or alumina. These non-conductive and chemically inert substrates are all sheet based materials, designed to be fairly rigid and simple to print on. As the exact size of electrodes to be printed, and the shape and design of these electrodes, is defined by the design of the print mesh, it is feasible to generate anything from microelectrodes to complete electrode sheets depending on the application. Thus it is possible to generate electrochemical sensor arrays consisting of multiple active surfaces and indented 'wells' for microfluidic handling, this array of sensors can then be used for the analysis of multiple analytes at once rather than individual measurements.[249] This particular application will be explored in later chapters in this work for detection of multiple RNA species in a urine sample.

However, as the formulations for ink based electronics have become a lot more sophisticated, enhancing both their electrochemical behaviour and ability to maintain performance during mechanical stress, numerous other substrates have become available. One significant advance is the ability to print electrochemical cells onto flexible materials such as malleable plastics and textiles.[250–252] This has ushered in a new world of 'wearable electronics' technology, finding application not only in devices such as smart watches and activity trackers, but also wearable medical devices for monitoring blood glucose in diabetes sufferers,[253] or for use in monitoring infant temperature/glucose levels/vitals et cetera.[254]

Despite many possible electrode construction options, the majority of commercial sensors follow a generic design. First the reference material and conductive 'tracks' are laid down, often as a silver/silver chloride material, with the exact choice again depending on the application. Next, the counter and working electrode surfaces are printed simultaneously, if they are using the same ink base, as the examples used throughout this project do, if not then each layer is printed consecutively. Finally, an electrical dielectric (insulator) ink is laid down, this ink is generally used to shield the electrode conductive trails from any chemical solvents, prevent any electrical noise and create a defined working area. However this material may

have additional functionality, such as changing colour in the presence of certain metals or compounds, if formulated appropriately. A general schematic of this procedure is shown for one of the designs in this project in Scheme 3.1.

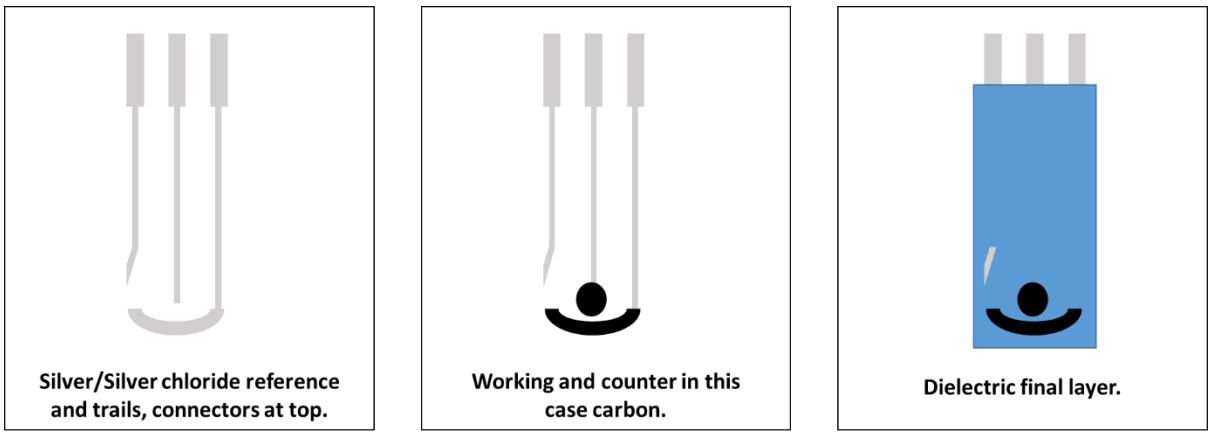

Scheme 3.1 The general screen printed electrode layering scheme that was used in this project.

Therefore the purpose of the research described herein is to develop the previously used GCE modification procedure for use with screen printed electrodes. A variety of designs was available from Gwent Electronic Materials (GEM) that were prototyped to test their applicability, and adapt the GCE protocol for optimal performance with these disposable electrodes. New designs and materials will be discussed in the final chapter for optimisation of the biosensor for the detection of multiple miRNA targets in urine.

3.2: Initial prototyping of the electrodes.

To start the prototyping process a set of GEM's most popular screen printed electrodes were tested, the only modification made to their design being the omission of the silver chloride reference and carbon auxiliary as the previously used external silver/silver chloride reference and platinum wire auxiliary were used. This was done for two reasons: firstly, the use of the three electrode design required a custom made connector, which was not deemed necessary during the prototyping stages; secondly, removal of these other sources of variability permitted direct focus on the reactivity of the working electrode. Thus the initial electrodes tested consisted of a silver/silver chloride track and connector, with a 2 mm diameter carbon working electrode and grey coloured standard dielectric coating. This design is displayed in Figure 3.1.

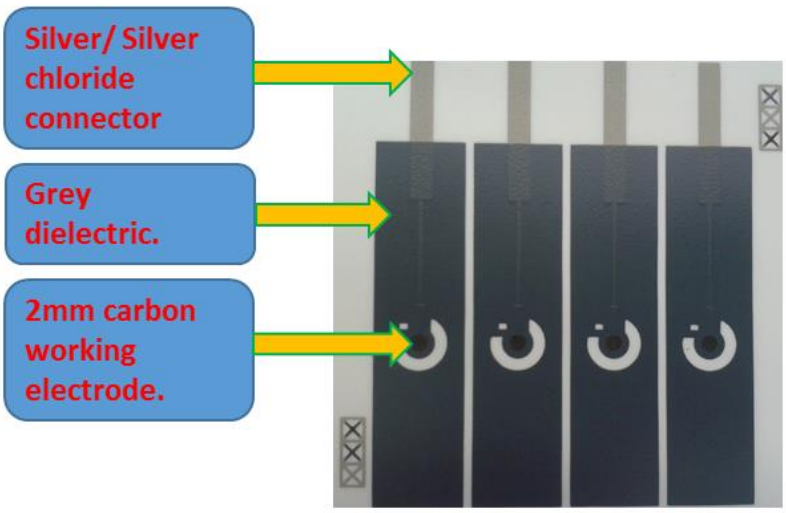

Figure 3.1 Initial prototyping design for the screen printed electrodes, supplied by Gwent Electronic Materials.

Very importantly for high-throughput and point of care applications, screen printed electrode use is straightforward. Each card, as shown in the previous figure, contains a number of electrodes, in this case 4, which can be simply cut out with scissors or a scalpel and used individually. The bottom section and sides of the electrode can also be shortened, as they contain no carbon or silver/silver chloride trace, if the design is too long to fit the desired working vessel. Once cut out, the electrode is then connected to the potentiostat using a crocodile clip at the silver/silver chloride connection and used in the same manner as the glassy carbon electrode i.e. in a 3 electrode cell with silver/silver chloride reference and a platinum wire auxiliary.

The first experiment performed using these electrodes was the standard deposition procedure using ANSA, to compare the electrochemical behaviour of the screen printed electrode (e.g. CV response curve) during this deposition to the GCE. Thus the screen printed carbon electrode (SPCE), the silver/silver chloride reference and the platinum auxiliary were submerged in a solution of ANSA and repeated cycles of cyclic voltammetry were performed to encourage deposition. The resulting cyclic voltammogram is given in Figure 3.2.

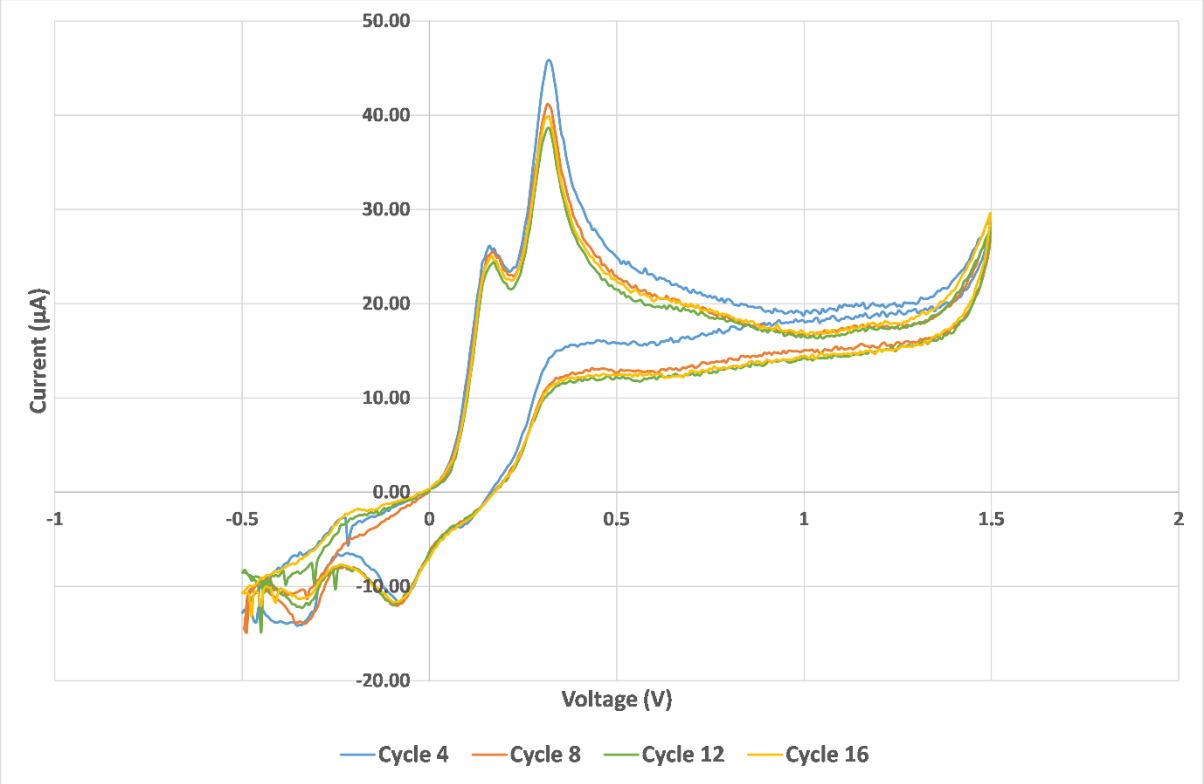

Figure 3.2 An overlay of the cyclic voltammograms obtained after 4, 8, 12 and 16 cycles in ANSA.

This plot shows a number of slight differences to the GCE while maintaining a similar shaped response voltammogram. The first difference is that the maximum current observed during the cycles is vastly reduced (almost 1/2 the GCE response for the later cycles), most probably due to the reduction in working electrode surface area from 3 mm to 2 mm. The second is that there is substantially more noise at the negative voltages, which may be an inherent issue with the materials used to produce the screen printed electrodes, as this was seen across the majority of electrodes used. However, the remainder of the cycle was reasonably well reproduced. Sixteen cycles were used in this experiment, but it can clearly be seen that after 8 cycles the difference in current response becomes very small, and there is an increase in response after 16 cycles. This suggested that, like the GCE, 8 deposition cycles were sufficient for the SPCEs.

At this point the screen printed electrodes were functioning as expected, and the chlorination step was then investigated. The GCE procedure was followed, then a 2 mL solution of acetone and PCl_5 was produced and the ANSA deposited electrode was submerged in it. Chlorination time was allowed, as before, after which the electrodes were removed, rinsed and analysed

via electrochemical methods using a ferricyanide electrolyte. This was repeated 5 times, with similar results in each case.

In most cases the dielectric layer became discoloured and dissociated, also in some cases the silver/ silver chloride connector became discoloured and peeled away in small areas. This may have resulted from acetone solubility of the polymers used to bind the inks to the substrate. Alternatively, the use of acetone may have removed some water from the hydrated polymers, causing them to lose their adhesive properties. Figure 3.3 shows an example cyclic voltammogram carried out at this stage compared with an analogous GCE output.

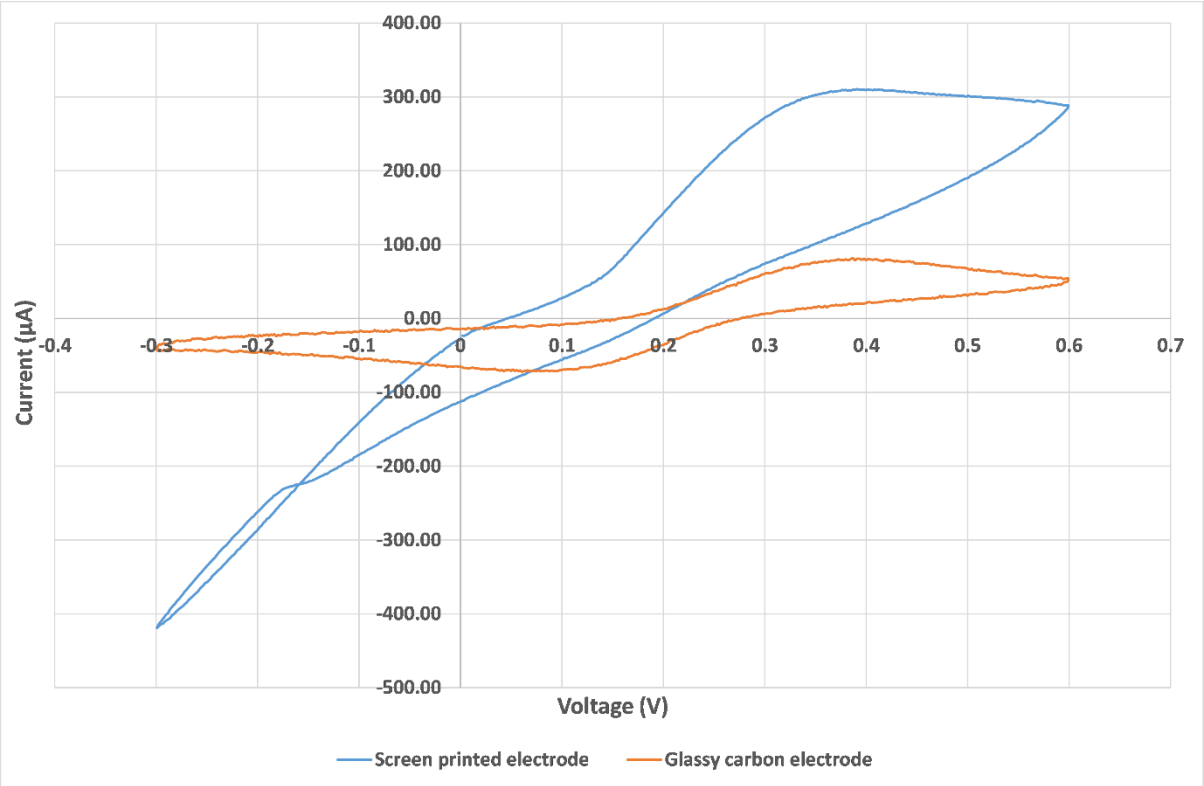

Figure 3.3 Comparative CV of the GCE following the chlorination step and the SPCE after chlorination under the same conditions. Performed using 5 mM $K_3[Fe(CN)_6]/K_4[Fe(CN)_6]$ in 0.1 M KCl electrolyte at room temperature.

The above data reflected the observed electrode damage following the chlorination procedure. The current response obtained from the SPCE was far higher than that observed for the GCE, with a peak of just over 0.3 mA compared to expected 0.08 mA, respectively. This difference in peak current might be due to the difference in electrode area, but as this electrode is smaller than the GCE a smaller peak current would be expected. The shape of the CV curve was also markedly different: it did not show the reversible oxidation and reduction peaks of the ferricyanide and tailed off in an unexpected way in the negative voltage range.

The chlorination procedure was therefore revised before continuing with the modification procedure.

A number of different PCl_5 solvents were tested for solubility to find one that both dissolved the reagent and left the electrode intact. As summarised in Table 3.1, the majority of solvents proved unsuccessful, either failing to show any dissolution of the PCl_5, or showing clear and severe damage of the SPCE. Also, the carbon disulfide solvent was deemed too dangerous to test due to the potential to generate mildly toxic thiophosgene ($CSCl_2$) in a side reaction.

Table 3.1 Solvent PCl_5 solubility and effect on the SPCE after 30 minutes.

Solvent	**Electrode damaged?**	**PCl_5 solubility.**
Water/ethanol	*No*	*Hydrolysis reaction*
Acetone	*Slow*	*Yes*
Hexane	*No*	*Slow*
Heptane	*No*	*No*
Cyclohexane	*Yes*	*Yes*
Tertiary-butyl-methyl-ether	*Yes*	*Yes*
Diethylether	*Yes*	*Yes*
Dichloromethane	*Yes*	*Yes*
Chloroform	*Yes*	*Yes*
Carbon disulphide	*Yes*	**Thiophosgene production*
Ethyl glycol dimethyl ether	*Slow*	*Yes*
Benzene	*Yes*	*Yes*
Toluene	*Yes*	*Yes*
Cyclohexyl methyl ether	*Yes*	*Yes*

The experimental observations listed in Table 3.1 show that the SPCE was highly susceptible to damage in most of the PCl_5 solvents tested. However, when submerged in hexane the SPCE

showed no visible signs of damage, even overnight. While the dissolution of PCl_5 was very slow in this solvent electrode damage was not observed, and hexane was therefore chosen.

Solution of PCl_5 in hexane was then tested to ensure that chlorination occurred as desired. The ANSA modified electrodes were submerged in the hexane/PCl_5 for 1 hour, 2 hours and 4 hours. Following this, they were analysed using ATR-IR by compressing the electrode surface against the ATR crystal and comparing the resulting spectra against that of an ANSA electrode subjected to the PCl_5 in acetone procedure. The blank and ANSA electrodes were also imaged for a reference (Figure 3.4).

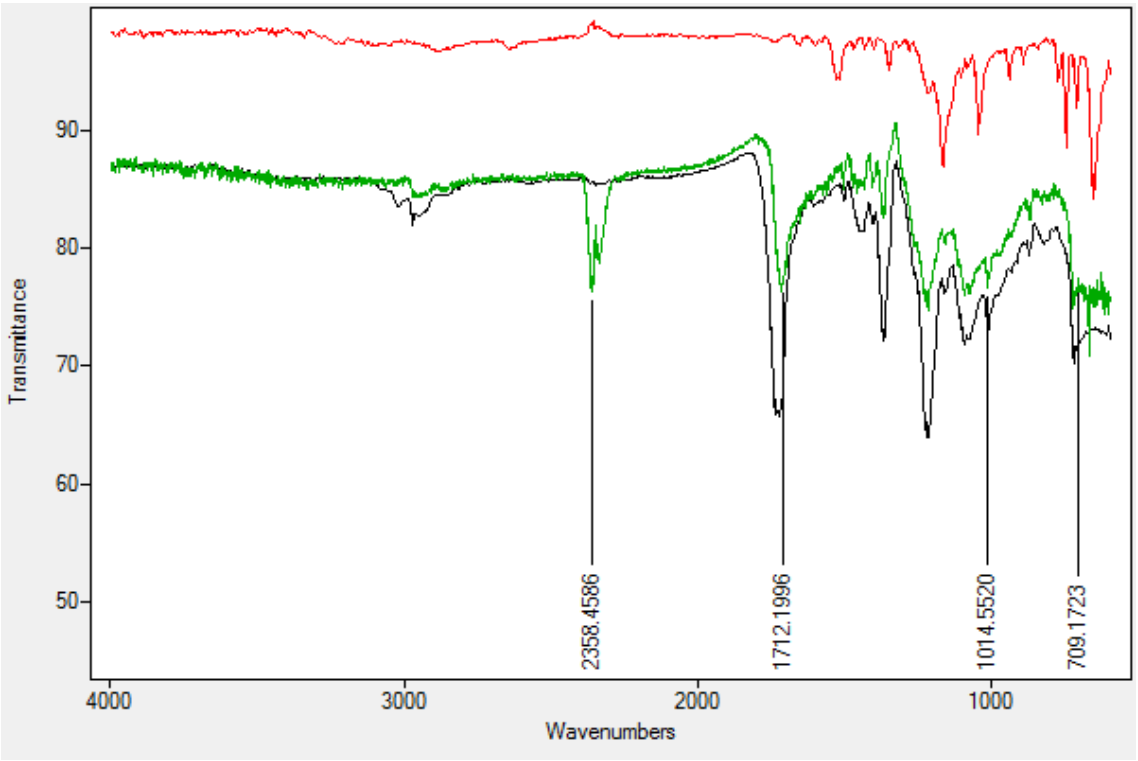

Figure 3.4 Overlaid ATR-IR spectra showing the unmodified SPCE (black) the isolated ANSA compound (red) and the ANSA modified electrode (green).

This initial IR spectrum shows how the SPCE appears when it is unmodified, and then how it changes following electrodeposition of the naphthalene sulfonic acid, the IR of the acid is also given for peak reference. From the spectrum, the most obvious change following the acid deposition was the presence of a new peak at 2360 cm^{-1}.

This peak usually indicates the presence of a nitrile (CN). However this would not be possible in the experimental system without being present in the ink, and was not observed in the unmodified electrode.

On the other hand, the ink did have a C=O stretch as indicated on the IR at around 1712 cm^{-1}, and the 2360 cm^{-1} peak might be a stretch resulting from the amine of the sulfonic acid reacting with a functional group on the carbon surface. Either through an isocyanate (N=C=O, ≈2270) or an isothiocyanate (N=C=S ≈2125), this would also be indicative of the mechanism by which the amino functionality binds to the carbon surface of the SPCE. However, as this peak is missing from some of the scans displayed in Figure 3.5, a more plausible explanation is that these peaks arise due to unresolved atmospheric CO_2 that was not removed during the background measurements. This is further indicated by its clear double peak. Having measured the deposited spectrum, the chlorination procedure was tested at a number of time points to determine time of completion (Figure 3.5).

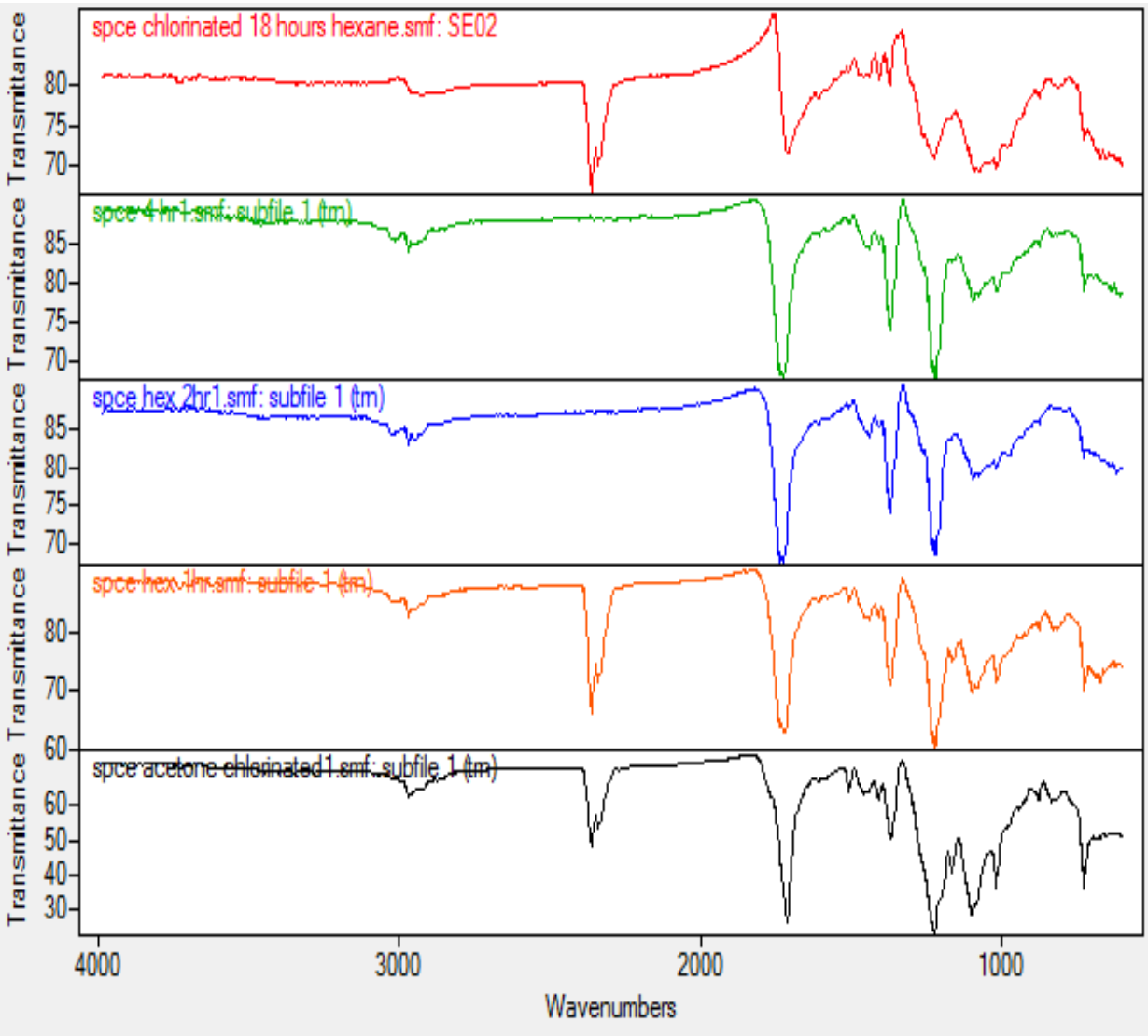

Figure 3.5 IR spectra recorded after different chlorination conditions, the first by submerging the ANSA modified SPCE electrodes in acetone/PCl_5 for 30 minutes (black) and the remainder by submerging in hexane/PCl_5 for different time periods: 18 hours (red), 4 hours (green) 2 hours (blue) and 1 hour (orange).

The data shown in Figure 3.5 are not conclusive regarding the time required for the electrode to react in hexane/PCl_5 and show only slight differences to acetone/PCl_5 treatment. The most obvious indicator would be a change around 700 cm^{-1} indicating the presence of a Cl, but in all cases this section was not well resolved. Notably, the peak at ≈2360 cm^{-1} appears in only 3 of the 5 surfaces tested, providing further evidence of unresolved atmospheric CO_2 not removed correctly during the background scans.

A reaction time of 4 hours was selected, as this was the first time point at which all of the ground PCl_5 had dissolved completely or the solution had become saturated. Importantly, subjecting the sensors to this chlorination mixture did not result in the same misshapen cyclic voltammetry plot recorded previously. An example voltammogram is given in Figure 3.6, and shows a GCE-like SPCE response following chlorination.

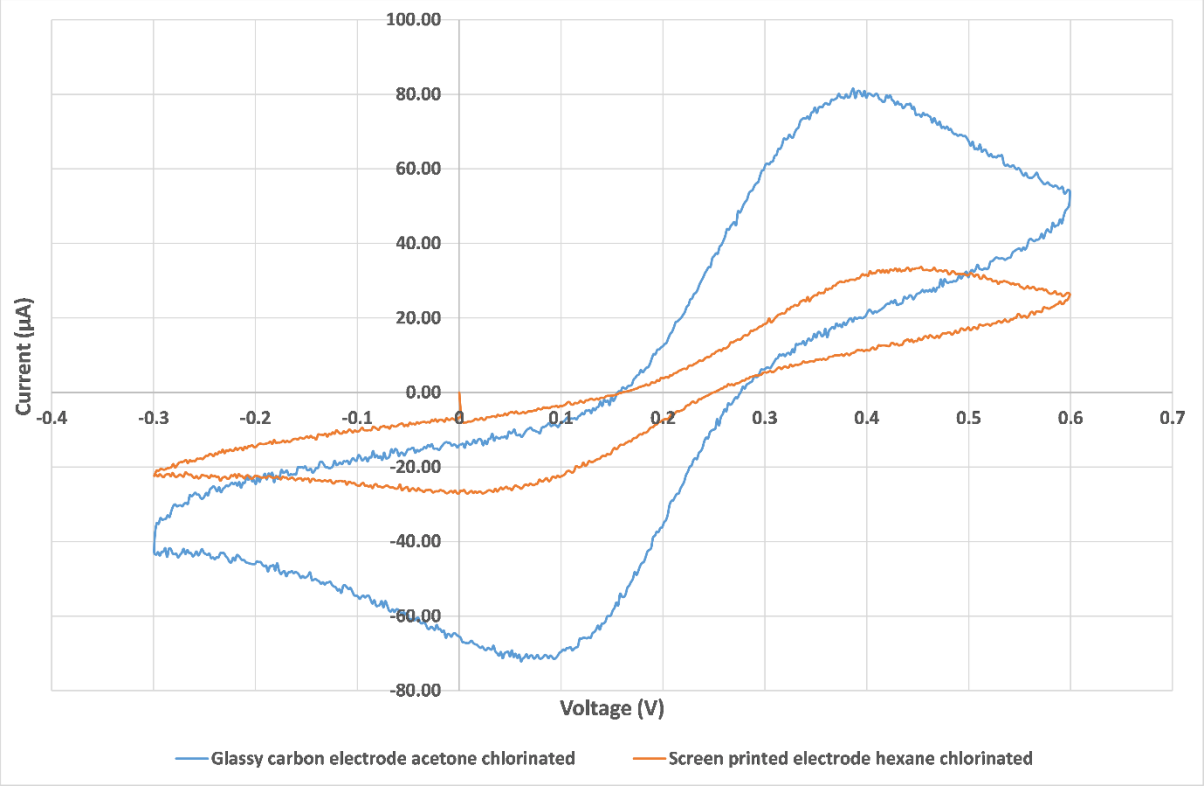

Figure 3.6 Comparative CV showing that the SPCE displays expected electrochemical behaviour following PCl_5 chlorination using hexane solvent (orange) compared to GCE chlorination with acetone solvent. Performed using 5 mM $K_3[Fe(CN)_6]/K_4[Fe(CN)_6]$ in 0.1 M KCl electrolyte at room temperature.

The above CV curve comparison (Figure 3.6) shows that the SPCE displayed the correct electrochemical redox behaviour following submersion in the hexane/PCl_5 chlorination mixture. Clear oxidation and reduction peaks were observed with no tailing off seen previously. The GCE response following chlorination in acetone is shown in Figure 3.6 for

comparison of the CV curve shape, but it was noted that the SPCE response was much smaller than that obtained from the GCE.

As mentioned previously this current response is likely due to the working areas of the SPCE (diameter of 2 mm) and GCE (diameter of 3 mm) differing. The area of a circle (A) is calculated using the equation $A = \pi \times radius^2$: a circle of 3 mm diameter has a total area of 9π mm^2, and a 2 mm diameter circle has a 4π mm^2 area. It is therefore conceivable that the current expected from a 2 mm diameter electrode would be below 0.5 × that for a 3 mm electrode. This assumption concurs with the observed data, the GCE giving a current of ≈80 µA and the SPCE a current of ≈35 µA.

Following the successful SPCE chlorination procedure, the electrodes were modified with the amine tagged DNA sequence complementary to miR-21, as carried out previously. For the purposes of prototyping the DNA was applied in a 10 µL droplet in buffer and allowed to air dry overnight at room temperature. The surface was then analysed using cyclic voltammetry in ferricyanide to analyse SPCE integrity, and no modification to the DNA addition procedure was required.

The final modification step to be tested was the submersion of the SPCEs into buffered miRNA solutions. Initially this was performed at 50 °C for 60 minutes to ensure that the predicted changes in response were observed. However, similar signal aberrations were observed to those seen following chlorination failures. Visually, it was apparent that the dielectric coating was peeling away from the Valox® backing, and bubbles were forming underneath the layer in the areas that were submerged for the hybridisation. Also, the silver connector pin showed discolouration, which was also unexpected since the only relatively volatile compound in the buffer was water. These observed changes were thought, at least in part, to explain the aberrant electrode response.

For the next trial, the outermost dielectric layer was strengthened using a commercially available fast drying resin used most often for hardening and sealing nail varnish. Application was carried out using an applicator brush around the active working surface, with particular attention to the edges where the electrode had been cut out and possible entry points for moisture had been generated, and the resin was left to air dry completely at room temperature (see Figure 3.7).

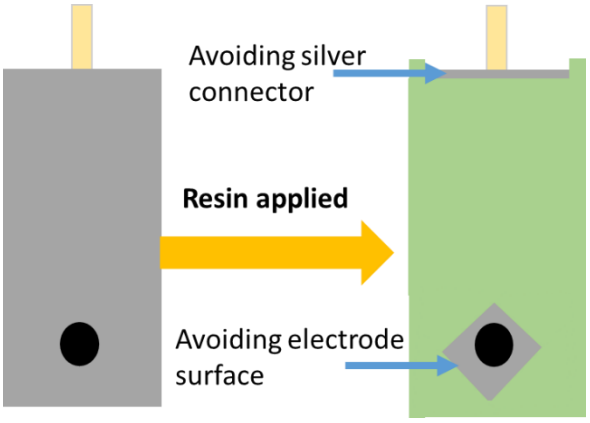

Figure 3.7 An illustration of commercial resin application to strengthen the dielectric layer and prevent water ingress.

Along with this modification, it was also deemed necessary to cover the silver connection pins with insulation tape in order to prevent any possible detrimental effect of buffer vapour, perhaps indicated by the discolouration noted above. The electrodes were then again submerged in buffered miRNA solution in a 1mL Eppendorf tube, and heated to 50 °C for 60 minutes to determine their stability. The resultant cyclic voltammogram in Figure 3.8 shows improved oxidation and reduction profiles, indicating that the treated electrode was more durable.

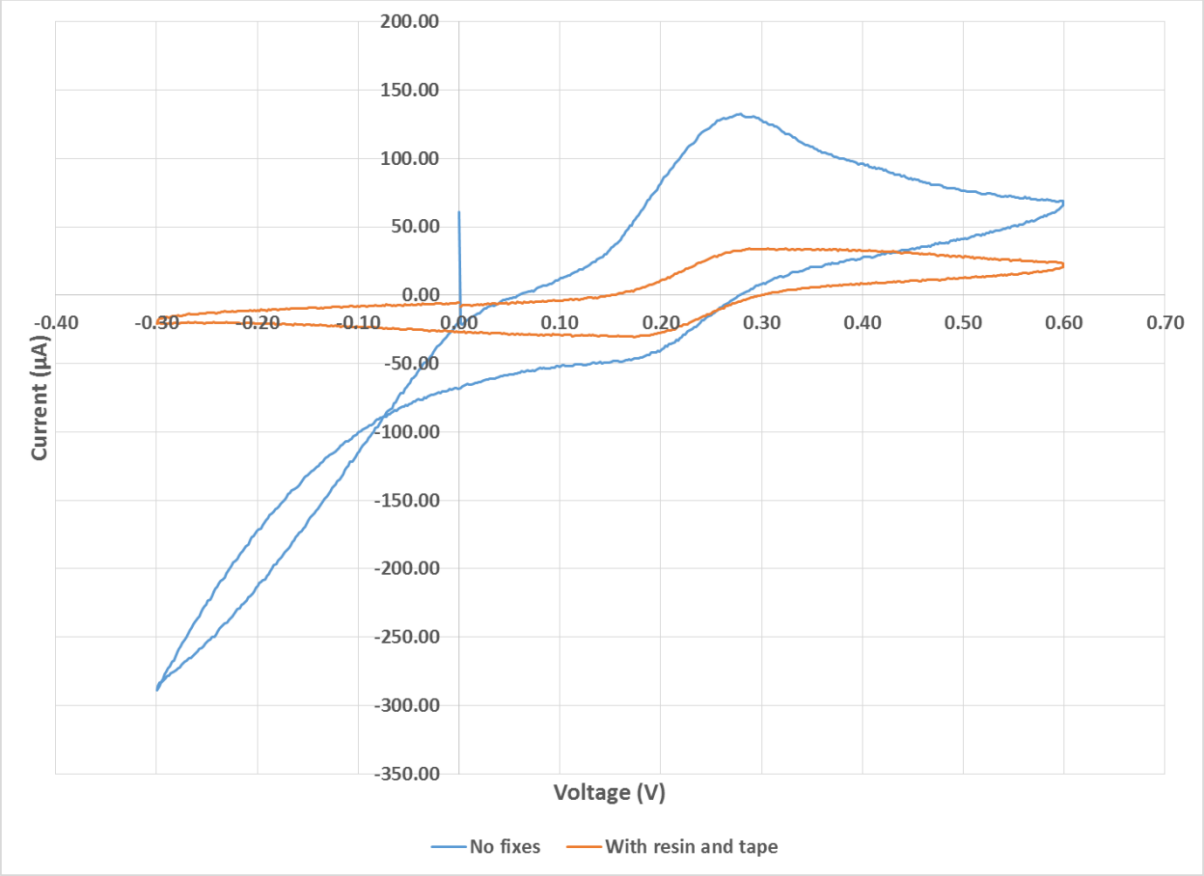

Figure 3.8 Overlaid cyclic voltammogram showing data for one SPCE strengthened with resin (orange) and one un-strengthened SPCE (blue) following incubation in buffered miRNA solution. Performed using 5 mM $K_3[Fe(CN)_6]/K_4[Fe(CN)_6]$ in 0.1 M KCl electrolyte at room temperature.

Figure 3.8 shows a misshapen voltammogram, similar to that obtained from chlorination in the acetone/PCl_5 mixture, for the un-strengthened SPCE. Although oxidation and reduction peaks were obtained, there was a rapid 'tailing off' of the current in the lower voltages, and the peak currents were much higher than expected. However, when the resin and tape were applied, a redox curve of the more expected shape was observed, with no tailing effect, and the peak currents were within ranges observed at previous steps in the modification procedure.

The SPCEs had therefore successfully survived each of the modification steps and displayed cyclic voltammograms similar to those obtained at each step of the GCE modification. It was then necessary to determine if SPCEs detected changes in electrochemical response similarly to the GCE. This would also provide data on the sensitivity of the SPCE, and how it compared to the previously obtained GCE sensitivity. Thus, the SPCEs were modified using the aforementioned changes to the original procedure, and then incubated in solutions of miR-

21 of varying concentrations for 30 minutes at 50 °C. They were then analysed using cyclic voltammetry and chronocoulometry as before.

However, the SPCEs were unsuitable for Nyquist electrical impedance spectroscopy analysis (shown Appendix 2 Figure A2.1 at the end of the thesis). By plotting the data as a Warburg plot however some analysis was possible by extrapolating the intercept of the linear section, this is also given in the Appendix (Appendix 2 Figures A2.2 and A2.3). The results of this first set of sensitivity tests are displayed in the plot in Figure 3.9 (raw data Appendix 2 Table A2.1).

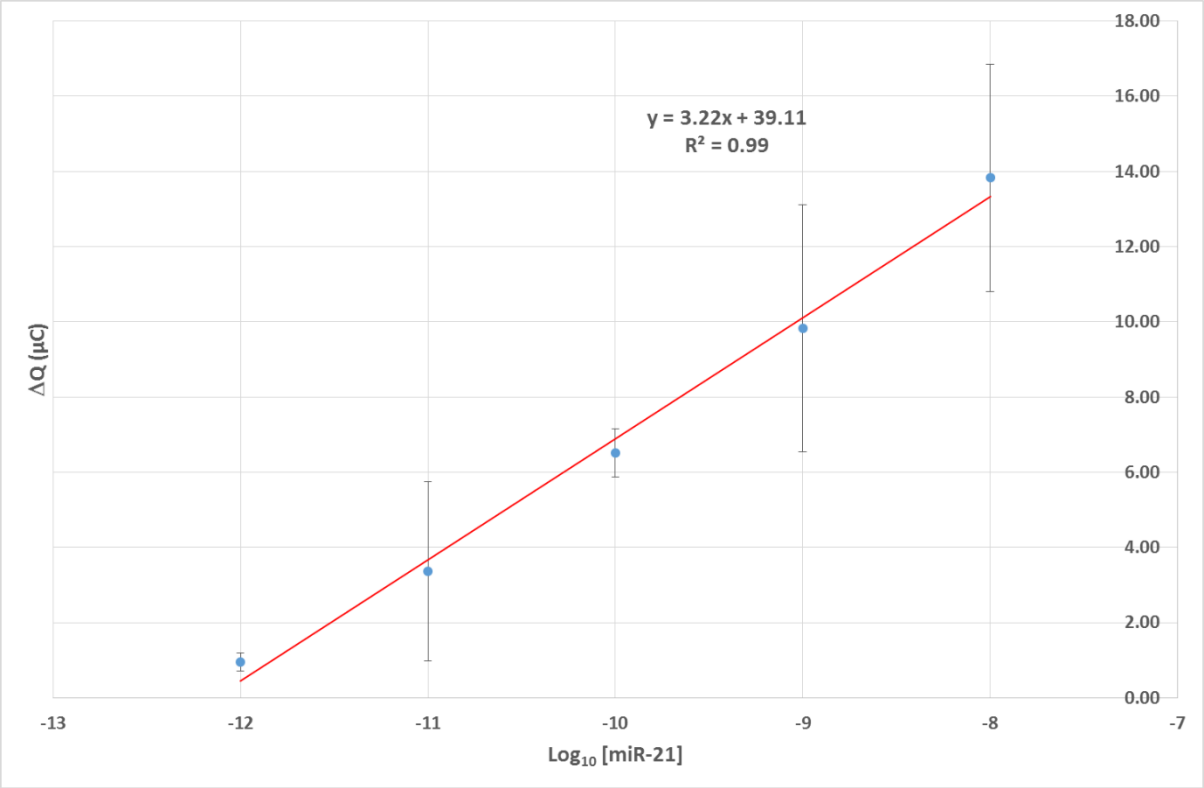

Figure 3.9 Coulometry change (ΔQ) between the DNA modified SPCE and the DNA/RNA modified SPCE for different miR-21 concentrations. Performed in triplicate using 5 mM $K_3[Fe(CN)_6]/K_4[Fe(CN)_6]$ in 0.1 M KCl electrolyte at room temperature.

Initial results using this adapted modification procedure seemed promising, a highly linear change in coulometric response was observed with the $\log_{10}$ of miR-21 concentration, as had been observed with the GCE. However, there were still major differences between these results and those obtained previously. Firstly, the SPCE sensitivity was much lower than that for the GCE, with an SPCE minimum observable concentration of 715 fM to the GCEs calculated limit of detection of 20 fM (and minimum extrapolated concentration of 6 fM). Also, the individual data points for 10^{-8}, 10^{-9} and 10^{-11} M show high variability compared to

those obtained in analysis using the GCE. In addition, the failure rate of the SPCEs, although much improved using the modified procedure, was still significant.

3.3: Using SPCEs with an increased working area diameter.

To address the issue of reduced SPCE sensitivity, a new electrode design was required which incorporated a 3 mm active surface to improve the limit of detection. GEM supplied the set of SPCEs shown in Figure 3.10, with a 3 mm diameter active surface suitable for testing ink materials as above.

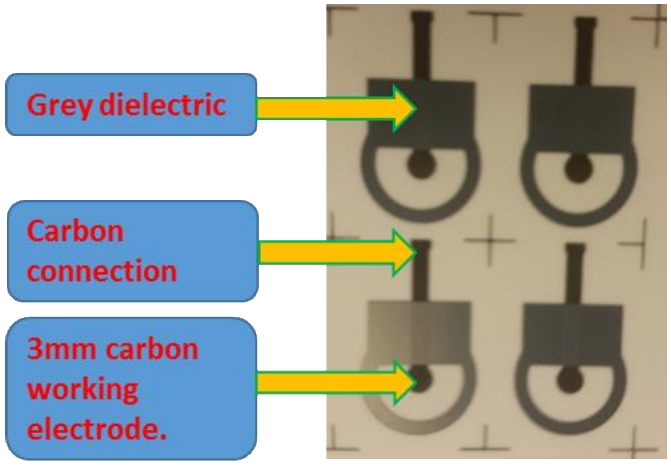

Figure 3.10 3 mm electrode design made available by Gwent Electronic Materials (GEM).

These 3 mm SPCEs did have some additional differences to the 2 mm electrodes described above. The grey dielectric no longer surrounded the entirety of the surface, the connection was carbon and not silver/silver chloride, and they were markedly smaller in length.

These electrodes maintained normal responses throughout the adapted modification procedure. The new SPCEs were then tested to determine the effect of surface size on the resulting signal obtained.

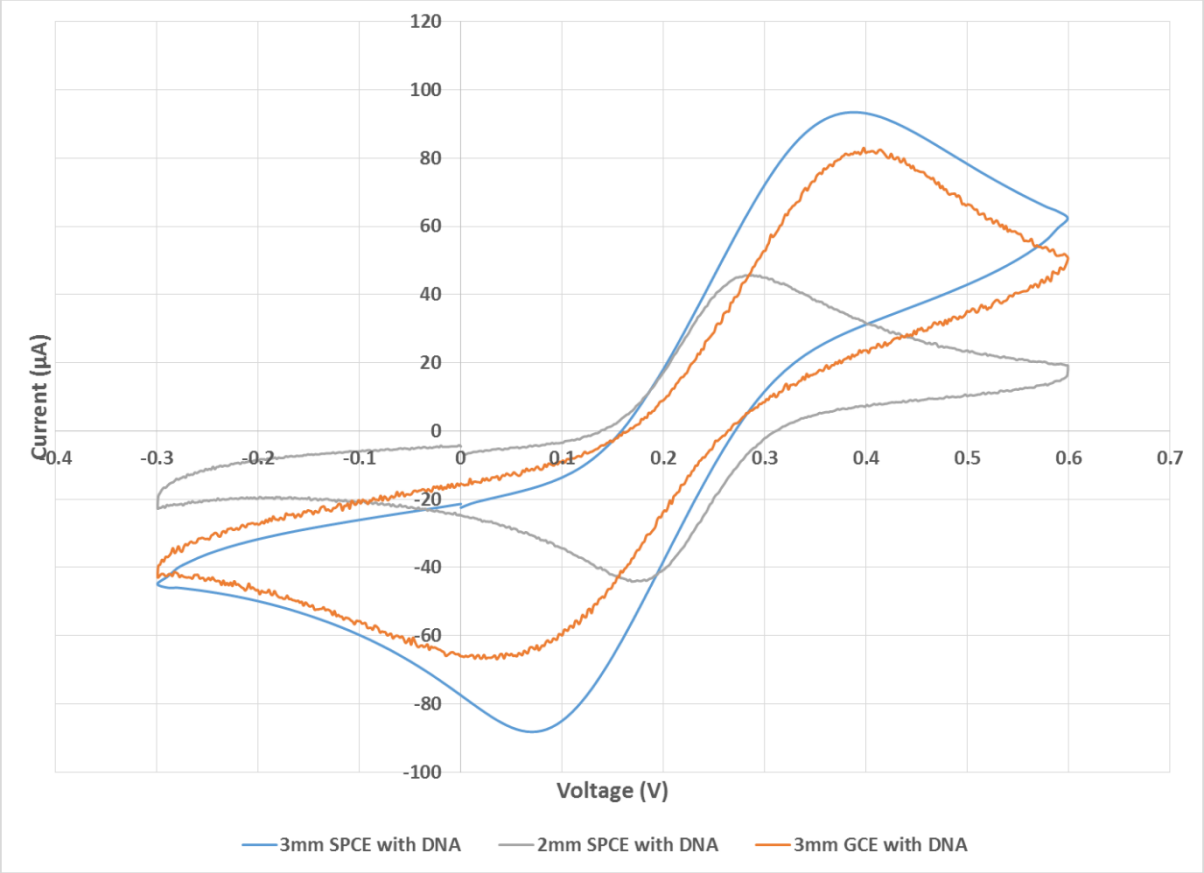

Figure 3.11 Cyclic voltammogram comparing current response from the GCE (orange), the 2 mm SPCE (grey) and the 3 mm SPCE (blue) following DNA addition. Performed using 5 mM $K_3[Fe(CN)_6]/K_4[Fe(CN)_6]$ in 0.1 M KCl electrolyte at room temperature.

The cyclic voltammogram in Figure 3.11 shows the current response compared to the GCE. The 3 mm diameter SPCE gave oxidation and reduction peaks much closer in magnitude to the GCE than the 2 mm electrode. Although there is still some difference, which could be down to a slightly different surface coverage or down to the properties of the ink over the GCE, the 3 mm diameter electrode does give a closer resemblance to the GCE than the 2 mm electrode.

Following the above findings, the sensitivity of the 3 mm SPCEs was then tested. The electrodes were modified as previously and hybridised with different miR-21 concentrations.

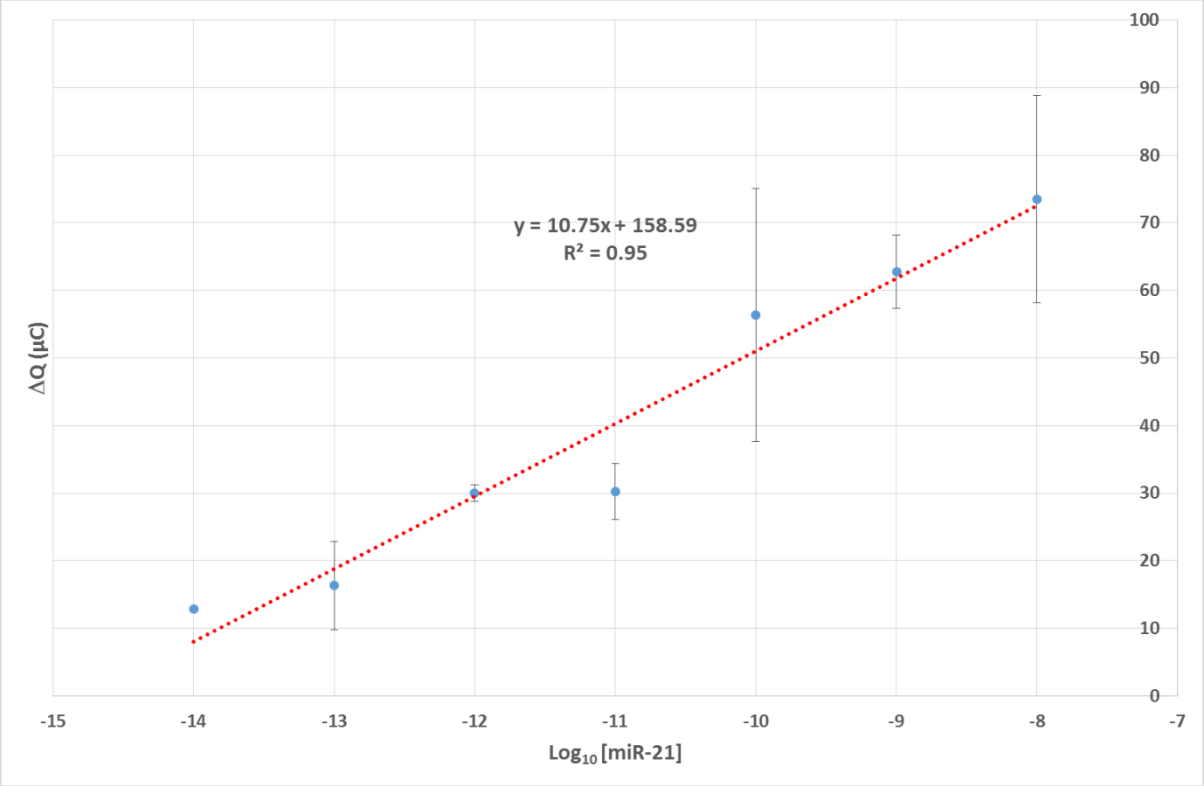

Figure 3.12 A plot to show the change in coulometry response (ΔQ) over a range of miR-21 concentrations. Performed in triplicate (except 10^{-14} M) using 5 mM $K_3[Fe(CN)_6]/K_4[Fe(CN)_6]$ in 0.1 M KCl electrolyte at room temperature.

The chronocoulometry data shown in Figure 3.12 (raw data Appendix 2 Table A2.2) suggest that SPCE sensitivity was related to working electrode diameter. Using the 2 mm SPCE gave a minimum extrapolated concentration of 715 fM, but the 3 mm electrode gave a minimum observable concentration of 1.8 fM. This was much closer to the GCE sensitivity (extrapolated as 6 fM, limit of detection of 20 fM), and the response magnitude of the 3mm SPCE was also more similar to the GCE than that obtained by the 2 mm electrode.

However, despite showing an extrapolated sensitivity increase for the 3 mm SPCE, it should be noted that the error for some points with this prototype, namely 10^{-10} and 10^{-8} M was clearly higher than that for the GCE. In addition, the 10^{-14} M data proved difficult to obtain reproducibly due to electrode failures and obvious anomalies (charge changes in the lower concentrations that are orders of magnitude larger than those obtained at 10 nM). This data point is reported only for one trial, and the absolute sensitivity cannot be accurately ascertained.

3.4: Surface imaging and analysis techniques.

Up to this point, the surface of each of the electrodes, from the GCE to each of the SPCE designs was analysed via electrochemical means, with one series of preliminary IR spectroscopy measurements. To further characterise the chemistry at the electrode surface, and to observe changes resulting from the modification and hybridisation, further analyses were carried out.

In order to first reveal the chemical changes that occurring over the course of the modification procedure, a set of the 2 mm electrodes were produced, each being analysed after each individual step in the experimental procedure. Laser ablation-inductively coupled plasma mass spectrometry (LA-ICPMS) was then performed on each electrode to determine the concentration of each element on the surface.

The key elements for each of the steps were chlorine, nitrogen, sulfur, phosphorus and carbon. These concentrations were also compared to a 'blank' sample, i.e. a fresh SPCE that was not modified, to determine approximate base values for each element at the electrode surface prior to modification. Exact values may vary slightly across each electrode, depending on variance at the time of printing. The values for the key elements are given in Table 3.2 and Figure 3.13 with the full data analyses are given in the Appendix (Appendix 2 Table A2.3).

Table 3.2 Elemental concentrations at the surface of an SPCE at different stages of modification. Obtained via LA-ICPMS and averaged over 3 readings. ANSAm-DNA indicating the DNA attached via sulfonamide link to the ANSA modified surface.

	Average atom concentration (ppb)				
	C	**Cl**	**S**	**P**	**N (ppm)**
Blank	*228595 +/- 11961*	*6138 +/- 248*	*300 +/- 44*	*209 +/- 15*	*39526 +/- 439*
SPCE-ANSA	*255050 +/- 3722*	*5684 +/- 65*	*263 +/- 43*	*258 +/- 10*	*37864 +/- 36*
SPCE-ANSCl (acetone/PCl_5)	*57254 +/- 201*	*1025 +/- 6*	*Not observed*	*113 +/- 5*	*7314 +/- 129*
SPCE-ANSCl (hexane/PCl_5)	*268197 +/- 7361*	*5580 +/- 35*	*282 +/- 27*	*4791 +/- 58*	*36443 +/- 401*

SPCE-ANSAm-DNA	*4325352 +/- 365964*	*4902 +/- 1246*	*954 +/- 171*	*6064 +/- 414*	*1696514 +/- 252657*
SPCE-ANSAm-DNA/miRNA	*2017832 +/- 582378*	*1534 +/- 544*	*657 +/- 94*	*9831 +/- 2792*	*723689 +/- 184944*
SPCE-ANSAm-DNA/non-complement	*2882532 +/- 102513*	*2732 +/- 113*	*341 +/- 46*	*283 +/- 9*	*73241 +/- 682*

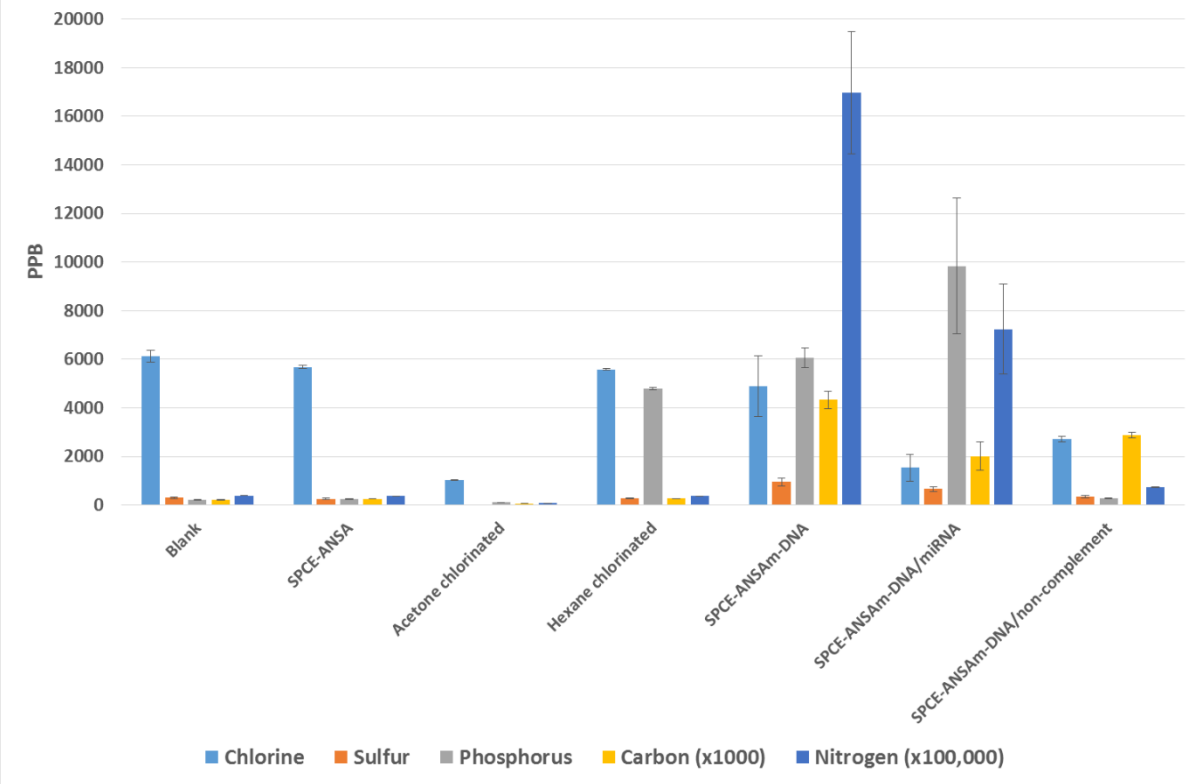

Figure 3.13 The ICP-MS data shown graphically, displaying the change in the key elements at each stage of SPCE modification.

The blank data show that the predominant electrode surface element was carbon, as would be expected from a screen printed carbon electrode, with some chlorine, sulfur and phosphorus compounds from the ink or its binding polymers. When the naphthalene sulfonic acid was deposited (SPCE-ANSA) the carbon concentration increased by a considerable ppb, as expected. However, the chlorine and sulfur levels fell slightly, possibly due to a slightly different ink constituent or due to the new polymer surface decreasing the laser's permeation depth.

Increased sulfur content would be predicted due to the new sulfur atom introduced for each sulfonic acid molecule, but this was not observed. It has already been mentioned that Cl may be difficult to measure as it does not readily form Cl^+ ions, so has low Cl measurement sensitivity, and for atomised sulfur ($^{32}S^+$) there is potential spectral overlap on the mass spectrum with atomised oxygen ($^{16}O_2^+$) if not standardised,[255] which may explain the unexpected trend in sulfur concentration.

Subsequent experiments added further clarity. The SPCE subjected to the acetone/PCl_5 chlorination conditions showed a dramatic decrease in the concentration of all key elements including carbon and nitrogen. This indicated that damage was occurring to the surface of the ink itself, particularly as its carbon content was reduced by ≈75% compared to the blank result.

Valox, made from a PET-based polymer, was not expected to contain nitrogen, but the carbon ink ingredients were. Decreases in carbon and nitrogen contents therefore suggested surface damage was causing ink to leach from the substrate during chlorination, supporting the above electrochemical observations in which the current response did not match the predicted redox behaviour.

By contrast, the hexane-based chlorination procedure did not result in decreased carbon concentration, which stayed around the same level as the SPCE-ANSA stage. The modest increase in this quantity was possibly due to slight differences in electrode inks, or residual hexane. The chlorine content varied little from the deposited electrode or the blank, perhaps for the above reasons of low sensitivity and difficulty producing Cl^+, The increase in phosphorus content showed residual PCl_5 was likely present in this sample, but the overall picture suggested that hexane chlorination did not cause the damage seen using acetone/PCl_5.

When DNA was added to the hexane chlorinated electrode to form the SPCE-ANSAm-DNA electrode surface, the carbon, nitrogen and phosphorus concentrations increased by a large amount, as expected. The chlorine concentration also appeared to drop slightly, as would be expected from the sulfonamide linkage reaction liberating some of the surface chlorine atoms as HCl. Then, when the electrode was submerged in a solution containing miRNA complementary to the attached DNA probe, there was a large increase in the phosphorus

content, indicating the presence of more phosphate backbones as expected from the additional RNA. This phosphate increase was not observed when a non-complementary sequence was used, in fact there is a substantial decrease in phosphorus and nitrogen, indicating that some of the original DNA probe strands were lost or degraded, perhaps due to the elevated hybridisation temperature.

The above observations suggested that the electrode not only survived the modification procedures, but that the DNA has been attached as desired, and that the desired hybridisation event was taking place. The experimental observations therefore support the use of the modified SPCEs hybridisation protocol described above as a viable methodology for the detection of miRNAs in solution.

Having used LA-ICPMS to analyse the surface chemistry, determine the electrodes survived the procedure and, at least chemically, functioned correctly, visualisation on a macroscale was then undertaken. This was especially necessary since some of the LA-ICPMS data were not predicted, for example the drop in nitrogen content on miRNA hybridisation, and the low sulfur content upon deposition of the sulfonic acid. Such analyses would also allow further scrutiny of the urinary miRNA detection procedure described in Chapter 2.

To achieve this macroscale visualisation, atomic force microscopy (AFM) techniques were used. The disposable SPCEs were readily sheared to fit into the AFM instrument. The GCE would have had to be destroyed for this purpose, at prohibitive expense for multiple images. Therefore the SPCE electrodes alone were used. Since the overarching aim of the project was to develop a test using disposable SPCE based sensors, this was deemed sufficient.

The first of AFM images are displayed in Figure 3.14 and show the surface of a blank 3mm diameter SPCE.

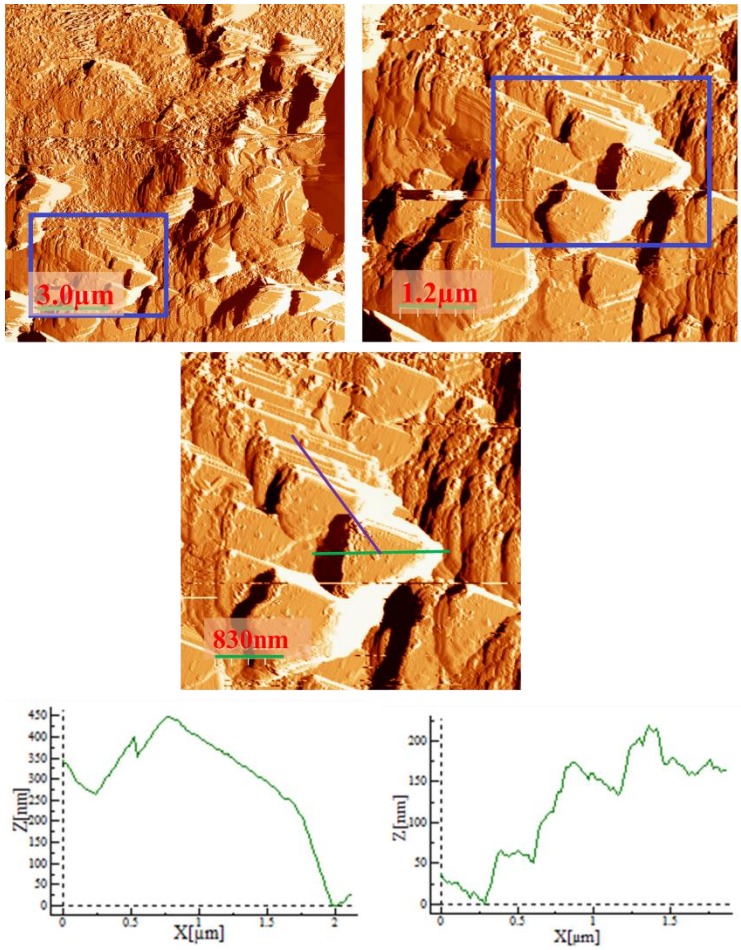

Figure 3.14 A TM (tapping mode)-AFM image and zooms of the 3 mm SPCE surface with no surface modifications, with a graphical indication of the triangular feature length (green line in image, left profile) and the average step height in the layers (purple line in image, right profile).

The AFM images of the unmodified SPCE show that the carbon surface of the working electrode consists predominantly of triangular layers, each approximately 1.75 µm in length as indicated by the green line with a layer step height of approximately 50 nm. The surface roughness analysis also indicated a roughness of 0.43 µm and an average height standardised of 1.61 µm from the lowest point. This is an important observation, showing that while there are areas of order along the surface (the around 1.75 µm for each top triangular feature) it is not planar as might be expected from a GCE as there is roughly a 10 % change in height across the surface (ink quoted as 16 µm average printed thickness, an average of 1.61 µm height difference from the standardised low point is measured by AFM roughness analysis). The roughness across the surface could also account for some of the variability noticed earlier as slightly different active areas may occur between each individual electrode on one substrate and across the whole batch. This is likely to average out over the whole surface, and will be depend on exact production conditions.

The images from this “bare” surface provide a baseline reference point for images generated at different stages of the SPCE modification process. With respect to the ink itself, the triangular features indicate that the carbon is graphitic in nature, the trigonal planar geometry of graphite resulting in the triangular shape in bulk. A similar image of layered triangles has been reported for isolated graphite nanosheets by Shang *et al,*[256] and also in a 3D AFM image of a screen printed carbon electrode shown by Wongkaew and Poosittisak.[257] Interestingly, throughout all the images collected where these triangular graphite features are visible, there appears to be directional bias with the tip of the triangles pointing to the right. Were this bias due to the action of the squeegee during printing, the direction of bias would be expected to differ in different images, since the exact orientation in the AFM machine compared to the time of printing was not controlled. This same directional bias can be seen in the image by Wongkaew and Poosittisak, therefore it is possible that this is occurring due to the action of the AFM tip horizontal movement.

Figure 3.15 shows an image obtained following deposition of the naphthalene sulfonic acid.

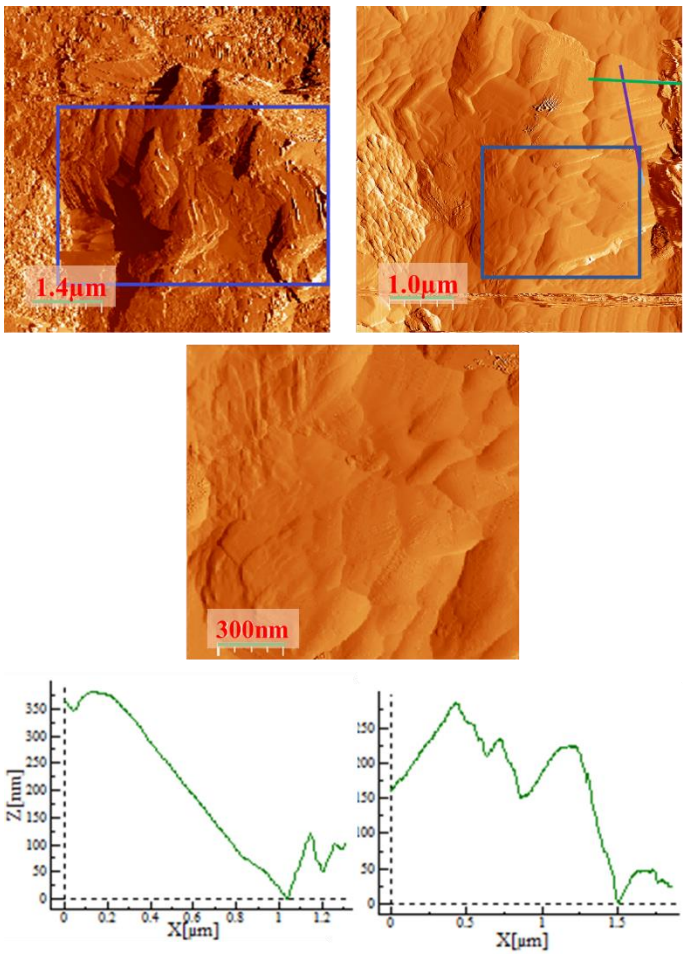

Figure 3.15 A TM-AFM image and zooms of the 3mm SPCE surface following ANSA deposition. The length of the feature highlighted by the green line is also given graphically (left profile) and the step height by the purple line (right profile)

These images show the same triangular features as the unmodified surface, as seen by both the visible shapes and the approximate 1 µm length of the highlighted example (the tip appears covered by another feature). However, the deposited ANSA had a profound effect. Rather than the sharp edges observed previously, the presence of ANSA caused the layers to become much less pronounced, and gave rise to a more uniformly smooth surface. This would be expected if a polymer was being generated, as hypothesised previously.

Despite the triangular features losing their sharp edges, the roughness across the bulk surface increased slightly from 0.43 µm to 0.46 µm, there was also a slight increase in average height across the surface from 1.61 µm to 1.64 µm, possibly indicative of the polymer being deposited over the surface. The layered step heights were still apparent, with an approximate step of 70 nm, however they were not as defined in this case with the profile curve being smoother, and the individual steps appeared to merge in some cases (hence the steady drop at the right hand side), again suggesting the presence of a rounded coating rather than a flat

surface. The surface coverage of the naphthalene sulfonic acid might also explain the dramatic drop in electrochemical response obtained following the deposition procedure using the GCE, as seen in Chapter 2.

The next images taken compared an SPCE surface following chlorination in hexane/PCl_5 (Figure 3.16) and one submerged in acetone/PCl_5 (Figure 3.17).

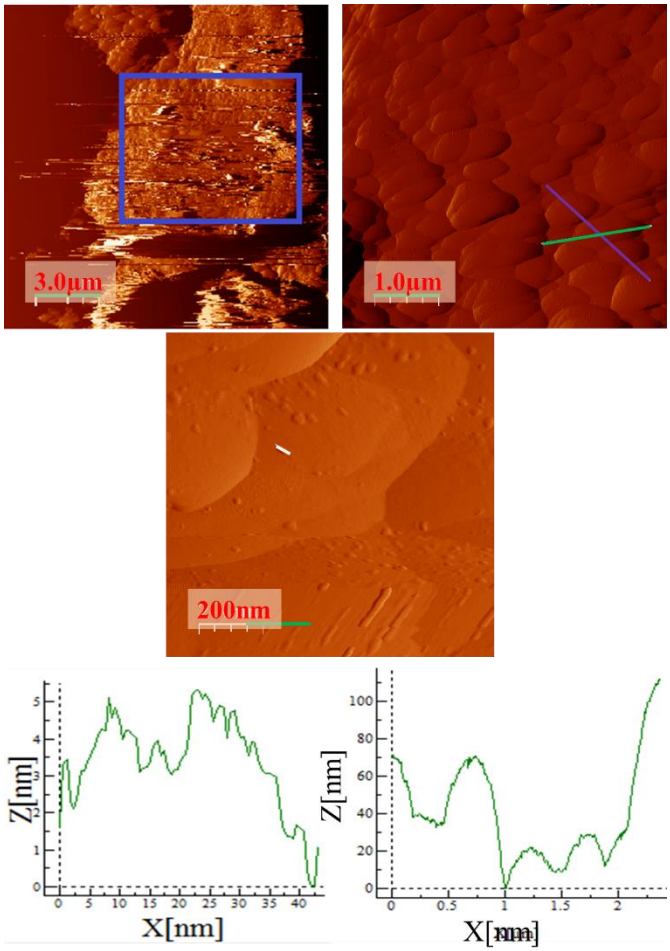

Figure 3.16 An AFM image and zooms of the 3mm SPCE surface following chlorination in hexane/PCl_5. The length of the triangular region was given according to the green line and the layer step height by the purple line (right hand profile). The white line in the lower image indicates the section used to analyse a rounded artefact (left profile).

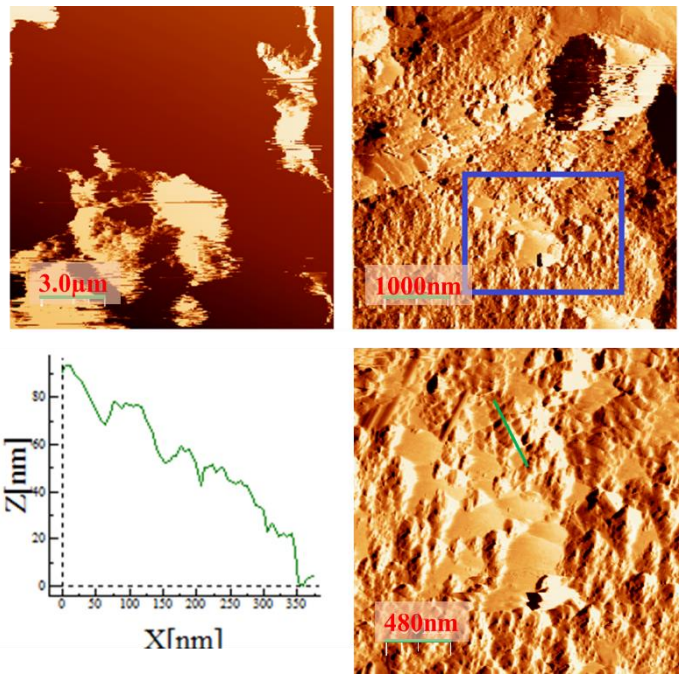

Figure 3. 17 An AFM image and zooms of the 3mm SPCE surface following chlorination in acetone/PCl5. The length of the round features and the step heights are given by the green line and the graphical profile.

In the lowest magnification image of the hexane/PCl_5 chlorinated SPCE (top left), some areas of undefined space to the left might indicate that the surface damage, or more likely areas where the tip did not come into contact with the surface. However, the average height of the surface was 1.14 µm, and with a roughness of 0.38 µm, this indicated a slight reduction in the average height and a slightly smoother surface than previously observed. Also, the same rounded triangular shapes seen in Figure 3.15 were still observed, with a length of ≈1.2 µm as expected, but here the step in layers was much lower, being only 20 nm and much more rounded. This might indicate that the layered structure was being stripped during this treatment and leaving a smoother surface for the electrochemistry. This in turn could explain the drop in average peak height observed and, if there was a dramatic change in height at different areas of the surface, why the tip did not always make contact. In this image there are also a number of smaller circular features that can be found throughout. The size of these (≈45 nm) would not be observed for an atomic change from OH to Cl alone, and could signify a cluster of sulfonyl chlorides or, more worryingly, macroscopic interferents. They are dispersed throughout however, whereas interferent adsorbate compounds would be expected to adsorb at the edges of any surfaces rather than being dispersed across the whole system.

The lowest magnification image (top left) obtained from an SPCE submerged in an acetone/PCl_5 solution (Figure 3.17) shows more undefined area than the corresponding hexane/PCl_5 image. This might be due to surface damage, but is most likely due to the tip not making correct contact with the surface in this area. When a section showing some visible features was measured at an increased magnification it was observed that, while the triangular backing structure was seen in places, many round features cover the surface.

The average surface roughness was only 0.21 µm, much lower than observed previously, indicating ridges and valleys in the surface. The average height was almost halved at 0.52 µm, possibly as a result of many ink layers being stripped by the acetone/PCl_5 solution. This would also explain the smoother surface, since the layers causing the previously observed increased roughness had been removed.

The size of the round features was also significantly bigger than previously (between 50 and 100 nm compared to the ≈45 nm of Figure 3.16), with the step heights between them hard to distinguish but ≈10-20 nm, as before. The increased size of these features, along with the

potential stripping of the electrode graphite layers suggests surface damage, the rounded features likely being artefacts and representing areas where the binding material or the ink itself was swollen due to attack from the acetone/PCl_5. The hexane/PCl_5 chlorinated electrodes showed the expected CV behaviour and fewer surface artefacts, the surface visually resembling more closely the SPCE-ANSA stage. It was thus concluded that the acetone/PCl_5 procedure irreparably affected the electrode surface, and therefore, at least with the carbon ink used, could not be implemented satisfactorily in biosensor production.

Figure 3.18 shows AFM images of an SPCE with DNA probe strands attached. The image was taken following biosensor modification by attachment of DNA strand complementary to miR-21. This image was taken for the purposes of comparison with DNA/RNA hybrid scans with untreated and proteinase K treated urine samples.

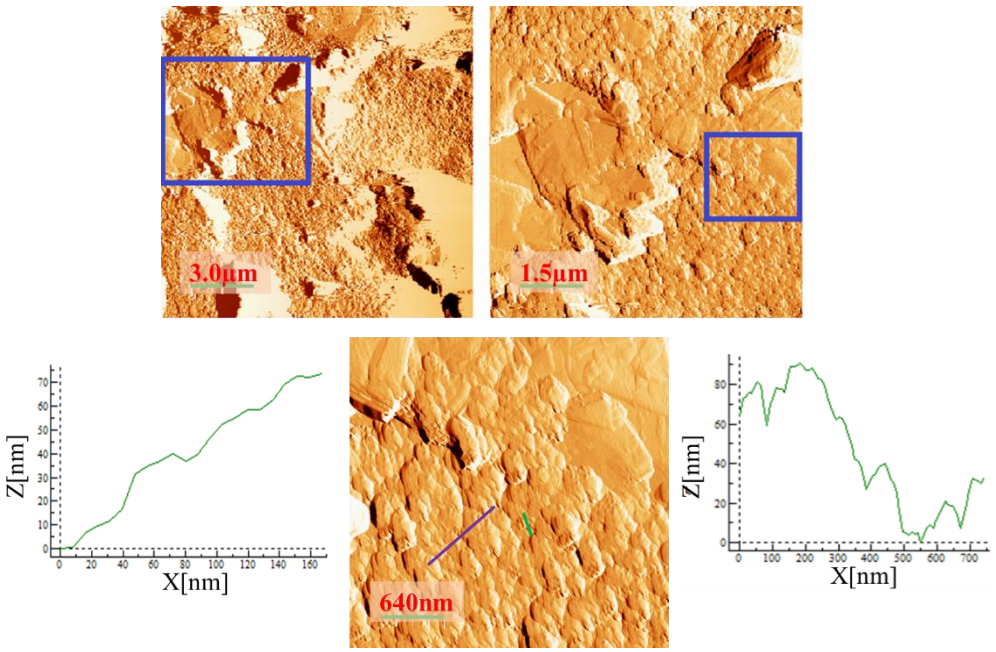

Figure 3.18 An AFM image and zooms of the 3mm SPCE surface following addition of anti-miR-21 DNA. The graphical representation of the length of the round features is given by the green line in the image (left profile) with the step height indicated by the purple line in the image (right profile).

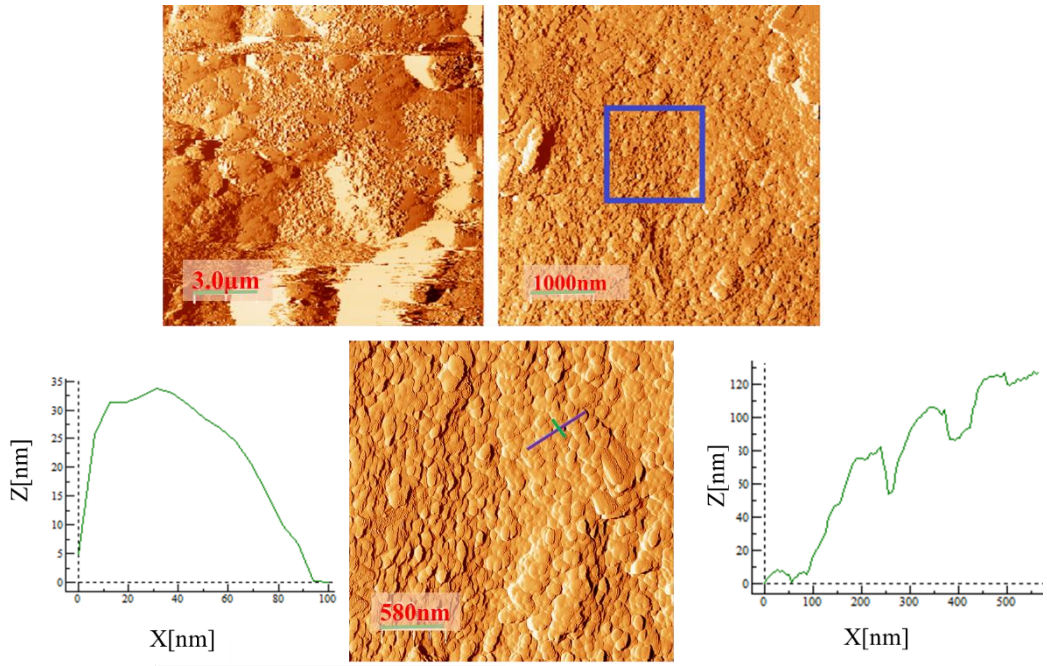

Figure 3.19 An AFM image and zooms of the 3mm SPCE surface following hybridisation with miR-21 in buffer. The length of one of the rounded features is given as indicated by the green line in the image (left profile) with the step heights being given by the purple line in the image (right profile).

Figure 3.18 shows that there was a substantial amount of surface coverage of some form of adsorbate following the application of the DNA droplet. It should be noted that the electrode in this instance was developed using the hexane/PCl_5 treatment that showed only slight

artefact coverage following chlorination, and that the electrode was thoroughly rinsed with water multiple times before submitting for AFM analysis.

Surface roughness analysis showed an average roughness of 0.41 µm and an average height across the surface of 1.63 µm, both of which were higher than that observed when chlorinated in hexane, indicating the deposition of objects roughly 590 nm in length. The rounded features themselves they were ≈40 nm in length, with a step height between each of ≈10-20 nm indicating their proximity and very limited layering. This suggested that the features seen here were likely areas where the DNA strands were localised as they were highly abundant, of similar size, and were dispersed along the surface, not just along the edges as would be expected for unwanted surface contamination. Ink blistering or swelling was not suspected since the maximum ink height increased on the hexane/PCl_5, and the layer loss as seen with acetone was not observed. There were also sections where triangular graphite was still observed.

Figure 3.19 shows an SPCE modified with DNA following hybridisation of miR-21 target in buffer. As with the DNA modified SPCE the surface of this electrode was covered with highly dispersed, rounded features. These features may show areas where DNA/RNA duplexes are forming, on account of their highly dispersed and regularly shaped nature. As seen in the lowest magnification image, these features aggregate only in certain areas, not as a general electrode coating or around the edges of any ridges/valleys in the surface. This would be predicted if there was an underlying polymer layer with DNA attachments, not just a layered graphite structure. Thus it is unlikely that they are caused by a general covering of the electrode by any unwanted macromolecules.

By analysing the surface roughness it was determined that the roughness was 0.47 µm, meaning that the change in height across the surface had become more pronounced. The maximum height was displayed as 1.67 µm, both values being larger than those for DNA alone, and thus suggesting the attachment of a second molecule. The height difference was not expected, since length of the DNA/RNA hybrid was not expected to differ from the DNA probe. A possible explanation might be that the new hybrid lowered the degrees of freedom, increasing DNA rigidity about the sulfonamide bond.

The profile graph shows the round features to be roughly 90 nm in length, approximately double what the length of DNA alone, with a height of approximately 35 nm. This would again point to the formation of a duplex from the single chains that were present previously. This image, together with the electrochemical behaviour, suggest that RNA/DNA hybridisation event was taking place, and also acts as a reference for comparison with the urine based images to follow.

Figure 3.20 displays AFM images taken after submersion of a DNA modified SPCE in an untreated urine sample.

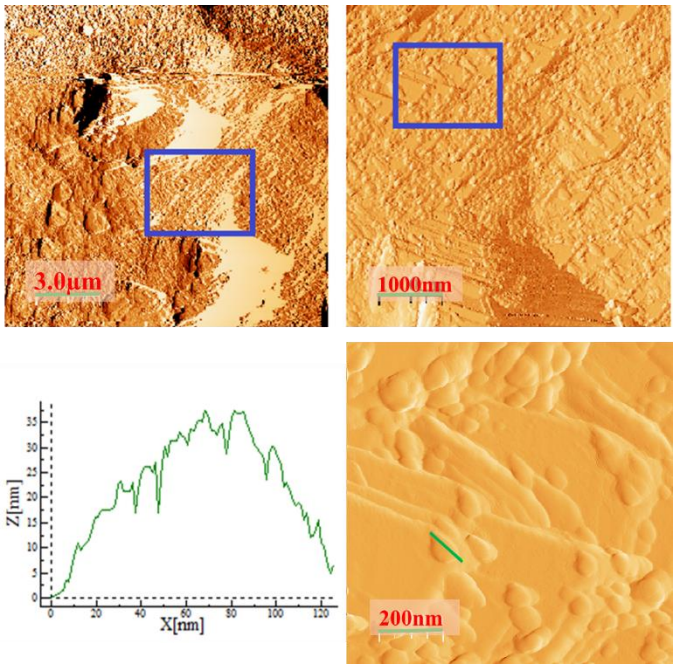

Figure 3.20 An AFM image and zooms of the 3mm SPCE surface following hybridisation in untreated urine. The graphical surface profile of the rounded features highlighted by the green line is also given.

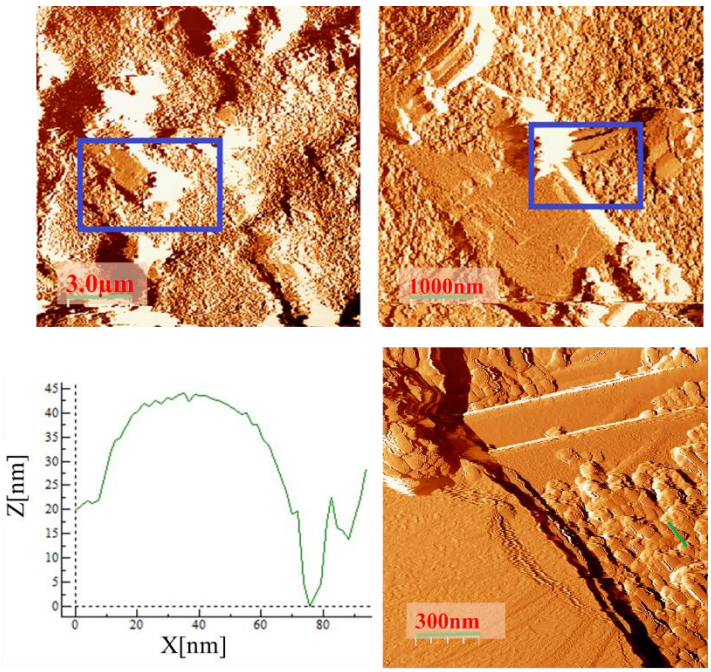

Figure 3.21 An AFM image and zooms of the 3mm SPCE surface following hybridisation with urine treated with proteinase K and spin filtered. The length of one of the round features, highlighted by the green line, is also given graphically.

Much like the previous images of both DNA and DNA/RNA hybrid electrodes, this untreated urine sample also resulted in many rounded features. However from the mid zoom image shown top right, and the high zoom image shown bottom right, it appears that these features were not as dispersed across the triangular surfaces as previously. Instead, most often they

aggregated predominantly at the corners and edges of the triangular surfaces of the carbon/graphite ink. Indicating that they were likely interferent artefacts as oppose to true DNA/RNA features.

Surface roughness analysis indicated that the surface roughness was 0.40 µm with an average height of 1.05 µm. These values were much closer to those obtained when the hexane/PCl_5 chlorination procedure was performed (1.14 µm and 0.38 µm respectively) and much lower than those obtained for the DNA containing electrode (1.63 µm and 0.41 µm respectively), possibly suggesting that DNA was no longer attached to the surface. However, it seems more likely that the artefacts/proteins present in the urine were forming a second coating of the electrode in between the DNA strands. This would result in an increase in the standardised zero height value, making the surface appear uniformly thicker so that the change in height observed due to the DNA appeared smaller.

The rounded features were much larger than those observed previously, ≈120 nm in length with a rounded height of ≈35 nm. It therefore appeared that many contaminating macromolecules coated the electrode surface, for example lipids and proteins, most likely what caused the large drop in current response seen in the GCE urine control tests. While the GCE would likely not be expected to have this triangular topology, there would still be surface defects to which these macromolecules could adsorb.

The final AFM image in this, shown in Figure 3.21, shows an SPCE that had been immersed in a urine sample treated with proteinase K and spin filtered, as used in the optimised urine analysis tests performed using the GCE in Chapter 2.4.

These images, when compared to those in Figure 3.20, allow several conclusions to be drawn. Average roughness was 0.37 µm, with an average height of 1.4 µm. This was lower than expected with a surface of DNA/RNA hybrids (0.47 µm and 1.67 µm with synthetic miR-21), possibly due to the lower miRNA concentration in the urine sample coupled with minimal amounts of the layering effect, seen for the untreated urine sample from smaller proteins and lipids, increasing the baseline height slightly. When each image was viewed individually it was observed that in both the lowest magnification image (top left), and the next magnification (top right), there was increased coverage of round features compared with previous observations. In addition, these features aggregated around each other over large areas, as

seen for the DNA/miRNA hybrid images in Figure 3.19. The positioning of the features was also different in Figure 3.21. In Figure 3.20, the round features were found at the edges and corners of the triangular geometries, but in Figure 3.21 they appeared more frequently along the flat surfaces as opposed to the vertices and edges.

As stated above this was thought to signify the RNA/DNA hybridisation event as uniform coverage rather than non-specific adsorption of macromolecules at crevices. The general appearance of these features also resembled those in Figure 3.19. Finally, the length of one of these features was measured via profiling to be approximately 80 nm, rather than the ≈120 nm found without treatment of urine, and a height of approximately 40 nm. These lengths are again more consistent with those found for the DNA/RNA hybrid images in Figure 3.19.

Taking all the imaging techniques into account, both the LA-ICPMS and the AFM, it appeared that the modified SPCE survived hexane/PCl_5 treatment, bound DNA, and mediated RNA/DNA hybridisation as intended. From the AFM data it may also be posited that the urine treatment with proteinase K and spin filtration resulted in fewer contaminating macromolecule interferents found at the surface of the carbon ink. The data obtained following this treatment are thus more plausible than those showing much lower current response / greater resistance shown in the urine control experiments (Chapter 2.4).

3.5: Chapter conclusions.

Over the course of this chapter, prototyping and troubleshooting of two individual SPCE designs were explored. The modification procedure employed for the GCE was not appropriate for use with the SPCEs, as it resulted in loss of electrochemical response and visible surface damage. Also discussed were the various alterations required in the modification procedure, including an increased reaction time in the different chlorination solvent of hexane, and the use of a commercial nail hardening resin for protection against water ingress during the hybridisation event. These alterations allowed a sensitivity curve to be produced for the first 2 mm SPCE design that showed a greatly reduced sensitivity over that of the GCE.

Thus a new design was trialled using a 3 mm diameter working electrode, the same as that of the GCE and therefore the data could be compared directly. Use of this design increased

sensor sensitivity and produced an overall minimum response much closer to the GCE while still having a large degree of variability.

Finally, the surfaces of these electrodes were analysed using LA-ICPMS and imaged using AFM in order to visualise how the surface of the ink changed during the different modification steps. These data showed that the hexane solvent led to improved electrode survival compared to the acetone/PCl_5 mixture. The effectiveness was also seen of proteinase K treatment and spin filtration treatment of urine samples to remove undesired macromolecules, resulting in the electrochemical analyses shown in Chapter 2.4.

The final chapter will discuss the work performed during a 3 month placement at Gwent Electronic Materials®, and how trialling different carbon and silver inks and dielectrics might allow us to overcome the solvent difficulties seen here. A new electrode design to allow the simultaneous analysis of a number of different microRNA targets in a urine sample using an electrode array will also be discussed. This will also be used to determine if differences in urinary miRNA biomarker concentrations can be detected between the healthy individuals and diabetic kidney disease patients.

Chapter 4: Multi-electrode Array Prototyping

Chapter 4: Multi-electrode array prototyping

4.1: Introduction to screen printing methodology

In Chapter 3 were discussed the various layers that make up the screen printed electrodes used throughout this project, along with a very generic schematic of the order these layers are printed. During this project a 3 month industrial placement at Gwent Electronic Materials (GEM) was undertaken to further develop the design of the electrodes and the materials which they are made from. A brief discussion of exactly how the electrodes are printed, along with some of the tools and techniques used for precise printing, is discussed in this section.

In order to screen print electrodes one needs three key items, starting with the inks that they will be printing with. These can be made from a number of materials, most mentioned in the previous chapter, but are often carbon/graphite, gold, silver or platinum based for the working electrode,[258] carbon or silver for the counter electrode and silver/silver chloride for the reference. A final dielectric (insulating) ink,[259] in the case of GEM commonly polymer or silicone based, is also often used in order to define the surface area and reduce the variability of said area between each electrode,[260] and provide a protective layer for the conductive traces from solvents.

Secondly a screen is needed to supply the template for each layer of the electrode, these can be custom designed to fit a specific purpose. Those used at GEM have an aluminium frame for stability with the mesh material consisting of polyester or stainless steel, the latter of which being used when high tension (and thus greater registration accuracy in printing intricate/highly designs) and non-electrostatic printing is required.[261]

Finally a method of performing the screen printing is required, although this can be done by hand for very simple testing of the ink materials, often a screen printing machine is used to ensure consistent prints for precise electrode sensors. Again there are many examples of screen printing machines, some designed for large substrates and mass production, others for low throughput, some with laser guided print alignment others aligned by eye. The machine used to print the electrodes in this project is a DEK 1202, a picture of this and the tools used are shown in Figure 4.1.

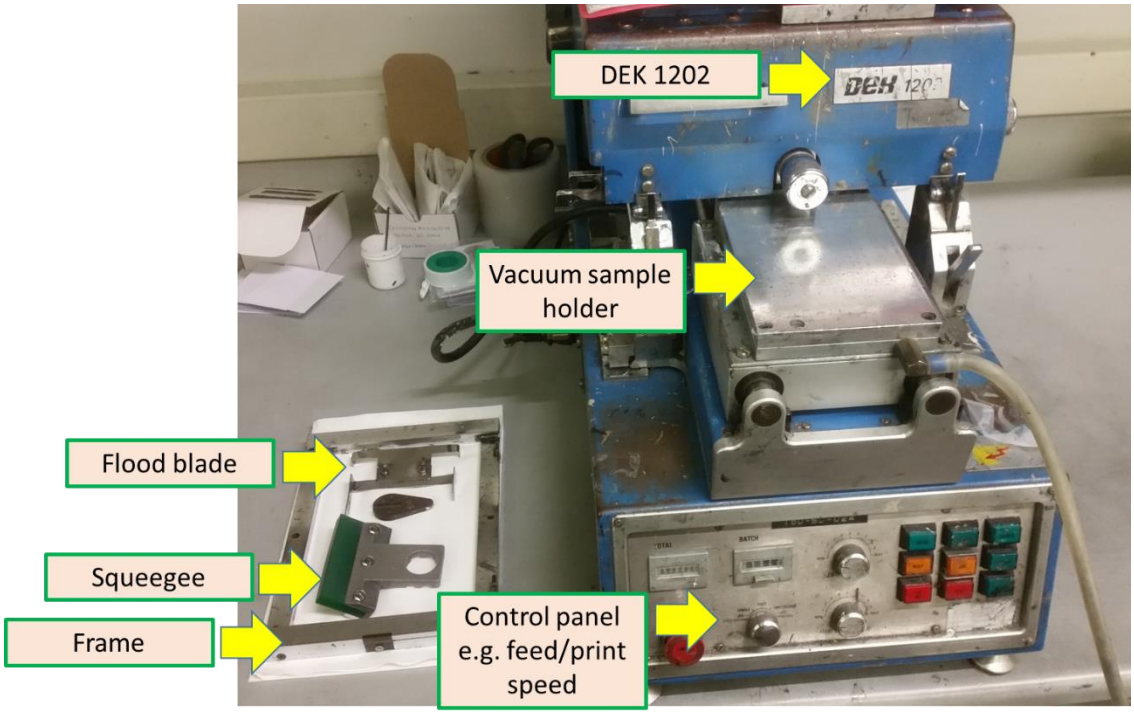

Figure 4.1 The DEK 1202 screen printing machine used to print the electrodes used in this chapter. Also shown are the important small parts used within the printer.

In order to perform a screen print, firstly the chosen screen designed for the bottommost layer (usually the conductive tracks e.g. silver/silver chloride) is screwed into the aluminium holding frame and this is placed into the printer. The chosen substrate is then loaded onto the vacuum sample holder, which has been lined with porous paper, and fed into the printer to align the screen design with the edges of the substrate. Once aligned a set of plastic guides is glued into place around the substrate edges to ensure near perfect reproduction of the alignment between each batch. Next the flood blade is placed into the machine, then the squeegee is wetted with the ink, secured in place, and the ink is loaded onto the screen. Finally the feed and print speeds are set, the squeegee pressure is selected and printing commences.

When a print is performed, first the arms of the machine push the flood blade forward causing the ink to be spread evenly over the screen, then the squeegee is lowered to push against the sample holder and screen and pulled back over the substrate. This pressure forces the ink through the design on the screen which has pores to allow the ink through, thus leaving a thin layer of the ink on the substrate in the design chosen. Finally the squeegee is lifted off the screen and the flooding procedure is repeated ready for the next print. This is repeated until the desired number of prints have been performed, stopping the last flood on the final print

in order to allow the screen to be removed and cleaned. The general schematic for this is shown in Scheme 4.1.

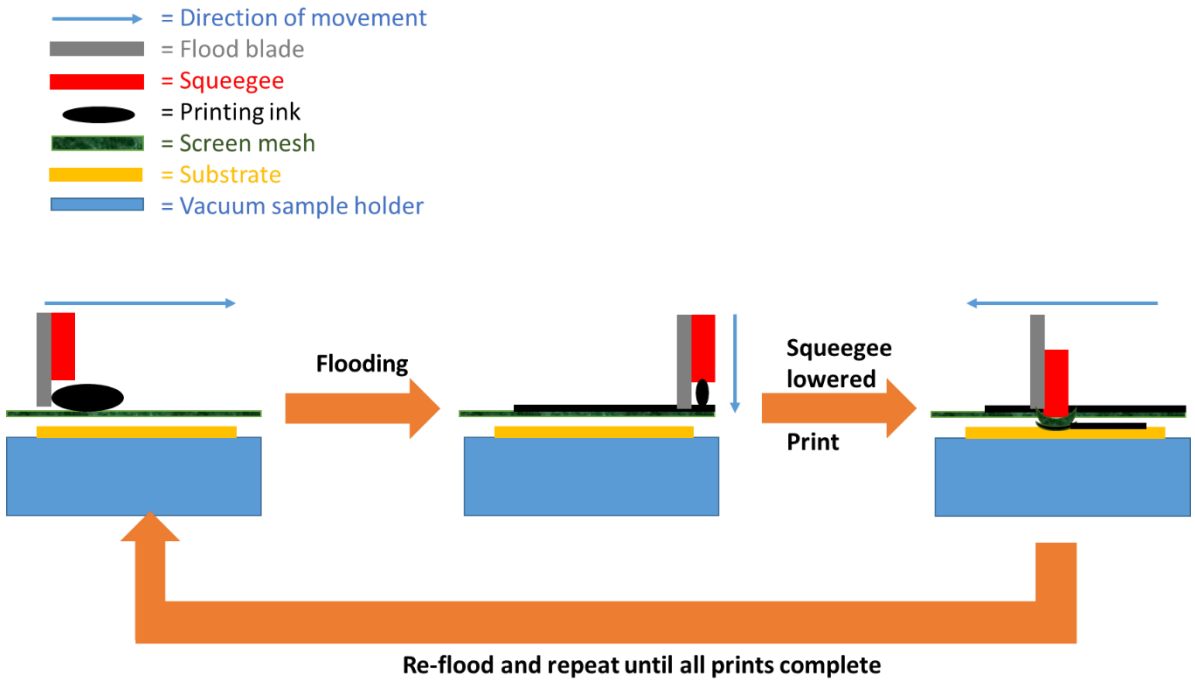

Scheme 4.1 The mechanical procedure for screen printing an electrode. The system floods, the squeegee is then lowered and pushes the ink through the screen mesh. Finally this repeats until the desired number of prints are complete.

This whole procedure is repeated for each subsequent screen and layer, with the fiducial on the print (small crosses shown in the designs in Figure 4.3) used to line up each layer with the next screen correctly.

4.2: Aims for the design of the multi-electrode array and remaining prototyping.

The aim while on placement was to trial a variety of different carbon, silver/silver chloride and dielectric inks, determining an optimal set that would be most likely to survive the acetone/PCl_5 treatment that had been used in the GCE modification procedure. This would allow us to not only speed up the modification procedure, over that of the previous set of SPCEs, but would also allow us to better relate the SPCE data to that obtained using the GCE. Finally, once the ink materials had been optimised, a new electrode design was to be developed with multiple active surfaces which would allow for repeated analyses using one electrode, and making future adaptation into a multi-target array possible. The ability to perform repeated analysis on one sensor being important for future employment as a biosensor.

Unfortunately the exact chemical formulation of each ink is not able to be discussed due to its commercial protection. However the product number of each ink is given so that it can be found in the Gwent product range easily in future.

4.3: Testing the carbon ink materials.

The first material to be tested while at GEM was the carbon ink that forms the basis of the SPCE. We wanted to determine which of the inks available would be most likely to survive the acetone/PCl_5 treatment and still give readily interpretable and reproducible electrochemical responses. To do this, two of their inks, designed to be more solvent resistant through a cross-linking polymer binder, were selected and printed as simple stick electrodes. The product codes for these carbon inks are given in Table 4.1 and the stick design is shown in Figure 4.2

Table 4. 1 The product codes of the two thermoset cross linked inks used for increased chemical stability.

Carbon ink
C2100126_D6 : Thermoset (cross-linked) carbon/graphite ink
C2050517_P1 : Thermoset (cross-linked) carbon/graphite ink

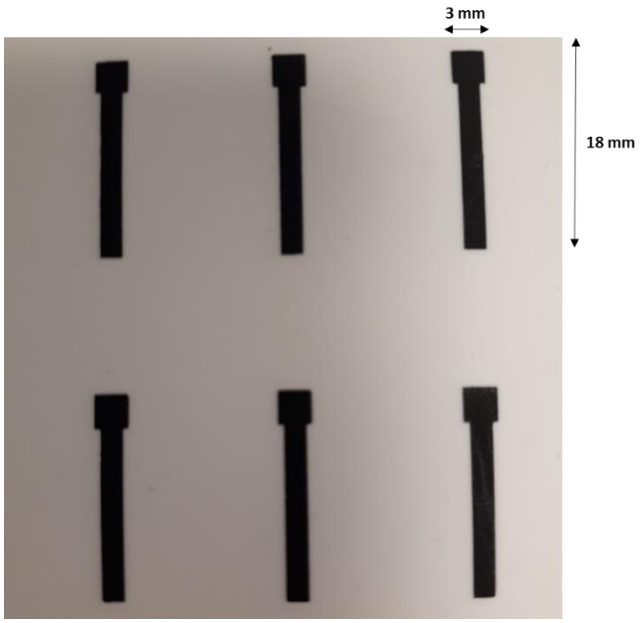

Figure 4.2 The basic carbon stick electrode design used for determining the chemical stability of the carbon inks alone.

Using these carbon stick based electrodes it was possible to perform a simple stability test by submerging an electrode produced using each ink in a solution of PCl_5 dissolved in acetone, in a similar fashion to that of the GCE. After submerging for 30 minutes, and then allowing to dry, the sticks were visually inspected for any signs of damage such as peeling or cracking,

however no such damage was seen for either ink. Thus this procedure was repeated again using a new set of carbon sticks made of the two inks, some having resin and insulation tape to protect and define the electrode active surface and others used as they appear in Figure 4.2. They were then analysed electrochemically.

As a final experiment both carbon inks were used to produce a set of complete SPCEs using the design shown in Figure 4.3, these were also exposed to the chlorination solution then tested electrochemically using an external reference and counter rather than those contained within the electrode. The resulting observations for these tests are summarised in Table 4.2 with an example of a successful and unsuccessful electrochemical measurement, determined by the presence of clear oxidation and reduction peaks of the reversible ferri/ferrocyanide analyte system, also shown in Figure 4.3.

Table 4.2 A summary table of all the carbon ink compatibility tests towards the chlorination procedure. Those that appeared reasonably undamaged, and displayed the expected electrochemical oxidation and reduction peaks, are highlighted.

Carbon ink	Electrode type	Acetone or PCl_5/Acetone	Submerged or droplets	Electrochemistry successful?
C2100126_D6	*STICKS*	*PCl_5/Acetone*	*Submerged*	*No*
C2100126_D6	*STICKS*	*PCl_5/Acetone*	*Submerged*	*No*
C2100126_D6	*STICKS*	*PCl_5/Acetone*	*Submerged*	*No*
C2100126_D6	*STICKS*	*PCl_5/Acetone*	*Submerged*	*No*
C2100126_D6	*STICKS*	*PCl_5/Acetone*	*Submerged*	*No*
C2100126_D6	*STICKS*	*PCl_5/Acetone*	*Submerged*	*No*
C2100126_D6	*STICKS*	*PCl_5/Acetone*	*Submerged*	*Yes*
C2050517_P1	*STICKS*	*PCl_5/Acetone*	*Submerged*	*No*
C2050517_P1	*STICKS*	*PCl_5/Acetone*	*Submerged*	*Yes*
C2050517_P1	*STICKS*	*Acetone*	*Submerged*	*Yes*
C2100126_D6	*FULL ELECTRODE*	*PCl_5/Acetone*	*Droplets*	*No*
C2100126_D6	*FULL ELECTRODE*	*PCl_5/Acetone*	*Submerged*	*No*
C2050517_P1	*FULL ELECTRODE*	*PCl_5/Acetone*	*Droplets*	*Yes*
C2050517_P1	*FULL ELECTRODE*	*PCl_5/Acetone*	*Submerged*	*Yes*
C2050517_P1	*FULL ELECTRODE*	*PCl_5/Acetone*	*Droplets*	*Yes*
C2050517_P1	*FULL ELECTRODE*	*PCl_5/Acetone*	*Droplets*	*Yes*
C2050517_P1	*FULL ELECTRODE*	*PCl_5/Acetone*	*Droplets*	*Yes*

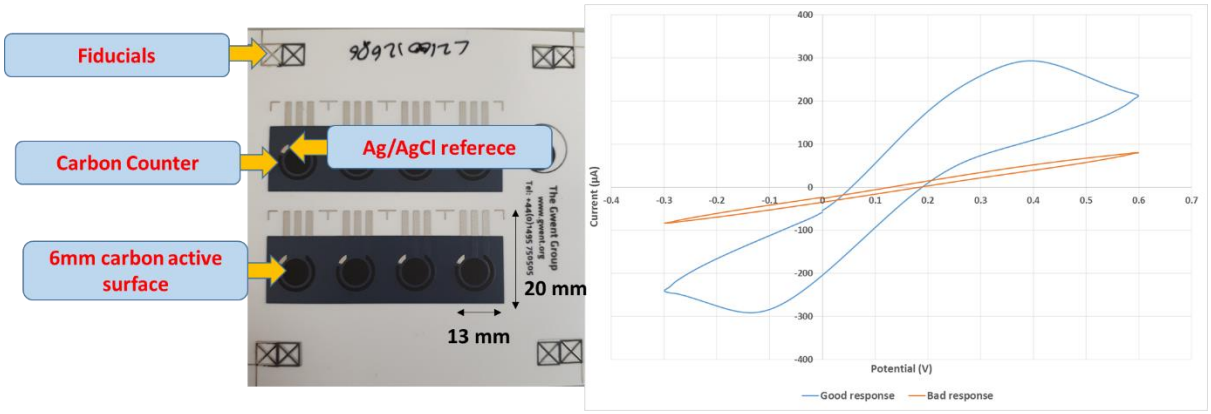

Figure 4.3 The 6 mm SPCE design and an example of a successful (blue) and unsuccessful (orange) CV electrochemical response. A successful CV showing clear oxidation and reduction peaks occurring as a result of the 5 mM ferri/ferrocyanide redox activity.

From these preliminary stability tests it was concluded that the carbon ink C2050517_P1 was the best ink to use for the future electrodes. This ink survived the greatest number of exposure tests, giving a readily interpretable electrochemical response following said exposure, and from experience was also easier to print with than the C2100126_D6 ink. However, when using the full electrode prints, another important observation was that both the dielectric coating and silver/silver chloride reference and connections were heavily damaged. For those electrodes that were submerged in the chlorination solution it was noted that the PCl_5/acetone solution turned cloudy when hydrolysed with water, further indicating that some material was leaching from the electrode during the chlorination procedure (shown in Figure 4.4). Therefore it was deemed necessary to test a series of silver and dielectric inks in order to enhance their stability also.

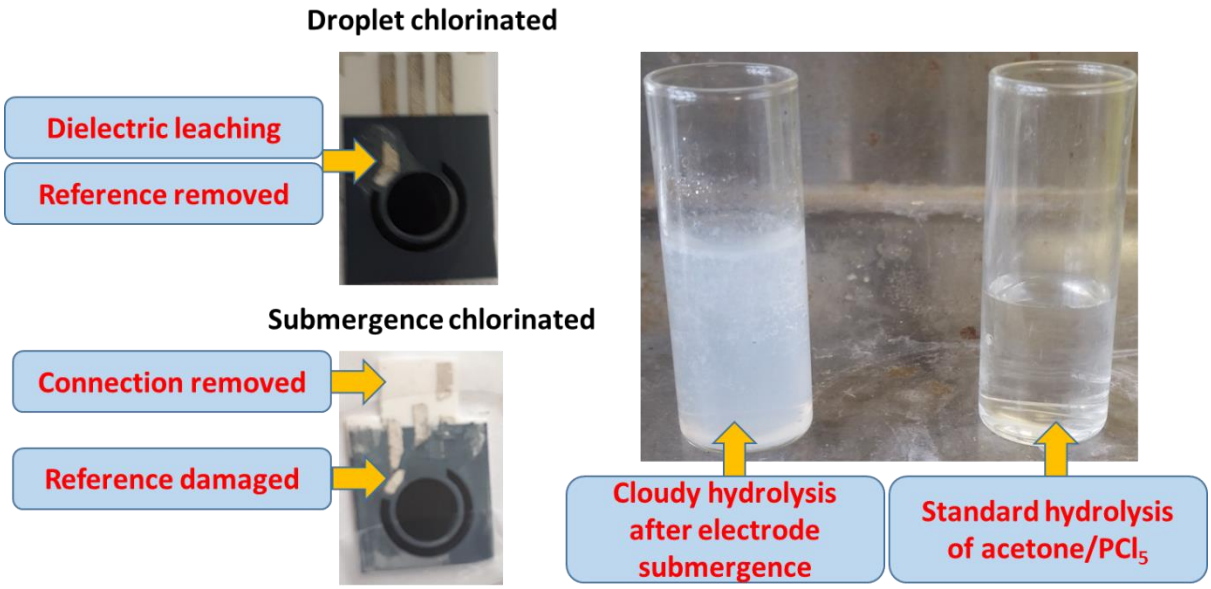

Figure 4.4 Images showing the 6 mm electrode design and how the exposure to the acetone/PCl_5 solution results in damage to the silver and dielectric inks. The resulting cloudiness observed in the solution after electrode submergence and hydrolysis is also shown.

4.4: Optimising the silver/silver chloride and dielectric inks.

To further enhance the stability of the screen printed electrodes the best silver/silver chloride and dielectric inks that could be used with the PCl_5/acetone chlorination mixture were investigated. Therefore the first modification to be tested was the use of a different silver/silver chloride ink as the standard ink C2130809_D5 was shown to be damaged upon exposure to this mixture. Therefore, as the cross-linked carbon ink had shown the best stability previously, a cross-linked silver/silver chloride ink C2131016_D1 was selected as the most likely to also be stable under the chlorination conditions.

To test the stability of this new silver material another set of electrodes with the 2 mm electrode design (Figure 3.1) were printed using this new silver/silver chloride ink as the reference electrode and conductive track. For the working electrode the optimised carbon ink was used and finally the standard grey dielectric (D2070423_P5) was printed as the final layer. These electrodes were then tested by being submerged in the PCl_5/acetone solution for 30 minutes, after which they were inspected visually for any signs of damage or peeling of the silver layer. This was also repeated by submerging the electrodes upside down, submerging the connector pins at the top of the electrode and thus exposing the silver layer directly to the mixture without the protection of the dielectric. After exposure and subsequent drying, all silver surfaces were inspected visually, scratched to test the adhesion and then tested

electrochemically to ensure an electrochemical read-out was still obtainable. The exposed electrodes and example cyclic voltammogram obtained are given in Figure 4.5.

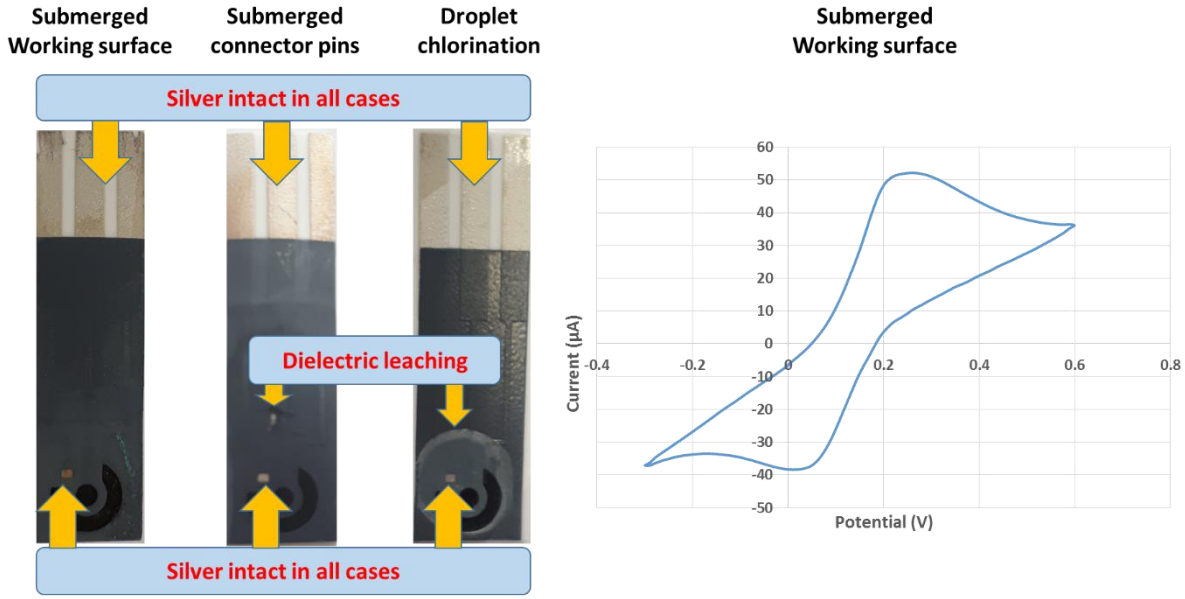

Figure 4.5 Images showing the stability of the carbon and silver inks, but the dielectric is still damaged. It was possible however to generate a CV from the leftmost electrode, displaying the characteristic oxidation and reduction peaks of the 5 mM ferri/ferrocyanide couple, which is displayed on the right.

The key observations at this stage were that the silver layer, despite some minor discolouration, remained intact and did not peel from the substrate as it did previously. However, as has been seen with all designs to this point, the grey dielectric layer is still showing signs of leaching as it shows major discolouration and smearing, indicating the damage that the chlorination mixture is causing to this dielectric layer. Despite some of the electrodes proving successful even with this damage to the dielectric, some of them were not, and those that were (as seen) also had some misshapen areas in their voltammograms. This poor reproducibility would not be ideal for use in biosensor technology. Therefore the dielectric layer also had to be optimised; not only to ensure the electrodes would survive the chlorination procedure every time, but also to ensure the visual appearance of the electrode is negligibly affected. This last point being important from a commercial aspect as visual defects would not pass quality control inspections and the sensor would be rejected.

Thus to determine the best dielectric material to be used throughout the future SPCEs, a number of different dielectric inks were selected, these are summarised in Table 4.3.

Table 4.3 The product codes, colours and GEM product description of the different dielectrics tested for stability.

Product code	Colour	GEM description
D2140114_D5	*Blue*	*Maximum resistance to solvents and their ingression*
D50706_P3	*Blue*	*Highest resistance to polar solvents*
D2130510_D2	*White*	*Cross linked material with good flexibility and high chemical resistance*
D50706_D2	*Cream*	*High resistance to polar solvents*

Of these the first two determined to be the most likely to withstand the chlorination treatment were the white and cream dielectric inks. The white ink being cross-linked, much like the carbon and silver, and so potentially having the greatest resistance, and the cream coloured ink having high polar solvent resistance according to GEMs product description. Therefore in order to test these two dielectric pastes a square of each was screen printed onto a Valox substrate and dried in a box oven. Once printed and dried a 100 µL droplet of acetone was placed onto the centre and edge of these squares and left at room temperature for approximately 30 minutes or until the acetone had dried. As with the silver and carbon inks these were then inspected visually to determine any peeling or signs of dissolution. Figure 4.6 shows the results of this visual experiment.

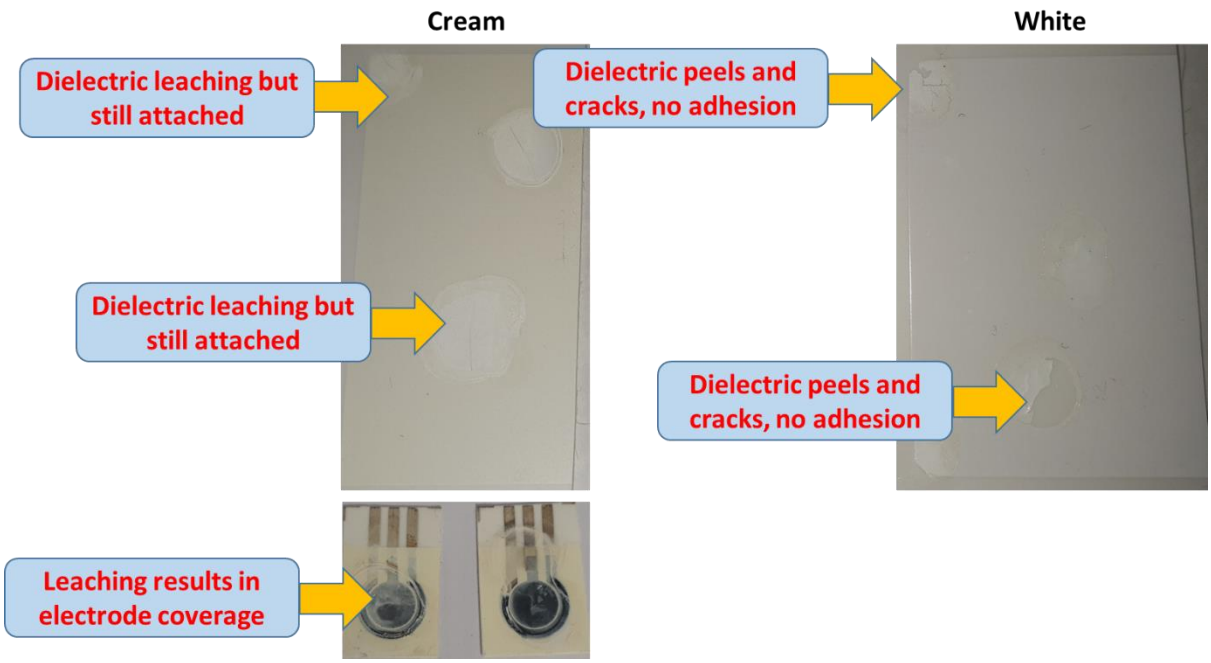

Figure 4.6 Images of the cream and white dielectric pastes, showing the cream leaching but remaining attached to the substrate, the white however peels and cracks. The cream leaching results in electrode coverage when printed as a full electrode.

Unfortunately, as can be seen in the pictures above, both dielectric inks showed visual signs of damage when exposed to the acetone solvent. The white (cross-linked) dielectric material became very dry, losing its glossy feel, and began to crack and peel particularly around the corners and edges. This indicated that it was losing both its structural integrity and its adhesion to the Valox substrate. When printed with the electrode shapes and submerged in acetone this effect was seen to a greater extent, with the entire exposed area coming away from the substrate within minutes. The cream dielectric, on the other hand, appeared to maintain its adhesion and shape, however there was significant leaching of the paste at the areas exposed to the acetone. This could be observed more clearly when the ink was used to produce a complete electrode, as the entire carbon surface became coated in a cream 'haze'. This indicated that the use of the cream dielectric would result in substantial interference downstream in the modification process.

When trialling the blue dielectrics however, much better results were obtained. The first trial used blue dielectric D2140114_D5 in square prints as before, this time having single and double layer prints due to the thinness of the paste. Using acetone droplet exposure as the initial stability test showed that in both cases the dielectric only showed mild discolouration around the exposed area with the double layer print having less of this effect. For D50706_P3

the dielectric shape from the 6 mm electrode design was used, with 1 and 2 layers and droplet exposure to the acetone, in order to show any effects on the finer details of the electrode shape. Again, especially when the print had been dried at a higher temperature, this dielectric also showed only minor discolouration, with the detailed shape still being present. Therefore in order to ascertain exactly which dielectric to use we moved forward to printing a full 6 mm SPCE using both dielectric pastes and then exposed them to the acetone/PCl_5 mixture by submersion and via 10 µL droplets over time. The visual results of these tests are shown in Figure 4.7.

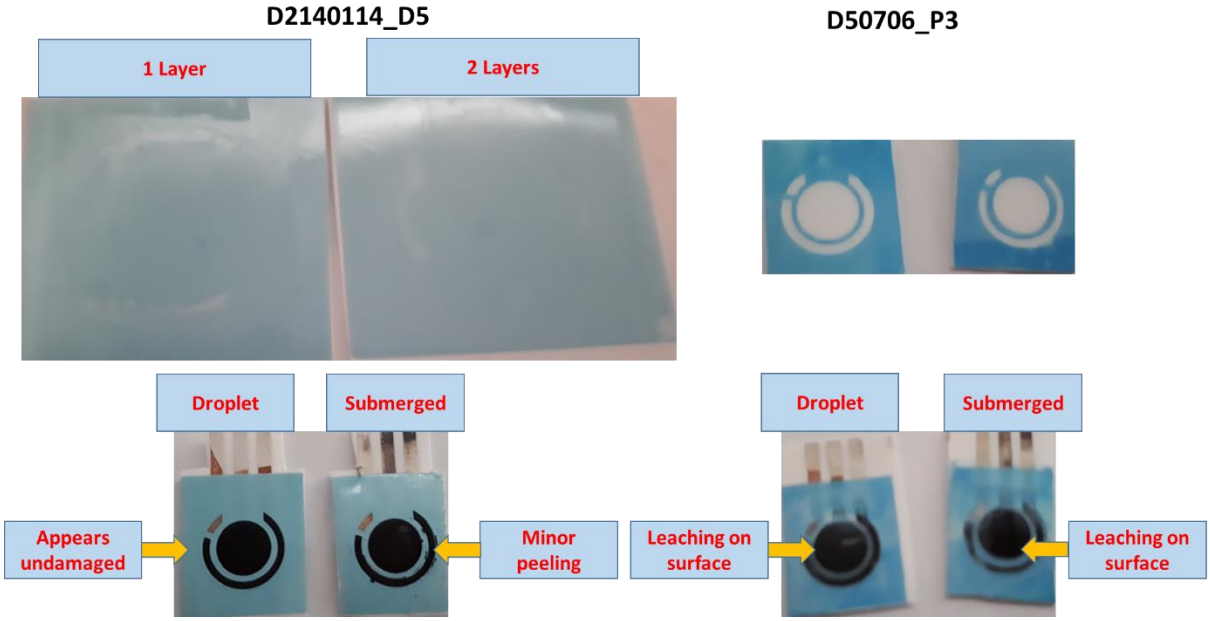

Figure 4.7 The visual inspections of each blue dielectric tested, D2140114_D5 printed as squares and D50706_P3 as the electrode outline. D2140114_D5 printed as 2 layers shows little to no damage on droplet chlorination, D50706_P3 however leaches.

By printing full electrodes using these dielectrics it became much more apparent which would be the most ideal material for the optimised electrodes. When exposed to the acetone/PCl_5 mixture, both by submersion and by droplet pipetting, the blue dielectric D50706_P3 showed the same leaching effect as the cream dielectric, covering areas of the carbon surface in a constituent of the paste which could not be easily removed. With the D2140114_D5 dielectric however, the dielectric remained reasonably intact for both exposure methods, with the droplet method showing negligible visual damage and the immersed method showing only small areas of peeling.

Finally this dielectric was then used to print a set of electrodes using the 2 mm design, (as seen in Figure 4.7) which were exposed to the acetone/PCl_5 mixture once more. These were

then tested visually and electrochemically (Figure 4.8) with both giving the expected shape. Therefore this dielectric was chosen as the most optimised material with which to print our future electrodes. The stability of this dielectric is ensured when printed with 2 layers and dried at 130 °C for 30 minutes after printing.

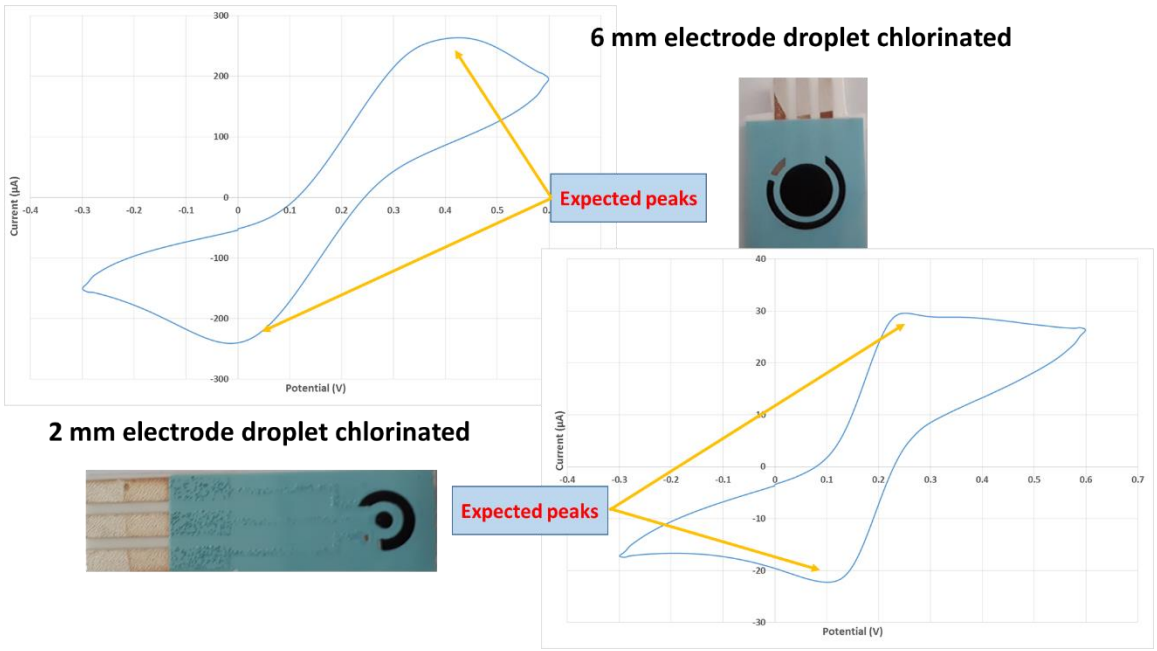

Figure 4.8 The 6 mm and 2 mm electrodes printed using blue dielectric D2140114_D5 and chlorinated via pipetted droplets. The expected oxidation and reduction peaks for the 5 mM ferri/ferrocyanide redox couple, and limited surface damage can be seen.

4.5: New design for multiple miRNA detection.

Once the ink materials had been optimised to survive the harsh chlorination conditions, it was then possible to start designing our own custom electrode. Crucially we wanted this design to allow analysis repeats on one sensor. Also due to the ability of miRNA to have multiple targets in multiple biological pathways, each miRNA species expression level is relatable to multiple diseases.[262] Therefore any potential diagnostic biosensor would require the ability to detect multiple miRNAs simultaneously. Thus we wanted a design that would also allow for this adaptation in future projects,

With the assistance of GEM we were able to design a set of screens that allowed us to print an electrode with 3 carbon working electrodes and a shared carbon counter and silver/silver chloride reference. The working electrodes all had diameters of 3 mm, thus having the same diameter and active working area to the glassy carbon electrode used throughout Chapter 2, making any data obtained with this new design easier to relate back to that obtained with the

commercially available GCE standard. Figure 4.9 shows how the electrodes appear when printed with the new design, including how each individual electrode appears when cut out to be used.

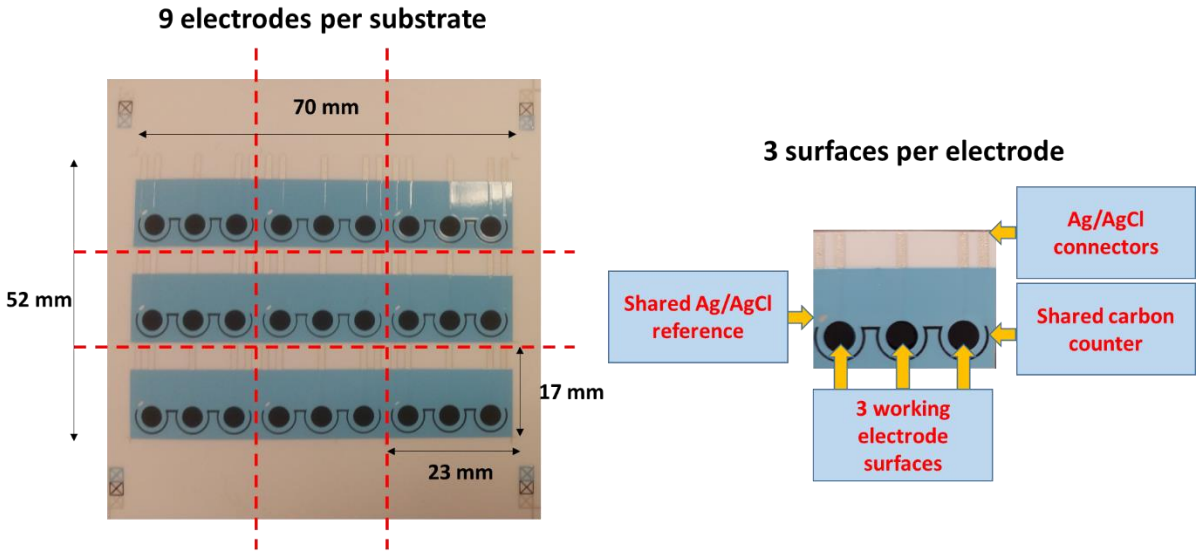

Figure 4.9 The design for the new 3 working electrode surfaces with shared counter and reference. There are 9 electrodes per substrate each with 3 surfaces for a total of 27 surfaces per substrate.

By having multiple active surfaces on these electrodes it is possible to use them in different ways. Firstly, it is possible to attach the same sequence of DNA, complementary to a single miRNA target, to each working electrode to produce a set of data in triplicate. As the same sample of miRNA is analysed by each surface, this allows for rapid determination of the reliability of the data, as the electrochemical response should be the same for each surface. If there are any large discrepancies between the surfaces, it is likely that an error has occurred in their use. However, in future projects it may also possible that by attaching a different DNA sequence to each electrode surface it would be possible to detect up to 3 different miRNAs in one sample. This would mean that it is possible to simultaneously determine up and down regulation in relation to a non-changing control species, giving the sensor greater applicability in a diagnostic sense.

As this design is a custom design and not a stock item from GEM it was necessary to develop a new connector for attaching the electrode to the potentiostat. The connector itself consists of a shortened, single row, printed circuit board (PCB) connector which has had colour coded wires soldered to the pins to indicate whether they are the location of the working (red), reference (blue) or counter (black) surfaces. Each of these wires terminates in a socket pin

and insulating shell for attachment to a crocodile clip. The electrodes are then able to be simply slid into place, making contact with the correct pin placement of the PCB connector for the respective surface. A multiplexer attachment on the potentiostat then acts as a switch to cycle between each surface during the potentiometric and EIS measurements. The completed connector and schematic of the multiplexer is shown in Figure 4.10.

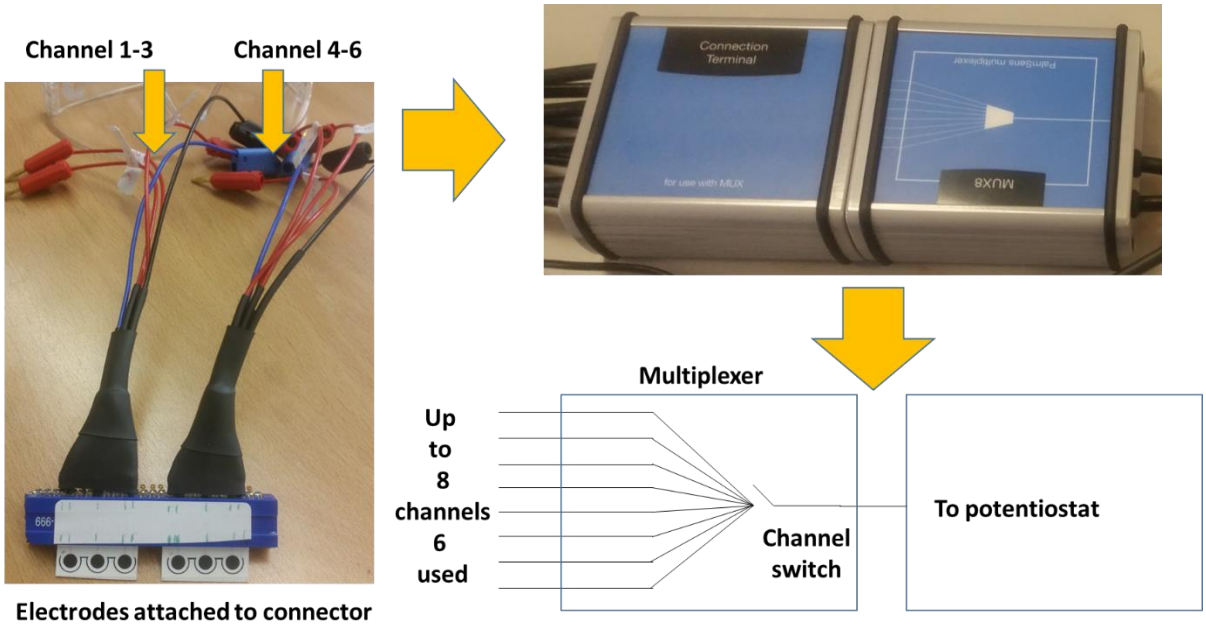

Figure 4.10 The completed PCB connector with example electrodes attached. This then attaches to the MUX 8 multiplexer which acts as an automated switch to switch between each surface or apply a single voltage to all surfaces.

4.6: Optimising the deposition procedure

Now that we have developed a new set of electrodes, with a new design and optimised materials, it was necessary to edit and optimise the modification procedure to better fit the new design. The first step to be tested and optimised for shortened reaction time is the deposition step, which, as the electrodes are now too wide to fit in the same vials that were used for the last design, can now be performed in two different fashions. In the first technique the ANSA compound can be pipetted onto each of the electrode surfaces separately, keeping the drops separate between each surface. By using this method it is possible to monitor the deposition step across each surface individually as a visual colour change occurs in the solution. The deposition itself takes place using cyclic voltammetry cycles in the same way as the GCE and previous SPCEs. This first deposition step, and the visual change across each surface, is shown in Figure 4.11.

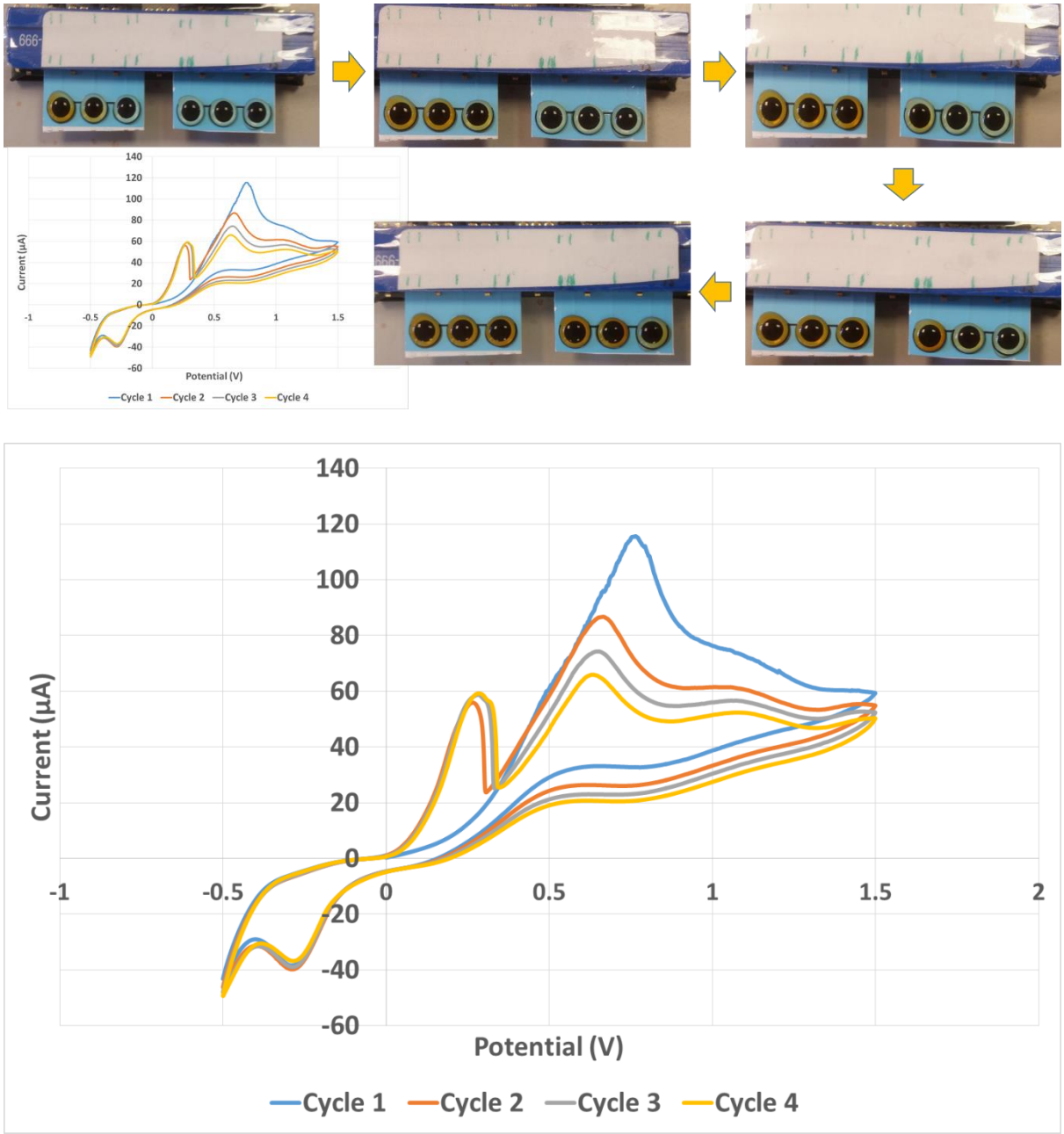

Figure 4.11 Images of the screen printed electrode surfaces as the deposition step occurs. Each surface becomes sequentially deeper in colour due to the deposition occurring. Also shown is an example after 4 cycles.

When performing these depositions a couple of important observations were made. The first is that for this first set of electrodes there is a minor shoulder peak at around 0.11 V which may pose a problem in the analysis of miRNA later if it is mistaken for a peak resulting from the miRNA presence. The second is that the main peaks of these cycles occur at around 0.6 – 0.65 V, and as these peaks reduce in magnitude as the number of cycles increase, it is at this potential that the electrodeposition is likely to take place. Also, as performing the full 8 cycles required in previous experiments would require approximately 27 minutes for each surface

(1 hour 21 for the full electrode), it was deemed important that this deposition time should be shortened.

Therefore an attempt was made to maintain the potential at 0.65 V for a period of time to perform the electrodeposition, using a single CV cycle afterwards to determine whether the deposition appeared to have taken place. Accordingly, for the next optimisation trial, the electrodes were prepared in the same fashion as above, with the ANSA solution separated over each surface, and then the voltage was held at 0.65 V for between 1 and 5 minutes before performing one CV cycle using the same ANSA solution. The result of this is shown in figure 4.12.

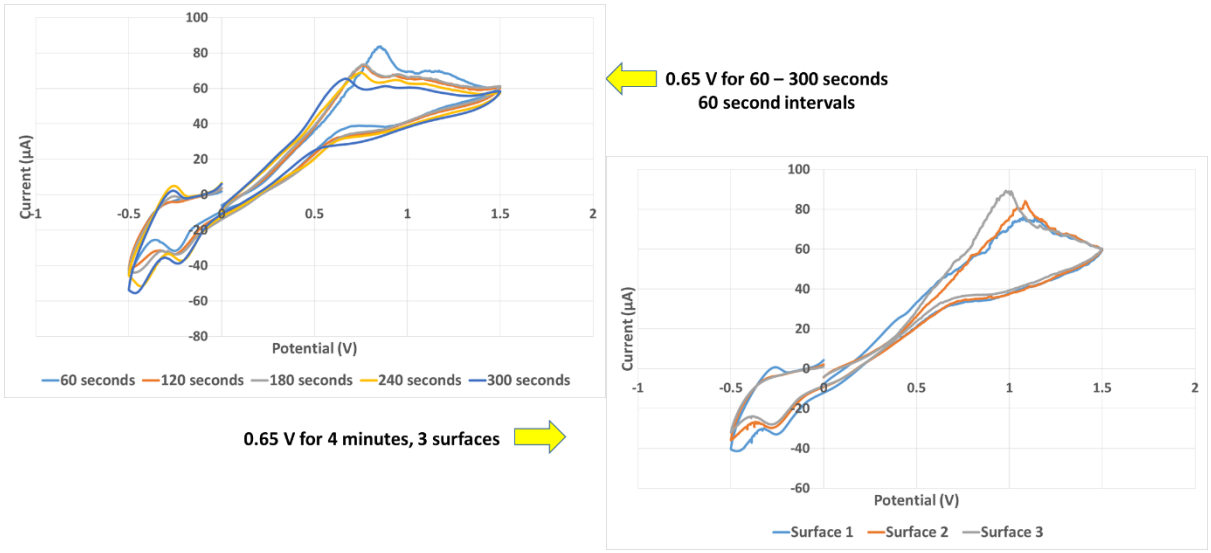

Figure 4.12 The deposition CV curves obtained when holding the electrode at 0.65 V for 60-300 seconds in 60 second intervals, and three repeats at 4 minutes when ANSA applied as droplets.

Performing the deposition in this fashion results in a single cycle voltammogram that shows peak currents at similar amplitudes as found after performing the repeated cycles. This is particularly the case after 4 minutes where the amplitude of the peak is at a level similar to that after 5 minutes and lower than the other time points. Therefore the experiment was repeated, this time holding the potential at 0.65 V for 4 minutes each time (also shown in figure 4.12). Again this shows very low peak currents, indicating that the deposition is taking place successfully, but it also does this in a reasonably repeatable fashion despite some noise in the voltammogram appearing at the higher positive potentials.

Finally, and for simplicity, the same procedure as above was repeated, this time however covering the electrode completely in the ANSA solution, with each surface sharing the one

solution rather than being separated. This was done to ensure that this would not have a detrimental effect on the deposition, as maintaining the separation across the electrode surfaces can be difficult due to the close proximity of the droplets when applied to them. Consequently if the ANSA solution can be applied across electrode surfaces at once the pipetting would be easier and therefore quicker to perform. The result of this test is shown in Figure 4.13.

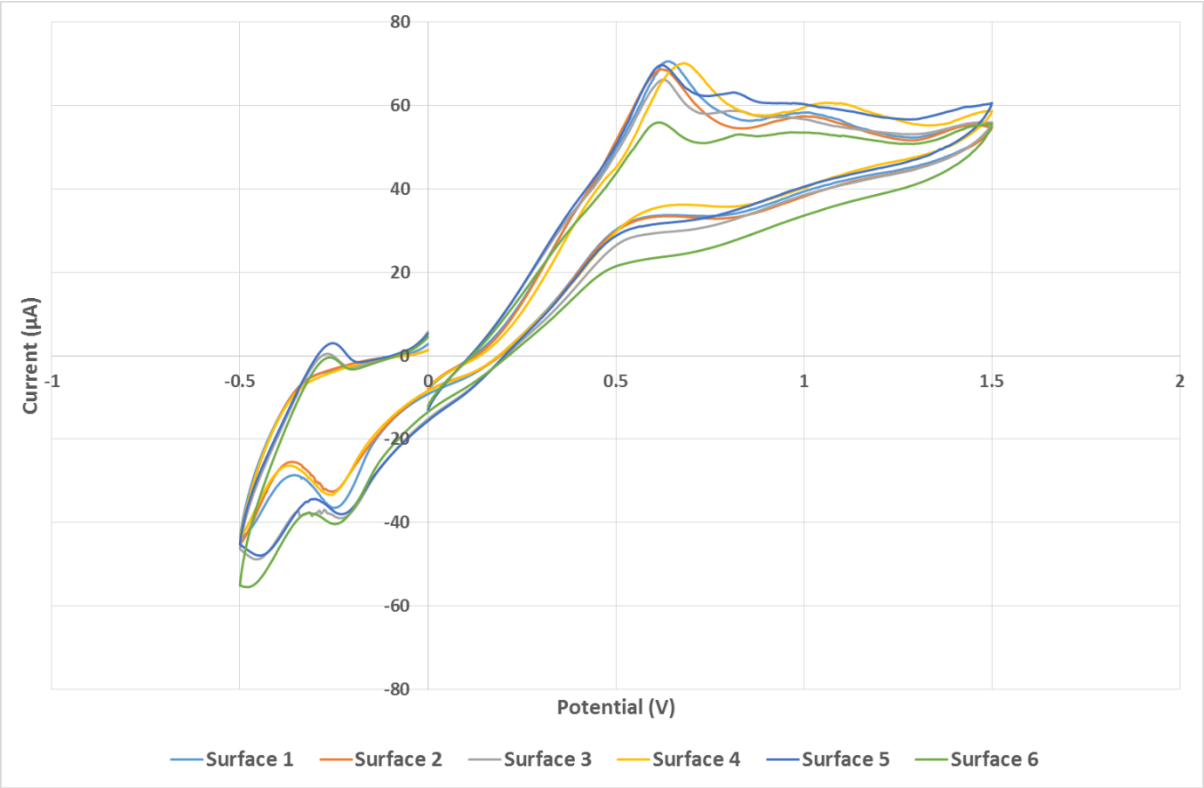

Figure 4.13 The CV curves obtained over 2 electrodes following deposition of ANSA at 0.65V for 4 minutes via total electrode coverage method.

Happily, as can be seen by the reasonably similar peak currents obtained between the CV curves shown above (with the exception of surface 6), this method does not have a detrimental effect. In fact it appears that this method results in as good, if not better, repeatability as using individual droplets. The droplet method resulted in different peak currents and gave a substantial amount of noise, whereas this is not seen when the whole electrode is covered.

4.7: Optimising the chlorination procedure

During the placement at Gwent, the inks used to produce these electrodes were optimised for stability in the acetone/PCl_5 chlorination mixture. However, up until this point they have

not been fully tested using this new design. Therefore as a final optimisation test the electrode was modified by electrodeposition of the ANSA compound, and was then either submerged in the chlorination mixture or exposed to the solution via pipetted droplets over time. Examples of CV outputs of each of these are shown in Figure 4.14, along with a picture of how the electrodes appeared after droplet chlorination.

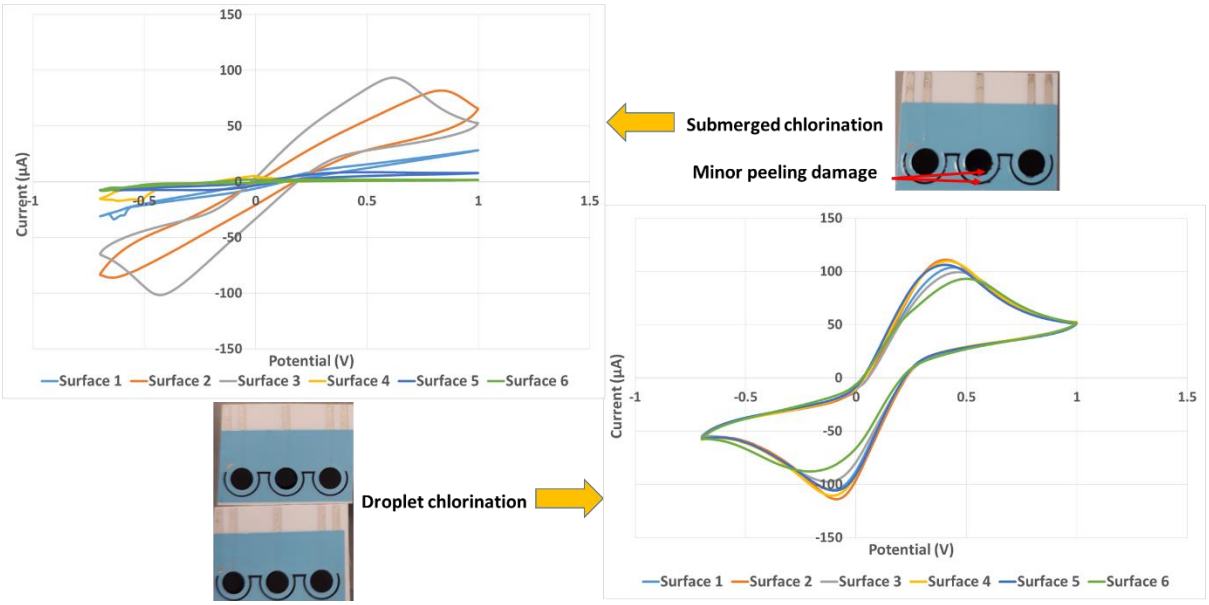

Figure 4.14 The visual and electrochemical inspections of the electrodes following the droplet and submerged chlorination procedure. For the submerged electrodes there is minor peeling of the dielectric and poor electrochemical response. Cyclic voltammograms performed using 5 mM ferri/ferrocyanide redox couple.

As can be seen from these images, the droplet chlorination is a much more reliable method for ensuring electrode stability. The electrodes also appear visually unaffected by the solution, with no cracking, peeling or discolouration, which is very important for the commercial applications of the modification procedure using these electrodes. The electrodes not being visually changed after the modification procedure would allow higher percentage of them to pass visual quality control tests if they were to be commercialised. Submerging the electrode affected both the electrochemistry, but also the same peeling around the working electrode was seen and the substrate was prone to bending. Therefore from this point the chlorination was performed using droplet exposure over time.

4.8: First sensitivity tests

Once the multi-surface electrodes had been shown to survive the deposition and chlorination steps of the modification procedure it was then possible to perform some initial sensitivity tests. These tests were performed in a similar fashion as the previous SPCEs and the initial

glassy carbon electrode tests from Chapter 2. The electrodes were modified with DNA complementary to a miR-21 target and then used to analyse solutions containing different concentrations of miR-21 in buffer between 10 nM and 10 fM. This was done by pipetting 300 µL droplets of the sample to cover all electrode surfaces, and then heating the sample in a hybridisation oven. The change in coulometry response (ΔQ) between the DNA containing electrode and the DNA/RNA hybridised electrode is then plotted against the corresponding concentration. The data is displayed in Figure 4.15 (raw data appendix 3 Table A3.1).

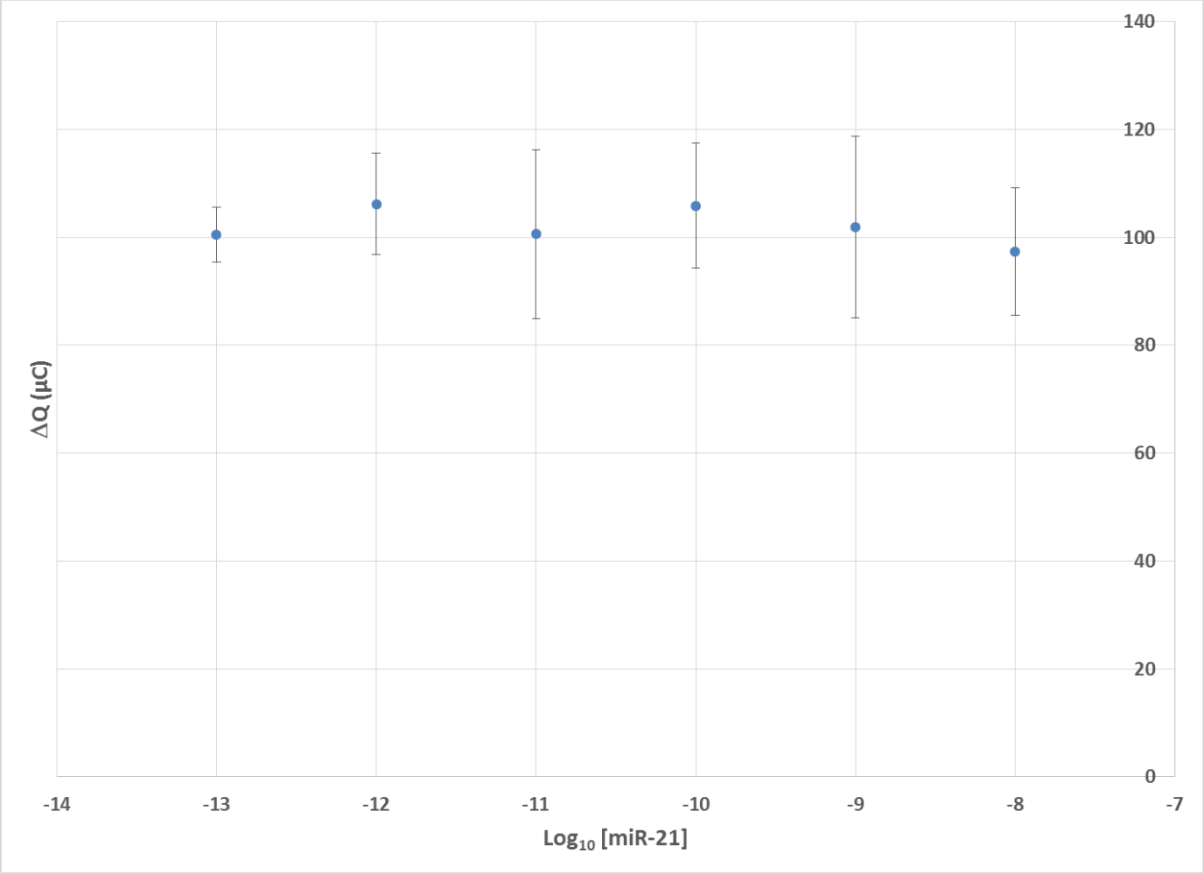

Figure 4.15 An attempt at a calibration plot for the change in coulometric response (ΔQ) vs. log_{10} [miR-21] (M) using the multiple surface SPCEs. A different concentration of miR-21 was pipetted to each surface. Performed in duplicate using 5 mM $K_3[Fe(CN)_6]/K_4[Fe(CN)_6]$ in 0.1 M KCl electrolyte at room temperature.

Unfortunately no significant change was observed throughout this concentration range, and all responses were at a magnitude similar to the highest observed during the GCE calibration test. With the GCE (Figure 2.5) and SPCE data (Figures 3.9 and 3.12), despite some variance, there was an overall positive correlation with higher concentrations of miR-21 resulting in a greater change in response, this was not the case with this data. Although this is a problem, the fact that the presence of the miRNA is resulting in a change in response led to the conclusion that the sensor is functioning correctly at the surface, the lack of any correlation

between miRNA concentration and the resulting change in coulometric response has therefore been attributed to miRNA over concentration during analysis.

Previously the electrodes had been submerged completely in a 1 mL solution of the target miRNA in a micro-centrifuge tube and heated via a thermo mixer heat block, with these electrodes however, as their dimensions do not allow for placement in a micro-centrifuge tube the solution was simply pipetted onto the surfaces directly. Hence, as the solution is spread over a larger area and heated in a hybridisation oven, it had evaporated by the time it was removed from said oven. Therefore it was inferred that the reason no change is observed using different concentrations is because as the buffer is evaporated the miRNA is becoming more concentrated, to the point of maximum response.

In order to combat this evaporation a new vessel which could be used to incubate the electrodes with the sample during hybridisation was needed. This vessel had to be inert to biological and chemical materials and have a large enough gap to hold the electrode while also keeping the exposed area of the solution to a minimum to reduce the rate of evaporation. Therefore a Teflon block was constructed which had these features and could be used with up to 6 electrodes at any one time. The schematic design of this block and the finished item are shown in Figure 4.16.

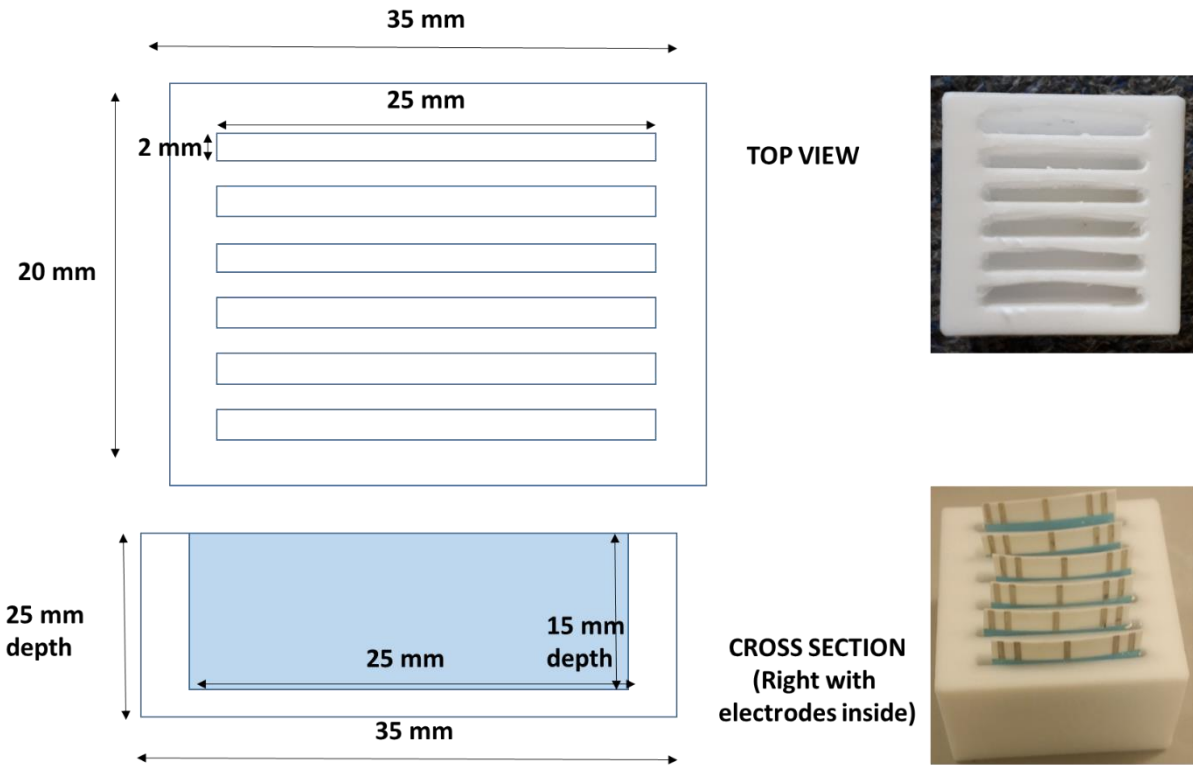

Figure 4.16 The schematic design of the Teflon block wells from the top and in cross section. Also included are photographs of the top of the Teflon block and the side view including how the electrodes fit inside.

The electrodes were placed in the Teflon block slots along with the buffer and heated in the hybridisation oven to simulate incubation with a solution of miRNA. After which the slots were inspected and it was observed that very little of the buffer had evaporated over the time period, thus it appears that the use of this block is capable of preventing the over concentration of miRNAs as desired. Therefore the sensitivity testing measurements were repeated once more, this time using the Teflon block to contain the electrodes during hybridisation with the target miRNA. The results are displayed in Figure 4.17 (raw data Appendix 3 Table A3.2).

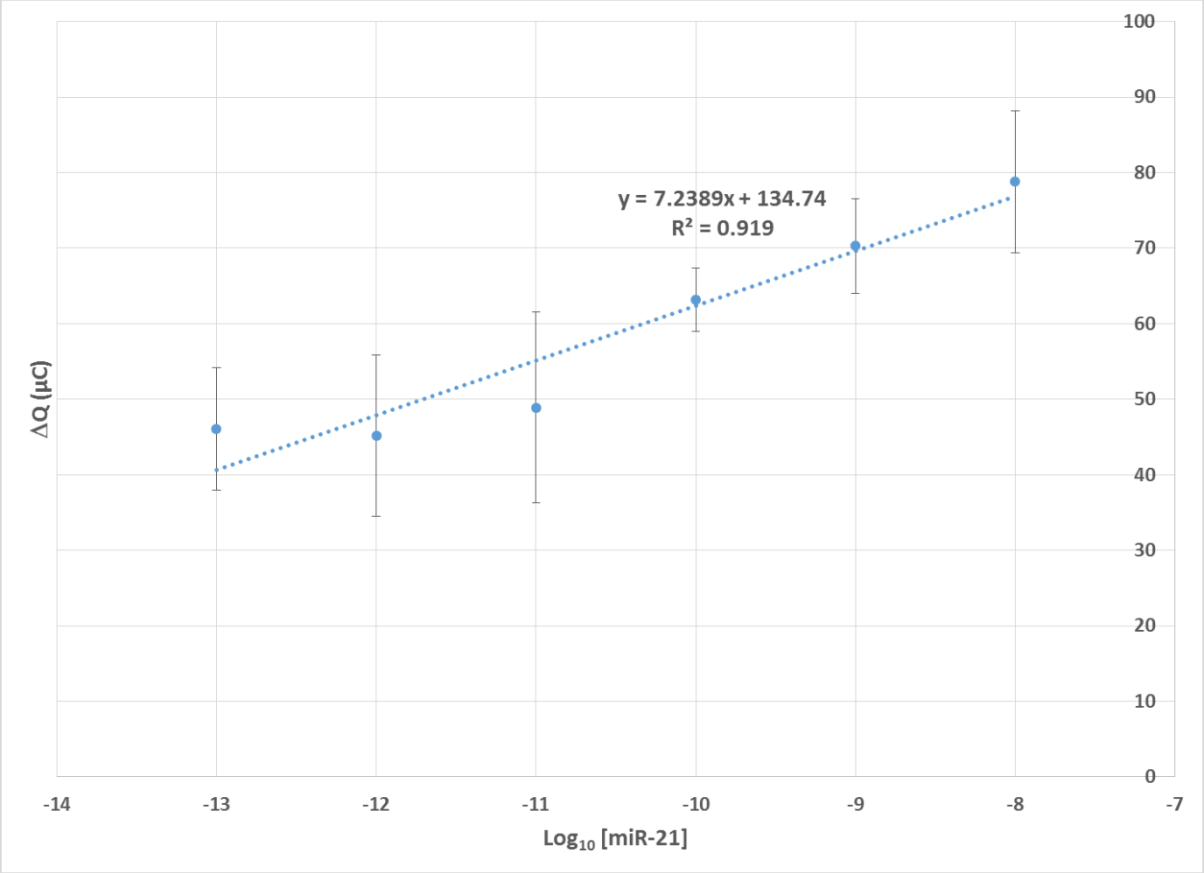

Figure 4.17 A calibration plot showing the change in coulometric response (ΔQ) vs. log_{10} [miR-21], obtained by incubation with samples in Teflon block slots. Each point is collected in triplicate using the three surfaces on each sensor. Performed using 5 mM $K_3[Fe(CN)_6]/K_4[Fe(CN)_6]$ in 0.1 M KCl electrolyte at room temperature.

Clearly the Teflon block is having a positive effect on the miR-21 concentration vs. charge change relationship readout of the biosensor, as there is now a correlation between the logged miR-21 concentrations and the change in coulometric response between the DNA containing electrode and the hybridised electrode. However the gradient of this relationship is very shallow and the error is still problematic, thus making clear distinctions between each concentration is difficult. The average of the data points collected for the final concentration breaks this correlation and loses linearity as well and therefore could be unreliable at this low concentration. These data are very recent however and before it can be used as a quantitative calibration plot it should be repeated multiple times to determine the reliability, with further optimisation being performed if the results prove to be unrepeatable. However, for the purposes of this research we moved on to determining whether a distinct difference can be obtained between patient and control urine samples.

4.9: Comparison between healthy control urine and patient samples

As a final investigation of these electrode prototypes a comparative analysis between both healthy control urine and patient derived urine samples was required. If the sensors are to be adapted for future use in a diagnostic point of care environment then it is important that a significant difference can be observed between a healthy individual and an individual with DKN.

Thus in order to test the sensors, a set of three miRNA targets were chosen, two of which have been shown by the host laboratory to show a difference in expression between a control group and nephropathy patients via RT-qPCR experiments. MiRNAs 191 and 126 have been investigated in patient samples and seen to vary in expression levels between controls and patients, miR-192 however has not yet been investigated but was also suggested as a potential miRNA sequence of interest for us to investigate electrochemically. A set of sensors were therefore modified with antisense DNA complementary to each miRNA of interest, each electrode detecting a different target in triplicate. Two control and two patient urine samples were then treated with proteinase K and spin filtration prior to being analysed by these electrochemical sensors. The resulting change in coulometric response, between the DNA containing electrodes and their subsequent hybrids, obtained for each sample and for each miRNA target is shown in Figure 4.18 (raw data Appendix 3 Table A3.3).

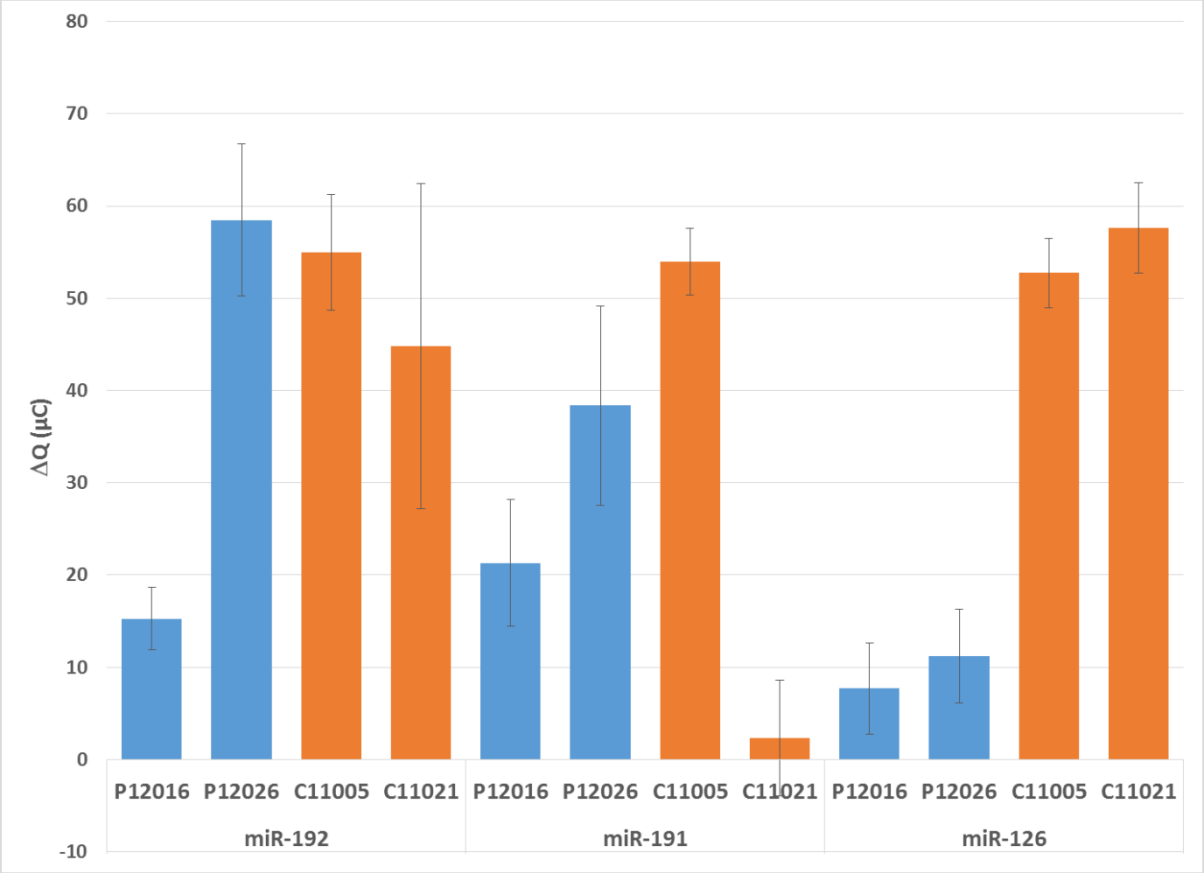

Figure 4.18 The change in coulometric response (ΔQ) obtained for each miRNA target using 2 patient urine samples (blue) and 2 healthy control urine samples (orange) for 3 miRNA targets. A lower response indicates a lower concentration. Controls miR-191 and patients miR-126 performed in duplicate all others in triplicate, using 5 mM $K_3[Fe(CN)_6]/K_4[Fe(CN)_6]$ in 0.1 M KCl electrolyte at room temperature.

This data, although only performed on a small number of samples, shows that the sensors are indeed detecting a change between the healthy samples and the patient samples. For miR-192 patient sample P12026 is of a similar response as control samples C11005 and C11021, with a possible slight up regulation, however with P12016 giving much smaller a response than the other patient sample, indicating a significant down regulation from patient to control. This significant difference between the two patient measurements appears to indicate the likely presence of an outlier, which, if P12026 is the outlier and after more repeats becomes more like P12016 would indicate that miR-192 is downregulated in patients. More samples in the future would therefore be required to determine whether miR-192 is of a similar concentration in both controls and patients or if there is indeed a down regulation.

For miR-191, both patient samples give a smaller response than control sample C11005, thus indicating a down regulation from controls to patients. However the control sample C11021 response for miR-191 is much lower than for the other 2 miRNAs and the other control,

therefore it is possible this is also an outlier. Therefore it is also difficult to draw an accurate conclusion for this miRNA target as well, and analysing more samples in the future would help with this.

Finally however, the data for miR-126 does appear to show an electrochemical response significantly lower than both controls, indicating a potential down regulation from control to patient, although a larger sample size is needed to confirm this. All of these combined differences in response indicate the potential of the sensor analysing patient and control samples, and possibly, as differences can be seen between each sample and for each miRNA species, differentiating between them. Nevertheless there is a long way to go before the sensor can be optimised for diagnostic use, and many more samples would be required to make the data statistically relevant. This is discussed further in Chapter 5.

4.10: AFM imaging of new carbon ink

As the carbon ink has been changed for this new electrode design it was necessary to perform the AFM measurements to analyse the topographical features of the new ink during the different modification steps. These AFM images were therefore performed again on an unmodified electrode consisting of this carbon ink, an ANSA modified electrode, an electrode chlorinated via PCl_5 in acetone and finally an electrode that has been used to analyse a urine sample. The first of these images, the unmodified electrode surface, is shown in Figure 4.19.

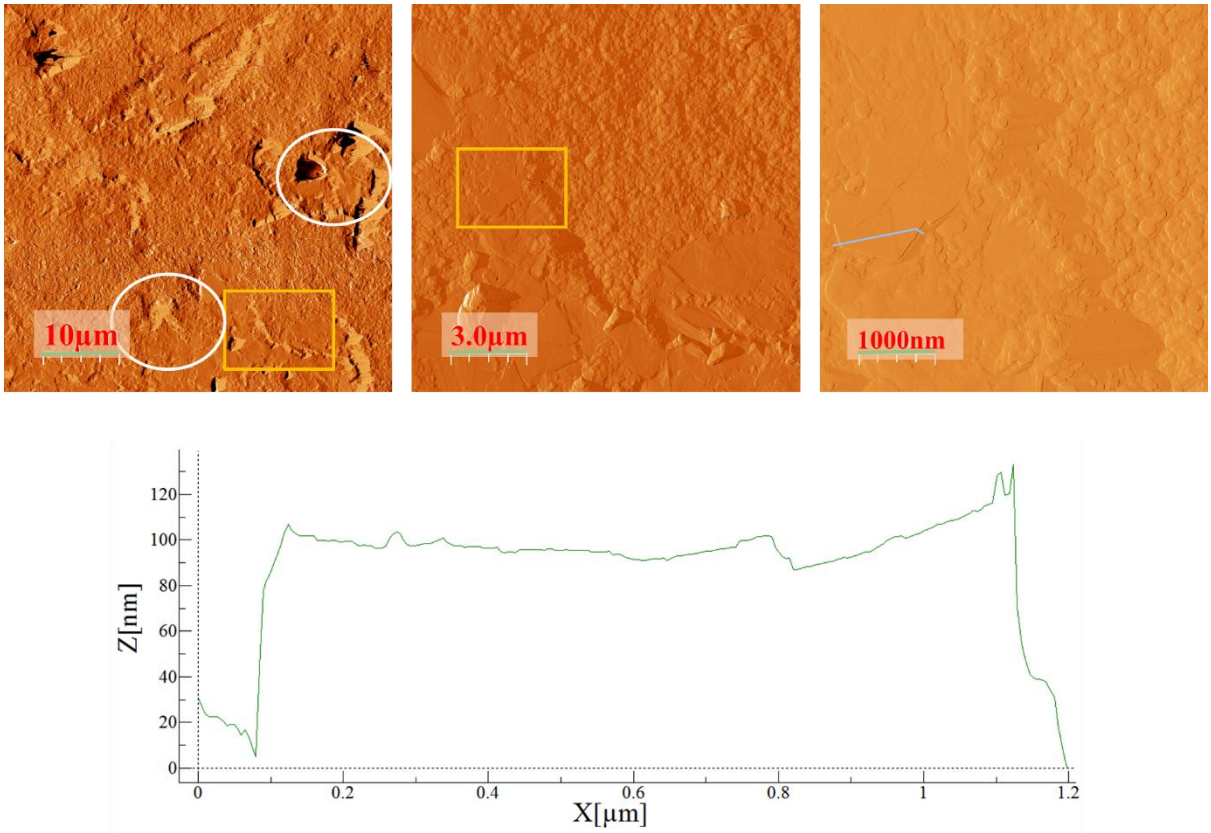

Figure 4.19 AFM image of the new carbon ink that is unmodified. The yellow boxes are the zoom areas and the round circles are areas of further interest. Also given is the surface length and height of one of the larger flat artefacts.

These images show that the surface is indeed different to the original carbon surface. The areas that are flat are not as triangular in nature and are not layered, they are in general around 100 nm high with the surrounding sections being around 20 nm high. This could indicate that the cross linking of the carbon ink is forming a more monolayer like graphitic surface. The presence of a binding polymer could be responsible for the rounded artefacts. The carbon ink used in Chapter 3 is much more triangular and layered than seen here, as would be expected from a graphitic ink. This ink does have areas that show this triangular shape, as seen in the areas in the white circles, and when roughness analysis is performed at the same scale for the previous ink and this ink it can be seen that not only is this ink smoother with an average roughness of 0.31 µm vs. 0.34 µm but the average height of the surface artefacts is also smaller at 0.99 µm compared to 1.26 µm. Therefore this ink is displaying a thinner average coverage compared to the previous ink. This data is shown in Figure 4.20.

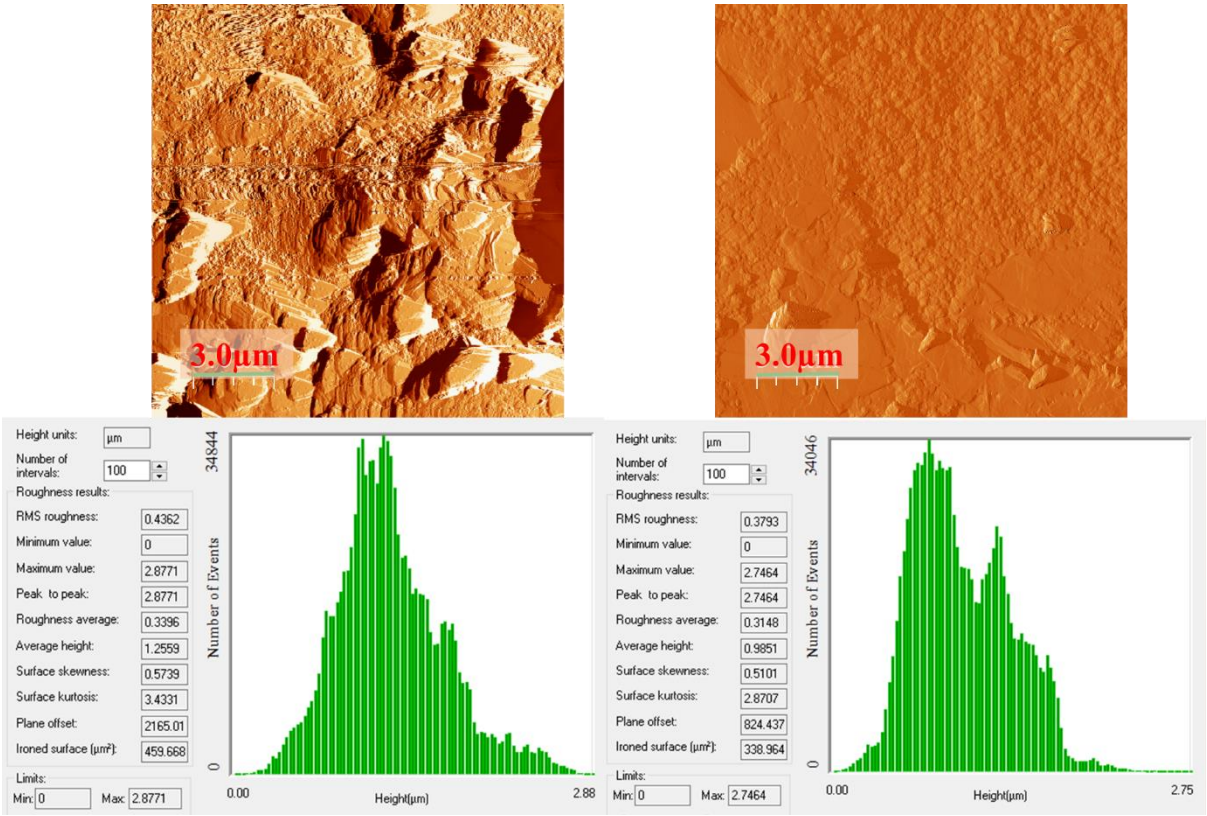

Figure 4.20 The surface roughness data and average height data obtained for the previous ink from Chapter 3 (left) and the new ink used herein (right).

However the remaining AFM images may help to elucidate whether the surface behaves the same throughout the rest of the modification steps as the previous ink did. Therefore a second surface was imaged, this time being modified electrochemically with the ANSA compound. These images are shown in Figure 4.21.

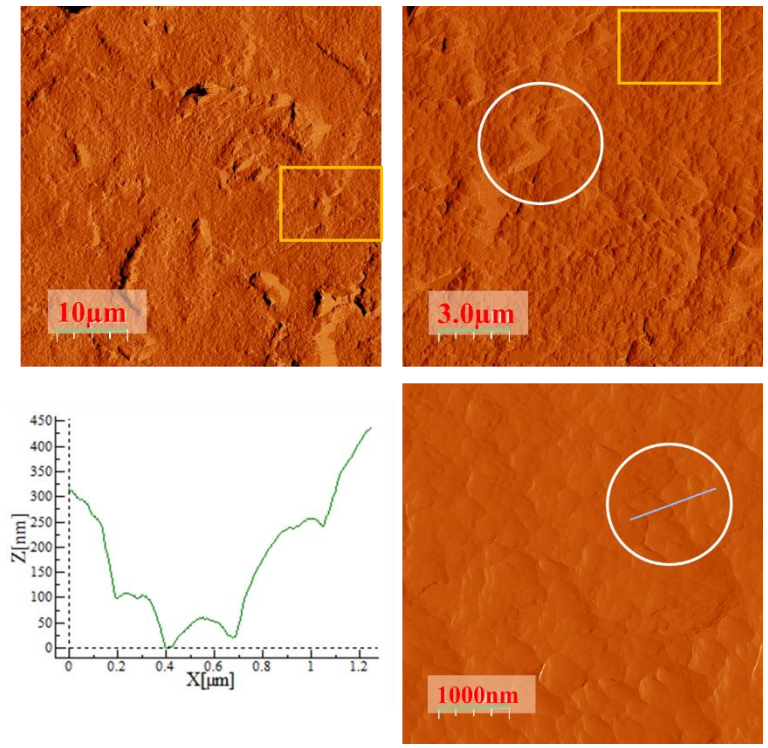

Figure 4.21 The AFM images of the electrode following deposition of the ANSA with the width and height of some of the artefacts indicated

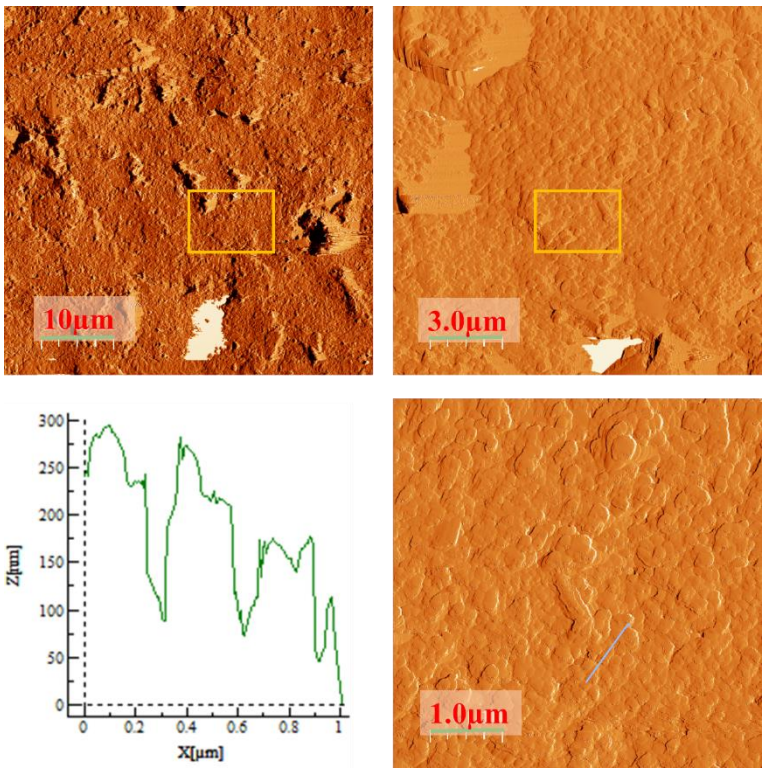

Figure 4.22The AFM images of the electrode following chlorination in a PCl_5/acetone solution including the surface profile of some of the artefacts indicated.

.

These images show that the flattened areas seen in Figure 4.19 are no longer as prevalent, instead there are many more smooth rounded artefacts as shown in the white circles. These rounded artefacts were also seen in the images from Chapter 3, thus indicating that this carbon ink is behaving in much the same way at this stage. The surface itself however has a roughness of 0.4 μm and average height of 1.15 μm indicating the presence of a new deposited layer, this increase also occurred with the previous ink at this stage (Figure 3.14). It is also possible to see slightly more triangular shapes across this surface, although not as well defined as in the previous ink, and much smaller in size, these triangular shapes are indicative of the graphitic nature of this cross linked ink as well. From the topographical information it can be seen that the surface changes in height smoothly from around 50 nm to 400 nm with each artefact being around 0.3 μm wide. This smooth change in height would indicate the deposition of the ANSA onto crevices of differing heights, the shape of the profile curve also indicates that the deposition is giving rounded artefacts.

The ink in these electrodes has been selected in order to survive treatment with PCl_5 in acetone, thus performing an AFM of the surface following this modification was also possible and is shown in Figure 4.22.

Unlike the previous carbon ink, which was unable to generate an ideal image of the electrode following PCl_5/acetone treatment, and where it did showing high levels of swelling, this cross-linked ink was able to be successfully imaged and shows only very small areas of poor definition. As far as the appearance of the image goes, the surface shows less defined triangular shapes as before, in fact the majority of the surface consists of sharper rounded artefacts again with a width of approximately 0.3 μm, in this case the stepwise changes in surface height 300 nm to 50 nm are much sharper, the exact variance at the peak height also being sharper.

The sharpness of these artefacts display a change from the smoothness of the ANSA modified surface, indicating that the chlorination procedure has resulted in a change of the surface as would be expected by the substitution of the sulfonic acid for a sulfonyl chloride functional group. The appearance of these sharp edged artefacts at this stage could also indicate the partial removal of the top carbon surface, revealing the detail of the graphitic plates below. However from the roughness analysis the roughness is given as 0.46 μm with an average height of 1.79 μm. Therefore at this stage the height average height of the surface is

increasing which would not be expected if a layer of the carbon ink was being removed, therefore the sharpness is likely due to the functional group change.

However, it should be noted that when a hexane/PCl_5 mixture was used with the previous ink (Figure 3.15) there was actually a slight reduction in average height and roughness over the deposited electrode. The previous ink, when treated with an acetone/PCl_5 mixture, resulted in a vast reduction in both roughness and height, assumed to be due to surface damage and/or swelling, this is not seen here.

Finally the electrode was modified with DNA complementary for miR-21 and used to analyse a urine sample, the result being shown in Figure 4.23.

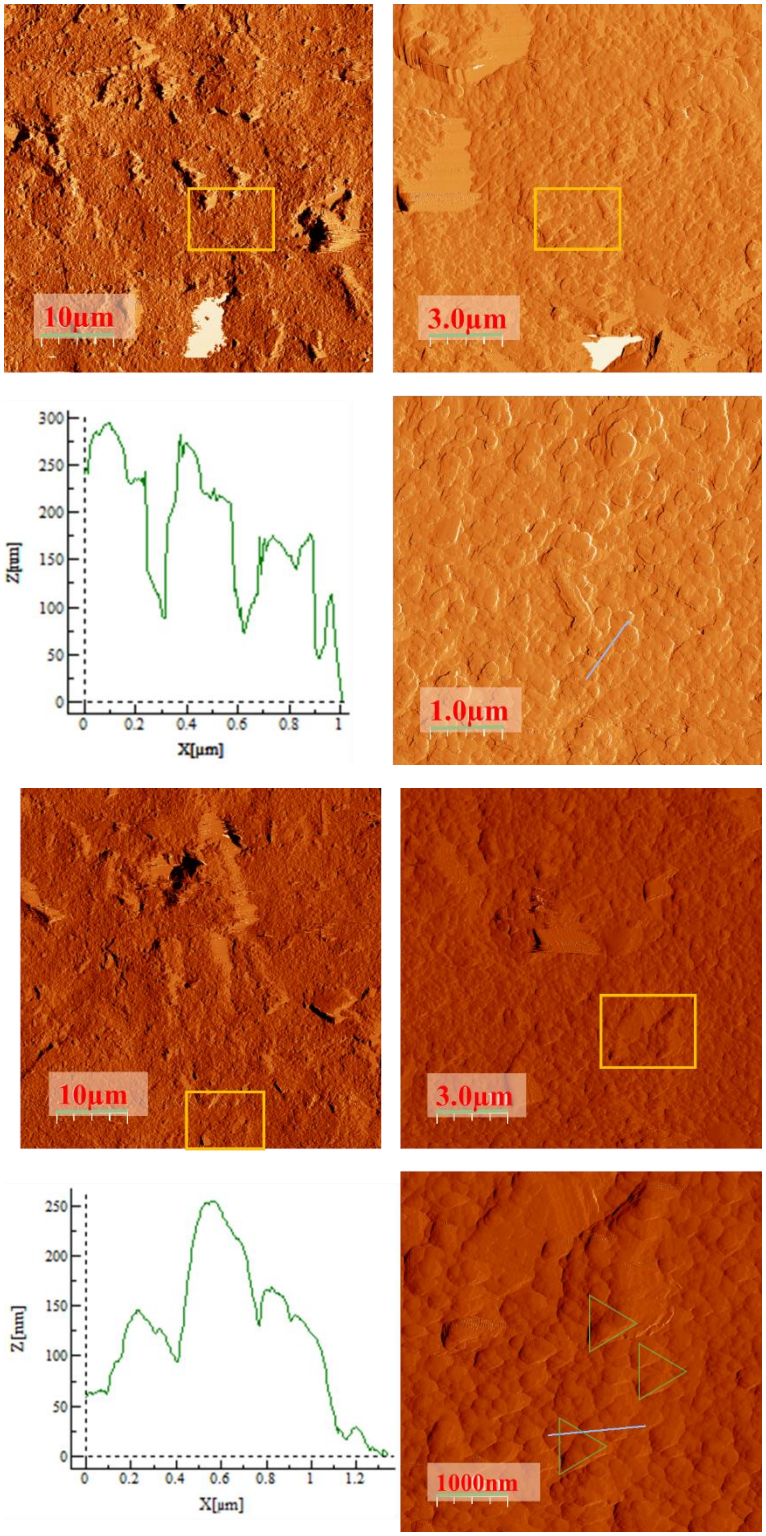

Figure 4.23 The AFM image of the electrode following hybridisation in a urine sample and a surface profile showing the height and width of the artefacts. The possible triangular graphite layers are also shown and the previous chlorinated surface is given in the top images for comparison.

These final images show that the rounded artefacts are still present but are once again smoother in nature, also they appear to be forming across small triangular shapes (shown by the green dotted lines). These artefacts are approximately 0.3 µm in width as before, and thus

bigger than the 80-90 nm seen at this stage in the previous ink. However the change in height from approximately 20 nm to 250 nm is again much smoother indicating a change in the surface from that of the sulfonyl chloride. In fact, when the roughness analysis is performed the average roughness is 0.29 µm, with an average height of 1.18 µm. This, along with the similar width of the artefacts as seen in previous stages indicate that although the surface has changed as a result of incubation in urine it is not likely due to adsorption of large lipid or protein molecules (see Figure 3.19 for increased artefact length over these same stages). Once again suggesting that the electrochemical response obtained is due to the presence of miRNA not interferent macromolecules. The general appearance is also close to the miR-21 and urine analyses seen in Figures 3.18 and 3.20 respectively.

4.11: Conclusion

Throughout this chapter the optimisation of SPCE inks and subsequent design and prototyping of a new multi-surfaced SPCE has been discussed. This includes work performed at GEM as part of an industrial placement, testing carbon, silver/silver chloride and dielectric inks for stability in a solution of PCl_5 in acetone and then using these inks to produce the electrodes using the new 3 surface design. Once the ideal inks had been found the electrochemical deposition step of the modification procedure was shortened to reduce the time required to produce each sensor, and then the electrodes were used to generate a calibration plot.

The first of these showed that no relationship between concentration and electrochemical response was obtained, which was deemed to be a result of the buffered miRNA solution evaporating when heated, resulting in a new Teflon block being produced to prevent the reduction of buffer volume during heating. Using this new block a new coulometry based calibration plot was obtained showing that there is indeed a negative correlation between miR-21 concentration and the resulting electrochemical response. This calibration plot could be repeated in future work to ensure its reproducibility and reliability.

The electrodes were then used to analyse two patient and two control samples for miRNAs 192, 191 and 126 in order to determine if the probe could detect a difference between the expression levels of these miRNAs depending on the health of the donor. Of these, 192 and 191 were inconclusive, however 126 showed a down regulated expression level in the patient sample compared to the control. Despite this, the small sample size used so far cannot be

used as validation of the sensor and the use of a larger cohort will help elucidate these relationships.

Finally AFM images were scanned of the new ink when unmodified, modified with ANSA, chlorinated with PCl_5 in acetone and after analysis of a urine sample. These images showed distinct differences compared to the previous ink used in Chapter 3, and although the deposition stage showed similar surface change behaviour, and that in this case the chlorination treatment resulted in a readily analysable surface, it was more difficult to determine any surface artefact changes as a result of the hybridisation procedure from the rest of the surface artefacts after urine analysis.

Despite the simple DNA probe based hybridisation based detection method used by us being similar to that employed by Cardoso *et al*., the sensitivity observed throughout the screen printed electrode chapters 3 and 4, was far removed from the aM sensitivities observed by Cardoso for gold screen printed electrodes.[185] However our method does make potential commercialisation and patenting easier to achieve due to the modification technique employed. We have also explored the quantification of miRNA targets from urine in order to discriminate between healthy and diseased samples. At this time, our technique therefore shows greater promise over Cardosos' methodology as a potential commercial biosensor following further optimisation. Our method is also a modification procedure that does not require the addition of potentially expensive gold nanoparticles or caliper proteins as has been employed by Labib *et al*.[184]

Therefore the work done in this chapter forms a basis to show the potential of the sample, and provides a key starting point for any future work performed in the project, the possibilities of which is described in Chapter 5.

Chapter 5: Epilogue

Chapter 5: Epilogue

5.1: Appraisal and discussion

Throughout the last 4 chapters of this research we have described a method to modify a series of glassy carbon and screen printed carbon electrodes for use in microRNA detection. Starting with a research standard glassy carbon electrode we were able to chemically manipulate the surface to contain a DNA strand complementary to a miR-21 target, and thus detect synthetic miR-21 in a buffered solution to a concentration of 20 fM. This same method was then used to detect a miR-16 target as well as determining the specificity using mismatched miRNA sequences before finally being applied to the detection of miR-21 in a set of 5 urine samples. The calculated concentration of miR-21 in these urine samples showed a similar expression level between each sample as was indicated by RT-qPCR analysis, however the absolute concentration appeared higher for the electrochemical analysis than the PCR analysis. A set of controls were therefore performed to ensure the response obtained was due to the miR-21 concentration of the urine and not due to interferents. This data was then published in Sensors and Actuators B: Chemical (Appendix 4).

In the subsequent results Chapters, 3 and 4, the modification method was adapted for use in disposable screen printed carbon electrodes, indicating their future potential as diagnostic products. Initially the screen printed electrodes had a single active surface and were not chemically stable enough to survive the acetone/PCl_5 treatment, thus the chlorination solvent was modified to use a hexane solvent and an external reference and counter was used in place of those on the electrodes themselves. This allowed for the production of calibration plots for a set of 2 mm and 3 mm electrode designs. In Chapter 4 a new set of inks were investigated for their solvent stability in order to find a combination which would allow the use of the starting PCl_5/acetone solution, after which they were used to produce a set of electrodes containing 3 active surfaces potentially allowing the detection of multiple miRs in one sample. In this case the electrodes were used to individually analyse 2 patient and 2 control samples for one of 3 chosen miRNA sequences by using each electrode to analyse one sample in triplicate. The data obtained through this analysis indicated a possible down regulation of miR-126 in the patient samples compared to the controls, with the other miRNA

species being so far inconclusive, however the small sample size means this has not been validated. Thus this chapter forms the basis of this appraisal and acts as a key foundation for the discussion of future work.

Despite the data given throughout this investigation showing great promise, there are areas that have been problematic and may require further development and/or repeat experiments before the data can be subject to further publication, and the sensors applicable for diagnostic use. The first example of a potential problem area is seen in the screen printed data in Chapter 3, the calibration curves obtained in this chapter show much greater variance than those obtained for the glassy carbon electrode which, in turn, made it difficult to obtain reliable data and on a number of occasions these electrodes stopped functioning correctly or resulted in outliers. This was particularly true following the hybridisation procedure where the use of resin was difficult to reproduce each time as the resin was applied manually using an applicator brush. Also, for the 3 mm single electrode design, the dielectric did not entirely surround the working surface, therefore the absolute surface area available may vary from one printed set of electrodes to the next, this may account for some of the variability using this design. These problems largely guided the direction of the research for Chapter 4.

In Chapter 4 we described how the screen printing materials were investigated for better solvent resistance, and then these materials were used to produce electrodes which were then used to analyse different concentrations of miR-21 solution in buffer. Initially meaningful data proved difficult to obtain as the first results showed no relationship between the change in coulometric response with varying miR-21 concentrations, however when a Teflon block was used to minimise the evaporation of the buffer a new set of data did show a negative correlation. These results did show high variability however, and the gradient of the correlation was very shallow which made it difficult to distinguish between each concentration by its electrochemical response. This data is very preliminary however, therefore it is clear that this data will require an extra set of carefully controlled and analysed repeats to ensure its reliability, further optimisation will then be needed to remove variability and maximise the correlation before it can be used to accurately quantify urinary miRNA concentrations. With this in mind a set of urine analyses was also performed to determine if there is a change in the expression of miRs 192, 191 and/or 126 when a healthy control sample is compared to that of a DKN patient, using 2 samples of each type. From this data a

clear down regulation was observed for the patient samples compared to the healthy control samples, however for the analysis of 192 and 191 the data proved inconclusive as at least one of the results prevented the observation of a specific pattern. In order to get a better distinction between healthy samples and patient samples a larger sample size would be required and would be the first experiments performed if more time was available. In order to fully display the potential of the sensors as diagnostic tools more work would also be required on detecting multiple miRNAs on one electrode, each of the 3 working surfaces detecting a different sequence, which has not yet been investigated due to time constraints.

5.2: Future work

This project has a great deal of potential for future avenues of research to further enhance the applicability of the sensors towards use as a diagnostic tool. These avenues revolve around making the modification procedure more reliable i.e. no longer having some electrodes producing outliers or unreadable response, as well as making the sensor patent protectable, increasing the sensitivity of the sensors and better demonstrating their ability to distinguish between healthy controls and patients when used to analyse urine samples. Should the project be taken forward, the following suggestions may prove useful in the development of the sensors.

The first, and possibly most important suggestion, is to perform more repeats of the calibration experiments to get more reliable data on the relationship between the electrochemical response and the miR-21 concentration. Once the repeatability of the previously obtained data has been established, it may be necessary to further manipulate and optimise the technique to ensure that the variability between each sensor is reduced and the data obtained becomes more reliable. Once this has been done obtaining a better calibration plot will be possible and we will be able to more accurately determine the absolute concentration of miRNA in the control and patient urine samples. For even greater accuracy, producing a calibration plot for each miRNA of interest may also be of use. After obtaining these curves it will then be important to increase the sample size of the patient and control samples to get a better indication of how the expression of the chosen miRNA species varies between healthy individuals and DKN patients. The future success of the sensor as a potential diagnostic tool would rely on a distinct expression level differences between the patient and controls being measurable in the urine through other, more biologically standard, analytical

means such as RT-qPCR. These differences would also have to be statistically different so that any error rate does not deter from the result and will not result in a false positive/negative result, the use of ROC (receiver operating characteristic) curve, which in short illustrates the true positive and false positive rates according to a chosen threshold, would help to ensure this. If there is we would need to determine if it can also be detected electrochemically. Once this difference has been confirmed, analysing a greater sample size will be of high importance.

After demonstrating the potential of the sensor using a larger patient/control sample size it will then be important to improve the novelty of the modification procedure to make it more easily patent protectable. In the process of doing this, it may even be possible to further optimise the technique to be sensitive to a lower concentration and/or decreasing the number of steps required to produce the sensor, thus removing the problematic chlorination step and speeding up the modification. One possible way of doing this would be to substitute the ANSA compound for carboxylic acid based analogues such as those shown in Figure 5.1.

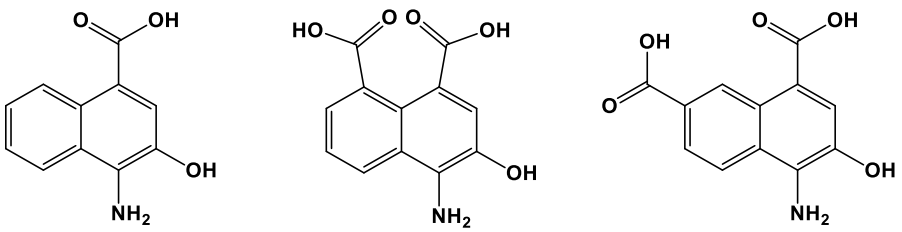

Figure 5.1 Two potential carboxylic acid based analogues of the ANSA compound.

Using a carboxylic acid based derivative may allow for the avoidance of the chlorination step as, despite the carboxylic acid simply being deprotonated and resulting in the formation of the ammonium salt, by heating the reaction to drive off water production (>100 °C) or using a water soluble coupling reagent such as EDC (1-ethyl-3-(3-dimethylaminopropyl)carbodiimide) it may be possible to push the reaction forward without needing to produce the acyl chloride.[263] If this does prove possible, using the dual carboxylic acid containing analogue could strengthen the bonding of the DNA to the sensor by producing a napthalimide derivative (via middle structure, a similar functional group transformation is performed by Ringk *et al.*),[264] or alternatively could allow the attachment of 2 DNA strands per monomer (via right structure), which in turn could increase the sensitivity of the resulting sensor.

Another suggestion to increase the sensitivity of the sensor would be to use PNA or LNA based antisense strands in place of the DNA strands used previously. As discussed in Chapter 1, PNA and LNA have the ability to form more stable duplexes with RNA than DNA does, due to the decreased electrostatic repulsion of PNA and the restricted degrees of conformational freedom for LNA.[126] Using either of these could result in much greater binding affinity with the target miRs which could result in both greater sensitivity and greater selectivity than previously obtained.

As a final potential modification to the sensor, it may be worth looking into the development of a bifunctional probe, as in a sensor that works by giving both an electrochemical reading and also a second analysable readout such as a fluorescence signal. If it was feasible to develop a sensor which could give two different forms of analytical responses, which when used together would reinforce the conclusions made from them individually, it would almost certainly help to increase the potential of the biosensor being applied as a diagnostic tool. Such an approach has been shown to be possible for the detection of circulating tumour cells so may be possible for oligonucleotide based detection also.[265] Utilising the carboxylic acid ANSA derivatives described previously will also add in their described advantages. One example of how a dual mode probe may work is given in Figure 5.2.

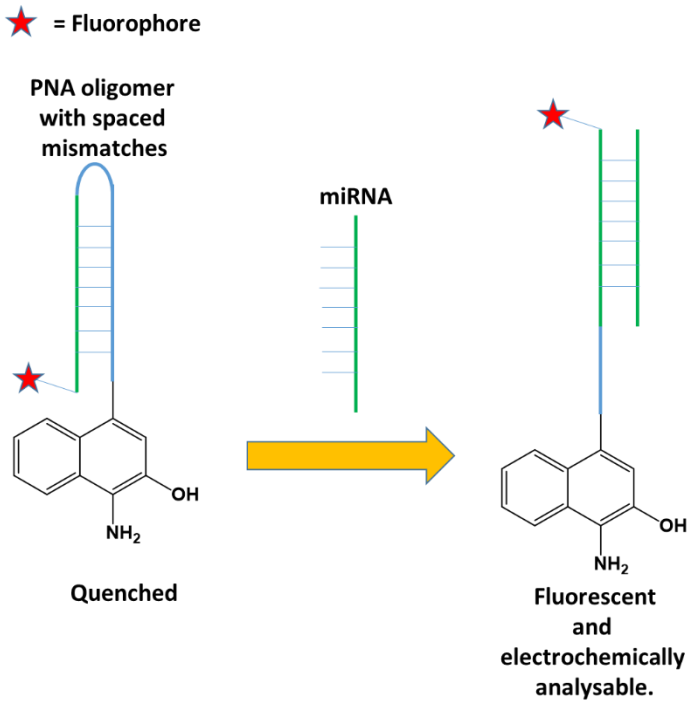

Figure 5.2 A diagram of how a potential bifunctional probe could function.

Although not shown in the above diagram, careful design of the fluorophore could result in a fluorophore that is both fluorescent and can act as a redox reporter, thus reducing the number of chemicals required to perform the analyses.

Furthermore, once the modification procedure itself has been adapted, it may be useful to test the technique on more biological matrices such as blood or synovial fluid. These additional analyses would validate the scope of the biosensor for detecting miRNA in multiple biological matrices, and potentially allowing the detection of miRNA sequences with expression levels related to more diseases than just DKN. Then, once the biosensor shows promise in multiple diagnoses, the use of automated fluidics to handle the urine treatments and electrochemical reagents could result in a potential product that reduces the exposure of the user to any chemicals or biological matrices and ensures that each reading is performed in a perfectly repeatable manner. This would further enhance the sensors potential for application in clinical based trials.

These suggestions barely scratch the surface of the potential of this project, and we predict that many more ideas will present themselves if the project is carried forward.

Chapter 6: Materials and Methods

Chapter 6: Materials and methods

The experimental procedures used throughout this project is described in the following section. For simplicity the experimental procedures are ordered in order of where they appear throughout the previous chapters. The DNA probe strands used throughout were supplied by Sigma-Aldrich and the synthetic miRNA strands by IDT, the RT-qPCR materials were supplied by Qiagen®, and the PNA strands were synthesised and purchased from Eurogentec®.

Electrochemical analysis

Analyses for following the initial modification procedure steps and generating the sensitivity data for miR-21 were performed using a PARSTAT-2283 potentiostat and Powersuite® software. All other analyses were performed using a PalmSens3® potentiostat and PSTrace 4.7. EIS circuit fitting analysis was performed using EIS spectrum analyser, (the program is available online at http://www.abc.chemistry.bsu.by/vi/analyser/ ©Aliaksandr Bandarenka and Genady Ragoisha) and fitted using a Randles circuit and a Levenberg–Marquardt (damped least squares) minimisation algorithm.

Electrochemical measurements were performed using 5 mM $K_3[Fe(CN)_6]$/ 5 mM $K_4[Fe(CN)_6]$ (Sigma-Aldrich®) in 0.1 M KCl (Fisher scientific®) and consisted of i) CVs run between 0.6 V and −0.3 V at a scan rate of 100 mVs^{-1}, ii) chronocoulometry/coulometry performed at 0.3 V for 0.1 s, 0.0 V for 2 s and 0.5 V for 2 s and iii) EIS run at a DC potential of 0.23 V between frequencies of 0.01 Hz to 10 kHz with an AC amplitude of 5 mV.

Oligonucleotide sequences used throughout

Table 6.1 The sequences of all oligonucleotides used throughout this investigation.

Species Name	Species Sequence
Anti-miR-21 (DNA)	5′NH_2-C_6-TCA ACA TCA GTC TGA TAA GCT A
hsa-miR-21-5p (RNA)	5′-UAG CUU AUC AGA CUG AUG UUG A
Anti-miR-16 (DNA)	5′NH_2-C_6-CGC CAA TAT TTA CGT GCT GCT A
hsa-miR-16-5p (RNA)	5′-UAG CAG CAC GUA AAU AUU GGC G

miR-21 1 mismatch	5′-UAG CUU AUC **G**GA CUG AUG UUG A
miR-21 2 mismatches	5′-UAG CUU AUC **G**GA CUG AUG UUG **C**
miR-21 3 mismatches	5′-**A**AG CUU AUC **G**GA CUG AUG UUG **C**
Anti-miR-192 (DNA)	5′NH_2-C_6-GGC TGT CAA TTC ATA GGT CAG,
hsa-miR-192-5p	5′-CUG ACC UAU GAA UUG ACA GCC
Anti-miR-191 (DNA)	5′-NH_2-C_6-CAG CTG CTT TTG GGA TTC CGT TG
hsa-miR-191-5p	5′-CAA CGG AAU CCC AAA AGC AGC UG
Anti-miR-126 (DNA)	5′-NH_2-C_6-CGC ATT ATT ACT CAC GGT ACG A
hsa-miR-126-3p	5′-UCG UAC CGU GAG UAA UAA UGC G

6.1 Experimental procedures used throughout Chapter 2.

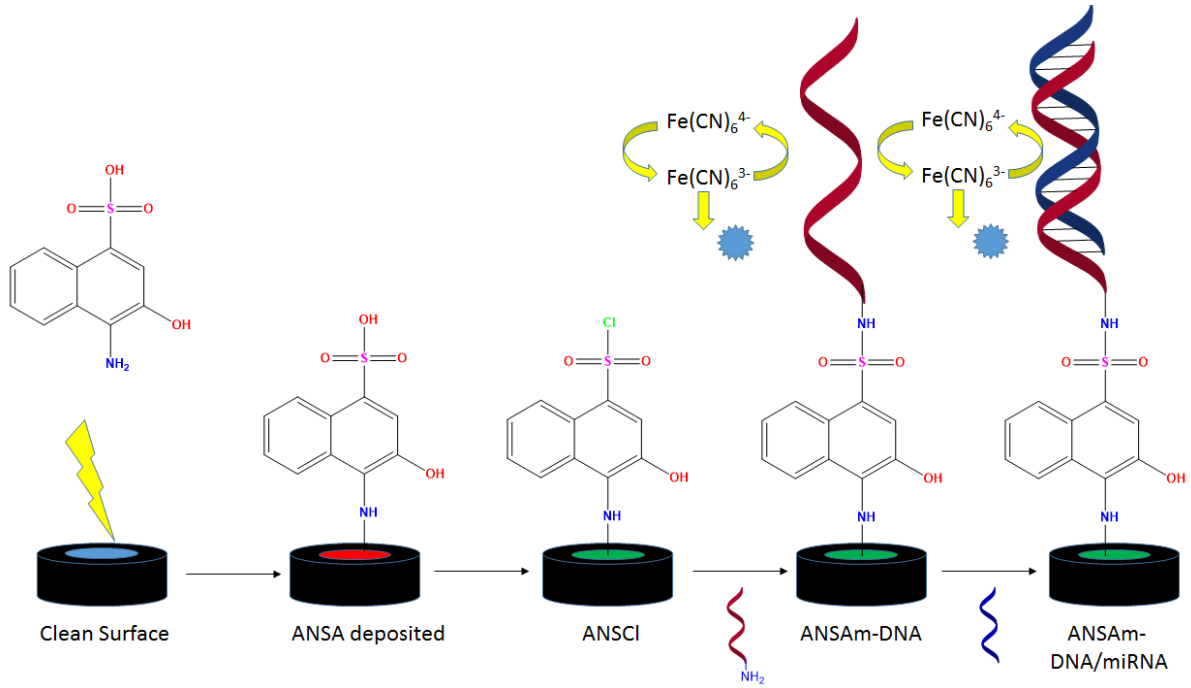

Figure 6.1 The generalised scheme of the electrode modification procedure as previously shown in Figure 2.3.

6.1.1 Glassy carbon electrode polishing procedure.

A 3 mm diameter glassy carbon electrode (BASInc®) was polished to a 'mirror like' finish via sequential applications of 3 µm and 1 µm diamond polish, and then with a final polish using 0.05 µm alumina, all supplied as part of a polishing kit (Alvatek®). Following manual polishing the electrode was sonicated for 90 s each in acetone, ethanol and water. During optimisation

of this polishing the efficiency was tested using cyclic voltammetry as described under the heading 'electrochemical analysis' with the result shown in Chapter 2.2.

6.1.2 Electrode modification procedure

This experimental procedure was also used to produce the data shown in Chapter 2.2.

A glassy carbon electrode was cleaned to a 'mirror like' finish using the polishing procedure described previously (6.1.1). The electrode was submerged in a solution of 1-amino-2-naphthol-4-sulfonic acid (Acros organics®, 12 mL, 10 mM, 28.7 mg) dissolved in phosphate buffer solution (PBS, 25 mM, pH 7.0), along with a silver/silver chloride reference electrode and platinum wire counter. This 3 electrode cell was used to perform a series of CV scans between 1.5 V and -0.5 V at a rate of 20 mVs^{-1} to induce electrodeposition of the sulfonic acid. This was performed until there was negligible difference between each cycle which occurred after a total of 8 cycles. The electrode was rinsed with deionised water for 30 s to remove any physisorbed sulfonic acid residue and shaken to dryness. The first time this was performed the electrode was analysed via CV using 5 mM $K_3[Fe(CN)_6]$/ 5 mM $K_4[Fe(CN)_6]$ in 0.1 M KCl and compared to the clean electrode voltammogram in order to ensure the deposition had occurred.

The deposition modified electrode was submerged in a solution of PCl_5 (Alfa Aesar®, 16.7 mg, 40 mM) in acetone (2 mL) for 30 min, with CV analysis performed the first time. A droplet of chemically synthesised amine labelled DNA anti-miR-21 (10 µL, 1 µM), dissolved in TMD buffer (50 mM Tris-HCl, 20 mM $MgCl_2$, pH 8.0) and denatured for 2 min at 80 °C (calculated T_m 74.7 °C) was pipetted onto the surface of the electrode. The electrode was heated to dryness under vacuum at 80 °C for 90 min. This electrode was rinsed for 30 s using the TMD buffer and analysed via CV, chronocoulometry and EIS using 5 mM $K_3[Fe(CN)_6]$/ 5 mM $K_4[Fe(CN)_6]$ in 0.1 M KCl to give the DNA only response. Finally the DNA modified electrode was submerged in a 1.5mL microcentrifuge tube containing a solution of synthetic miR-21 target also dissolved in TMD buffer (1 mL, 0.1 nM) for 60 min at 50 °C with shaking in an Eppendorf Thermomixer, to induce a hybridisation event. Finally the hybridised probe was rinsed with TMD buffer for 30 s and once again analysed via CV, chronocoulometry and EIS measurements. The charge at the peak minimum in the chronocoulometry results at this stage were then subtracted from the charge peak minimum of the DNA only response to determine the coulometry change as a result of the hybridisation event.

6.1.3 Hybridisation timescale optimisation

The anti-miR-21 biosensor was generated as previously described (6.1.2) and then in order to determine the most optimum hybridisation time the hybridisation procedure was performed for 40 min, 30 min and 10 min over separate experiments. The resulting change in coulometry response between the DNA containing probe and the resulting hybrid probe at each time was compared to that obtained after 60 min hybridisation. This showed that 30 min hybridisation time was enough to produce a similar response to that at 60 min and was thus chosen as the optimum time. The data being given in the appendices (Appendix 1 Figure A1.2)

6.1.4 Sensitivity determination

An anti-miR-21 containing electrode was generated as previously described (6.1.2) and hybridised with synthetic miR-21 over a range of concentrations between 10 nM and 10 fM. The electrode was cleaned after each concentration measurement and the whole procedure repeated in triplicate. The change in coulometric response and EIS charge transfer resistance between the DNA containing probe and the hybridised probe was then plotted against the respective concentrations to generate the calibration plot shown in Chapter 2.3.

The limit of detection quoted for the coulometric plot was determined using 3 × standard deviation of the coulometry response obtained when a solution of buffer alone was used as the hybridisation target, again performed in triplicate (Appendix 1 Table A1.3).

6.1.5 Selectivity determination

The anti-miR-21 DNA containing electrode was generated as previously described (6.1.2). This was then hybridised with miRNA strands with different sequences containing 1 mismatch, 2 mismatches, 3 mismatches and a final miR-16 sequence (10 nM). This was performed in triplicate by cleaning and re-modifying the probe for each analysis, the changes in coulometric and EIS responses were then compared to those obtained for the complementary miR-21 target to determine the selectivity of the probe towards the complementary sequence. Again this is described in Chapter 2.3.

To perform the miR-16 tests the electrode was modified to the sulfonyl chloride modification step as previously mentioned. This time however a droplet of amine tagged anti-miR-16 DNA oligonucleotide (10 µL, 1µM) and used as before to analyse a miR-16 target, (1 mL) in TMD buffer

6.1.6 Synthetic urine analyses

The following experimental procedures form the basis of the data displayed in Chapter 2.4.

The glassy carbon electrode was modified to attach the anti-miR-21 DNA oligonucleotide probe strand as described previously (6.1.2), however the matrix for the miR-21 hybridisation event was modified to simulate the constituents of human urine. Thus to test the effect of salt two solutions of miR-21 was prepared in TMD buffer (1 mL, 0.1 nM) and NaCl was added to each (3 mg and 10 mg respectively) to simulate potential low and high concentrations of salt that could be expected for urine. The solution was then analysed as described previously, with each sample being performed in triplicate. The resulting change in coulometry and EIS responses were plotted against those obtained for the miR-21 results with no salt additions.

To simulate the urea content of urine the electrode was modified to contain the anti-miR-21 DNA strand as previously described. The electrode was submerged in miR-21 (1 mL, 10 pM) in TMD buffered urea (9.3 g/L) and heated to 50 °C with shaking for 90 min in a Thermomixer. The resulting change in coulometric response was plotted with that obtained for the miR-21 target in TMD buffer for comparison.

For the simulation of proteinaceous urine the anti-miR-21 modified electrode was prepared as before and the miRNA solution matrix modified using BSA (Sigma®). Thus a solution of miR-21 (1 mL, 0.1 nM) was prepared in TMD buffer as before, then BSA (3 mg) was added and the DNA modified electrode submerged in this mixture at 50 °C for 30 min with shaking. EIS analysis was then performed and the resulting Nyquist data compared to that of the miR-21 target in buffer alone to determine the effect of the protein content on the response. As mentioned this results in a much more impeded response than expected. Therefore the hybridised electrode was submerged in a solution of proteinase K (1 mg/mL) dissolved in TMD buffer and $CaCl_2$ (1 mg/mL) for 30 min at 50 °C with shaking. EIS analysis was then performed once again and the response again compared to that expected for a miR-21 solution of the same concentration in TMD buffer alone.

6.1.7 Urine analysis

Table 6.2 The healthy control urine samples used in the testing stages of Chapter 2.

Urine Sample	**Registry Identifier**
1	*C11007_02*

2	*C11008_02*
3	*C13001_03*
4	*C13002_03*
5	*C13024_03*

The experimental procedure described here relates to the data shown in Chapter 2.5.

The DNA modified electrode was generated via the method mentioned previously (6.1.2) to contain complementary strands for a miR-21 target. The first analysis of the urine sample was then performed by submerging the DNA bound electrode in a solution of urine sample 1 (500 µL) and heated to 50 °C for 30 min with shaking in a Thermomixer. The sensor was then rinsed with TMD buffer and chronocoulometric analysis was then performed and the resulting data plotted against that of the DNA strand alone. As this proved unsuccessful, the electrode was then submerged in a solution of proteinase K (ThermoFisher®, 1 mg/mL) and $CaCl_2$ (BDH®, 1 mg/mL) in TMD buffer at 37 °C for 20 min, after which the electrode was rinsed with TMD and the chronocoulometric analysis repeated. This was then compared to the urine response pre-proteinase K treatment and showed that protein 'fouling' was taking place.

The modified urinary analysis methodology is described herein. Before each analysis the glassy carbon electrode was cleaned and modified to contain the anti-miR-21 DNA strand using the method mentioned previously. The urine sample to be used (490 µL) was then pipetted into a 1.5 mL eppendorf tube and proteinase K (10 µL, 20 mg/mL) dissolved in water was added along with $CaCl_2$ (1 mg). The resulting mixture was then incubated at 50 °C for 10 min with shaking in a thermo mixer to digest any proteins present in the urine sample. Following this the sample was added to a 10 kDa spin filter and centrifuged at 14,000 rcf (12,300 rpm) for 20 min at 20 °C. The DNA modified electrode was incubated in the filtrate for 50 °C for 30 min with shaking. Finally the electrode was rinsed with TMD buffer and chronocoulometry analysis performed, with the change in response between the hybridised electrode and the DNA only electrode used to calculate the concentration of miR-21 in the urine sample. The electrode was cleaned after each sample measurement and the full procedure performed in triplicate.

6.1.8 RT-qPCR based calibration

To generate a calibration plot of qPCR based CT value vs. miR-21 concentration a serial dilution of synthetic miR-21 in TMD buffer underwent RT and qPCR steps. As such, solutions of miR-21 in TMD buffer were made up in 10 fold serial dilutions between 10 nM and 10 fM. Then an RT master mix was produced containing standardised amounts of RT materials per sample required (1.5 µL 10x RT mix, 0.1 µL RNase inhibitor, 0.5 µL 25x DNTP mix, 3 µL 5× miR-21 specific primer, 1 µL multiscribe and 4.25 µL water per sample). An aliquot of this master mix (10 µL) was then added to an aliquot (5 µL) of miR-21 at each concentration in an Eppendorf RT strip. The aliquots were then placed in an RT thermocycler to induce transcription of cDNA complementary to the miR-21 target. Following the RT procedure each aliquot was diluted with water (30 µL). A Taqman PCR master mix was according to the number of samples required (10 µL Taqman master mix, 1 µL miR-21 primer assay number 000397, and 5 µL water per sample). An aliquot of the master mix (16 µL) was then mixed with an aliquot of the cDNA mixture (4 µL) in each well of a 96 well PCR plate. These were then amplified using a Taqman assay pre-programmed procedure (heating to 50 °C and held for 2 minutes before being heated to 95 °C and held for a further 10 minutes, then 40 cycles of 15 seconds at 95 °C and cooling to 60 °C for 1 minute before reheating to 95 °C for 15 seconds etc. with all heating/cooling stages being performed at 1.6 °C/s) on a ViiA 7 real time PCR system from Life Technologies Applied Biosystems. The CT values at a threshold of 0.15182 were then plotted against the corresponding concentration to generate the RT-qPCR calibration plot for quantifying the concentration of miR-21 from the corresponding analysis from urinary extracts.

6.1.9 RT-qPCR urine analysis

To analyse the urine samples an extraction procedure was performed to isolate the RNA prior to the RT and qPCR steps. For each sample an aliquot (350 µL) was pipetted into a 1.5 mL eppendorf tube following which carrier RNA (MS2 RNA, 1.25 µL, 1 µg) was also added. Next Qiazol lysis reagent (Qiagen®, 750 µL) and cel-miR-39 housekeeping miR (1 µL, 0.5 pM) was added and the solution incubated at room temperature for 5 min to break down any proteins, cells and extracellular vesicles. Following this chloroform (Sigma ®) was also added (200 µL) and the whole mixture was vortexed briefly to mix before being allowed to incubate for 2-3 min and then centrifuged for 15 min at 12,000 rcf and at 4 °C. After centrifugation 2 clear layers had formed in the mixture, the aqueous (upper) phase (600 µL) was transferred to

another eppendorf tube and absolute ethanol added with mixing (900 µL). An aliquot of the resulting mixture (750 µL) was pipetted into a mini centrifuge column, as part of the miRNeasy kit from Qiagen, and centrifuged at 12,000 rcf for 30 s, after which the filtrate was discarded. The remaining ethanol/RNA mixture (750 µL) was then added to the column and spun again at 12,000 rcf for 30 s, again discarding the filtrate. The isolated sample in the column was then washed with RWT buffer, again from the miRNeasy kit, (700 µL) and centrifuged at 12,000 rcf for 60 s, discarding the flow through filtrate. A second buffer, RPE, (500 µL) was then added to the column and spun at 12,000 rcf for 2 min after which the filtrate was discarded. The column was then centrifuged for a further 1 minute at 12,000 rcf to dry before being placed in a new 1.5 mL collection tube at which point 50 µL of RNase free water was added and centrifuged at 8,000 rcf for 1 minute to release and collect the isolated RNA. This was then stored at -80 °C for further use.

Once isolated the RT and qPCR procedure mentioned previously was performed using these miRNA isolates, in place of the buffered synthetic miRNA, in exactly the same fashion.

6.1.10 PNA based negative control

The anti-miR-21 DNA bound electrode was generated as mentioned previously (6.1.2). A solution of miR-21 complementary PNA (50 µL, 10 nM, final concentration 1 nM) was added to an aliquot of urine sample 1 (450 µL), that had been treated with proteinase K and spin filtered via the procedure described (6.1.7). The electrode was then incubated in this solution for 30 min at 50 °C with shaking, it was then rinsed with TMD and chronocoulometry analysis performed and compared to the result obtained for the electrode with DNA alone. Finally an aliquot of this mixture (450 µL) was mixed with a solution of synthetic miR-21 (50 µL, 1 nM, final concentration 0.1nM) in TMD and the electrode incubated in this solution once again for 30 min at 50 °C. The electrode was then rinsed with TMD and analysed via coulometry.

6.1.11 PNA based positive control

A glassy carbon electrode was modified to contain a DNA probe strand complementary to miR-16 as described earlier (6.1.5). Following this an aliquot of urine sample 1 that has been treated with proteinase K and spin filtered using the method described previously (6.1.7, 450 µL) was mixed with a solution of PNA complementary to miR-21 (50 µL, 10 nM, 1 nM final concentration) in TMD. The electrode was then submerged in this solution and incubated at 50 °C for 30 min prior to being rinsed with TMD buffer and analysed via coulometry.

6.1.12 RNase controls

Again the electrode was modified to contain anti-miR-16 as described previously (6.1.5), after which an aliquot of urine sample 1 (490 µL) was mixed with RNase A (Sigma-Aldrich®, 1mg) and incubated for 20 min at 50 °C. Following this the same sample was treated with proteinase K and spin filtered using the same methodology mentioned previously (6.1.7) and the DNA modified electrode was then submerged in the resulting solution for 30 min at 50 °C, it was then rinsed with TMD buffer and chronocoulometry analysis performed. Finally an aliquot of the treated urine sample (450 µL) was mixed with synthetic miR-16 (50 µL, 0.1 nM, 10 pM final concentration) and once again incubated at 50 °C for 30 min. The hybridised electrode was then once again rinsed with TMD and analysed via coulometry.

6.1.13 Shelf life of the sensor

This experimental procedure relates to the data in Chapter 2. 6 (Appendix 1 Figure A1.3 and A1.4 and Table A1.2).

To determine the length of time the DNA modified electrode can be stored for while maintaining an acceptable level of sensitivity, a set of 3 glassy carbon electrodes were modified to contain anti-miR-21 and then stored for 24 hours at different temperatures before being used. The first set of 3 electrodes were modified to contain the anti-miR-21 DNA as earlier described and then immediately incubated with miR-21 (1 mL, 0.1 nM) for 30 min at 50 °C, they were then rinsed with TMD buffer and analysed via coulometry, with the change in response between the electrode with DNA alone and the hybridised electrode being plotted. The electrodes were then cleaned and modified to contain the anti-miR-21 DNA as before and were then stored for 24 hours at 4 °C, 25 °C, 30 °C, 40 °C and 50 °C with each respective experiment. The rate of decay over these temperatures was then assumed as 1st order and used to plot an Arrhenius plot with the potential storage time decided as the point when the response reaches 50% of the response obtained for the immediately used electrodes.

6.1.14 Biosensor regeneration procedure

The experimental procedure described here is used to obtain the data in Appendix 1 Figure A1.1 showing that, although not routinely performed throughout this project, it is possible to denature the DNA-RNA hybrid on the electrode and reobtain an electrochemical response of the same magnitude of the DNA alone response.

To perform this the hybridised electrode was submerged in a solution of TMD buffer (1 mL) and heated to 95 °C for 20 min to denature the DNA/RNA hybrid. Following this the electrode was transferred to a second solution of ice cold TMD buffer (1 mL) and cooled on ice for a further 10 min before being sonicated for 2 min in the TMD buffer and rinsed. Performing coulometric analysis on the electrode at this point shows the DNA only response has been regenerated. The electrode was then incubated with miR-21 (1 mL, 0.1 nM) in TMD buffer at 50 °C for 30 min to re-hybridise before being rinsed with TMD buffer and analysed via coulometry. This coulometric response is reliable after 2 regenerations but begins to decline with subsequent regenerations.

6.2 Experimental procedures of Chapter 3

6.2.1 Initial testing of the full modification procedure

The experimental procedure described here relates to the data shown in Chapter 3.2.

A 2 mm electrode, of the kind described in Figure 3.1, was rinsed with deionised water and then attached to the working electrode cable via its silver/silver chloride connection and a crocodile clip. This was submerged in a solution of 1-amino-2-naphthol-4-sulfonic acid (15 mL, 10 mM, 35.9 mg) along with a silver/silver chloride reference and a platinum wire counter. Electrodeposition then takes place by using 8 cycles (the first procedure uses 16 with 8 being chosen as the ideal number) of CV between 1.5 V and -0.5 V at a rate of 20 mVs^{-1} until a negligible change in the voltammograms was obtained. At this point the electrode was submerged in a solution of PCl_5 (16.7 mg, 40 mM) in acetone (2 mL) for 30 min. Unfortunately, despite multiple attempts, visual damage and peeling of the electrode was noticed, and subsequent CV analyses further showed the loss of any analysable signal.

6.2.2 Solvent compatibility testing

In order to find a suitable solvent for the chlorination step, the PCl_5 reagent (16.7 mg, 40 mM) was dissolved in the desired solvent (2 mL) and a screen printed electrode was then submerged in the mixture for 30 min. After this time, any solvents that had visually damaged the electrodes were not considered further, and any which failed to dissolve PCl_5 were also removed. This left hexane as the most suitable solvent that was used in the future.

6.2.3 IR analysis

After the deposition of the sulfonic acid had been completed, the active working surface of the electrode was compressed onto the sampling crystal of an ATR-FTIR and IR analysis performed. The resulting spectrum was compared to one obtained analysing an electrode surface that has not been modified, and one obtained using the sulfonic acid alone.

As well as this, a selection of sulfonic acid modified electrodes were submerged in a solution of PCl_5 (16.7 mg, 40 mM) in hexane (2 mL) for 18 hours, 4 hours, 2 hours and 1 hour. After which the surfaces were again analysed by IR spectroscopy and compared to one chlorinated using acetone as the solvent. This was done in order to try and determine the reaction time required for the hexane/PCl_5 solution, however, as all spectra appeared very similar, 4 hours was chosen as the reaction time due to a combination visual, electrochemical, spectroscopic and (as described later) spectrometric analysis.

6.2.4 Modification procedure using hexane solvent

A 2 mm screen printed electrode was modified with 1-amino-2-naphthol-4-sulfonic acid as previously described (6.2.1), after which it was submerged in a solution of PCl_5 (16.7 mg, 40 mM) in hexane (2 mL) for 4 hours. After this the electrode was rinsed quickly with water (for this initial stability test only) and analysed via CV, with the resulting voltammogram compared to that obtained after chlorination of the glassy carbon electrode, in order to determine whether it had successfully survived the procedure.

A second 2 mm screen printed electrode was then modified to the sulfonyl chloride stage, as described above, at which point a synthetic DNA oligonucleotide anti-miR-21 (10 µL, 1 µM) dissolved in TMD buffer was pipetted onto the electrode surface and the electrode allowed to dry overnight at room temperature. The electrode was then analysed via CV, coulometry and EIS measurements. Finally the electrode was submerged in a solution of synthetic miR-21 (1 mL, 10 nM) dissolved in TMD buffer and incubated in a 1.5 mL eppendorf tube with shaking at 50 °C for 60 min in a Thermomixer. Unfortunately at this point the dielectric layer showed visual signs of water ingression and peeling, and the silver/silver connector showed discolouration, analysis via CV showed the extent of this damage which prevented useable analysis due to misshapen peaks.

6.2.5 Final modification procedure using hexane and applied nail hardening resin

In order to combat the water ingression and potential damage of the silver connector a commercially available nail hardening resin from a local beauty store and insulation tape were employed to protect the electrode.

A 2 mm screen printed electrode was modified to contain anti-miR-21 on its surface as described previously (6.2.4) and analysed via CV, coulometry and EIS. After this the electrode was rinsed with water and shaken to dryness, following which the nail hardening resin was cautiously applied to the area surrounding the active surface of the electrode. The electrode was then left to dry for 3 min before insulation tape was wrapped around the silver/silver chloride connector pin and the electrode was submerged in a solution of synthetic miR-21 (1 mL, 10 nM) and incubated with shaking for 60 min at 50 °C in a Thermomixer. The hybridised electrode was then analysed via CV, coulometry and EIS measurements, the results of which were consistent with the electrode now surviving the miRNA incubation.

6.2.6 Sensitivity determination of screen printed electrodes

A set of 2 mm diameter and 3 mm diameter screen printed carbon electrodes were modified using the hexane, resin and tape edited modification procedure described previously (6.2.5). They were then incubated with serial dilutions of miR-21 solutions from 10 nM to 1 pM for the 2 mm electrodes and from 10 nM to 10 fM for the 3 mm electrodes with each hybridisation being performed in triplicate using 3 individual screen printed electrodes. The change in coulometry between the DNA containing electrodes and the hybridised electrodes was then plotted against the respective concentration. Thus generating a calibration curve for the 2 mm electrode (Chapter 3.2) and the 3 mm electrode (Chapter 3.3).

6.2.7 AFM based surface imaging

AFM imaging of the working electrode surface was performed by Matteo Lo Cicero of Cardiff University School of Chemistry, using tapping mode (TM-AFM) in air at 293 K using a Nanoscope V instrument (Veeco, USA) type multimode 8. PPP-NCHR PointProbe Plus® silicon-SPM-sensor probes were used (Nanosensors™, resonance frequency 33 kHz, force constant 42 N/m, length 125 µm) operating at a frequency of 321.5 kHz to image the surfaces through Scan Asyst®-air mode. The data produced was processed and analysed by the author with WSxM software.

6.3 Experimental procedures of Chapter 4

6.3.1 Testing the carbon ink

The experimental procedure described here was used to collect the data in Chapter 4.3.

To test the two selected inks (C2050517_P1, a cross linked and thixotropic carbon/graphite ink with a printed thickness of 12 µm, and C2100126_D6, a cross linked carbon/graphite ink of 25-36 µm printed thickness), a set of carbon sticks of each was produced using a DEK 2230 screen printer, a nylon mesh and a Valox substrate, a description of how the printer works is given in Chapter 4.1. These were then submerged in PCl_5 (16.7 mg, 40 mM) in acetone (2 mL) for 30 min and observed visually. This however only showed that no visible signs of damage were present.

Then to determine whether the electrode could be electrochemically analysed following the acetone/PCl_5 treatment a selection of the sticks and full screen printed electrodes were produced using both inks, and incubated in the solution of PCl_5 (16.7 mg, 40 mM) in acetone (2 mL) for 30 min, some being protected with the nail resin and insulation tape and some not. Each electrode was then analysed using CV, coulometry and EIS in order to determine if the expected peak shapes were obtained. Of these the carbon ink C2050517_P1 showed the best stability.

6.3.2 Testing the silver/silver chloride ink

This experimental procedure was used to obtain the data in Chapter 4.4.

Once the most ideal carbon had been determined the silver/silver chloride also needed to be tested. To do this a fully layered screen printed electrode was produced using the C2050517_P1 carbon ink as the working and counter electrodes, the silver/silver chloride reference and conductive tracks using 60:40 silver/silver chloride ink C2130809_D5 (20 µm printed thickness) and the grey coloured dielectric layer D2070423_P5. This electrode was then exposed to a solution of PCl_5 (16.7 mg, 40 mM) in acetone (2 mL) either by complete submersion or via pipetting droplets (100 µL initially and another set using 10 µL every 60 s) onto it, focussing on the working electrode surface. Unfortunately the submersion technique showed complete peeling of the silver ink and minor leaching of the dielectric layer.

Therefore another silver ink needed to be tested this time being the silver ink C2131016_D1 (silver/silver chloride 70:30, cross linked ink). Then to test the stability of this silver the

electrode was submerged in a solution of PCl_5 (16.7 mg, 40 mM) in acetone (2 mL) for 30 min and inspected visually. This showed that the silver no longer peeled from the substrate and subsequent CV, coulometry and EIS measurements showed the expected peak behaviour.

6.3.3 Testing the dielectric inks.

To test the stability of the available dielectric inks, a set of squares was printed with each of the dielectrics chosen (blue D2140114_D5, a water ingression resistant polymer dielectric, blue D50706_P3, a polymer dielectric with high resistance to polar solvents, white D2130510_D2, a cross-linked dielectric with high solvent resistance, and cream D50706_D2, a dielectric with high solvent resistance) and then a drop (100 µL) of acetone was placed onto the centre of the dielectric. The dielectrics which showed the least damage (blue) were then printed again as squares containing 2 layers of the dielectric. The exposure to the PCl_5/acetone solution was then repeated showing that the dual layers enhanced the stability.

Finally the two blue dielectrics were used in combination with the previously optimised carbon and silver/silver chloride inks to produce a set of full screen printed electrodes. One set was then submerged in the acetone/PCl_5 solution for 30 min, and another had a droplet (10 µL) of the same solution added at a rate of 10 µL/min over 30 min, before being inspected visually and via CV, coulometry and EIS measurements. Dielectric D21140114_D5 gave a greater proportion of visibly undamaged electrodes via the droplet method.

6.3.4 Optimising the deposition of sulfonic acid

The experimental procedure described here relates to the data in Chapter 4.6.

A set of electrodes consisting of 3 working electrode surfaces, one shared counter and one shared reference, printed using carbon ink C2050517_P1, silver/silver chloride ink C2131016_D1 and 2 layers of blue dielectric D2140114_D5 were sonicated in ethanol for 20 s before being rinsed with water to remove any interferents. After this, the deposition of the 1-amino-2-naphthol-4-sulfonic acid was performed using 3 individual procedures.

In the first procedure, aliquots (50 µL) of the 1-amino-2-naphthol-4-sulfonic acid (14.4 mg, 6 mL, 10 mM) dissolved in PBS were placed onto each of the working area surfaces and 4 CV cycles were performed between -0.5 V and 1.5 V at a scan rate of 20 mVs^{-1} to induce electrodeposition.

In the second procedure an aliquot (300 µL) of the 1-amino-2-naphthol-4-sulfonic acid (14.4 mg, 6 mL, 10 mM) dissolved in PBS was pipetted over the three surfaces of the electrode. At which point the voltage was maintained at 0.65 V for 1 minute and then a standard CV was performed for 1 cycle between -0.5 V and 1.5 V at a scan rate of 20 mVs^{-1}. This procedure was then repeated a number of times, each time increasing the number of min that the 0.65 V potential was maintained, over 2, 3, 4, 5 and 6 min. 4 minutes was then chosen as the ideal reaction time.

In the third technique all 3 surfaces shared a full coverage of the 1-amino-2-naphthol-4-sulfonic acid (14.4 mg, 6 mL, 10 mM) dissolved in PBS, via pipetting one large drop (300 µL) of the solution across all 3 of the electrode surfaces. After which point the surface is held at a voltage of 0.65 V for 4 min after which a CV cycle was performed between -0.5 V and 1.5 V at a scan rate of 20 mVs^{-1} to ensure the deposition had occurred.

This third technique proved to give the most repeatable results.

6.3.5 Optimising the chlorination

This procedure is in reference to the data in Chapter 4.6.

The final optimisation step revolved around the chlorination procedure. Thus to test this 2 electrodes were produced using the 4 minute maintenance of 0.65 V procedure described above (6.3.4 technique 3). After this one of the electrodes was submerged in PCl_5 (16.7 mg, 40 mM) in acetone (2 mL) for 30 min and the other had the same concentration of PCl_5/acetone mixture pipetted at a rate of 10 µL/min on each of the three active surfaces for a total of 30 min. Finally the electrode was rinsed with water and shaken to dryness before being analysed via CV, coulometry and EIS. Both visually and using the electrochemical measurements it could be seen that the droplet method resulted in the surfaces producing the desired peaks much more reliably than the submergence method.

6.3.6 miR-21 sensitivity testing

The experimental procedures described here relate to the results shown in Chapter 4.7.

For initial sensitivity testing of the biosensor a set of electrodes were modified to the naphthalene sulfonyl chloride step as described in 6.3.5, at which point a droplet of anti-miR-21 DNA (10 µL, 1 µM) was pipetted onto the each of the three working surfaces and allowed to dry at 80 °C for 90 mins in a fan hybridising oven. The electrode was then rinsed with TMD

buffer and analysed by CV, coulometry and EIS. After this a sample of miR-21 (300 µL, 10 nM) dissolved in TMD buffer was pipetted onto the electrode, covering all working surfaces and allowed to hybridise in a hybridising oven for 30 mins at 50 °C. This final step was repeated using one of a series of serial dilutions of miR-21 (10 nM to 100 fM) on each separate electrode. After hybridisation, each electrode was rinsed with TMD buffer and analysed via CV, coulometry and EIS. The resulting change in coulometry between the DNA only electrode and the hybridised electrode was then plotted for each concentration. Unfortunately this did not show any correlation.

Therefore, for a second set of analyses, the Teflon well block described in Chapter 4.7 was used as the incubation vessel. The electrodes were produced to contain anti-miR-21 and analysed electrochemically as described in the procedure above, at which point the serial dilutions were once again prepared in TMD using a slightly larger volume (500 µL, 10 nM to 100 fM) and each concentration pipetted into an individual well in the Teflon. An anti-miR-21 containing electrode was then inserted into each well and allowed to incubate for 30 mins at 50 °C in a hybridising oven. Each electrode was then rinsed with TMD buffer and analysed via CV, coulometry and EIS, with the change in coulometric response between the DNA containing electrode and the hybridised electrode being plotted for each concentration. This time the data showed a correlation shown in Figure 4.17.

6.3.7 Optimised modification procedure for urine analysis

Table 6.3 The healthy and DKD patient urine samples used for the testing in Chapter 4.

Registry identifier	**Patient/Control**
C11005	*Control*
C11021	*Control*
P12016	*Patient*
P12026	*Patient*

A screen printed electrode containing 3 working surfaces and 1 shared counter and reference was sonicated in ethanol for 20 s and rinsed with water to clean of any interferents. An aliquot (300 µL) *of the* 1-amino-2-naphthol-4-sulfonic acid (14.4 mg, 6 mL, 10 mM) dissolved in PBS

was then pipetted over the surfaces of the electrode and a potential of 0.65 V applied for 4 min to induce electrodeposition, a 1 cycle CV is then performed between -0.5 V and 1.5 V at a scan rate of 20 mVs^{-1}. This was repeated for each working surface. The electrode was then rinsed with water and shaken to dryness, after which a solution of PCl_5 (16.7 mg, 40 mM) dissolved in acetone (2 mL) was pipetted over each surface at a rate of 10 µL/min for 30 min. The electrode was then very briefly rinsed with acetone to remove the remaining PCl_5/acetone mixture and shaken to dryness. A synthetic DNA oligonucleotide anti-192 (10 µL, 1 µM), complementary to hsa-miR-192-5p was then pipetted onto each electrode surface and dried for 80 °C for 90 min in a fan hybridising oven. After this the electrode was rinsed with TMD buffer and analysed via CV, EIS and coulometry. During this time the urine sample was treated with proteinase K and spin filtered using the same procedure mentioned previously (6.1.7). The electrode was then placed in a custom produced slot on a Teflon well block, and the well was filled with the treated urine sample. The block was then put in the fan hybridiser oven at 50 °C for 30 min. Finally the electrode was removed from the Teflon and rinsed with TMD before being analysed via CV coulometry and EIS. The resulting change in coulometric response was compared between each urine sample, with particular emphasis on the difference between patient and control samples.

The above procedure was then repeated using anti-miR-191 and anti-miR-126 DNA to detect miRs hsa-miR-191-5p and hsa-miR-126-3p respectively.

6.3.8 AFM imaging of new inks

The working surface of these new electrodes were once again imaged by Matteo Lo Cicero when unmodified, modified with the sulfonic acid (ANSA), following chlorination in PCl_5 in acetone and after incubation in the pre-treated urine. The analysis was performed as described in 6.2.7.

References

1 R. C. Lee, R. L. Feinbaum and V. Ambros, *Cell*, 1993, **75**, 843–854.
2 B. Wightman, I. Ha and G. Ruvkun, *Cell*, 1993, **75**, 855–862.
3 A. E. Pasquinelli, B. J. Reinhart, F. Slack, M. Q. Martindale, M. I. Kuroda, B. Maller, D. C. Hayward, E. E. Ball, B. Degnan, P. Müller, J. Spring, A. Srinivasan, M. Fishman, J. Finnerty, J. Corbo, M. Levine, P. Leahy, E. Davidson and G. Ruvkun, *Nature*, 2000, **408**, 86–89.
4 B. J. Reinhart, F. J. Slack, M. Basson, A. E. Pasquinelli, J. C. Bettinger, A. E. Rougvie, H. R. Horvitz and G. Ruvkun, *Nature*, 2000, **403**, 901–906.
5 S. Roush and F. J. Slack, *Trends Cell Biol.*, 2008, **18**, 505–516.
6 B. Boyerinas, S.-M. Park, A. Hau, A. E. Murmann and M. E. Peter, *Endocr. Relat. Cancer*, 2010, **17**, F19-36.
7 H. Dong, J. Lei, L. Ding, Y. Wen, H. Ju and X. Zhang, *Chem. Rev.*, 2013, **113**, 6207–6233.
8 S. Griffiths-Jones, H. K. Saini, S. van Dongen and A. J. Enright, *Nucleic Acids Res.*, 2008, **36**, D154-158.
9 miRBase, http://mirbase.org/, (accessed 9 September 2016).
10 Y. Lee, M. Kim, J. Han, K.-H. Yeom, S. Lee, S. H. Baek and V. N. Kim, *EMBO J.*, 2004, **23**, 4051–4060.
11 K. Simpson, A. Wonnacott, D. J. Fraser and T. Bowen, *Curr. Diab. Rep.*, 2016, **16**, 35.
12 J. Han, Y. Lee, K.-H. Yeom, J.-W. Nam, I. Heo, J.-K. Rhee, S. Y. Sohn, Y. Cho, B.-T. Zhang and V. N. Kim, *Cell*, 2006, **125**, 887–901.
13 R. I. Gregory, K.-P. Yan, G. Amuthan, T. Chendrimada, B. Doratotaj, N. Cooch and R. Shiekhattar, *Nature*, 2004, **432**, 235–240.
14 E. Lund, S. Güttinger, A. Calado, J. E. Dahlberg and U. Kutay, *Science*, 2004, **303**, 95–98.
15 J. Liu, M. A. Valencia-Sanchez, G. J. Hannon and R. Parker, *Nat. Cell Biol.*, 2005, **7**, 719–723.
16 D. S. Schwarz, Y. Tomari and P. D. Zamore, *Curr. Biol. CB*, 2004, **14**, 787–791.
17 G. L. Sen and H. M. Blau, *Nat. Cell Biol.*, 2005, **7**, 633–636.
18 S. Yekta, I.-H. Shih and D. P. Bartel, *Science*, 2004, **304**, 594–596.
19 J. Brennecke, D. R. Hipfner, A. Stark, R. B. Russell and S. M. Cohen, *Cell*, 2003, **113**, 25–36.
20 C. Fernández-Hernando, Y. Suárez, K. J. Rayner and K. J. Moore, *Curr. Opin. Lipidol.*, 2011, **22**, 86–92.
21 L. Song and R. S. Tuan, *Birth Defects Res. Part C Embryo Today Rev.*, 2006, **78**, 140–149.
22 R. A. Shivdasani, *Blood*, 2006, **108**, 3646–3653.
23 A. Siwaszek, M. Ukleja and A. Dziembowski, *RNA Biol.*, 2014, **11**, 1122–1136.
24 F. M. Hamid and E. V. Makeyev, *Bioessays*, 2016, **38**, 830–838.
25 L. Shi, J. Chen, J. Yang, T. Pan, S. Zhang and Z. Wang, *Brain Res.*, 2010, **1352**, 255–264.
26 Y. J. Kim, S. J. Hwang, Y. C. Bae and J. S. Jung, *Stem Cells*, 2009, **27**, 3093–3102.
27 L. E. B. Buscaglia and Y. Li, *Chin. J. Cancer*, 2011, **30**, 371–380.
28 D. Hanahan and R. A. Weinberg, *Cell*, 2011, **144**, 646–674.
29 M. E. Hatley, D. M. Patrick, M. R. Garcia, J. A. Richardson, R. Bassel-Duby, E. van Rooij and E. N. Olson, *Cancer Cell*, 2010, **18**, 282–293.
30 D. Frezzetti, M. De Menna, P. Zoppoli, C. Guerra, A. Ferraro, A. M. Bello, P. De Luca, C. Calabrese, A. Fusco, M. Ceccarelli, M. Zollo, M. Barbacid, R. Di Lauro and G. De Vita, *Oncogene*, 2011, **30**, 275–286.
31 M. A. Rivas, L. Venturutti, Y.-W. Huang, R. Schillaci, T. H.-M. Huang and P. V. Elizalde, *Breast Cancer Res. BCR*, 2012, **14**, R77.
32 R. I. Aqeilan, G. A. Calin and C. M. Croce, *Cell Death Differ.*, 2010, **17**, 215–220.

33 Z. Hua, Q. Lv, W. Ye, C.-K. A. Wong, G. Cai, D. Gu, Y. Ji, C. Zhao, J. Wang, B. B. Yang and Y. Zhang, *PLoS ONE*, 2006, **1**, e116.
34 A. Chamorro-Jorganes, E. Araldi, L. O. F. Penalva, D. Sandhu, C. Fernández-Hernando and Y. Suárez, *Arterioscler. Thromb. Vasc. Biol.*, 2011, **31**, 2595–2606.
35 A. Stark, J. Brennecke, N. Bushati, R. B. Russell and S. M. Cohen, *Cell*, 2005, **123**, 1133–1146.
36 D. P. Bartel and C.-Z. Chen, *Nat. Rev. Genet.*, 2004, **5**, 396–400.
37 K. K.-H. Farh, A. Grimson, C. Jan, B. P. Lewis, W. K. Johnston, L. P. Lim, C. B. Burge and D. P. Bartel, *Science*, 2005, **310**, 1817–1821.
38 F. Loayza-Puch, Y. Yoshida, T. Matsuzaki, C. Takahashi, H. Kitayama and M. Noda, *Oncogene*, 2010, **29**, 2638–2648.
39 X. Liang, Z. Xu, M. Yuan, Y. Zhang, B. Zhao, J. Wang, A. Zhang and G. Li, *Int. J. Mol. Med.*, 2016, **37**, 967–975.
40 J. Pothof, N. S. Verkaik, W. van IJcken, E. A. C. Wiemer, V. T. B. Ta, G. T. J. van der Horst, N. G. J. Jaspers, D. C. van Gent, J. H. J. Hoeijmakers and S. P. Persengiev, *EMBO J.*, 2009, **28**, 2090–2099.
41 A. Cimmino, G. A. Calin, M. Fabbri, M. V. Iorio, M. Ferracin, M. Shimizu, S. E. Wojcik, R. I. Aqeilan, S. Zupo, M. Dono, L. Rassenti, H. Alder, S. Volinia, C. Liu, T. J. Kipps, M. Negrini and C. M. Croce, *Proc. Natl. Acad. Sci. U. S. A.*, 2005, **102**, 13944–13949.
42 V. Y. Shin, H. Jin, E. K. O. Ng, A. S. L. Cheng, W. W. S. Chong, C. Y. P. Wong, W. K. Leung, J. J. Y. Sung and K.-M. Chu, *Carcinogenesis*, 2011, **32**, 240–245.
43 S. Zafari, C. Backes, P. Leidinger, E. Meese and A. Keller, *Genomics Proteomics Bioinformatics*, 2015, **13**, 159–168.
44 K. G. Biden, L. A. Simms, M. Cummings, R. Buttenshaw, E. Schoch, J. Searle, G. Gobe, J. R. Jass, S. J. Meltzer, B. A. Leggett and J. Young, *Oncogene*, 1999, **18**, 1245–1249.
45 A. Pierce and J.-F. Pittet, *Curr. Opin. Anaesthesiol.*, 2014, **27**, 246–252.
46 A. Akcay, Q. Nguyen, Z. He, K. Turkmen, D. Won Lee, A. A. Hernando, C. Altmann, A. Toker, A. Pacic, D. G. Ljubanovic, A. Jani, S. Faubel and C. L. Edelstein, *J. Am. Soc. Nephrol. JASN*, 2011, **22**, 2057–2067.
47 G. A. Calin, C. D. Dumitru, M. Shimizu, R. Bichi, S. Zupo, E. Noch, H. Aldler, S. Rattan, M. Keating, K. Rai, L. Rassenti, T. Kipps, M. Negrini, F. Bullrich and C. M. Croce, *Proc. Natl. Acad. Sci. U. S. A.*, 2002, **99**, 15524–15529.
48 E. van Rooij and S. Kauppinen, *EMBO Mol. Med.*, 2014, **6**, 851–864.
49 Y. K. Ho, W. T. Xu and H. P. Too, *PLOS ONE*, 2013, **8**, e72463.
50 N. Ludwig, P. Leidinger, K. Becker, C. Backes, T. Fehlmann, C. Pallasch, S. Rheinheimer, B. Meder, C. Stähler, E. Meese and A. Keller, *Nucleic Acids Res.*, 2016, gkw116.
51 P. S. Mitchell, R. K. Parkin, E. M. Kroh, B. R. Fritz, S. K. Wyman, E. L. Pogosova-Agadjanyan, A. Peterson, J. Noteboom, K. C. O'Briant, A. Allen, D. W. Lin, N. Urban, C. W. Drescher, B. S. Knudsen, D. L. Stirewalt, R. Gentleman, R. L. Vessella, P. S. Nelson, D. B. Martin and M. Tewari, *Proc. Natl. Acad. Sci.*, 2008, **105**, 10513–10518.
52 X. Chen, Y. Ba, L. Ma, X. Cai, Y. Yin, K. Wang, J. Guo, Y. Zhang, J. Chen, X. Guo, Q. Li, X. Li, W. Wang, Y. Zhang, J. Wang, X. Jiang, Y. Xiang, C. Xu, P. Zheng, J. Zhang, R. Li, H. Zhang, X. Shang, T. Gong, G. Ning, J. Wang, K. Zen, J. Zhang and C.-Y. Zhang, *Cell Res.*, 2008, **18**, 997–1006.
53 T. O. Yau, C. W. Wu, C.-M. Tang, Y. Chen, J. Fang, Y. Dong, Q. Liang, S. S. Man Ng, F. K. L. Chan, J. J. Y. Sung and J. Yu, *Oncotarget*, 2015, **7**, 1559–1568.
54 A. Gallo and I. Alevizos, *Methods Mol. Biol.*, 2013, **1024**, 183–190.

55 C. Beltrami, A. Clayton, A. O. Phillips, D. J. Fraser and T. Bowen, *Biochem. Soc. Trans.*, 2012, **40**, 875–879.
56 J. Zhang, S. Li, L. Li, M. Li, C. Guo, J. Yao and S. Mi, *Genomics Proteomics Bioinformatics*, 2015, **13**, 17–24.
57 C. Beltrami, A. Clayton, L. J. Newbury, P. Corish, R. H. Jenkins, A. O. Phillips, D. J. Fraser and T. Bowen, *Non-Coding RNA*, 2015, **1**, 151–166.
58 A. Gallo, M. Tandon, I. Alevizos and G. G. Illei, *PLOS ONE*, 2012, **7**, e30679.
59 M. K. McDonald, K. E. Capasso and S. K. Ajit, *J. Vis. Exp. JoVE*, 2013, e50294.
60 C. Lässer, M. Eldh and J. Lötvall, *JoVE J. Vis. Exp.*, 2012, e3037–e3037.
61 T. Thum, C. Gross, J. Fiedler, T. Fischer, S. Kissler, M. Bussen, P. Galuppo, S. Just, W. Rottbauer, S. Frantz, M. Castoldi, J. Soutschek, V. Koteliansky, A. Rosenwald, M. A. Basson, J. D. Licht, J. T. R. Pena, S. H. Rouhanifard, M. U. Muckenthaler, T. Tuschl, G. R. Martin, J. Bauersachs and S. Engelhardt, *Nature*, 2008, **456**, 980–984.
62 Y.-H. Feng and C.-J. Tsao, *Biomed. Rep.*, 2016, **5**, 395–402.
63 G. Wang, B. C.-H. Kwan, F. M.-M. Lai, K.-M. Chow, P. K.-T. Li and C.-C. Szeto, *Am. J. Nephrol.*, 2012, **36**, 412–418.
64 S. Mukhadi, R. Hull, Z. Mbita and Z. Dlamini, *Non-Coding RNA*, 2015, **1**, 192–221.
65 K. M. Pauley, S. Cha and E. K. L. Chan, *J. Autoimmun.*, 2009, **32**, 189–194.
66 N. Meola, V. A. Gennarino and S. Banfi, *PathoGenetics*, 2009, **2**, 7.
67 M. Rubio, Q. Bassat, X. Estivill and A. Mayor, *Malar. J.*, 2016, **15**, 167.
68 C. Castro-Villegas, C. Pérez-Sánchez, A. Escudero, I. Filipescu, M. Verdu, P. Ruiz-Limón, M. A. Aguirre, Y. Jiménez-Gomez, P. Font, A. Rodriguez-Ariza, J. R. Peinado, E. Collantes-Estévez, R. González-Conejero, C. Martinez, N. Barbarroja and C. López-Pedrera, *Arthritis Res. Ther.*, , DOI:10.1186/s13075-015-0555-z.
69 H. M. A. Elsayed, W. S. Khater, A. A. Ibrahim, M. S. E. Hamdy and N. A. Morshedy, *Egypt. J. Med. Hum. Genet.*, **18**, 173–179.
70 H.-Y. Chien, C.-Y. Chen, Y.-H. Chiu, Y.-C. Lin and W.-C. Li, *Int. J. Med. Sci.*, 2016, **13**, 457–465.
71 E. Aguado-Fraile, E. Ramos, E. Conde, M. Rodríguez, L. Martín-Gómez, A. Lietor, Á. Candela, B. Ponte, F. Liaño and M. L. García-Bermejo, *PloS One*, 2015, **10**, e0127175.
72 W. Sui, Y. Dai, Y. Huang, H. Lan, Q. Yan and H. Huang, *Transpl. Immunol.*, 2008, **19**, 81–85.
73 H. He, K. Jazdzewski, W. Li, S. Liyanarachchi, R. Nagy, S. Volinia, G. A. Calin, C.-G. Liu, K. Franssila, S. Suster, R. T. Kloos, C. M. Croce and A. de la Chapelle, *Proc. Natl. Acad. Sci. U. S. A.*, 2005, **102**, 19075–19080.
74 F. Weber, R. E. Teresi, C. E. Broelsch, A. Frilling and C. Eng, *J. Clin. Endocrinol. Metab.*, 2006, **91**, 3584–3591.
75 A. Caporali, M. Meloni, C. Völlenkle, D. Bonci, G. B. Sala-Newby, R. Addis, G. Spinetti, S. Losa, R. Masson, A. H. Baker, R. Agami, C. le Sage, G. Condorelli, P. Madeddu, F. Martelli and C. Emanueli, *Circulation*, 2011, **123**, 282–291.
76 F. Wu, S. Zhang, T. Dassopoulos, M. L. Harris, T. M. Bayless, S. J. Meltzer, S. R. Brant and J. H. Kwon, *Inflamm. Bowel Dis.*, 2010, **16**, 1729–1738.
77 C. N. Hayes and K. Chayama, *Int. J. Mol. Sci.*, 2016, **17**, 280.
78 B.-X. Jin, Y.-H. Zhang, W.-J. Jin, X.-Y. Sun, G.-F. Qiao, Y.-Y. Wei, L.-B. Sun, W.-H. Zhang and N. Li, *Sci. Rep.*, 2015, **5**, 15026.
79 S. Bala and G. Szabo, *Int. J. Hepatol.*, 2012, **2012**, e498232.

80 D.-Z. Liu, Y. Tian, B. P. Ander, H. Xu, B. S. Stamova, X. Zhan, R. J. Turner, G. Jickling and F. R. Sharp, *J. Cereb. Blood Flow Metab. Off. J. Int. Soc. Cereb. Blood Flow Metab.*, 2010, **30**, 92–101.
81 S. S. Hébert, K. Horré, L. Nicolaï, A. S. Papadopoulou, W. Mandemakers, A. N. Silahtaroglu, S. Kauppinen, A. Delacourte and B. De Strooper, *Proc. Natl. Acad. Sci. U. S. A.*, 2008, **105**, 6415–6420.
82 J. Kim, K. Inoue, J. Ishii, W. B. Vanti, S. V. Voronov, E. Murchison, G. Hannon and A. Abeliovich, *Science*, 2007, **317**, 1220–1224.
83 N. J. Beveridge, P. A. Tooney, A. P. Carroll, E. Gardiner, N. Bowden, R. J. Scott, N. Tran, I. Dedova and M. J. Cairns, *Hum. Mol. Genet.*, 2008, **17**, 1156–1168.
84 Current Situation Of The Kidney Disease | Kidney Research UK - Kidney Research UK - Kidney Research UK, https://www.kidneyresearchuk.org/health-information/resources/kidney-disease-in-the-uk-today, (accessed 6 January 2017).
85 26a2c68f-ed7c-4e57-bc01-e97526a86c04.pdf, http://www.britishrenal.org/BritishRenalSociety/files/26/26a2c68f-ed7c-4e57-bc01-e97526a86c04.pdf, (accessed 6 January 2017).
86 K112-00 1..14 - web_book_07-04-16.pdf, https://www.renalreg.org/wp-content/uploads/2015/01/web_book_07-04-16.pdf, (accessed 6 January 2017).
87 Diabetes Prevalence 2016 (November 2016) - Diabetes UK, https://www.diabetes.org.uk/Professionals/Position-statements-reports/Statistics/Diabetes-prevalence-2016/, (accessed 6 January 2017).
88 M. Lopez-Anton, T. Bowen and R. H. Jenkins, *BioMed Res. Int.*, 2015, **2015**, 929806.
89 K. J. Siddle, L. Tailleux, M. Deschamps, Y.-H. E. Loh, C. Deluen, B. Gicquel, C. Antoniewski, L. B. Barreiro, L. Farinelli and L. Quintana-Murci, *PLoS Genet.*, 2015, **11**, e1005064.
90 G. S. Tillotson and S. H. Zinner, *Expert Rev. Anti Infect. Ther.*, 2017, 663–676.
91 E. Várallyay, J. Burgyán and Z. Havelda, *Nat. Protoc.*, 2008, **3**, 190–196.
92 D. W. Wegman and S. N. Krylov, *Angew. Chem. Int. Ed.*, 2011, **50**, 10335–10339.
93 Z. Shi, J. J. Johnson and M. S. Stack, *J. Oncol.*, 2012, **2012**, e903581.
94 S. F. Clarke and J. R. Foster, *Br. J. Biomed. Sci.*, 2012, **69**, 83–93.
95 R. Sanders, K. J. Koval, T. DiPasquale, G. Schmelling, S. Stenzler and E. Ross, *J. Bone Joint Surg. Am.*, 1993, **75**, 326–330.
96 M. Cox and D. L. Nelson, *Lehninger Principles of Biochemistry*, Palgrave Macmillan, New York, 4th Revised edition edition., 2008.
97 L. E. H. Trainor, *The Triplet Genetic Code: Key to Living Organisms*, World Scientific, 2001.
98 J. D. Watson and F. H. Crick, *Nature*, 1953, **171**, 737–738.
99 D. M. Perreault and E. V. Anslyn, *Angew. Chem. Int. Ed.*, 1997, **36**, 432–450.
100 K. L. Dueholm, M. Egholm, C. Behrens, L. Christensen, H. F. Hansen, T. Vulpius, K. H. Petersen, R. H. Berg, P. E. Nielsen and O. Buchardt, *J. Org. Chem.*, 1994, **59**, 5767–5773.
101 P. E. Nielsen, M. Egholm, R. H. Berg and O. Buchardt, *Science*, 1991, **254**, 1497–1500.
102 C. Avitabile, L. Moggio, L. D. D'Andrea, C. Pedone and A. Romanelli, *Tetrahedron Lett.*, 2010, **51**, 3716–3718.
103 D. Pokharel, S. Fueangfung, M. Zhang and S. Fang, *Biopolymers*, 2014, **102**, 487–493.
104 S. Ellipilli, S. Palvai and K. N. Ganesh, *J. Org. Chem.*, 2016, **81**, 6364–6373.
105 J. Tse, Y. Wang, T. Zengeya, E. Rozners and A. Tan-Wilson, *Anal. Biochem.*, 2015, **470**, 34–40.
106 M. Moccia, M. F. A. Adamo and M. Saviano, *Artif. DNA PNA XNA*, 2016, **5**, e11071716 1-15.

107 N. T. S. De Costa and J. M. Heemstra, *PLoS ONE*, 2013, **8**, e58670.
108 T. Akisawa, K. Yamada and F. Nagatsugi, *Bioorg. Med. Chem. Lett.*, 2016, **26**, 5902–5906.
109 S. Ellipilli and K. N. Ganesh, *J. Org. Chem.*, 2015, **80**, 9185–9191.
110 A. Kiviniemi, M. Murtola, P. Ingman and P. Virta, *J. Org. Chem.*, 2013, **78**, 5153–5159.
111 M. Hollenstein and C. J. Leumann, *Org. Lett.*, 2003, **5**, 1987–1990.
112 S. Siddiquee, K. Rovina and A. Azriah, *Adv. Tech. Biol. Med.*, 2015, **3**, 1–10.
113 S. K. Singh, A. A. Koshkin, J. Wengel and P. Nielsen, *Chem. Commun.*, 1998, 455–456.
114 A. A. Koshkin, S. K. Singh, P. Nielsen, V. K. Rajwanshi, R. Kumar, M. Meldgaard, C. E. Olsen and J. Wengel, *Tetrahedron*, 1998, **54**, 3607–3630.
115 W. Saenger, *Principles of Nucleic Acid Structure*, Springer Science & Business Media, 2013.
116 I. Faustino, A. Pérez and M. Orozco, *Biophys. J.*, 2010, **99**, 1876–1885.
117 H. Doessing and B. Vester, *Mol. Basel Switz.*, 2011, **16**, 4511–4526.
118 U. A. Ørom, S. Kauppinen and A. H. Lund, *Gene*, 2006, **372**, 137–141.
119 R. Nedaeinia, M. Sharifi, A. Avan, M. Kazemi, L. Rafiee, M. Ghayour-Mobarhan and R. Salehi, *Cancer Gene Ther.*, 2016, **23**, 246–253.
120 Z. S. Dean, P. Elias, N. Jamilpour, U. Utzinger and P. K. Wong, *Anal. Chem.*, 2016, **88**, 8902–8907.
121 E. E. Swayze, A. M. Siwkowski, E. V. Wancewicz, M. T. Migawa, T. K. Wyrzykiewicz, G. Hung, B. P. Monia and C. F. Bennett, *Nucleic Acids Res.*, 2007, **35**, 687–700.
122 P. P. Seth, A. Siwkowski, C. R. Allerson, G. Vasquez, S. Lee, T. P. Prakash, E. V. Wancewicz, D. Witchell and E. E. Swayze, *J. Med. Chem.*, 2009, **52**, 10–13.
123 S. M. Abdur Rahman, S. Seki, S. Obika, H. Yoshikawa, K. Miyashita and T. Imanishi, *J. Am. Chem. Soc.*, 2008, **130**, 4886–4896.
124 P. J. Hrdlicka, B. R. Babu, M. D. Sørensen and J. Wengel, *Chem. Commun.*, 2004, 1478–1479.
125 P. Kumar, M. E. Østergaard, B. Baral, B. A. Anderson, D. C. Guenther, M. Kaura, D. J. Raible, P. K. Sharma and P. J. Hrdlicka, *J. Org. Chem.*, 2014, **79**, 5047–5061.
126 C. Briones and M. Moreno, *Anal. Bioanal. Chem.*, 2012, **402**, 3071–3089.
127 J. Lee, I.-S. Park, H. Kim, J.-S. Woo, B.-S. Choi and D.-H. Min, *Biosens. Bioelectron.*, 2015, **69**, 167–173.
128 J. K. Watts, *Chem. Commun.*, 2013, **49**, 5618–5620.
129 D. Duan, K. Zheng, Y. Shen, R. Cao, L. Jiang, Z. Lu, X. Yan and J. Li, *Nucleic Acids Res.*, 2011, **39**, e154–e154.
130 M. C. Riedy, E. A. Timm and C. C. Stewart, *BioTechniques*, 1995, **18**, 70–74, 76.
131 M. K. Udvardi, T. Czechowski and W.-R. Scheible, *Plant Cell*, 2008, **20**, 1736–1737.
132 Y. Huang, W. Gong, H. Ren, J. Xiong, X. Gao and X. Sun, *Gene*, 2017, **626**, 298–304.
133 G. Klanert, V. Jadhav, V. Shanmukam, A. Diendorfer, M. Karbiener, M. Scheideler, J. H. Bort, J. Grillari, M. Hackl and N. Borth, *J. Biotechnol.*, 2016, **235**, 150–161.
134 A. Brunet-Vega, C. Pericay, M. E. Quílez, M. J. Ramírez-Lázaro, X. Calvet and S. Lario, *Anal. Biochem.*, 2015, **488**, 28–35.
135 R. He, X. Xie, L. Lv, Y. Huang, X. Xia, X. Chen and L. Zhang, *Biochem. Biophys. Res. Commun.*, 2017, **486**, 342–348.
136 C. Chen, D. A. Ridzon, A. J. Broomer, Z. Zhou, D. H. Lee, J. T. Nguyen, M. Barbisin, N. L. Xu, V. R. Mahuvakar, M. R. Andersen, K. Q. Lao, K. J. Livak and K. J. Guegler, *Nucleic Acids Res.*, 2005, **33**, e179.
137 M. F. Kramer, in *Current Protocols in Molecular Biology*, John Wiley & Sons, Inc., 2001.

138 X. Min, M. Zhang, F. Huang, X. Lou and F. Xia, *ACS Appl. Mater. Interfaces*, 2016, **8**, 8998–9003.
139 E. A. Hunt, A. M. Goulding and S. K. Deo, *Anal. Biochem.*, 2009, **387**, 1–12.
140 H. Wang, R. A. Ach and B. Curry, *RNA*, 2007, **13**, 151–159.
141 L. A. Neely, S. Patel, J. Garver, M. Gallo, M. Hackett, S. McLaughlin, M. Nadel, J. Harris, S. Gullans and J. Rooke, *Nat. Methods*, 2006, **3**, 41–46.
142 X.-P. Wang, B.-C. Yin and B.-C. Ye, *RSC Adv.*, 2013, **3**, 8633–8636.
143 X. Zhao, L. Xu, M. Sun, W. Ma, X. Wu, H. Kuang, L. Wang and C. Xu, *Small*, 2016, **12**, 4662–4668.
144 Y. Li, J. Zhang, J. Zhao, L. Zhao, Y. Cheng and Z. Li, *Analyst*, 2016, **141**, 1071–1076.
145 Y. Tu, P. Wu, H. Zhang and C. Cai, *Chem. Commun.*, 2012, **48**, 10718–10720.
146 S. Li, K. He, R. Liao, C. Chen, X. Chen and C. Cai, *Talanta*, 2017, **174**, 679–683.
147 Q. Xu, F. Ma, S. Huang, B. Tang and C. Zhang, *Anal. Chem.*, 2017, **89**, 7077–7083.
148 C. Ma, E. S. Yeung, S. Qi and R. Han, *Anal. Bioanal. Chem.*, 2012, **402**, 2217–2220.
149 K. Josefsen and H. Nielsen, *Methods Mol. Biol.*, 2011, **703**, 87–105.
150 D. C. Rio, *Cold Spring Harb. Protoc.*, 2014, **2014**, pdb.prot080838.
151 X. Su, H. F. Teh, X. Lieu and Z. Gao, *Anal. Chem.*, 2007, **79**, 7192–7197.
152 C. M. Lederer and V. S. Shirley, Eds., *Table of Isotopes*, Wiley-Blackwell, New York, 7th Edition edition., 1979.
153 A. Válóczi, C. Hornyik, N. Varga, J. Burgyán, S. Kauppinen and Z. Havelda, *Nucleic Acids Res.*, 2004, **32**, e175.
154 G. S. Pall, C. Codony-Servat, J. Byrne, L. Ritchie and A. Hamilton, *Nucleic Acids Res.*, 2007, **35**, e60.
155 S. W. Kim, Z. Li, P. S. Moore, A. P. Monaghan, Y. Chang, M. Nichols and B. John, *Nucleic Acids Res.*, 2010, **38**, e98.
156 S. H. Ramkissoon, L. A. Mainwaring, E. M. Sloand, N. S. Young and S. Kajigaya, *Mol. Cell. Probes*, 2006, **20**, 1–4.
157 Y. S. Choi, L. O. Edwards, A. DiBello and A. M. Jose, *Nucleic Acids Res.*, 2017, **45**, e87.
158 C. Li, D. Wu, X. Hu, Y. Xiang, Y. Shu and G. Li, *Anal. Chem.*, 2016, **88**, 7583–7590.
159 J. O. Bockris, *Volume 1: Modern Electrochemistry: Ionics*, Springer, New York, 2 edition., 2013.
160 L. Galvani, A. Volta, J. Zambelli and donor D. Burndy Library, *Aloysii Galvani De viribus electricitatis in motu musculari commentarius*, Bononiae : Ex Typographia Instituti Scientiarium, 1791.
161 E. Gileadi, *Physical Electrochemistry: Fundamentals, Techniques and Applications*, Wiley VCH, Weinheim, 2011.
162 J. Wang, *Analytical Electrochemistry*, Wiley-Blackwell, Hoboken, N.J, 3rd Revised edition edition., 2006.
163 C. H. Hamann, A. Hamnett and W. Vielstich, *Electrochemistry*, Wiley VCH, Weinheim, 2nd, Completely Revised and Updated Edition edition edn., 2007.
164 P. R. Roberge, *Corrosion Engineering: Principles and Practice*, McGraw-Hill Education, New York, 2008.
165 J. Kotz, P. Treichel and J. Townsend, *Chemistry and Chemical Reactivity*, Cengage Learning, 2008.
166 A. J. Bard and L. Faulkner, *Electrochemical Methods: Fundamentals and Applications*, John Wiley & Sons, New York, 2nd Revised edition edition., 2001.

167 A. E. Kaifer and M. Gómez-Kaifer, *Supramolecular Electrochemistry*, Wiley VCH, Weinheim ; New York, 1999.
168 D. A. Skoog, F. J. Holler and S. R. Crouch, *Principles of Instrumental Analysis 6th edition*, Thomson Brooks/Cole, 6th edition., 2007.
169 Z. Gao and Y. H. Yu, *Biosens. Bioelectron.*, 2007, **22**, 933–940.
170 Q. Wang, Y. Ding, F. Gao, S. Jiang, B. Zhang, J. Ni and F. Gao, *Anal. Chim. Acta*, 2013, **788**, 158–164.
171 Z. Gao, H. Deng, W. Shen and Y. Ren, *Anal. Chem.*, 2013, **85**, 1624–1630.
172 R. S. Nicholson, *Anal. Chem.*, 1965, **37**, 1351–1355.
173 O. Makhotkina and P. A. Kilmartin, *Anal. Chim. Acta*, 2010, **668**, 155–165.
174 H. Yang, Y. Gu, Y. Deng and F. Shi, *Chem. Commun.*, 2002, **0**, 274–275.
175 A. W. Bott and W. R. Heineman, Current Separations Vol.20 No.4, http://www.currentseparations.com/issues/20-4/index.html, (accessed 27 July 2017).
176 G. Inzelt, in *Electroanalytical Methods*, Springer, Berlin, Heidelberg, 2005, pp. 137–148.
177 Y. Zhou, M. Wang, X. Meng, H. Yin and S. Ai, *RSC Adv.*, 2012, **2**, 7140–7145.
178 H. Yin, Y. Zhou, C. Chen, L. Zhu and S. Ai, *The Analyst*, 2012, **137**, 1389–1395.
179 H. Yin, Y. Zhou, H. Zhang, X. Meng and S. Ai, *Biosens. Bioelectron.*, 2012, **33**, 247–253.
180 Y. Zhou, Z. Zhang, Z. Xu, H. Yin and S. Ai, *New J. Chem.*, 2012, **36**, 1985–1991.
181 B. Yao, Y. Liu, M. Tabata, H. Zhu and Y. Miyahara, *Chem. Commun.*, 2014, **50**, 9704–9706.
182 R. G. Compton, *Electrode Potentials*, Oxford University Press, U.S.A., Oxford ; New York, 1996.
183 A. C. Fisher, *Electrode Dynamics*, Oxford University Press, U.S.A., Oxford ; New York, 1996.
184 M. Labib, N. Khan, S. M. Ghobadloo, J. Cheng, J. P. Pezacki and M. V. Berezovski, *J. Am. Chem. Soc.*, 2013, **135**, 3027–3038.
185 A. R. Cardoso, F. T. C. Moreira, R. Fernandes and M. G. F. Sales, *Biosens. Bioelectron.*, 2016, **80**, 621–630.
186 F. M. Mirabella, *Internal Reflection Spectroscopy: Theory and Applications*, CRC Press, 1992.
187 B. C. Smith, *Fundamentals of Fourier Transform Infrared Spectroscopy, Second Edition*, CRC Press, 2011.
188 B. C. Smith, *Infrared Spectral Interpretation: A Systematic Approach*, CRC Press, 1998.
189 A. Burrows, A. Parsons, G. Price, G. Pilling and J. Holman, *Chemistry^3: Introducing inorganic, organic and physical chemistry*, OUP Oxford, Oxford ; New York, 2009.
190 C. J. Chen, *Introduction to Scanning Tunneling Microscopy*, Oxford University Press Inc, New York, 1993.
191 G. Haugstad, *Atomic Force Microscopy: Understanding Basic Modes and Advanced Applications*, Wiley-Blackwell, Hoboken, N.J, 1st edition., 2012.
192 N. J. DiNardo, *Nanoscale Characterization of Surfaces and Interfaces*, Wiley VCH, Weinheim, 1994.
193 J. Goldstein, D. E. Newbury, D. C. Joy, C. E. Lyman, P. Echlin, E. Lifshin, L. Sawyer and J. R. Michael, *Scanning Electron Microscopy and X-ray Microanalysis: Third Edition*, Springer, New York, 3rd Corrected ed. 2003. Corr. 2nd printing 2007 edition., 2007.
194 P. Eaton and P. West, *Atomic Force Microscopy*, Oxford University Press, 2010.
195 Y. Sugimoto, M. Abe and S. Morita, in *Imaging and Manipulation of Adsorbates Using Dynamic Force Microscopy*, Springer, Cham, 2015, pp. 49–62.
196 R. Barattin and N. Voyer, *SpringerLink*, 2011, 457–483.
197 K. Haase and A. E. Pelling, *J. R. Soc. Interface*, , DOI:10.1098/rsif.2014.0970.

198 A. L. Gray, *Analyst*, 1985, **110**, 551–556.
199 R. Thomas, *Practical Guide to ICP-MS: A Tutorial for Beginners, Third Edition*, CRC Press, 2013.
200 L. Dussubieux, M. Golitko and B. Gratuze, *Recent Advances in Laser Ablation ICP-MS for Archaeology*, Springer, 2016.
201 B. Hattendorf, C. Latkoczy and D. Günther, *Anal. Chem.*, 2003, **75**, 341 A-347 A.
202 D. Pozebon, G. L. Scheffler, V. L. Dressler and M. A. G. Nunes, *J. Anal. At. Spectrom.*, 2014, **29**, 2204–2228.
203 M. A. O. da Silva and M. A. Z. Arruda, *Metallomics*, 2012, **5**, 62–67.
204 I. Rodushkin and M. D. Axelsson, *Sci. Total Environ.*, 2003, **305**, 23–39.
205 A. Mohamad Ghazi, S. Shuttleworth, S. J. Angulo and D. H. Pashley, *J. Anal. At. Spectrom.*, 2000, **15**, 1335–1341.
206 S. Panighello, A. Kavčič, K. Vogel-Mikuš, N. H. Tennent, A. Wallert, S. B. Hočevar and J. T. van Elteren, *Microchem. J.*, 2016, **125**, 105–115.
207 R. Scarpelli, A. M. De Francesco, M. Gaeta, D. Cottica and L. Toniolo, *Microchem. J.*, 2015, **119**, 93–101.
208 H. A. Gasteiger, N. M. Markovic and P. N. J. Ross, *J. Phys. Chem.*, , DOI:10.1021/j100020a063.
209 H. Liu, Y. Zhang, Q. Ke, K. Hung Ho, Y. Hu and J. Wang, *J. Mater. Chem. A*, 2013, **1**, 12962–12970.
210 *Electrochemical Analysis of Proteins and Cells | Genxi Li | Springer*, .
211 D. M. Fouad and W. A. El-Said, *J. Nanomater.*, 2016, **2016**, e6194230.
212 A. Ulman, *Chem. Rev.*, 1996, **96**, 1533–1554.
213 L. D. Burke and P. F. Nugent, *Gold Bull.*, 1997, **30**, 43–53.
214 L. Y. S. Lee and R. B. Lennox, *Langmuir*, 2007, **23**, 292–296.
215 Y. Zhao, R. Wang, Z. Han, C. Li, Y. Wang, B. Chi, J. Li and X. Wang, *Electrochimica Acta*, 2015, **151**, 544–551.
216 M. Escudero-Escribano, C. Wildi, J. A. Mwanda and A. Cuesta, *J. Solid State Electrochem.*, 2016, **20**, 1087–1094.
217 JASDL » Analytical Electrochemistry, http://jasdl.asdlib.org/2009/06/analytical-electrochemistry-the-basic-concepts/, (accessed 16 March 2017).
218 N. Menegazzo, C. Jin, R. J. Narayan and B. Mizaikoff, *Langmuir*, 2007, **23**, 6812–6818.
219 Q.-L. Zhao, Z.-L. Zhang, L. Bao and D.-W. Pang, *Electrochem. Commun.*, 2008, **10**, 181–185.
220 D. E. García-Rodríguez, L. H. Mendoza-Huizar, C. H. Rios-Reyes and M. A. Alatorre-Ordaz, *Quím. Nova*, 2012, **35**, 699–704.
221 M. Sankararao, S. Anandhakumar and J. Mathiyarasu, *IJCT Vol226 Novemb. 2015*.
222 S. Ergun and V. H. Tiensuu, *Nature*, 1959, **183**, 1668–1670.
223 L. A. Pesin and E. M. Baitinger, *Carbon*, 2002, **40**, 295–306.
224 P. J. F. Harris, *Philos. Mag.*, 2004, **84**, 3159–3167.
225 Y. Xue, X. Li, H. Li and W. Zhang, *Nat. Commun.*, 2014, **5**, 4348.
226 N. Pourmand, M. Karhanek, H. H. J. Persson, C. D. Webb, T. H. Lee, A. Zahradníková and R. W. Davis, *Proc. Natl. Acad. Sci.*, 2006, **103**, 6466–6470.
227 L. Zou, Y. Xu, P. Luo, S. Zhang and B. Ye, *Analyst*, 2011, **137**, 414–419.
228 K. M. Millan, A. J. Spurmanis and S. R. Mikkelsen, *Electroanalysis*, 1992, **4**, 929–932.
229 BASi® | Working Electrodes, https://www.basinc.com/manuals/LC_epsilon/Maintenance/Working/working#glassy, (accessed 10 February 2017).

230 T. Mary Vergheese and S. Berchmans, *Electrochimica Acta*, 2006, **52**, 567–574.
231 M. Noel and P. N. Anantharaman, *Analyst*, 1985, **110**, 1095–1103.
232 F. Doğan, İ. Kaya and K. Temizkan, *Polym. Int.*, 2015, **64**, 1639–1648.
233 J. Clayden, N. Greeves and S. Warren, *Organic Chemistry*, OUP Oxford, 2012.
234 H. Lee, S. Han, C. S. Kwon and D. Lee, *Protein Cell*, 2016, **7**, 100–113.
235 *Composition and Concentrative Properties of Human Urine*, National Aeronautics and Space Administration, 1971.
236 R. C. Campbell, P. Ruggenenti and G. Remuzzi, *Curr. Diab. Rep.*, 2003, **3**, 497–504.
237 J. I. Park, H. Baek, B. R. Kim and H. H. Jung, *PLOS ONE*, 2017, **12**, e0171106.
238 E. V. Petrotchenko, J. J. Serpa, D. B. Hardie, M. Berjanskii, B. P. Suriyamongkol, D. S. Wishart and C. H. Borchers, *Mol. Cell. Proteomics*, 2012, **11**, M111.013524.
239 T. D. Schmittgen, E. J. Lee, J. Jiang, A. Sarkar, L. Yang, T. S. Elton and C. Chen, *Methods San Diego Calif*, 2008, **44**, 31–38.
240 J. Wang, L. Fang and D. Lopez, *The Analyst*, 1994, **119**, 455–458.
241 D. Zang, M. Yan, S. Ge, L. Ge and J. Yu, *The Analyst*, 2013, **138**, 2704–2711.
242 A. Avramescu, S. Andreescu, T. Noguer, C. Bala, D. Andreescu and J.-L. Marty, *Anal. Bioanal. Chem.*, 2002, **374**, 25–32.
243 G. Carpini, F. Lucarelli, G. Marrazza and M. Mascini, *Biosens. Bioelectron.*, 2004, **20**, 167–175.
244 M. Li, Y.-T. Li, D.-W. Li and Y.-T. Long, *Anal. Chim. Acta*, 2012, **734**, 31–44.
245 B. R. Šljukić, R. O. Kadara and C. E. Banks, *Anal. Methods*, 2011, **3**, 105–109.
246 R. O. Kadara and I. E. Tothill, *Anal. Chim. Acta*, 2008, **623**, 76–81.
247 E. Suprun, G. Evtugyn, H. Budnikov, F. Ricci, D. Moscone and G. Palleschi, *Anal. Bioanal. Chem.*, 2005, **383**, 597–604.
248 J. Wang, P. V. Pamidi and D. S. Park, *Anal. Chem.*, 1996, **68**, 2705–2708.
249 S. Mu, X. Wang, Y.-T. Li, Y. Wang, D.-W. Li and Y.-T. Long, *The Analyst*, 2012, **137**, 3220–3223.
250 S. Wang, N. Liu, C. Yang, W. Liu, J. Su, L. Li, C. Yang and Y. Gao, *RSC Adv.*, 2015, **5**, 85799–85805.
251 J. Suikkola, T. Björninen, M. Mosallaei, T. Kankkunen, P. Iso-Ketola, L. Ukkonen, J. Vanhala and M. Mäntysalo, *Sci. Rep.*, 2016, **6**, 25784.
252 J. Liang, K. Tong and Q. Pei, *Adv. Mater.*, 2016, **28**, 5986–5996.
253 R. D. Munje, S. Muthukumar and S. Prasad, *Sens. Actuators B Chem.*, 2017, **238**, 482–490.
254 C. P. Bonafide, D. T. Jamison and E. E. Foglia, *JAMA*, 2017, **317**, 353–354.
255 C. Stadlbauer, C. Reiter, B. Patzak, G. Stingeder and T. Prohaska, *Anal. Bioanal. Chem.*, 2007, **388**, 593–602.
256 J. Shang, F. Xue and E. Ding, *Chem. Commun.*, 2015, **51**, 15811–15814.
257 P. Wongkaew and S. Poosittisak, *Int. J. Geomate*, 2016, **11**, 2356–2362.
258 D. W. M. Arrigan, *Electrochemical Strategies in Detection Science*, Royal Society of Chemistry, 2015.
259 C. G. Zoski, *Handbook of Electrochemistry*, Elsevier, 2006.
260 P. N. Bartlett, *Bioelectrochemistry: Fundamentals, Experimental Techniques and Applications*, John Wiley & Sons, 2008.
261 D. R. Gamota, P. Brazis, K. Kalyanasundaram and J. Zhang, *Printed Organic and Molecular Electronics*, Springer Science & Business Media, 2013.
262 V. Jazbutyte and T. Thum, *Curr. Drug Targets*, 2010, **11**, 926–935.
263 H. S. Stoker, *General, Organic, and Biological Chemistry*, Cengage Learning, 2012.

264 A. Ringk, W. S. Christian Roelofs, E. C. P. Smits, C. van der Marel, I. Salzmann, A. Neuhold, G. H. Gelinck, R. Resel, D. M. de Leeuw and P. Strohriegl, *Org. Electron.*, 2013, **14**, 1297–1304.
265 Y. Wu, P. Xue, K. M. Hui and Y. Kang, *ChemElectroChem*, 2014, **1**, 722–727.

Appendix 1: Chapter 2 additional data.

Table A1.1 The raw data obtained for the coulometric response (C) of using an anti-miR-21 probe strand for target hsa-miR-21-5p hybridisation at different concentrations.

	Experiment number				Experiment number		
10^{-8} M	**1**	**2**	**3**	**10^{-12} M**	**1**	**2**	**3**
DNA only	-2.096E-04	-2.067E-04	-2.077E-04	**DNA only**	-2.194E-04	-2.143E-04	-2.322E-04
DNA/RNA	-1.641E-04	-1.637E-04	-1.633E-04	**DNA/RNA**	-1.983E-04	-1.991E-04	-2.139E-04
Change	4.554E-05	4.304E-05	4.448E-05	**Change**	2.115E-05	1.520E-05	1.833E-05
Average	4.435E-05	**Average(µC)**	44.353	**Average**	1.823E-05	**Average(µC)**	18.227
S.D	1.025E-06	**S.D (µC)**	1.025	**S.D**	2.430E-06	**S.D (µC)**	2.430
10^{-9} M	**1**	**2**	**3**	**10^{-13} M**	**1**	**2**	**3**
DNA only	-2.066E-04	-2.233E-04	-2.115E-04	**DNA only**	-2.330E-04	-2.341E-04	-2.156E-04
DNA/RNA	-1.691E-04	-1.868E-04	-1.817E-04	**DNA/RNA**	-2.159E-04	-2.176E-04	-2.047E-04
Change	3.756E-05	3.644E-05	2.982E-05	**Change**	1.706E-05	1.647E-05	1.092E-05
Average	3.461E-05	**Average(µC)**	34.607	**Average**	1.482E-05	**Average(µC)**	14.817
S.D	3.415E-06	**S.D (µC)**	3.415	**S.D**	2.766E-06	**S.D (µC)**	2.766
10^{-10} M	**1**	**2**	**3**	**10^{-14} M**	**1**	**2**	**3**
DNA only	-2.168E-04	-2.207E-04	-2.194E-04	**DNA only**	-2.398E-04	-2.241E-04	-1.989E-04
DNA/RNA	-1.894E-04	-1.915E-04	-1.876E-04	**DNA/RNA**	-2.241E-04	-2.249E-04	-1.943E-04
Change	2.743E-05	2.925E-05	3.183E-05	**Change**	1.570E-05	-8.600E-07	4.580E-06
Average	2.950E-05	**Average(µC)**	29.503	**Average**	6.473E-06	**Average(µC)**	6.473
S.D	1.805E-06	**S.D (µC)**	1.805	**S.D**	6.892E-06	**S.D (µC)**	6.892
10^{-11} M	**1**	**2**	**3**				
DNA only	-2.292E-04	-2.342E-04	-2.268E-04				
DNA/RNA	-2.064E-04	-2.070E-04	-2.084E-04				
Change	2.284E-05	2.725E-05	1.847E-05				
Average	2.285E-05	**Average(µC)**	22.853				
S.D	3.584E-06	**S.D (µC)**	3.584				

Table A1.2 The raw data for the R_{CT} (charge transfer) resistance response (Ω) of using an anti-miR-21 probe strand for target hsa-miR-21-5p hybridisation at different concentrations.

	Experiment number				Experiment number		
10^{-8} M	**1**	**2**	**3**	**10^{-12} M**	**1**	**2**	**3**
DNA only	794.9	791.8	883.8	**DNA only**	604.4	756.2	358.2
DNA/RNA	2129.2	2079.5	2099.1	**DNA/RNA**	1024.0	1212.1	731.2
Change	1334.3	1287.7	1215.3	**Change**	419.6	455.9	372.9
Average	1279.1			**Average**	416.1		
S.D	48.9			**S.D**	34.0		
10^{-9} M	**1**	**2**	**3**	**10^{-13} M**	**1**	**2**	**3**
DNA only	804.6	698.2	674.1	**DNA only**	439.2	494.9	810.2
DNA/RNA	1897.2	1746.9	1727.4	**DNA/RNA**	811.3	761.7	1086.8
Change	1092.6	1048.7	1053.3	**Change**	372.1	266.8	276.6
Average	1064.8			**Average**	305.2		
S.D	19.7			**S.D**	47.5		
10^{-10} M	**1**	**2**	**3**	**10^{-14} M**	**1**	**2**	**3**
DNA only	822.2	524.4	530.9	**DNA only**	455.7	518.3	746.2
DNA/RNA	1380.8	1209.8	1249.6	**DNA/RNA**	729.1	574.5	1175.3
Change	558.7	685.4	718.7	**Change**	273.4	56.2	429.1
Average	654.3			**Average**	252.9		
S.D	69.0			**S.D**	152.9		
10^{-11} M	**1**	**2**	**3**				
DNA only	394.5	418.1	478.8				
DNA/RNA	904.9	902.4	879.9				
Change	510.4	484.3	401.1				
Average	465.3						
S.D	46.6						

Table A1.3 The coulometry data collected using a solution of TMD buffer as the hybridisation target for an anti-miR-21 probe strand. Used in the calculation of limit of detection.

Buffer Responses	**1**	**2**	**3**	**4**
With DNA (C)	-1.57E-04	-1.48E-04	-1.34E-04	-1.32E-04
With hybrid (C)	-1.48E-04	-1.34E-04	-1.32E-04	-1.39E-04
Coulometry change (C)	9.49E-06	1.37E-05	1.92E-06	-6.62E-06
Average coulometry change (μC)	4.62			
Standard deviation	7.74			
3x Standard deviation	23.22			
3x Standard deviation/ gradient	3.96			
Above with average added	8.58			
Limit of detection (M)	**1.97E-14**			

Table A1.4 Coulometry response (C) raw data of using an anti-miR-21 probe strand for target hsa-miR-21-5p, along with mismatched sequences with 1, 2, and 3 mismatches and a hsa-miR-16-5p sequence, given for a 10 nM solution of each target.

	Experiment number		
Complement			
Average	4.435E-05	**Average (µC)**	44.353
S.D	1.025E-06	**S.D (µC)**	1.025
1 Mismatch	**1**	**2**	**3**
DNA alone	-2.046E-04	-2.202E-04	-2.200E-04
DNA/RNA	-1.851E-04	-2.054E-04	-2.048E-04
Change	1.956E-05	1.484E-05	1.516E-05
Average	1.652E-05	**Average (µC)**	16.520
S.D	2.154E-06	**S.D (µC)**	2.154
2 Mismatches	**1**	**2**	**3**
DNA alone	-2.133E-04	-2.212E-04	-2.175E-04
DNA/RNA	-2.073E-04	-2.098E-04	-2.039E-04
Change	6.080E-06	1.145E-05	1.353E-05
Average	1.035E-05	**Average (µC)**	10.353
S.D	3.139E-06	**S.D (µC)**	3.139
3 Mismatches	**1**	**2**	**3**
DNA alone	-2.094E-04	-2.283E-04	-2.193E-04
DNA/RNA	-2.036E-04	-2.240E-04	-2.110E-04
Change	5.890E-06	4.320E-06	8.340E-06
Average	6.183E-06	**Average (µC)**	6.183
S.D	1.654E-06	**S.D (µC)**	1.654
miR-16	**1**	**2**	**3**
DNA alone	-1.995E-04	-2.237E-04	-2.048E-04
DNA/RNA	-1.920E-04	-2.182E-04	-2.043E-04
Change	7.520E-06	5.430E-06	5.200E-07
Average	4.490E-06	**Average (µC)**	4.490
S.D	3.593E-06	**S.D (µC)**	3.593
1mm Signal drop (%)	62.75		
2mm Signal drop (%)	76.66		
3mm signal drop(%)	86.06		
miR-16 signal drop(%)	89.88		

Table A1.5 The raw data for the R_{CT} (charge transfer) resistance response (Ω) using an anti-miR-21 probe strand for target hsa-miR-21-5p, along with mismatched sequences with 1, 2, and 3 mismatches and a hsa-miR-16-5p sequence, given for a 10 nM solution of each target.

	Experiment number		
Complement			
Average	1279.1		
STD	48.9		
1 Mismatch	**1**	**2**	**3**
DNA alone	663.0	497.8	483.0
DNA/RNA	1348.3	933.4	906.2
Change	685.3	435.6	423.2
Average	514.7		
S.D	120.7		
2 Mismatches	**1**	**2**	**3**
DNA alone	537.4	520.9	413.5
DNA/RNA	803.3	870.7	916.4
Change	265.9	349.8	502.9
Average	372.9		
S.D	98.1		
3 Mismatches	**1**	**2**	**3**
DNA alone	534.5	332.4	399.6
DNA/RNA	869.3	557.2	731.8
Change	334.8	224.7	332.2
Average	297.2		
S.D	51.3		
miR-16	**1**	**2**	**3**
DNA alone	884.4	352.8	597.1
DNA/RNA	1333.2	604.5	783.9
Change	448.8	251.7	186.9
Average	295.8		
S.D	111.4		
1mm Signal drop (%)	59.76		
2mm Signal drop (%)	70.85		
3mm signal drop(%)	76.76		
miR-16 signal drop(%)	76.87		

Table A1.6 The raw data obtained for the coulometric response (C) of using an anti-miR-16 probe strand for target hsa-miR-16-5p hybridisation at different concentrations.

	Experiment number			Experiment number			
10^{-8} M	**1**	**2**	**3**	**10^{-12} M**	**1**	**2**	**3**
DNA only	-2.010E-04	-2.321E-04	-2.074E-04	**DNA only**	-2.342E-04	-1.801E-04	-1.877E-04
DNA/RNA	-1.688E-04	-1.878E-04	-1.625E-04	**DNA/RNA**	-2.081E-04	-1.639E-04	-1.665E-04
Change	3.220E-05	4.428E-05	4.484E-05	**Change**	2.611E-05	1.623E-05	2.116E-05
Average	4.044E-05	**Average(µC)**	40.440	**Average**	2.116E-05	**Average(µC)**	21.165
S.D	5.831E-06	**S.D (µC)**	5.831	**S.D**	4.035E-06	**S.D (µC)**	4.035
10^{-9} M	**1**	**2**	**3**	**10^{-13} M**	**1**	**2**	**3**
DNA only	-2.470E-04	-2.239E-04	-1.652E-04	**DNA only**	-2.179E-04	-2.308E-04	-2.228E-04
DNA/RNA	-2.204E-04	-1.841E-04	-1.218E-04	**DNA/RNA**	-2.034E-04	-2.134E-04	-2.131E-04
Change	2.662E-05	3.976E-05	4.335E-05	**Change**	1.451E-05	1.736E-05	9.690E-06
Average	3.658E-05	**Average(µC)**	36.577	**Average**	1.385E-05	**Average(µC)**	13.853
S.D	7.191E-06	**S.D (µC)**	7.191	**S.D**	3.166E-06	**S.D (µC)**	3.166
10^{-10} M	**1**	**2**	**3**	**10^{-14} M**	**1**	**2**	**3**
DNA only	-2.011E-04	-2.113E-04	-1.988E-04	**DNA only**	-2.308E-04	-2.427E-04	-1.963E-04
DNA/RNA	-1.704E-04	-1.785E-04	-1.705E-04	**DNA/RNA**	-2.218E-04	-2.291E-04	-1.868E-04
Change	3.071E-05	3.277E-05	2.827E-05	**Change**	8.980E-06	1.355E-05	9.507E-06
Average	3.058E-05	**Average(µC)**	30.583	**Average**	1.068E-05	**Average(µC)**	10.679
S.D	1.839E-06	**S.D (µC)**	1.839	**S.D**	2.042E-06	**S.D (µC)**	2.042
10^{-11} M	**1**	**2**	**3**				
DNA only	-2.300E-04	-2.162E-04	-2.236E-04				
DNA/RNA	-2.077E-04	-1.916E-04	-1.999E-04				
Change	2.236E-05	2.456E-05	2.366E-05				
Average	2.353E-05	**Average(µC)**	23.527				
S.D	9.031E-07	**S.D (µC)**	0.903				

Table A1.7 The raw data for the R_{CT} (charge transfer) resistance response (Ω) of using an anti-miR-16 probe strand for target hsa-miR-16-5p hybridisation at different concentrations.

	Experiment number		
10^{-8} M	**1**	**2**	**3**
DNA only	950.6	814.3	1357.0
DNA/RNA	2023.3	1489.4	2472.2
Change	1072.8	675.1	1115.2
Average	954.4		
S.D	198.2		
10^{-9} M	**1**	**2**	**3**
DNA only	399.5	834.1	1672.8
DNA/RNA	1061.9	1669.4	3358.7
Change	662.4	835.3	1685.9
Average	1061.2		
S.D	447.3		
10^{-10} M	**1**	**2**	**3**
DNA only	1080.4	957.8	1024.6
DNA/RNA	1985.6	1869.2	1587.6
Change	905.2	911.4	563.0
Average	793.2		
S.D	162.8		
10^{-11} M	**1**	**2**	**3**
DNA only	664.2	813.0	965.6
DNA/RNA	1225.3	1603.0	1348.0
Change	561.1	790.0	382.4
Average	577.8		
S.D	166.9		

	Experiment number		
10^{-12} M	**1**	**2**	**3**
DNA only	745.7	944.7	724.2
DNA/RNA	1105.3	1491.8	1185.9
Change	359.6	547.1	461.7
Average	456.1		
S.D	76.6		
10^{-13} M	**1**	**2**	**3**
DNA only	555.5	634.5	760.5
DNA/RNA	738.6	1084.1	1087.3
Change	183.1	449.6	326.8
Average	319.8		
S.D	108.9		
10^{-14} M	**1**	**2**	**3**
DNA only	364.0	604.5	532.5
DNA/RNA	549.6	1062.6	1001.7
Change	185.6	458.1	469.2
Average	371.0		
S.D	131.2		

Table A1.8 Raw data for coulometry response (C) using an anti-miR-21 probe following hybridisation with target miR-21 in urine samples as specified in Table 6.2.

	Experiment number		
Sample 1	**1**	**2**	**3**
DNA only	-1.996E-04	-1.990E-04	-1.808E-04
DNA/RNA	-1.901E-04	-1.724E-04	-1.543E-04
Change	9.484E-06	2.653E-05	2.651E-05
Concentration	-1.354E+01	-1.064E+01	-1.064E+01
Average (μC)	20.839	**Average**	2.084E-05
S.D (μC)	8.030	**S.D**	8.030E-06
Average Conc (log_{10}M)	-11.607		
S.D Conc	1.367		

Sample 2	**1**	**2**	**3**
DNA only	-1.785E-04	-1.675E-04	-1.813E-04
DNA/RNA	-1.408E-04	-1.308E-04	-1.558E-04
Change	3.764E-05	3.678E-05	2.553E-05
Concentration	-8.747E+00	-8.894E+00	-1.081E+01
Average (μC)	33.317	**Average**	3.332E-05
S.D (μC)	5.517	**S.D**	5.517E-06
Average Conc (log_{10}M)	-9.483		
S.D Conc	0.939		

Sample 3	**1**	**2**	**3**
DNA only	-1.730E-04	-1.804E-04	-1.748E-04
DNA/RNA	-1.467E-04	-1.474E-04	-1.531E-04
Change	2.630E-05	3.296E-05	2.169E-05
Concentration	-1.068E+01	-9.543E+00	-1.146E+01
Average (μC)	26.985	**Average**	2.698E-05
S.D (μC)	4.630	**S.D**	4.630E-06
Average Conc (log_{10}M)	-10.561		
S.D Conc	0.788		

Sample 4	**1**	**2**	**3**
DNA only	-1.785E-04	-1.897E-04	-1.932E-04
DNA/RNA	-1.423E-04	-1.579E-04	-1.676E-04
Change	3.626E-05	3.178E-05	2.556E-05
Concentration	-8.983E+00	-9.745E+00	-1.080E+01
Average (μC)	31.197	**Average**	3.120E-05
S.D (μC)	4.387	**S.D**	4.387E-06
Average Conc (log_{10}M)	-9.844		
S.D Conc	0.747		

Sample 5	**1**	**2**	**3**
DNA only	-1.691E-04	-1.751E-04	-1.756E-04
DNA/RNA	-1.403E-04	-1.486E-04	-1.468E-04
Change	2.879E-05	2.646E-05	2.880E-05
Concentration	-1.025E+01	-1.065E+01	-1.025E+01
Average (μC)	28.019	**Average**	2.802E-05
S.D (μC)	1.103	**S.D**	1.103E-06
Average Conc (log_{10}M)	-10.385		
S.D Conc	0.188		

Table A1.9 The CT values obtained using known hsa-miR-21-5p concentrations in buffer.

Log [miR-21]	ΔCT mean
-8	8.078
-9	12.047
-10	17.067
-11	20.981
-12	25.139
-13	29.623
-14	33.297

Table A1.10 PCR CT values for the urine samples specified in Table 6.2 and their extrapolated concentrations using buffered calibration plot.

Sample	ΔCT mean	Extrapolated log_{10} [miR-21]
1	32.643	-13.768
2	30.170	-13.185
3	31.426	-13.481
4	31.554	-13.511
5	32.248	-13.675

Table A1. 11 The PCR values obtained for buffered hsa-miR-21-5p solutions that have been extracted prior to RT-PCR, and the expected values.

Log_{10}[miR-21]	ΔCT mean Expected	ΔCT mean observed	Observed log_{10}[miR-21]
-8	8.078	24.456	-11.840
-10	17.067	28.711	-12.842
-12	25.139	30.350	-13.228
-14	33.297	36.835	-14.755
-16	Not taken	36.063	-14.573

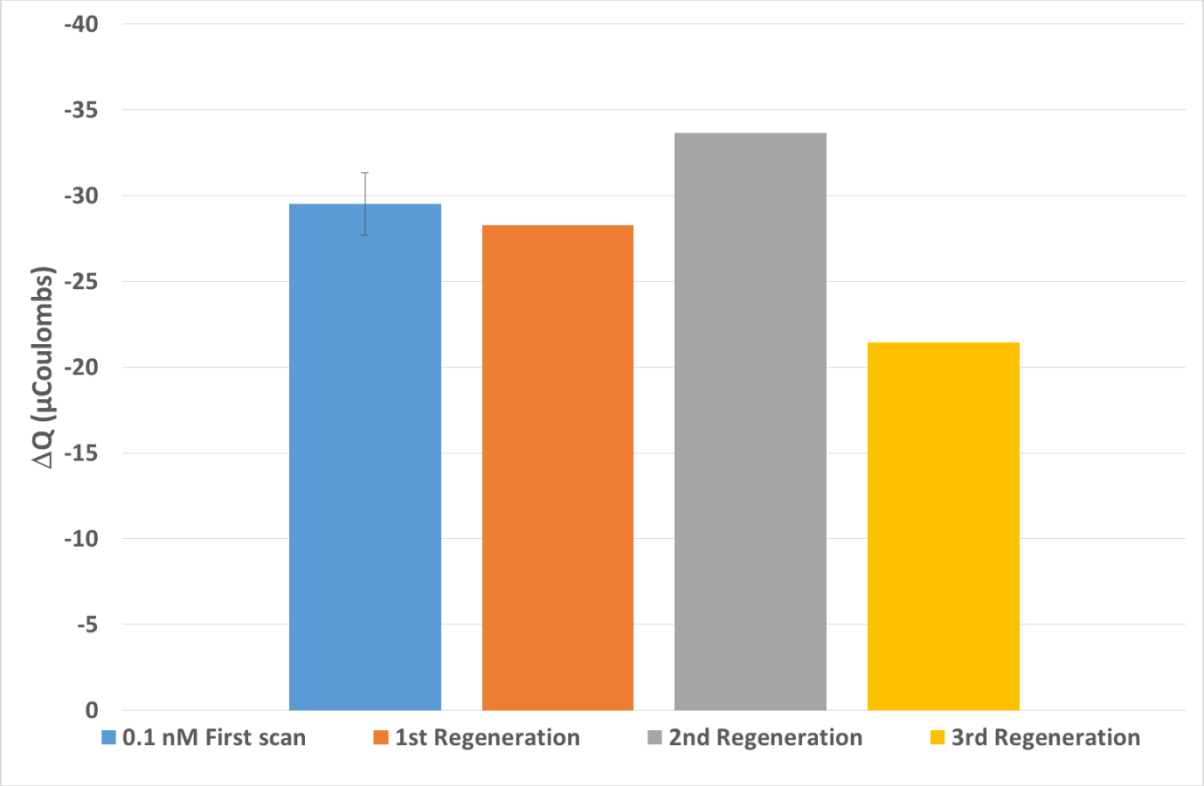

Figure A1.1 Data showing how the DNA/miRNA hybrid can be denatured and the anti-miR-21 probe re-used for detection of 10^{-10} M hsa-miR-21-5p following multiple heat treatment cycles.

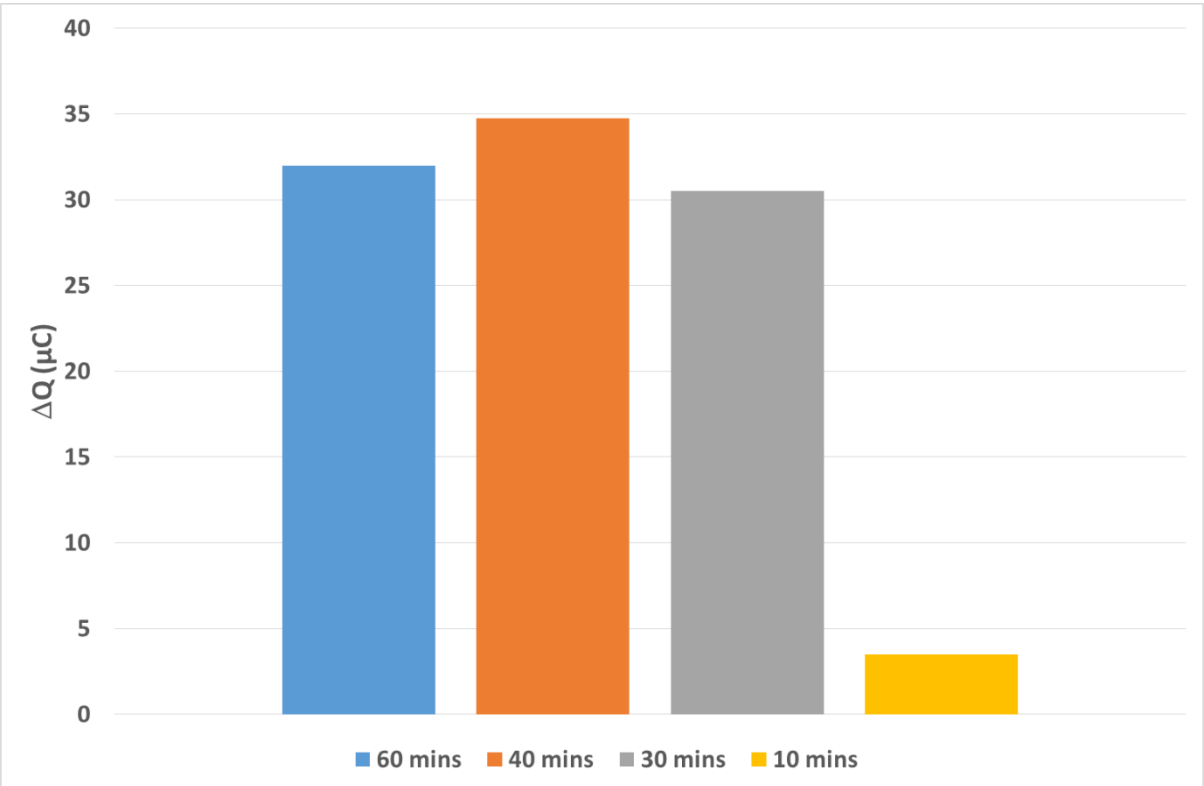

Figure A1.2 Coulometry data obtained after hybridising the hsa-miR-21-5p miRNA target (10^{-10} M) with the anti-miR-21 probe for different amounts of time.

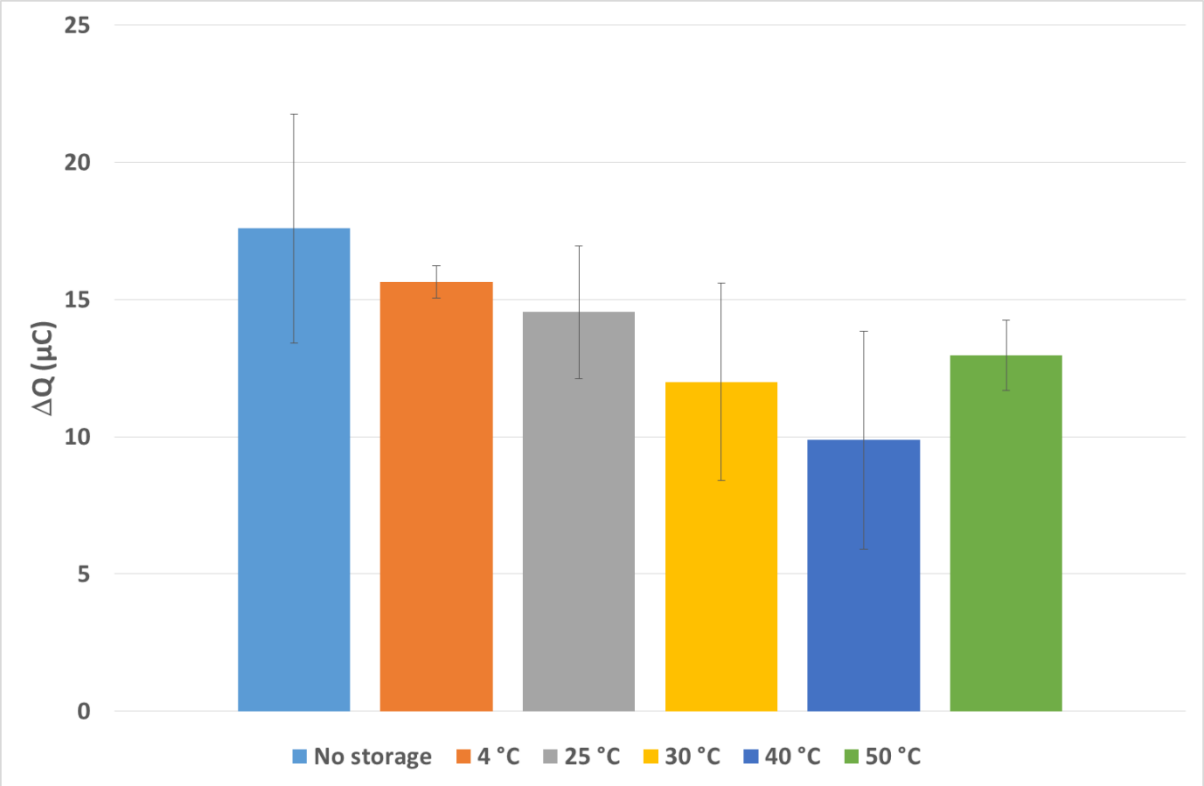

Figure A1.3 Data showing how the coulometry response changes when the anti-miR-21 probe is stored for 24 hours at different temperatures to simulate aging before being hybridised with 0.1 nM of hsa-miR-21-5p. The Arrhenius plot is calculated from the rate of decay at each temperature compared to the point of no storage.

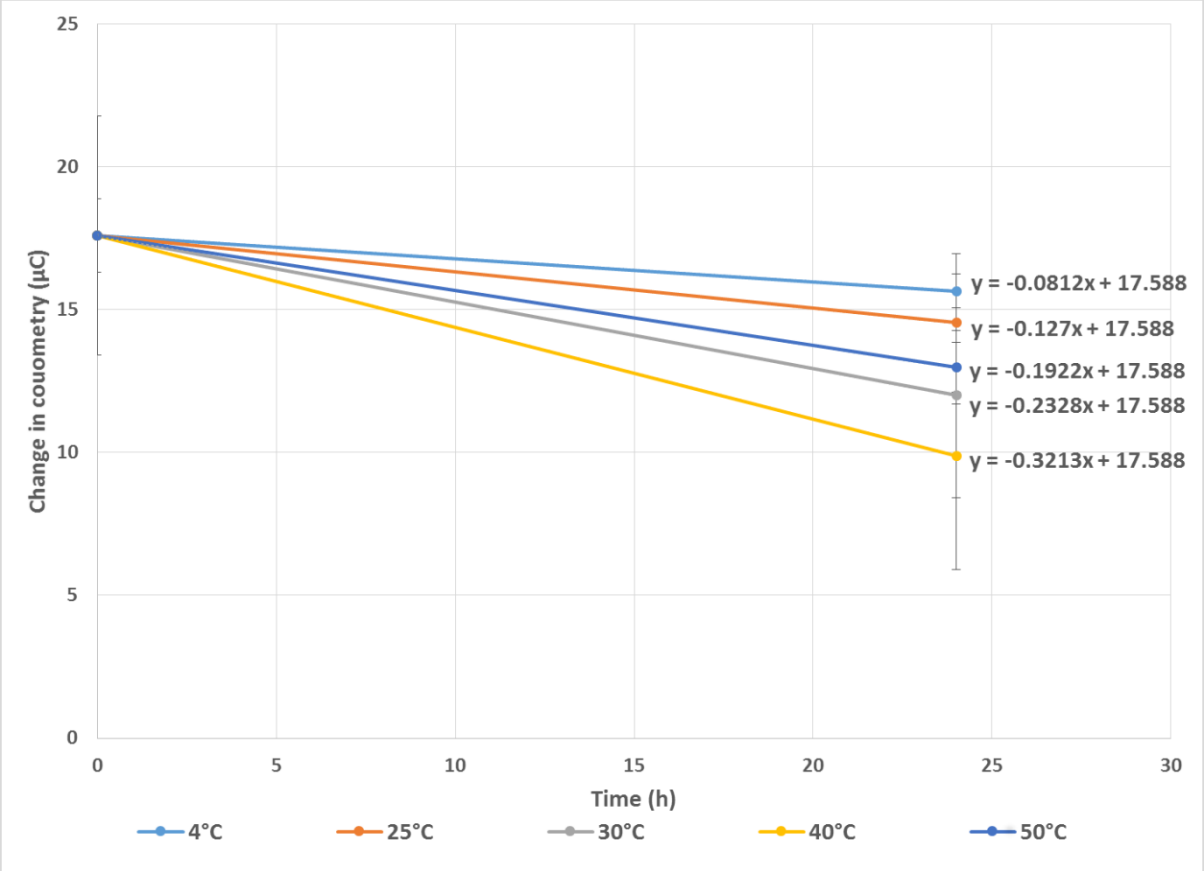

Figure A1.4 Data showing how the coulometry response changes when the anti-miR-21 probe is stored for 24 hours at different temperatures to simulate aging before being hybridised with 0.1 nM of hsa-miR-21-5p. Data plotted linearly for rate of change gradient.

Table A1.12 The data used to plot the Arrhenius plot and calculated storage lifetimes to 50% response.

	Signal at time zero (µC)	*17.59*	**Storage time (h)**	*24.00*							
T (°C)	**T (K)**	**Rate (µC/h/K)**	**1/T**	**ln rate**	**Actual Signal at 24 h**	**k first order (µC/h/K)**	**ln (k first order)**	**ln (k) from fit**	**k calc (µC/h/K)**	**t 90% first order from fit (h)**	**t 50% first order from fit (h)**
4.00	*277.15*	*0.08*	*3.61E-03*	*-2.51*	*15.64*	*4.89E-03*	*-5.32*	*-5.23*	*5.34E-03*	*19.74*	*129.88*
25.00	*298.15*	*0.13*	*3.35E-03*	*-2.06*	*14.54*	*7.93E-03*	*-4.84*	*-4.59*	*1.01E-02*	*10.38*	*68.30*
30.00	*303.15*	*0.23*	*3.30E-03*	*-1.46*	*12.00*	*1.59E-02*	*-4.14*	*-4.45*	*1.17E-02*	*9.03*	*59.38*
40.00	*313.15*	*0.32*	*3.19E-03*	*-1.14*	*9.88*	*2.40E-02*	*-3.73*	*-4.18*	*1.52E-02*	*6.92*	*45.50*
50.00	*323.15*	*0.19*	*3.09E-03*	*-1.65*	*12.97*	*1.27E-02*	*-4.37*	*-3.93*	*1.96E-02*	*5.39*	*35.44*

Appendix 2: Chapter 3 additional data.

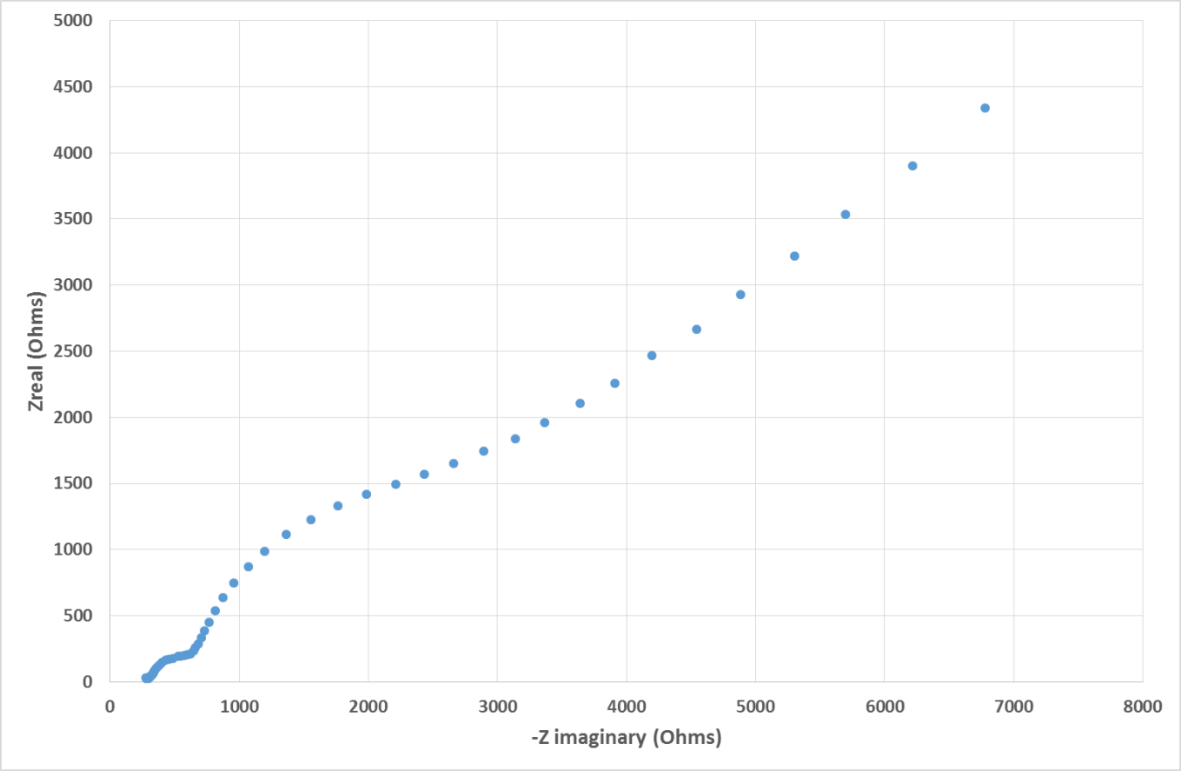

Figure A2.1 A Nyquist diagram obtained at 0.23 V and between 0.01Hz and 10 kHz using the 2 mm SPCE, this does not display the impedance behaviour previously observed so was not easily analysed and thus not used for prototyping. Performed using 5 mM $K_3[Fe(CN)_6]/K_4[Fe(CN)_6]$ in 0.1 M KCl electrolyte at room temperature

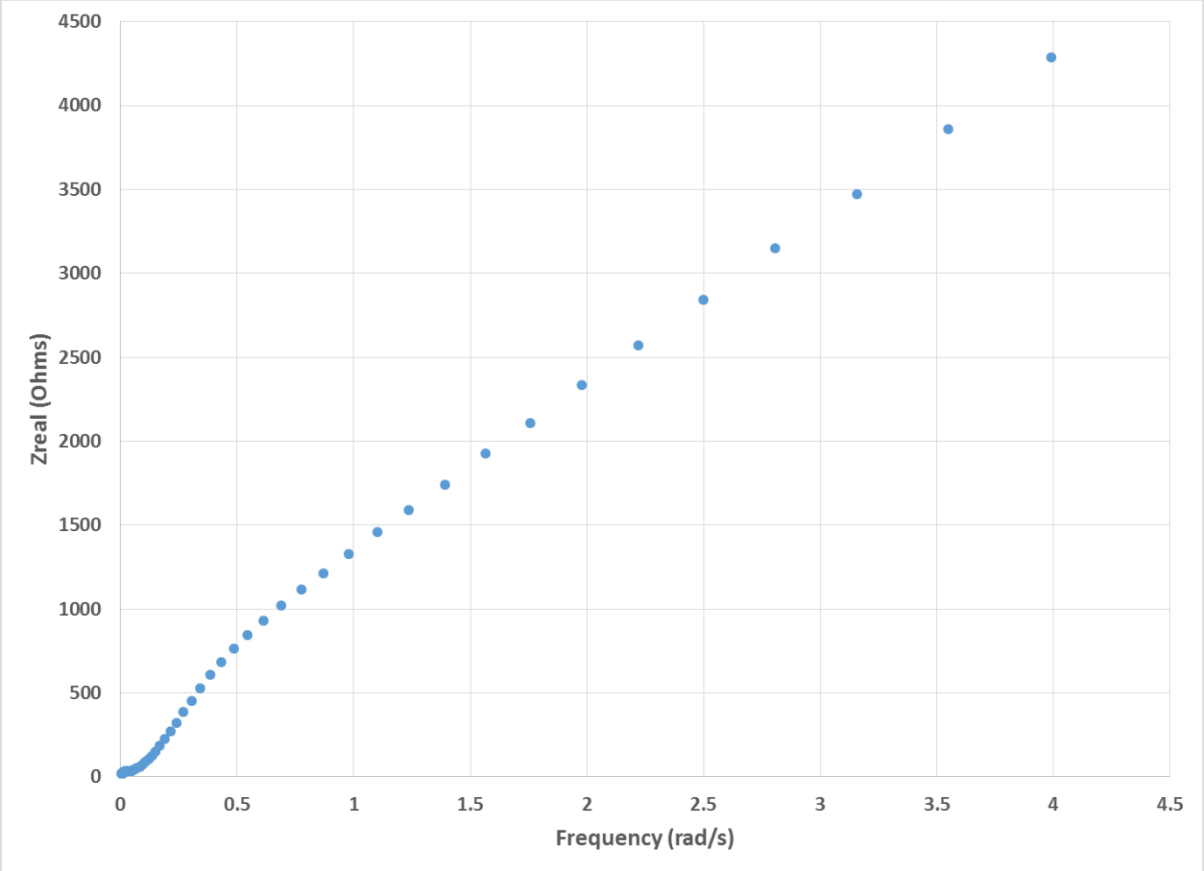

Figure A2.2 An example of the Warburg plot by plotting Z_{real} against 1/√Frequency (rad/s) obtained at 0.23 V and between 0.01 Hz ant 10 kHz. The intercept of the linear section is used as the readout. Performed using 5 mM $K_3[Fe(CN)_6]/K_4[Fe(CN)_6]$ in 0.1 M KCl electrolyte at room temperature

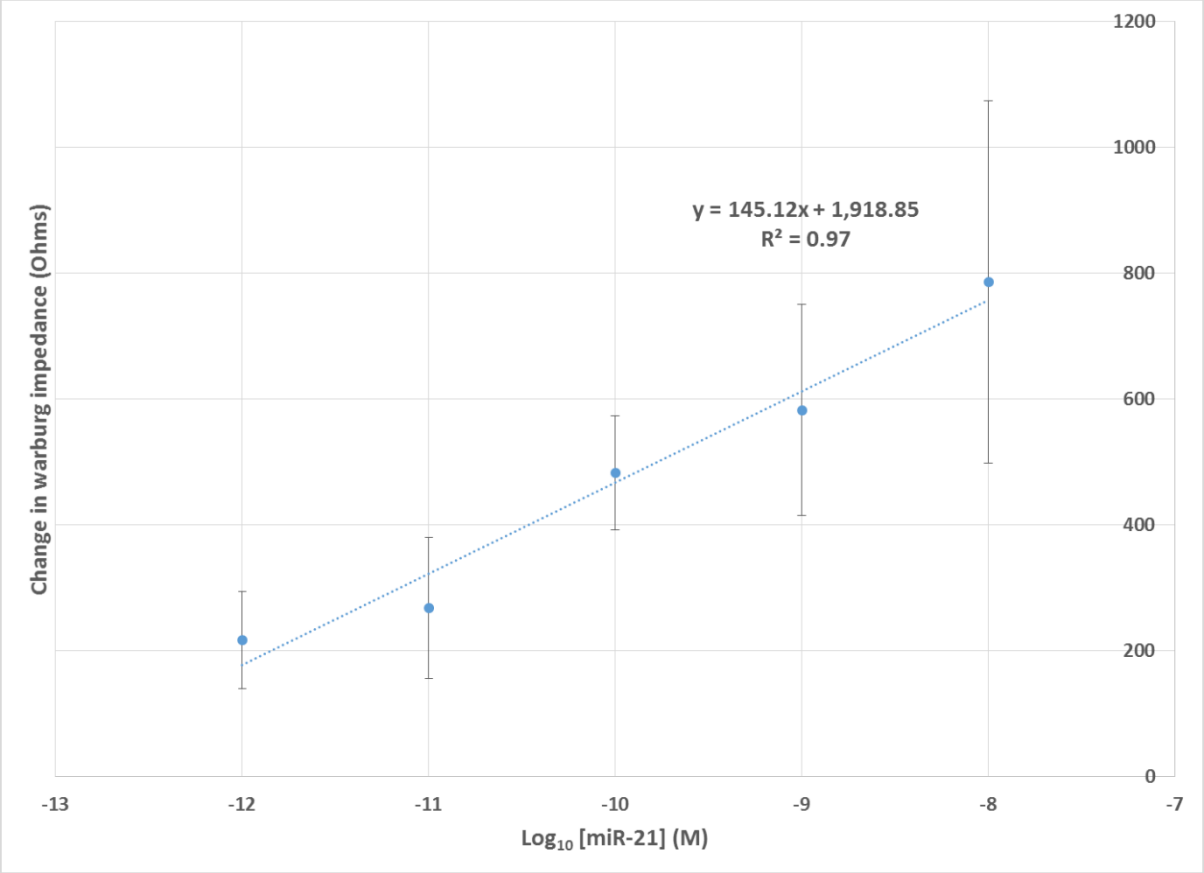

Figure A2.3 The calibration plot obtained following hybridisation of anti-miR-21 with its' hsa-miR-21-5p target, at different concentrations, for the 2mm SPCE design using the Warburg plot intercepts. Performed using 5 mM $K_3[Fe(CN)_6]/K_4[Fe(CN)_6]$ in 0.1 M KCl electrolyte at room temperature

Table A2. 1 The raw data obtained for the coulometric response (C) of using an anti-miR-21 probe strand for target hsa-miR-21-5p hybridisation at different concentrations using a 2 mm SPCE.

	Experiment number		
10^{-8} M	**1**	**2**	**3**
DNA only	-9.605E-05	-1.004E-04	-9.693E-05
DNA/RNA	-7.861E-05	-9.015E-05	-8.179E-05
Change	1.744E-05	1.021E-05	1.515E-05
Average (µC)	13.828		
S.D (µC)	3.016		
10^{-9} M	**1**	**2**	**3**
DNA only	-1.003E-04	-9.800E-05	-1.005E-04
DNA/RNA	-9.338E-05	-8.979E-05	-8.606E-05
Change	6.868E-06	8.207E-06	1.441E-05
Average (µC)	9.828		
S.D (µC)	3.285		
10^{-10} M	**1**	**2**	**3**
DNA only	-9.652E-05	-9.570E-05	-1.034E-04
DNA/RNA	-8.927E-05	-8.908E-05	-9.769E-05
Change	7.243E-06	6.620E-06	5.685E-06
Average (µC)	6.516		
S.D (µC)	0.640		

	Experiment number		
10^{-11} M	**1**	**2**	**3**
DNA only	-1.011E-04	-9.645E-05	-9.908E-05
DNA/RNA	-9.484E-05	-9.301E-05	-9.869E-05
Change	6.242E-06	3.445E-06	3.950E-07
Average (µC)	3.361		
S.D (µC)	2.388		
10^{-12} M	**1**	**2**	**3**
DNA only	-9.132E-05	-1.012E-04	-1.017E-04
DNA/RNA	-9.002E-05	-1.005E-04	-1.009E-04
Change	1.301E-06	7.500E-07	8.200E-07
Average (µC)	0.957		
S.D (µC)	0.245		

Table A2. 2 The raw data obtained for the coulometric response (C) of using an anti-miR-21 probe strand for target hsa-miR-21-5p hybridisation at different concentrations using a 3 mm SPCE.

	Experiment number		
10^{-8} M	**1**	**2**	**3**
DNA only	-172.406	-217.288	-267.604
DNA/RNA	-77.237	-156.146	-203.370
Change	95.168	61.143	64.234
Average	73.515		
S.D	15.363		
10^{-9} M	**1**	**2**	**3**
DNA only	-182.642	-204.860	-246.020
DNA/RNA	-118.884	-136.030	-190.294
Change	63.757	68.830	55.726
Average	62.771		
S.D	5.395		
10^{-10} M	**1**	**2**	**3**
DNA only	-195.087	-181.123	-223.022
DNA/RNA	-147.773	-98.777	-183.709
Change	47.314	82.346	39.312
Average	56.324		
S.D	18.688		
10^{-11} M	**1**	**2**	**3**
DNA only	-233.887	-196.151	-247.088
DNA/RNA	-197.893	-167.827	-220.612
Change	35.994	28.324	26.476
Average	30.264		
S.D	4.121		

	Experiment number		
10^{-12} M	**1**	**2**	**3**
DNA only	-246.873	-204.237	-193.162
DNA/RNA	-215.254	-174.604	-164.421
Change	31.619	29.633	28.740
Average	29.997		
S.D	1.203		
10^{-13} M	**1**	**2**	**3**
DNA only	-249.340	-199.746	-172.872
DNA/RNA	-234.993	-190.324	-147.710
Change	14.347	9.421	25.161
Average	16.310		
S.D	6.574		
10^{-14} M	**1**	**2**	**3**
DNA only	-206.268	-	-
DNA/RNA	-193.375	-	-
Change	12.892	-	-
Average	12.892		
S.D	-		

Table A2.3 The full set of LA-ICPMS data obtained for each of the target elements. Each performed in triplicate and the average concentration given in the main text (ppm). Given as appears on ICP-MS SQ report.

	C (ppm)				Cl (ppm)				S (ppm)			
Electrode Stage	**1**	**2**	**3**	**Average**	**1**	**2**	**3**	**average**	**1**	**2**	**3**	**average**
Blank	*211721*	*236005.9*	*238059.1*	***228595.3143***	*6111.725*	*6454.016*	*5848.901*	***6138.214***	*269.497*	*269.497*	*362.428*	***300.474***
ANSA	*253152.2*	*251746*	*260251.2*	***255049.8257***	*5720.552*	*5738.863*	*5592.197*	***5683.871***	*278.792*	*204.445*	*306.669*	***263.302***
ANSCl (Ace)	*57527.48*	*57180.02*	*57053.06*	***57253.52033***	*1032.781*	*1020.559*	*1020.56*	***1024.633***	-	-	-	**-**
ANSCl (hex)	*277762.1*	*266972.2*	*259855.3*	***268196.537***	*5598.312*	*5531.064*	*5610.527*	***5579.968***	*315.962*	*250.913*	*278.79*	***281.8883***
ANSm-DNA	*3823720*	*4465854*	*4686482*	***4325351.964***	*3404.047*	*4846.469*	*6454.197*	***4901.571***	*715.566*	*1040.825*	*1105.883*	***954.0913***
ANSm-DNA/miRNA	*1351657*	*1931509*	*2770329*	***2017831.861***	*965.556*	*1368.902*	*2267.278*	***1533.912***	*585.461*	*594.755*	*789.911*	***656.709***
ANSm-DNA/mismatch	*2878723*	*3009945*	*2758928*	***2882532.189***	*2799.083*	*2823.537*	*2572.946*	***2731.855***	*278.794*	*390.306*	*353.134*	***340.7447***

	P (ppm)				N (ppm)			
	1	**2**	**3**	**Average**	**1**	**2**	**3**	**average**
Blank	*229.245*	*200.142*	*196.983*	***208.79***	*39819619.4*	*39852444.4*	*38905033.7*	***39525699.17***
ANSA	*250.953*	*250.079*	*272.595*	***257.8757***	*37822344.4*	*37860323.4*	*37909336.1*	***37864001.31***
ANSCl (Ace)	*119.828*	*109.209*	*110.15*	***113.0623***	*7463540.7*	*7330612.75*	*7149341.32*	***7314498.256***
ANSCl (hex)	*4853.673*	*4804.94*	*4714.197*	***4790.937***	*36981367.5*	*36325585.6*	*36020754.5*	***36442569.2***
ANSm-DNA	*5527.563*	*6131.69*	*6534.057*	***6064.437***	*1371752144*	*1729855932*	*1987933436*	***1696513837***
ANSm-DNA/miRNA	*13371.55*	*9574.447*	*6545.92*	***9830.638***	*512539826*	*695589995*	*962937441*	***723689087.4***
ANSmDNA/mismatch	*276.626*	*295.916*	*277.231*	***283.2577***	*72305419*	*73504292.9*	*73912969.5*	***73240893.81***

Appendix 3: Chapter 4 additional data

Table A3.1 The first set of raw data obtained for the coulometric response (C) of using an anti-miR-21 probe strand for target hsa-miR-21-5p hybridisation at different concentrations using the 3 surfaced SPCE.

	Experiment number			Experiment number	
10^{-8} M	**1**	**2**	**10^{-11} M**	**1**	**2**
DNA only	-132.727	-174.895	**DNA only**	-126.611	-176.380
DNA/RNA	-47.131	-65.758	**DNA/RNA**	-41.620	-60.186
Change	85.596	109.137	**Change**	84.991	116.194
Average	97.366		**Average**	100.593	
S.D	11.771		**S.D**	15.601	
10^{-9} M	**1**	**2**	**10^{-12} M**	**1**	**2**
DNA only	-150.151	-179.100	**DNA only**	-137.934	-185.334
DNA/RNA	-65.135	-60.407	**DNA/RNA**	-41.179	-69.806
Change	85.016	118.693	**Change**	96.755	115.528
Average	101.854		**Average**	106.142	
S.D	16.838		**S.D**	9.386	
10^{-10} M	**1**	**2**	**10^{-13} M**	**1**	**2**
DNA only	-147.197	-182.758	**DNA only**	-141.043	-165.669
DNA/RNA	-52.852	-65.343	**DNA/RNA**	-45.573	-60.098
Change	94.344	117.415	**Change**	95.470	105.571
Average	105.879		**Average**	100.520	
S.D	11.535		**S.D**	5.051	

Table A3.2 The first set of raw data obtained for the coulometric response (C) of using an anti-miR-21 probe strand for target hsa-miR-21-5p hybridisation at different concentrations. Performed using the 3 surfaced SPCE and the Teflon wells.

	Experiment number				Experiment number		
10^{-8} M	**1**	**2**	**3**	**10^{-11} M**	**1**	**2**	**3**
DNA only	-95.112	-119.932	-150.532	**DNA only**	-97.840	-154.968	-144.661
DNA/RNA	-24.988	-28.059	-76.090	**DNA/RNA**	-31.077	-114.450	-105.265
Change	70.124	91.873	74.442	**Change**	66.763	40.518	39.396
Average	78.813			**Average**	48.892		
S.D	9.401			**S.D**	12.645		
10^{-9} M	**1**	**2**	**3**	**10^{-12} M**	**1**	**2**	**3**
DNA only	-139.450	-97.840	-141.787	**DNA only**	-162.750	-112.424	-102.448
DNA/RNA	-61.717	-35.435	-71.040	**DNA/RNA**	-102.592	-76.720	-62.827
Change	77.733	62.404	70.747	**Change**	60.158	35.704	39.621
Average	70.295			**Average**	45.161		
S.D	6.266			**S.D**	10.724		
10^{-10} M	**1**	**2**	**3**	**10^{-13} M**	**1**	**2**	**3**
DNA only	-95.112	-96.156	-118.325	**DNA only**	-127.084	-62.601	-113.039
DNA/RNA	-28.361	-30.616	-61.105	**DNA/RNA**	-81.928	-26.009	-56.556
Change	66.752	65.540	57.220	**Change**	45.156	36.592	56.483
Average	63.170			**Average**	46.077		
S.D	4.237			**S.D**	8.146		

Table A3. 3 The raw coulometry responses obtained for patient and control urine samples using a multiplexed electrode and Teflon wells.

	Experiment number				Experiment number		
miR-192	**C11005**			**miR-192**	**C11021**		
DNA only	-95.112	-119.932	-150.532	**DNA only**	-97.840	-154.968	-144.661
DNA/RNA	-24.988	-28.059	-76.090	**DNA/RNA**	-31.077	-114.450	-105.265
Change	70.124	91.873	74.442	**Change**	66.763	40.518	39.396
Average	78.813			**Average**	48.892		
S.D	9.401			**S.D**	12.645		
miR-191	**C11005**			**miR-191**	**C11021**		
DNA only	-139.450	-97.840	-141.787	**DNA only**	-162.750	-112.424	-102.448
DNA/RNA	-61.717	-35.435	-71.040	**DNA/RNA**	-102.592	-76.720	-62.827
Change	77.733	62.404	70.747	**Change**	60.158	35.704	39.621
Average	70.295			**Average**	45.161		
S.D	6.266			**S.D**	10.724		
miR-126	**C11005**			**miR-126**	**C11021**		
DNA only	-95.112	-96.156	-118.325	**DNA only**	-127.084	-62.601	-113.039
DNA/RNA	-28.361	-30.616	-61.105	**DNA/RNA**	-81.928	-26.009	-56.556
Change	66.752	65.540	57.220	**Change**	45.156	36.592	56.483
Average	63.170			**Average**	46.077		
S.D	4.237			**S.D**	8.146		
miR-192	**P12016**			**miR-192**	**P12026**		
DNA only	-95.112	-119.932	-150.532	**DNA only**	-97.840	-154.968	-144.661
DNA/RNA	-24.988	-28.059	-76.090	**DNA/RNA**	-31.077	-114.450	-105.265
Change	70.124	91.873	74.442	**Change**	66.763	40.518	39.396
Average	78.813			**Average**	48.892		
S.D	9.401			**S.D**	12.645		
miR-191	**P12016**			**miR-191**	**P12026**		
DNA only	-139.450	-97.840	-141.787	**DNA only**	-162.750	-112.424	-102.448
DNA/RNA	-61.717	-35.435	-71.040	**DNA/RNA**	-102.592	-76.720	-62.827
Change	77.733	62.404	70.747	**Change**	60.158	35.704	39.621
Average	70.295			**Average**	45.161		
S.D	6.266			**S.D**	10.724		
miR-126	**P12016**			**miR-126**	**P12026**		
DNA only	-95.112	-96.156	-118.325	**DNA only**	-127.084	-62.601	-113.039
DNA/RNA	-28.361	-30.616	-61.105	**DNA/RNA**	-81.928	-26.009	-56.556
Change	66.752	65.540	57.220	**Change**	45.156	36.592	56.483
Average	63.170			**Average**	46.077		
S.D	4.237			**S.D**	8.146		

Appendix 4: Sensors and Actuators B: Chemical publication.